FUNDAMENTAL SOLID MECHANICS STUDIES ON PLATE AND SHELL STRUCTURES WITH APPLICATIONS TO VIBRATION ANALYSIS OF HIGH-SPEED TRAINS

by

Arghavan Louhghalam

A dissertation submitted to The Johns Hopkins University in conformity with the requirements for the degree of Doctor of Philosophy.

Baltimore, Maryland

May, 2010

Abstract

In this thesis, new methods in solid mechanics are developed for analyzing vibrations in structural systems with particular emphasis on passenger cars in high-speed trains. Three interrelated problems are examined.

The first part of the thesis is on the propagation of vibration energy from the wheels to the car body. System identification is used to estimate the dynamic properties of the suspension using acceleration data from full speed test runs of a prototype train. Fatigue reliability is assessed using deterministic and stochastic methods, and static and dynamic fatigue test procedures are developed for an experimental test facility at the Korea Railroad Research Institute.

The highest stresses are found to be at the corners of the windows and doors of the aluminum car body panels. In the next part of the thesis, a semi-analytical method is developed for analyzing these stress concentrations. The basic idea is to combine a conformal mapping approach based on complex variable theory with finite element analysis. In this manner, a relatively coarse mesh can be used to predict highly localized stresses around openings in plates under bending loads. The approach is useful for complex structures

where it would be difficult to include fine meshes around every panel opening.

Since advanced car body designs tend to have tubular frames, the last part of the thesis focuses on free vibrations of orthotropic cylindrical shells. Perturbation theory is used to derive closed-form analytical expressions for the frequency-wavelength dispersion relation and for the natural frequencies and mode shapes. These new analytical results provide insight into the characteristics of cylinder vibrations and are also useful for system identification.

Advisor: Dr. Takeru Igusa

Readers: Dr. Benjamin W. Schafer and Dr. James K. Guest

Acknowledgements

I would like to thank my advisor Professor Takeru Igusa for his generous support, continuous guidance and inspiration during the course of my doctoral work at the Johns Hopkins University. He is a wonderful mentor whose great vision and high standards has helped me shape my academic life.

My special thanks goes to my committee members and the readers of this thesis, Professor Ben Schafer and Professor James Guest for the precious time they put in reading my dissertation. Their invaluable comments and suggestions are greatly acknowledged. I would also like to thank Professor Sanjay Arwade of University of Massachusetts at Amherst for the role he has played in enhancing my academic abilities. Financial and technical support from the Korea Railroad Research Institute (KRRI) is gratefully appreciated. Drs. Kihwan Kim, Choonsoo Park, and Sunghoon Choi are the key researchers from KRRI that made this support possible.

I am also very thankful to my parents, Mohammadreza and Maliheh and my two sisters, Yasaman and Ladan, without whose encouragement, I would not be able to complete this journey.

ACKNOWLEDGEMENTS

During my PhD studies I made many wonderful friends. I would like to thank all my dear friends and fellow graduate students, in civil engineering department, especially my office mates who always provided me with their delightful friendship and valuable scientific comments.

Finally I am particulary grateful to my dear husband, Mazdak, for his patience, unconditional love and for all the valuable discussions I have had with him during these years regarding my research. This thesis is dedicated to him who has been a tremendous source of support and encouragement.

Dedication

To my beloved husband, Mazdak

Contents

List of Tables

LIST OF TABLES

List of Figures

Chapter 1

Introduction

Many structural systems such as automotive, naval, and aerospace vehicles as well as fixed structures such as buildings and bridges are subject to dynamic loads. Under certain situations, such as when the frequency of the vibration is close to one of the natural frequencies of the structure, the dynamic loads can lead to excessive displacements and stresses. In some structures, repetitive dynamic loads lead to fluctuating stresses which may cause failure due to fatigue. Therefore the study of dynamic response of structures is important for design. In high performance structures, which tend to be lightweight and flexible, the analysis of vibration is even more important since these structures are more susceptible to vibration.

The purpose of this thesis is to develop new methods in solid mechanics that can be used for analysis of vibrations of structural systems. Here the focus is on the vibration analysis of the passenger car body of high-speed trains. In the course of the development of these

methods, it was found that vibration in high-speed trains is a complex problem with a vast number of phenomena that can be explored using numerical, analytical and experimental techniques. While this thesis is not meant to be a comprehensive study of those vibration phenomena, all three types of exploration techniques are used. The focii of this research were on three interrelated topics: the propagation of vibration energy from the wheels to the car body frame and its effect on fatigue reliability, the stress concentrations at the corners of window and door openings and the overall vibration characteristics of tubular structures.

The HSR-350x, a highly instrumented prototype of the most recent generation of high-speed trains in South Korea, was used as the example system for this study. Since the response data under test run conditions and a 650,000 degree of freedom NASTRAN model were provided by the Korea Railroad Research Institute, it was possible to focus on more fundamental issues in this research.

In the first part of this thesis, the dynamic response of a passenger car body in a high-speed train is examined and failure due to fatigue is investigated. The car bodies are lightweight structures made of aluminum. The applied cyclic loadings are due to different sources of vibration such as rail and wheel irregularities. Since the dynamic loads have random fluctuations in time, random vibration techniques were used to examine the relationships between the statistical characteristics of the excitation and response. The goal of this study is to determine the fatigue reliability of the car body and to recommend fatigue test procedures.

In the next part of the thesis, highly localized stresses near the openings in the wall

panels for doors and windows are examined. Since these stresses can lead to fatigue failure, many studies have been performed on the stress concentrations around such geometric irregularities using analytical methods, numerical simulations and experiments. Herein, the analytical methods based on theory of elasticity are used to find the stress distribution around openings. These methods are relatively complicated and are applicable only for simple loads. To obtain these stresses using finite element analysis, fine meshes need to be used around each opening, making the model and analysis more complicated and computationally time consuming. Therefore a more practical solution for finding the stress concentrations is of interest. Herein, a semi-analytical approach is proposed to incorporate the result of a coarse mesh finite element analysis with an analytical solution to predict the stress concentration around plate openings.

In the last part of the thesis, the global characteristics of car body vibrations are examined. Since advanced car body designs for high-speed rail in Asia and Europe tend to have tubular frames, cylinders are used to represent the canonical shape of these designs. Isotropic, orthotropic and more general anisotropic material properties are considered. A number of different shell theories based on different assumptions for the strain-displacement relationships lead to a variety of equations of motion. In many cases, such as when the cylinder is free at its ends, these equations do not have a closed-form solution. Researchers have proposed several numerical and approximate analytical approaches to solve for the natural frequencies and mode shapes of these cylinders. Some of these methods use numerical analysis to solve for the equilibrium equations with the boundary

conditions. Others use energy approaches such as the Rayleigh-Ritz method by assuming a specified mode shape for the cylinder. While the Rayleigh-Ritz methods are relatively simple to implement, the mode shapes in many cases only approximately satisfy the boundary conditions. In the last part of the thesis, a perturbation method is used to find the natural frequencies and mode shapes of a vibrating cylinder. The goal was to derive relatively simple expressions for the dispersion relation and modal properties using a small number of parameters. It is shown that these expressions are useful in their own right because they lead to enhanced insight into the characteristics of cylinder vibrations and are also useful for system identification.

1.1 Road map of the dissertation

The chapters of this dissertation are organized as follows.

In Chapter 2, the characteristics of the response of the passenger car body is studied. Experimental acceleration measurements along with the results of a finite element analysis of the car body are used for system identification of the dynamic properties of the suspension. Using these frequency dependent properties of the suspension, the power spectral density of stresses in the car body is also calculated.

Chapter 3 focuses on the study of fatigue in the car body due to the dynamic loads. The power spectral density of stress is used in assessing fatigue reliability. By examining the stress patterns in the car body due to harmonic loads, loads for full-scale fatigue tests are

proposed.

In Chapter 4, the stress concentrations around plate openings are studied. After a brief review of the method of complex variables [Muskhelishvili, 1975], some new analytical results are derived for finding the stress distribution around holes. Unlike previous methods, a least squares technique is used instead of a contour integral for satisfying the boundary conditions at the plate opening. It is then shown how the analytical results can be used to enhance the results of coarse mesh finite element analyses to estimate stress concentrations around rectangular openings.

In Chapter 5, the free vibrations of cylinders is examined. The mechanics and vibration of cylindrical shells are briefly reviewed. A numerical method for solving the exact equations for the natural frequencies and mode shapes is also reviewed and compared with the energy approach for solving the free vibration problem.

In Chapter 6, perturbation is used to find approximate analytical expressions for the dispersion relation between the frequency and wavelength and to develop a simple approach to obtain the cylinder modal properties. It is shown how the results provide insight into the characteristics of cylinder vibration. The results are also useful for identifying the basic material properties of the cylindrical shell given experimental data.

Concluding remarks and future research directions are presented in Chapter 7.

Chapter 2

Propagation of vibration energy from the bogies to the car body frame

2.1 Introduction

Many researchers including T.X. Wu and D.J. Thompson [2000, 2001], Farm [2000], T.X. Wu and D.J. Thompson [2003], M. Heckl et al. [1996], D.J. Thompson and C.J. Jones [1999], I.L. Ver et al. [1976] studied different sources of noise and vibration in trains and investigated their effect on the comfort and reliability of the structure. Rolling, impact and squeal noise are different categories of noise due to rail/wheel interaction that have been reviewed in detail by D.J. Thompson and C.J. Jones [1999].

Rolling noise is due to roughness, the small scale unevenness between the rail and wheel, which results in high frequency vibration. If the roughness is small, the rail/wheel

interaction is linear which means that a linear spring can be used to model the contact between rail and wheel, while when the roughness is large or the car body is very light, nonlinear behavior must be considered [T.X. Wu and D.J. Thompson, 2000].

Impact noise is generated due to rail discontinuities such as joints and switches and wheel discontinuities such as flattened wheel segments caused by braking [I.L. Ver et al., 1976]. The train speed is an important parameter in the latter kind of impact noise, since the wheel is separated from the rail at the discontinuities if the train speed is higher than a critical speed. Noise generation is completely different above and below this threshold speed.

The stiffness of the rail is also an important parameter in impact noise generation. Resiliently supported rails need higher speeds to lose their contact with the wheel compared with rigidly supported rails, since they can easily stay in contact with the wheel. They can also follow the shape of the contact surface easier and therefore impose less impact forces with the same speed [I.L. Ver et al., 1976].

Another important source of vibration is due to passage over the periodically placed sleepers. The sleeper passing frequency is equal to $f_s = V/L$, where V is the train speed and L is the sleeper distance. Farm [2000] and T.X. Wu and D.J. Thompson [2003] studied the effect of sleeper passing frequency on the vibrations of the passenger car.

The wheel passing frequency $f_w = V/a$ is also another source of noise where a is the distance between two wheels in a bogie.

The ride comfort of trains is also very important and it is usually affected by the above

sources of vibrations. Y. G. Kim et al. [2008] determined the ride comfort for the HSR350x high speed train. Ride comfort is evaluated considering different parameters such as train speed, track conditions and vibrations.

A number of studies have also been performed on the fatigue reliability of high speed trains. Kim [2006] studied the fatigue strength of the bogie in tilting trains using a combination of finite element analyses and static tests. S. I. Seo et al. [2005] performed full-scale dynamic fatigue tests on urban transit cars and compared the results with static tests and finite element analyses.

2.2 Motivation and research goal

Fatigue in the car body is due to repeated cyclic loads. There are two main sources of cyclic loads on the car body. The first is due to the vibrations from the track, wheel and bogie. The second is due to the pressure fluctuations when the train travels through tunnels. The goal of this study is to determine the relationships between the first sources of loads and the cyclic stresses within the car body. The effect of pressure fluctuations is not considered in this study.

The direct approach for evaluating fatigue loads is not economical because of the multiple, complex sources of loads and the numerous unknown locations of critical stress. In other words, it is too costly to test a car body for the combined vibration loads and to check the stresses in various locations. One of the main goals of this research is to find a systems-

level approach for evaluating fatigue loads. The systems-level approach would combine information from different sources to make reliability predictions for fatigue-related safety. The four main sources of information for this reliability study are:

1. Vibration data from previous high speed trains (HST). Vibration from the HSR-350x (a previously built HST) will be used to develop models for the vibration and load for the new HST.

2. Stochastic models for the loads. Extrapolation is needed to extend the data from the previous HST to the higher speed of the new HST. Stochastic analysis is also needed to describe the randomness in the loads.

3. Finite element model (FEM) for the car body. In the design phase, the FEM can be used for predicting stresses throughout the car body due to vibrations. FEM is useful for loads up to the mid-frequency range (100 Hz).

4. Reliability analysis for fatigue. In usual fatigue analysis, the predicted stress cycles are input into a fatigue criterion to obtain a probability of fatigue failure. For the new HST, however, it is necessary to expand this analysis to include several sources of uncertainties and randomness.

The systems-level approach would result in a comprehensive reliability analysis of fatigue and provide a better understanding of the behavior of the car body under vibration loads. However, to develop specifications, it is necessary to reduce these results of the reliability analysis into simple criteria. These criteria must then be checked using economical tests.

Hence, the second main goal of this research is to develop a testing procedure for car bodies for fatigue reliability. In general, it is difficult, expensive and impractical to perform full-scale fatigue vibration tests. With the systems-level approach, however, it is possible to use simplified equivalent static and harmonic tests to approximate the effects of vibration loads due to the motion of the bogies.

In this chapter, a model for predicting car body stresses due to vibrations at the underlying bogies is developed. The chapter begins with a review of random vibration techniques needed in this analysis. Then the response characteristics of the HSR-350x is studied using measured acceleration data during high-speed test runs along with a NASTRAN model provided by KRRI. Then using system identification techniques, the frequency dependent properties of suspension between the car body and bogie is determined. This model for the suspension is used to find the ratio of predicted car body stresses over the bogie acceleration (stress transfer function). The spatial patterns of stress distribution in the car body are also studied.

2.2.1 Random vibration theory: A brief review

Let $X(t)$ be a random process. The collection of the different realizations of the random process is called an ensemble. The mean value of the the random process is:

$$\mu_X(t) = E[X(t)]$$

where $E[\cdot]$ is the expected value operator which is evaluated across the ensemble. The second moment of a random process, the auto-correlation function, is expressed as follows:

$$R_{XX}(t,s) = E[X(t)X(s)]$$

To determine the relation between two random processes, consider another random process $Y(t)$. The cross-correlation between random processes $X(t)$ and $Y(t)$ is:

$$R_{XY}(t,s) = E[X(t)Y(s)]$$

A random process $X(t)$ is called *strictly stationary* if all of its probability distribution functions are invariant of time. The term *weakly stationary* is used for the random processes whose first and second moments do not depend on absolute time. For a stationary process therefore, one can write:

$$\mu_X(t) = \mu_X(t+\tau)$$

$$R_{XX}(t,t+\tau) = E[X(t)X(t+\tau)] = R_{XX}(\tau)$$

$$R_{XY}(t,t+\tau) = E[X(t)Y(t+\tau)] = R_{XY}(\tau)$$

The correlation coefficient or normalized covariance between two random processes is defined as:

$$\rho_{XY} = \frac{E[(X-\mu_X)(Y-\mu_Y)]}{\sigma_X \sigma_Y}$$

where σ_X and σ_Y are the standard deviations of random processes X and Y respectively. Therefore for a stationary process the cross-correlation is always bounded:

$$-\sigma_X\sigma_Y\rho_{XY} + \mu_X\mu_Y \leq R_{XY}(\tau) \leq \sigma_X\sigma_Y\rho_{XY} + \mu_X\mu_Y$$

For most random processes the correlation coefficient goes rapidly to zero as τ approaches infinity which implies that for zero-mean random processes one can find the Fourier transforms of the auto-correlation and cross-correlation functions.

The auto-power spectral density (PSD) of a stationary random process is the Fourier transform of the auto-correlation function:

$$S_X(\omega) = \frac{1}{2\pi}\int_{-\infty}^{\infty} R_X(\tau)e^{-i\omega\tau}d\tau$$
$$R_X(\tau) = \int_{-\infty}^{\infty} S_X(\omega)e^{i\omega\tau}d\omega$$

Since the auto-correlation function is even, the auto-PSD is real and even. It can also be shown that the auto-PSD is a nonnegative function. The Wiener-Khinchin theorem states the useful result that the area under the auto-PSD is the mean square of the random process:

$$R_X(\tau = 0) = E\left[X(t)^2\right] = \int_{-\infty}^{\infty} S_X(\omega)d\omega$$

The cross-PSD of two random processes is:

$$S_{XY}(\omega) = \frac{1}{2\pi}\int_{-\infty}^{\infty} R_{XY}(\tau)e^{-i\omega\tau}d\tau$$

Since $R_{XY}(\tau) = R_{YX}(-\tau)$, it can be concluded that $S_{XY}(\omega) = S^*_{YX}(\omega)$, where the superscript $*$ denotes the complex conjugate.

The power spectral density is often estimated using the Fourier transform $X(\omega)$ of the random process $x(t)$ as follows:

$$S_{XX}(\omega) = \frac{2\pi}{T}E\left[|X(\omega)|^2\right]$$

where T is the duration of the essentially stationary portion of the random process, and the random process is windowed with respect to this duration (and additional scale factors are used in approximating the Fourier transform according to the type of window used).

2.2.1.1 Time domain random vibrations

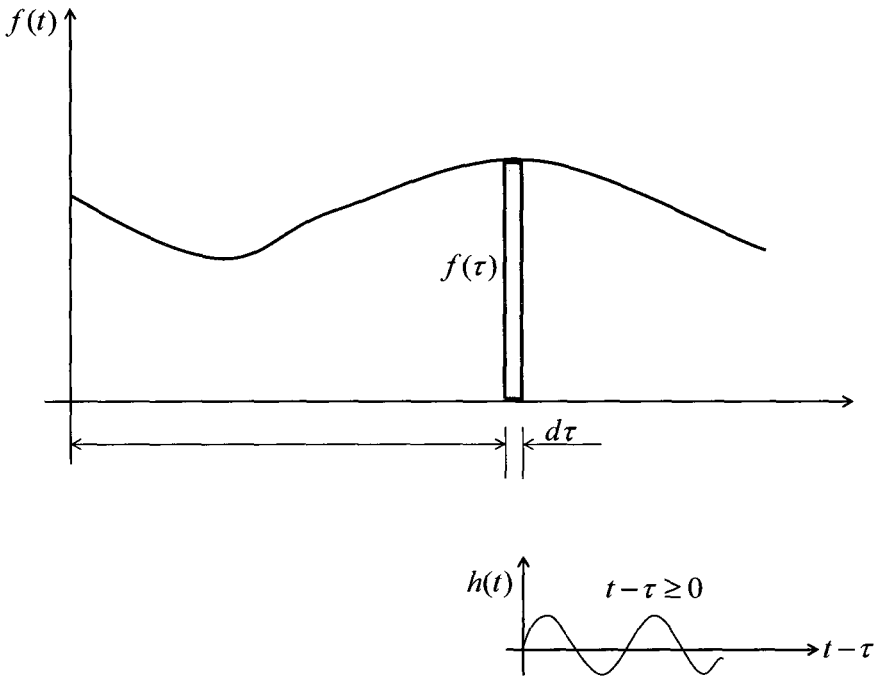

Figure 2.1: The use of impulse response function for finding the response due to a general load (after Clough and Penzien [1993]).

It is usual to study the dynamic characteristics of a system by examining its response due to an impulsive load. This load can be theoretically represented by the Dirac delta

function:

$$f(t) = I\delta(t)$$

where I is a constant representing the magnitude of impulse. The time integral of the force is simply:

$$\int_{-\infty}^{\infty} f(t)dt = I$$

The response of an oscillator due to a unit impulse $I = 1$ at $t = 0$ is called the impulse response function $h(t)$ and can be evaluated by solving the following equation of motion:

$$m\ddot{h}(t) + c\dot{h}(t) + kh(t) = \delta(t)$$

where m, c and k are the mass, damping and stiffness of the oscillator. Since the impulse has a short duration, for $t > 0$ the oscillator is under free vibration and the equations of motion can be written in homogenous form:

$$m\ddot{h}(t) + c\dot{h}(t) + kh(t) = 0$$

Using Newton's second law, the change of the momentum due to the impulse load is $m\Delta v = I = 1$. Since the mass is initially at rest the velocity after the impulse would be $v = 1/m$. The free vibration response of the oscillator with zero initial displacement and initial velocity of $v_0 = 1/m$ is:

$$h(t) = \frac{1}{\omega_d} e^{-\omega\xi t} \sin(\omega_d t)$$

where ω is the undamped natural frequency of the oscillator, $\xi = c/2m\omega^2$ is the damping ratio and $\omega_d = \omega\sqrt{1-\xi^2}$ is the damped natural frequency.

If the system is linear, a general loading can be expressed as the superposition of impulse loads of different magnitudes $f(\tau)d\tau$ at different times τ as shown in Figure 2.1. The response of an oscillator to general loads can then be evaluated using the impulse response function:

$$y(t) = \int_{-\infty}^{t} h(t-\tau)f(\tau)d\tau$$

2.2.1.2 Frequency domain random vibrations

Another approach to find the characteristics of a linear dynamic system is to study the response to a unit harmonic input:

$$f(t) = e^{i\omega t}$$

The steady state response of the oscillator is:

$$y(t) = H(\omega)e^{i\omega t}$$

where $H(\omega)$ is the frequency response function. Substituting $y(t)$ in the equations of motion one can write:

$$\left(-m\omega^2 + ic\omega + k\right) H(\omega) = 1$$

Dividing the equation by mass m, the frequency response function can be expressed as:

$$H(\omega) = \frac{1}{-\omega^2 + 2i\xi\omega\omega_n + \omega_n^2}$$

where ω_n is the natural frequency of the oscillator.

The relation between input and response can be expressed in terms of the frequency response function. Let $F(\omega)$ be the Fourier transform of the input excitation and let $X(\omega)$

and $Y(\omega)$ be the responses in the frequency domain such that:

$$X(\omega) = H_x(\omega)F(\omega)$$

$$Y(\omega) = H_y(\omega)F(\omega)$$

The mean value and auto-power spectral density of the response can be expressed as:

$$\mu_X(\omega) = H_x(\omega)\mu_F(\omega)$$

$$S_{XX}(\omega) = |H_x(\omega)|^2 S_{FF}(\omega)$$

The cross-power spectral density between the input excitation and response can be written as:

$$S_{XF}(\omega) = H_x(\omega)S_{FF}(\omega) \tag{2.1}$$

Finally the cross-power spectral density between two responses $X(\omega)$ and $Y(\omega)$ is:

$$S_{XY}(\omega) = H_x(\omega)H_y^*(\omega)S_{FF}(\omega)$$

2.2.1.3 Relation between the impulse response and frequency response function

Since the response characteristics of an oscillator can either be represented by the impulse response function $h(t)$ or the frequency response function $H(\omega)$, it is useful to determined their relationship. Let $Y(\omega)$ be the Fourier transform of the response $y(t)$:

$$Y(\omega) = \frac{1}{2\pi}\int_{-\infty}^{\infty} y(t)e^{-i\omega t}dt$$

Writing the response $y(t)$ in term of the impulse response function:

$$Y(\omega) = \frac{1}{2\pi} \int_{-\infty}^{\infty} \left(\int_{-\infty}^{\infty} h(\theta) f(t-\theta) d\theta \right) e^{-i\omega t} dt$$

and changing the variable $t' = t - \theta$ one can rewrite the above equation as:

$$Y(\omega) = \frac{1}{2\pi} \int_{-\infty}^{\infty} h(\theta) \left(\int_{-\infty}^{\infty} f(t') e^{-i\omega(t'+\theta)} dt' \right) d\theta$$

$$Y(\omega) = \left(\int_{-\infty}^{\infty} h(\theta) e^{-i\omega\theta} d\theta \right) \left(\frac{1}{2\pi} \int_{-\infty}^{\infty} f(t') e^{-i\omega t'} dt' \right)$$

$$Y(\omega) = F(\omega) \left(\int_{-\infty}^{\infty} h(\theta) e^{-i\omega\theta} d\theta \right)$$

Comparing the above with $Y(\omega) = H(\omega)F(\omega)$ it is concluded that [Newland, 1995]:

$$H(\omega) = \int_{-\infty}^{\infty} h(\theta) e^{-i\omega\theta} d\theta$$

2.3 Stress prediction model

As indicated in section 2.2 this study focuses on two main goals: the analysis of fatigue reliability and the development of testing procedures. To achieve these goals, it is necessary to build a model for predicting stresses. Here a model is developed using two sources of information: the measured accelerations of the car body and bogies and the finite element model of the car body. These are integrated into a stress transfer function, which is the fundamental function that relates the bogie acceleration to car body stresses.

2.3.1 Response characteristics

In this section the characteristics of the response of the high speed train is determined by studying the relationship between the bogie and car body responses.

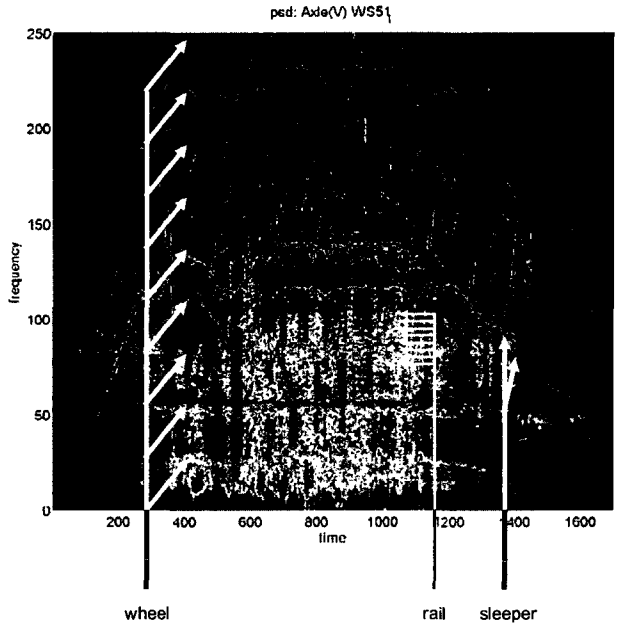

Figure 2.2: Time dependent PSD of the axle.(Time in seconds, frequency in Hz.)

2.3.1.1 Review of previous studies

On the HSR-350x, accelerometers were installed in the car body, bogies and axles. The analysis of the recorded accelerations was documented in another study [Igusa, 2008]. In

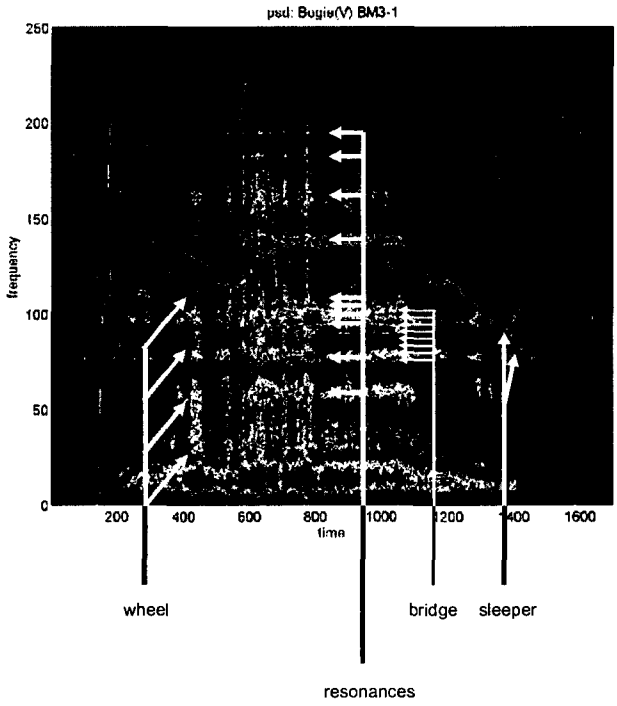

Figure 2.3: Time dependent PSD of the bogie.(Time in seconds, frequency in Hz.)

that study, the short-term Fourier transform (STFT) was used to obtain the time-varying Fourier transform of the response. Much of the vibration load is dependent on the velocity of the train, and since a simple PSD will not show this velocity-dependent behavior, the time-dependent PSD was used. The time dependent PSD of the axle bogie and car body are shown in Figures 2.2, 2.3 and 2.4 respectively.

It is well known that vehicles with wheels such as trains have vibration loads with frequencies that are proportional to the velocity. These are known as the kinematic vibration loads. The kinematic vibrations are related to a length scale, such as the spacing of the

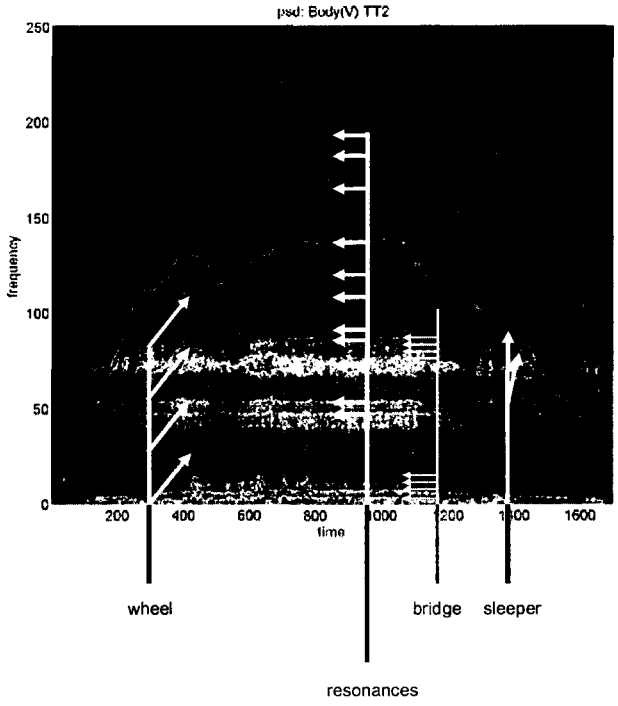

Figure 2.4: Time dependent PSD of the car body.(Time in seconds, frequency in Hz.)

sleepers or the circumference of the wheel. The fundamental frequency of the kinematic vibration is obtained by the simple formula:

$$\text{fundamental kinematic frequency} = \frac{\text{train speed}}{\text{length scale}} \tag{2.2}$$

Therefore, for each kinematic source for vibration, there will be a length scale and a corresponding fundamental kinematic frequency. This means that the response due to this kinematic source has a frequency proportional to the train speed. In the time-dependent PSD, this response appears as a curve with the same shape as the plot of the train speed

(vertical axis) with respect to time (horizontal axis). The kinematic excitations have sharp peaks while the resonances are broad peaks. If the kinematic source such as the sleepers causes a nearly sinusoidal response, then most of the response is at the fundamental kinematic frequency. If the kinematic source such as the wheels has a more irregular response, then there will be responses at higher multiples of the fundamental kinematic frequency due to the harmonic nature of the vibrations:

$$\text{higher kinematic frequencies} = i \times \frac{\text{train speed}}{\text{length scale}} \tag{2.3}$$

where $i = 2, 3, ...$ In Figures 2.2, 2.3 and 2.4 one can see three main sources of kinematic vibrations:

- Sleepers: The vertical profile of the rail has peaks at the sleepers and valleys between the sleepers. This causes a nearly sinusoidal acceleration of the axle. When the train is traveling at approximately 300 km/hr = 83 km/s, the sleeper traveling frequency is approximately 83 km/s / 0.6 m = 138 Hz. The response due to the sleeper is indicated by the fairly prominent curve in Figures 2.2 and 2.3. This curve has the same shape as the train speed plotted versus time.

- Wheel irregularities: The wheel has irregularities and flat spots due to braking and other routine wear. Since the response of the axle due to the rotation of the wheel is periodic, the PSD will have responses appearing at periodic frequency intervals as given by equation (2.3). The wheel circumference is approximately 2.9 m. At 300 km/hr, the fundamental kinematic frequency due to the wheel is given by equation

(2.2): 83 km/s / 2.9 m = 28.6 Hz. The higher kinematic frequencies, given by equation (2.3), are 57.2, 85.9, 114.5, ... Hz. As noted earlier, all of these curves have the same shape as the plot of train speed versus time. The effect of wheel irregularities is unnoticeable in the bogie and car PSDs due to the low pass filtering effects of the suspension.

- Periodic bridge irregularities: In the PSD shown in Figure 2.2, a series of closely spaced curves can be seen. A closer examination shows that these curves are spaced in the vertical frequency direction at approximately 3.1 Hz intervals when the train is traveling at approximately 300 km/hr. This corresponds to a length scale of approximately 25 meters which is the spacing between bridge supports.

It is noted that the vibrations due to resonance are independent of speed and appear as horizontal lines in the time dependent auto-PSD plots for the bogie and car body. Some of the bogie resonances in Figure 2.3 are sharp, and correspond to low damping. Others are broad, and correspond to moderate to high damping. For the car body PSD in Figure 2.4, most of the resonances are around 50 Hz and 75 Hz which are much fainter than the resonances for the bogie.

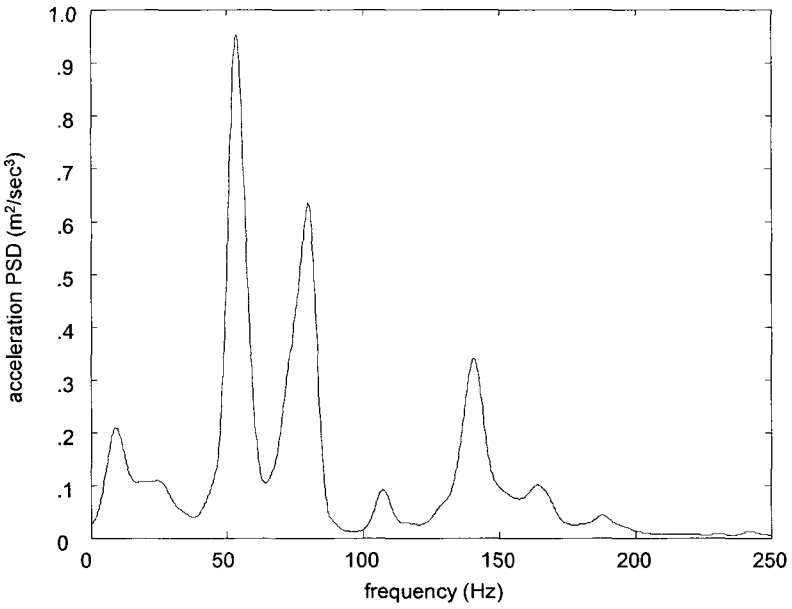

Figure 2.5: Auto-PSD of the bogie acceleration.

2.3.1.2 Response characteristics at cruising speed

Here, we determine the characteristics of the accelerations that are most relevant to the analysis and testing of fatigue. The basic data are the time-history accelerations:

$$a(t) = \quad \text{car body acceleration}$$

$$a_b(t) = \quad \text{bogie acceleration}$$

where we use the subscript b for bogie. In this study, we focus only on the STFT when the HSR-350x is traveling at its cruising speed of approximately 278 km/h. This is the speed

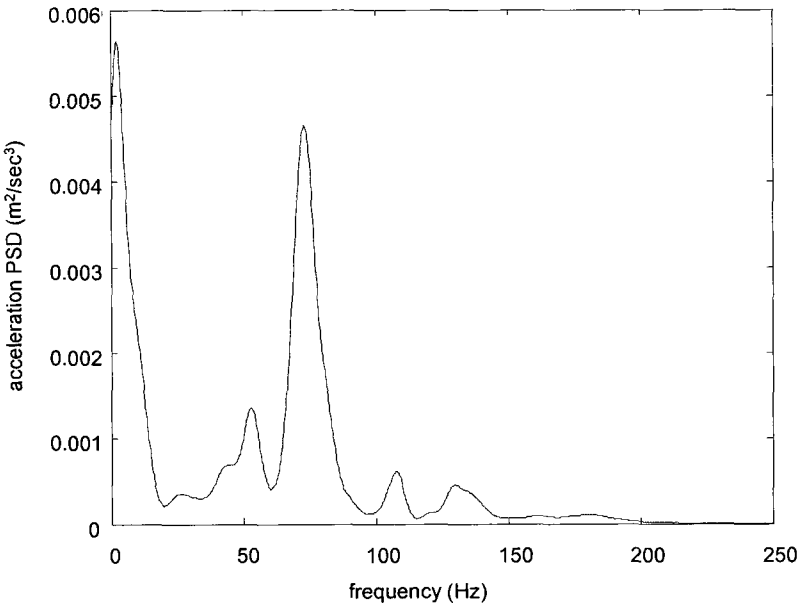

Figure 2.6: Auto-PSD of car body acceleration.

that the high speed train will travel for most of its duration under commercial operation. The techniques explained in this chapter can be expanded to include variable speed data. The STFT at cruising speed is denoted as:

$A(f) =$ STFT of car body acceleration at cruising speed

$A_b(f) =$ STFT of bogie acceleration at cruising speed

In order to get a smooth model for the frequency-dependent model for the suspension between the bogie and car body, it is necessary to use a smoothed power spectral density. So

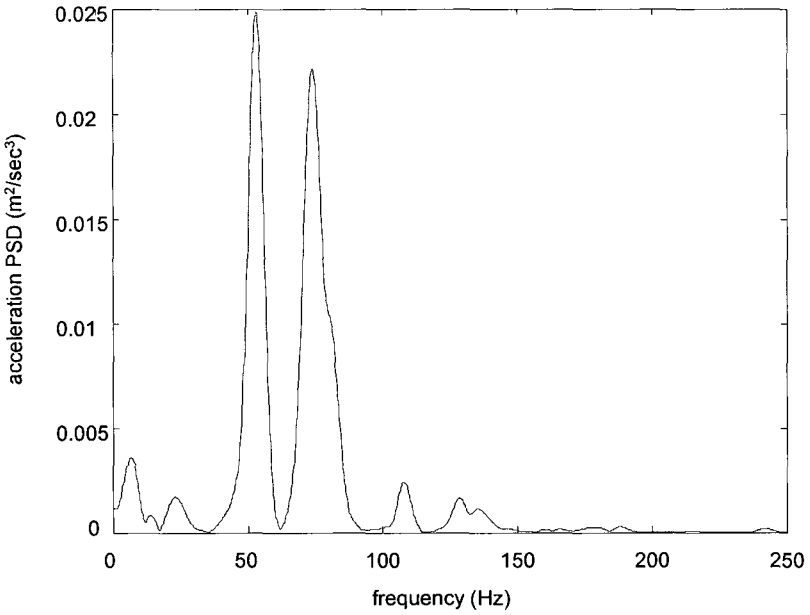

Figure 2.7: Cross-PSD of bogie-car body acceleration.

a frequency domain filter is performed on the absolute STFT squared of the acceleration:

$$S_{cc}(f) = \int_0^{f_{Nyquist}} |A(f')|^2 H_{filter}(f - f')df' = \quad \text{Auto-PSD of the car body}$$

$$S_{bb}(f) = \int_0^{f_{Nyquist}} |A_b(f')|^2 H_{filter}(f - f')df' = \quad \text{Auto-PSD of the bogie}$$

$$S_{cc}(f) = \int_0^{f_{Nyquist}} A_b(f')A(f')H_{filter}(f - f')df' = \quad \text{Cross-PSD of the bogie-car body}$$

where the subscript c denotes the car body. In this analysis a Gaussian filter is used:

$$H_{filter}(f) = \frac{1}{\sqrt{(2\pi)}\sigma_{filter}} \exp -\frac{f^2}{2\sigma^2_{filter}}$$

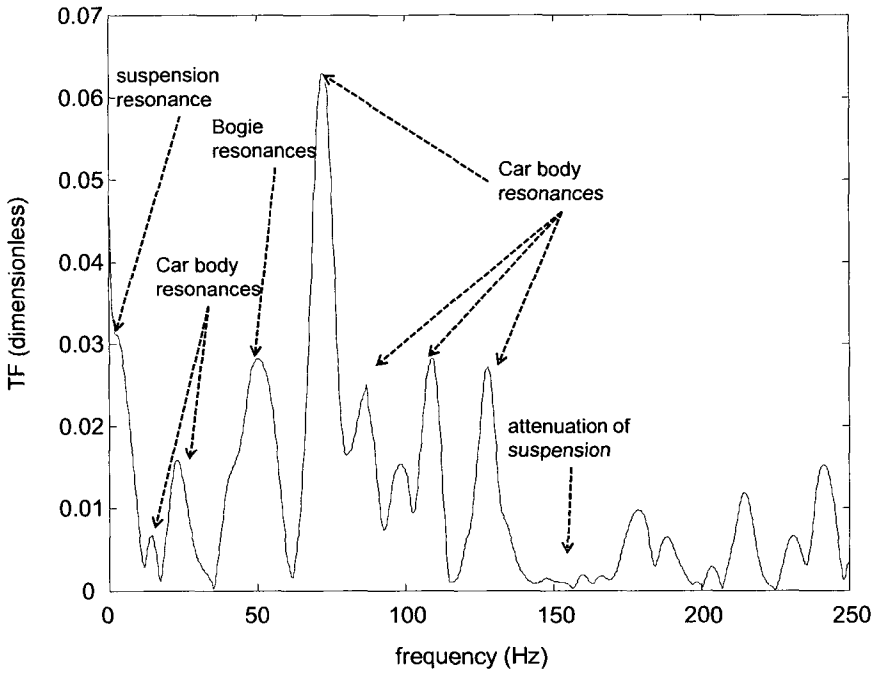

Figure 2.8: TF, $\hat{H}^{a}_{a_b}$, of bogie to car body accelerations.

where the Gaussian width of the filter is $\sigma_{filter} = 2.5$ Hz. The result for the auto-PSD of the bogie is shown in Figure 2.5. The most prominent peaks in the PSDs are at:

- 53 Hz = first group of major resonances
- 75 Hz = second group of major resonances
- 138 Hz = sleeper frequency at cruising speed

The auto-PSD of the car body is shown in Figure 2.6. Here, the first peak at 53 Hz is reduced as compared with the auto-PSD of the bogie. This indicates that this resonance

may be related more to the bogie vibrations than the car body vibrations. The second peak at 75 Hz is still high, indicating that this resonance is related to car body vibrations. The vibrations at the sleeper frequency is significantly reduced, indicating that the suspension is effective in attenuating this high-frequency motion. The auto-PSD of the car body also shows a significant peak between 0 to 10 Hz. This is primarily due to the low stiffness of the air bag suspension.

The cross-PSD is shown in Figure 2.7. This result shows a combination of effects between the bogie and car body. This figure is somewhat difficult to interpret because of this combination effect, but the primary purpose of the cross-PSD is to obtain the transfer function (TF), which is explained next.

The acceleration TF from bogie to car body is in terms of the Fourier transform of bogie and car body accelerations:

$$H^a_{a_b} = \frac{A(f)}{A_b(f)}$$

While the TF can be obtained directly from this ratio of Fourier transforms, the result tends to be very irregular and noisy. A statistical estimate of the transfer function can be written in terms of the auto-PSD of the bogie and the bogie-car body cross-PSD as explained earlier in equation (2.1).

$$\hat{H}^a_{a_b} = \frac{S_{cb}(f)}{S_{bb}(f)}$$

The plot of the absolute value of the estimated TF is shown in Figure 2.8. In terms of the structural dynamics of the bogie-car body system, the TF captures the resonance and attenuation effects of the suspension between the bogie and car body as well as the resonances

of the car body. The dynamic coupling of these resonances are important, and are discussed in subsection 2.3.2.

There are a set of major peaks in the TF and one major valley:

- 0 - 10 Hz = suspension resonance
- 20 - 26 Hz = car body resonance
- 40 - 58 Hz = resonances associated primarily with the bogie
- 67 - 77 Hz = resonances associated primarily with the car body
- 87, 98, 109, 128 Hz = additional resonances
- 140 - 170 Hz = attenuation due to suspension

The resonances described above were also identified in the STFT analysis in the previous studies on high speed train response characteristics [Igusa, 2008]. The magnitude of the responses is in agreement with an earlier study on the ride comfort of the HST [Y. G. Kim et al., 2008]. The attenuation is important because the frequency range covers the sleeper frequency at cruising speed. This explains the lack of a sleeper frequency peak in the auto-PSD of the car body in Figure 2.6.

2.3.2 Analytical forms for the transfer functions

In this section the properties of the suspension between the bogie and car body is determined. To perform this analysis, it is necessary to define several TFs. The analytical

formulations for the TFs are in terms of the dynamic properties of the suspension and the car body dynamic properties.

2.3.2.1 System dynamic properties

The suspension is described by its stiffness. The car body is described by the modal properties:

$\phi_j(x)$	j^{th} mode shape, as a function of location x
f_j	j^{th} natural frequency
ξ	damping ratio

It is assumed that the modal masses are unity so that the units for the mode shapes are $1/\sqrt{mass}$. To obtain relatively smooth acceleration and stress transfer functions, a damping value of $\xi = 10\%$ was used in the analysis.

To begin the analysis, it is necessary to assign a temporary stiffness value k_0 to the suspension so that FEM can be used to obtain the mode shapes. First the bogie is fixed when deriving the mode shapes. Later, this temporary constant stiffness is replaced with a frequency dependent stiffness $k(f)$ which more accurately models the behavior observed in the measured data.

For the HSR-350x car body, a 109,857 node 138,623 element NASTRAN FEM model shown in Figure 2.9 is used [Park, 2004]. This NASTRAN model was translated to ABAQUS 6.7 [Abaqus documentation, 2007] using the NASTRAN-to-ABAQUS trans-

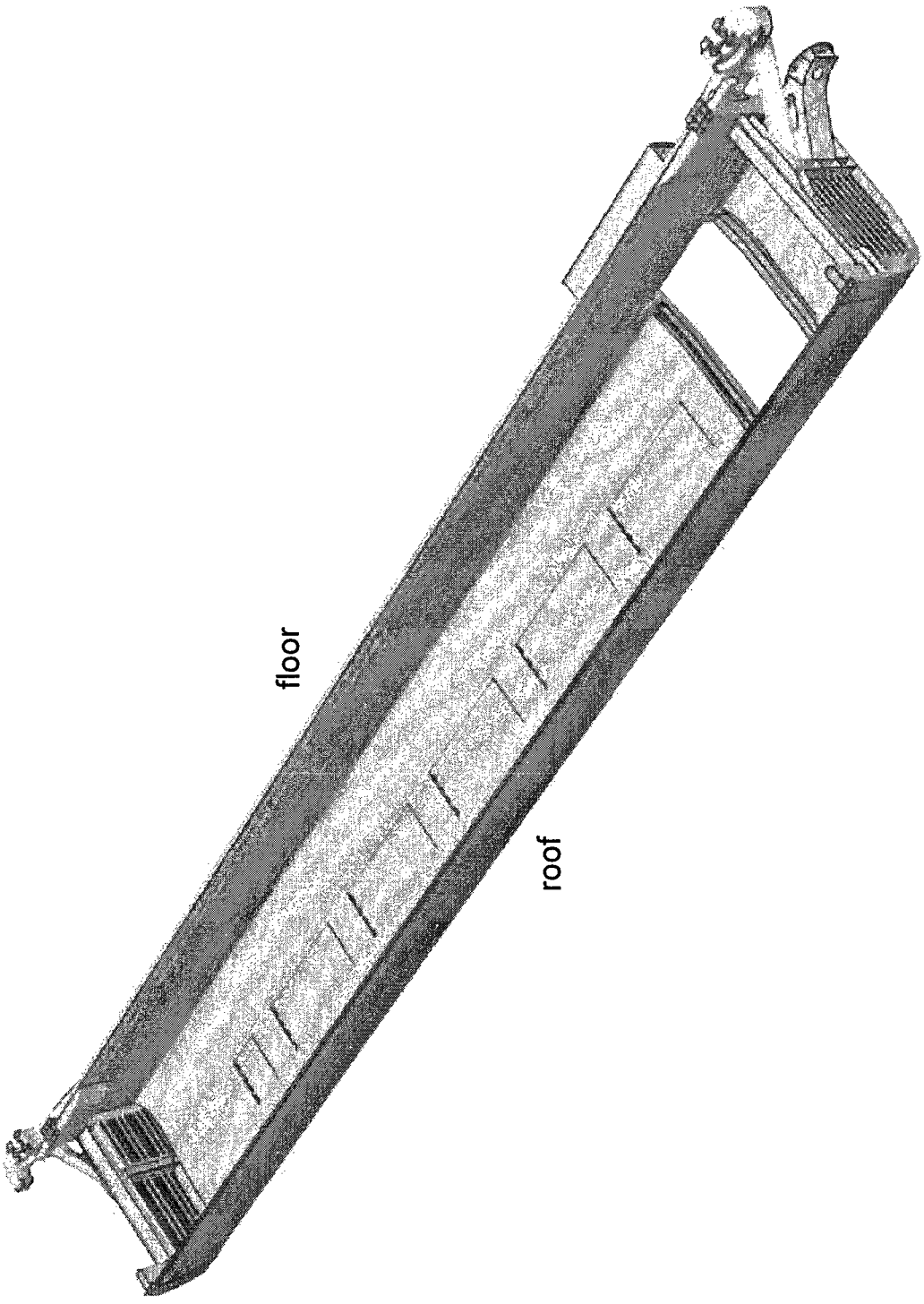

Figure 2.9: Finite element model of the car body

lation utility. Since this model was only for the car body, vertical springs were used at each bogie connection as shown in Figure 2.10. The initial temporary stiffness k_0 was assigned at these supports such that the fundamental mode (assuming the car body is a rigid mass at low frequencies) is 1 Hz. A modal analysis is performed to determine the natural frequencies and mode shapes of the body. Figure 2.10 only shows half of the car since symmetry can be used to represent the motion of the other half of the car.

As expected, the first three natural frequencies of the system are close to 1 Hz. In these modes, the car body is moving almost as a rigid body with nearly all of the strain energy localized at the two support springs. The next two natural frequencies are at 11.35 and 11.73 Hz. The mode shapes show highly localized deformation at the two ends of the car body. This is illustrated in Figure 2.11 for mode shape 4. The properties of the first set of modes are shown in Table 2.1 and Figures 2.11 – 2.16.

In the modal analysis, 110 modes were computed, with natural frequencies up to 200 Hz. It is noted that the units of the mode shapes is $ton^{-1/2}$ since metric tons are used in the FEM model.

2.3.2.2 Derivation of TFs

In this section the transfer functions (TFs) are derived. These TFs are needed later for fatigue stress analysis. We introduce the following notation:

- A, A_s, A_b : acceleration at the car body, support above the suspension, and bogie
- D_s, D_b : displacement at the support above the suspension and bogie

Table 2.1: Description of modes

mode number	frequency	description
4	11.35	local mode near door
5	11.73	local mode far from door
6	21.12	global mode
7	23.94	global mode
8	26.65	global mode
9	33.50	global mode
10	38.53	global mode

Table 2.2: Description of transfer functions

TF	unit input	acceleration output	suspension
$H_F^A(x)$	force at the support	car body, location x	stiffness k_0
$H_F'^A(x)$	force at the support	car body, location x	no stiffness
$H_{A_s}^A(x)$	acceleration at the support	car body, location x	–
$H_{A_b}^A(x)$	acceleration at the bogie	car body, location x	stiffness k

Figure 2.10: FEM model and support configuration for determining modal properties.

- F : force at the support
- x : location on car body for determining the acceleration
- x_s : support location on the car body

The locations of the accelerations are shown in Figure 2.17. The force F is positive if the support spring is in compression so that it is in the upward direction when acting on the car body. Using this notation, the TFs of interest are summarized Table 2.2.

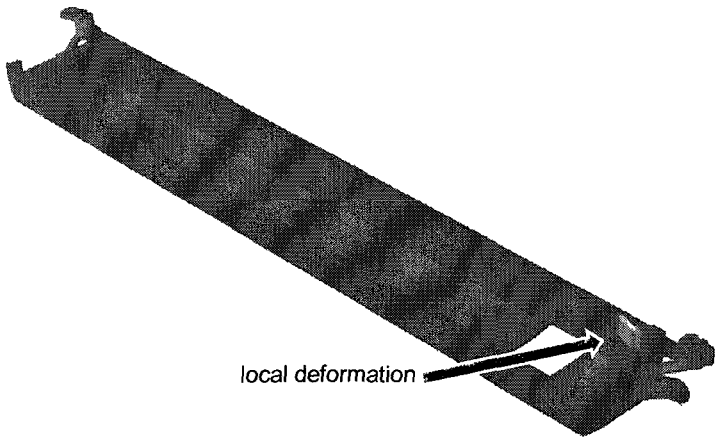

Figure 2.11: Mode shape 4 (11.35 Hz) illustrating a local displacement pattern.

It is also noted that in the frequency domain the relation between the displacement and acceleration is as follows:

$$A_s = -\omega^2 D_s$$

$$A_b = -\omega^2 D_b$$

where $\omega = 2\pi f$ is the circular frequency.

The fundamental TF is between the support force F and car body acceleration A. This TF can be computed directly from the finite element model using the mode shapes $\phi_j(x)$

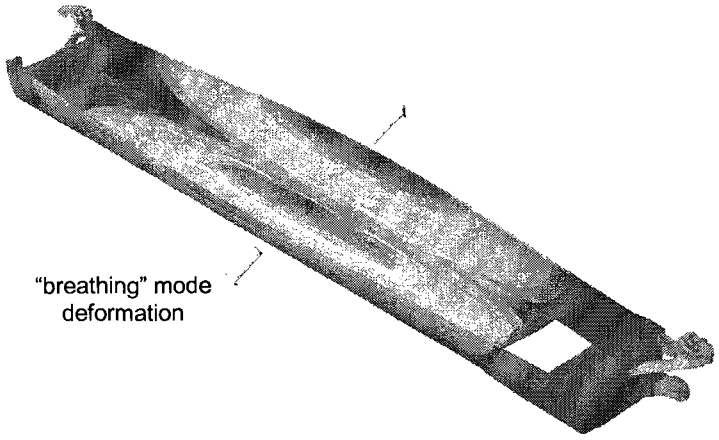

Figure 2.12: Mode shape 6 (21.12 Hz) illustrating a simple breathing mode displacement pattern.

and natural frequencies f_j :

$$H_F^A(x) = \frac{A}{F} = -f^2 \sum_j \frac{\phi_j(x)\phi_j(x_s)}{f_j^2 - f^2 + 2i\xi f_j f} \tag{2.4}$$

The unit is $1/mass$, which for the FEM model is $1/ton$. In the above expression it can be seen that the denominator becomes small when the excitation frequency f approaches a natural frequency f_j of the system. Hence, in typical TFs, there are well-defined peaks at each natural frequency. For the HSR-350x, however, there are a very large number of

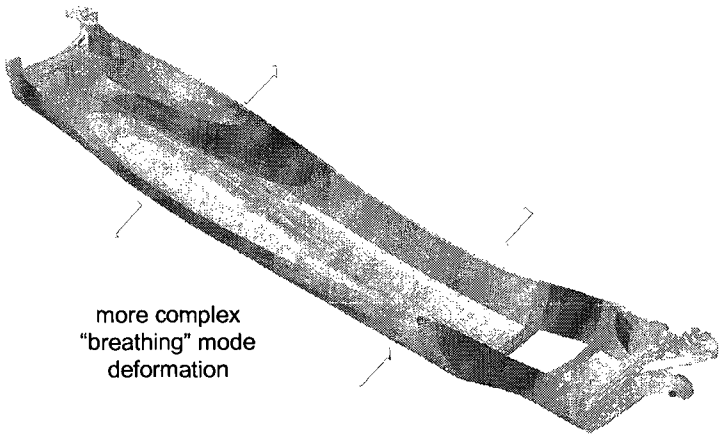

Figure 2.13: Mode shape 7 (23.94 Hz) illustrating a more complex breathing mode displacement pattern.

modes at very closely spaced natural frequencies.

In Figure 2.18(a) the fundamental TF for support motion at both ends of the car body is plotted. The natural frequencies are shown as circles at the horizontal axis of Figure 2.18. There will not be a peak at each natural frequency because for most of the modes j , either $\phi_j(x)$ or $\phi_j(x_s)$ is small. To show this, the amplitudes $\phi_j(x_s)$ and $\phi_j(x)$ of the mode shapes is shown at the support (near the door) and in the middle of the car body floor in Figures 2.18(b) and (c). It can be seen that only a small subset of the modes have

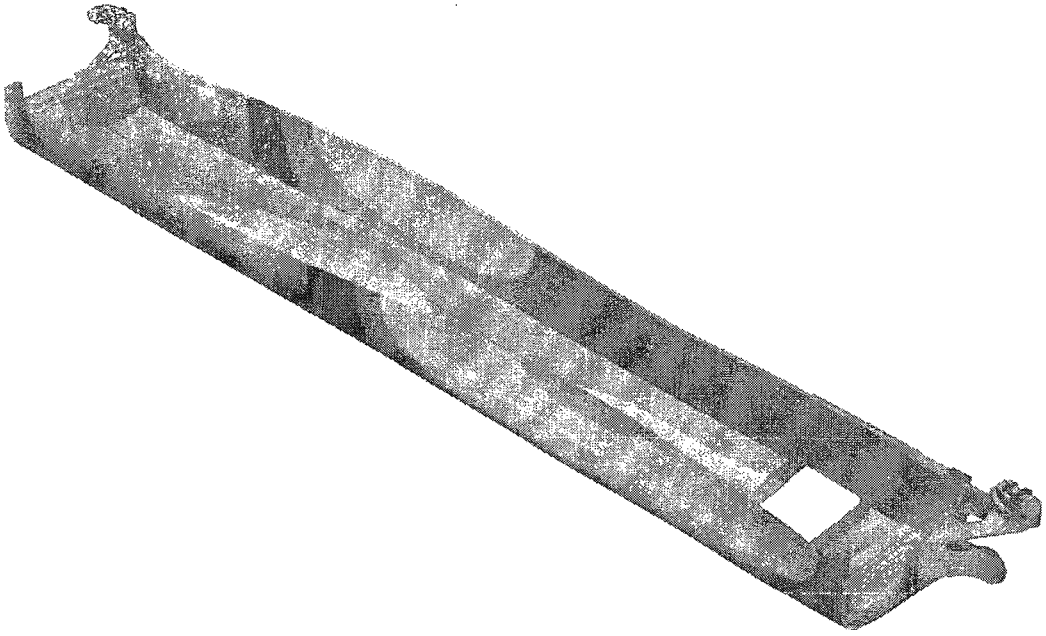

Figure 2.14: Mode shape 8 (26.65 Hz) global mode

significantly non-zero mode shapes at these two locations. In Figure 2.18(d) we show the product of mode shapes, $\phi_j(x)\phi_j(x_s)$, which appears in the numerator of equation (2.4). At low frequencies, below 50 Hz, it can be seen that when this product is large, there will be a peak at the TF as shown by comparing Figures 2.18(a) and (d) in this frequency range. At higher frequencies, some of the modes with closely spaced natural frequencies have a product of mode shapes with fluctuating signs. Such fluctuating signs leads to a cancelation effect in equation (2.4). This can be seen by comparing Figures 2.18(a) and (d) in the frequency range of approximately 60 to 90 Hz, where the product of mode shapes is

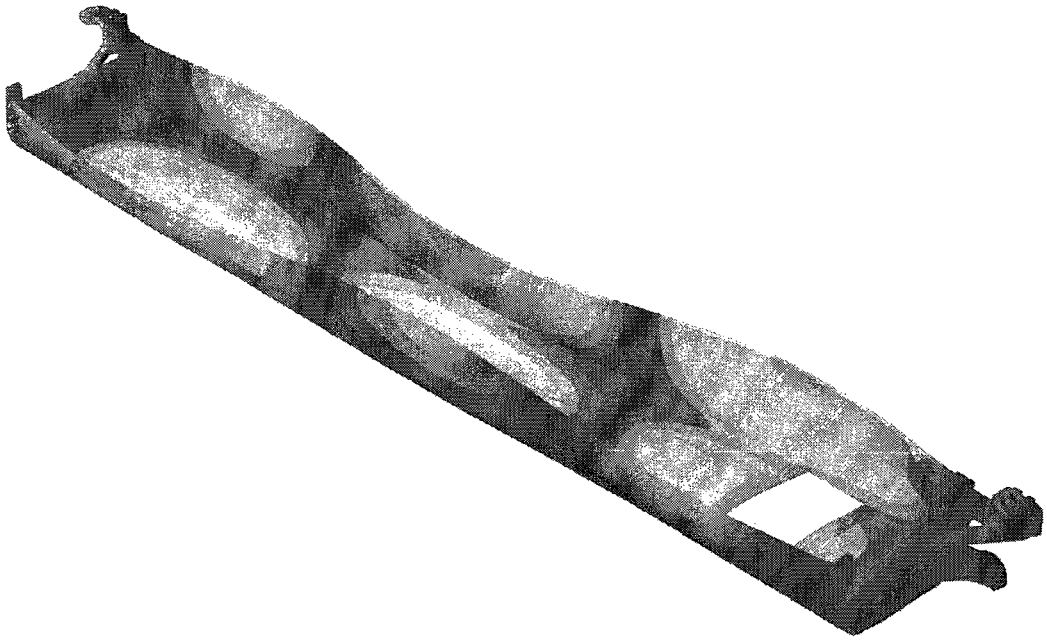

Figure 2.15: Mode shape 9 (33.50 Hz) global mode

small and fluctuating above and below zero and in the frequency range of 175 to 190 Hz where the product of mode shapes is sometimes relatively large, but the sign is fluctuating.

From this fundamental TF for support force F to car body acceleration A, one can construct the TF $H^A_{A_s}(x)$ between support acceleration A_s and A

$$H^A_{A_s} = \frac{A}{A_s} = \frac{A/F}{A_s/F} = \frac{H^A_F(x)}{H^A_F(x_s)} \tag{2.5}$$

This non-dimensional TF is shown in Figure 2.19 for the right bogie near the door. The large peak slightly below 25 Hz corresponds to the seventh mode shape with natural fre-

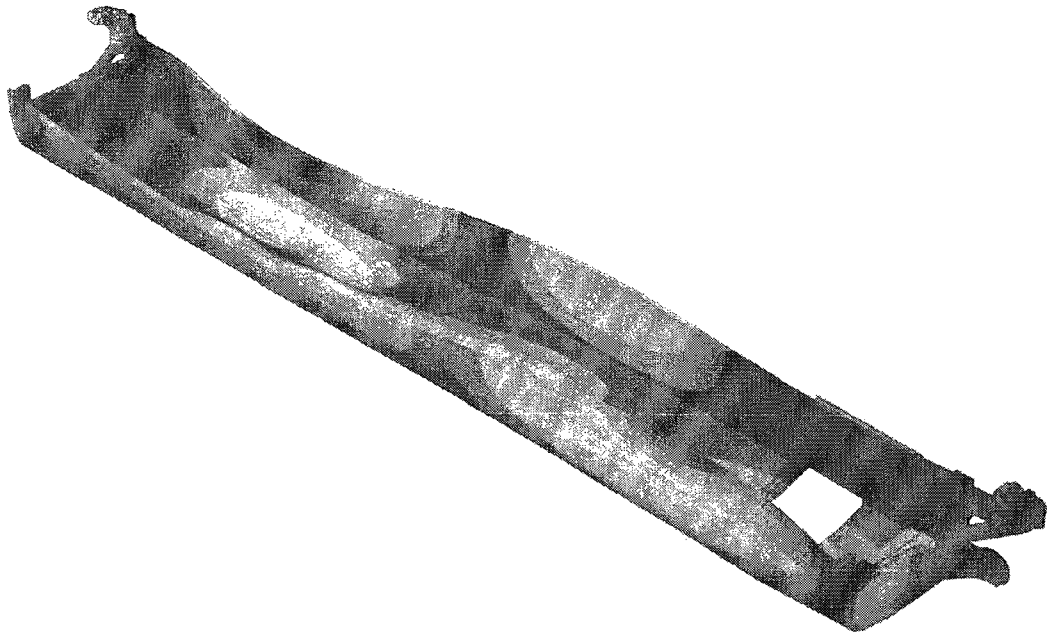

Figure 2.16: Mode shape 10 (38.53 Hz) global mode

quency of 23.94 Hz shown in Figure 2.13. There are other groups of resonances that contribute to peaks near 110 and 150 Hz.

One can also construct the TF $H_F'^A(x)$ between the support force F and car body acceleration A when the support stiffness k_0 is removed. The following relationship can be used between the forces with and without the support stiffness:

$$\text{force with no support stiffness} = (\text{force with support stiffness } k_0) - (\text{displacement} \times k_0)$$
$$= F - D_s k_0 = F + \frac{A_s}{\omega^2} k_0$$

Then the TF $H_F^{'A}(x)$ is

$$H_F^{'A} = \frac{A}{\text{force with no support stiffness}} = \frac{A}{F + \frac{A_s}{\omega^2} k_0} = \frac{\frac{A}{F}}{1 + \frac{k_0}{\omega^2} \frac{A_s}{F}} = \frac{H_F^A(x)}{1 + \frac{k_0}{\omega^2} H_F^A(x_s)}$$

In obtaining the mode shapes, it was assumed that the bogies are fixed. In this stage of the analysis, the TFs are reexamined without this assumption, where bogie motion is allowed at one end. The other bogie is fixed with the spring support of stiffness k_0 as shown in Figure 2.17. (Later, superposition is readily applied to consider simultaneous motion at both bogies.) The goal is to find the acceleration A of the car body due to acceleration A_b at the moving bogie. First, the force F in the suspension is obtained in terms of the accelerations A_b and A_s at the bogie and suspension:

$$F = k(D_b - D_s) = k\frac{A_b - A_s}{-\omega^2}$$

The ratio of the bogie and car body accelerations is the TF $H_{A_b}^A = A/A_b$. One can rewrite the car body acceleration A in terms of the bogie acceleration A_b by using the preceding expression for the force:

$$A = H_F^{'A} F = \frac{H_F^A(x)}{1 + \frac{k_0}{\omega^2} H_F^A(x_s)} k \frac{A_b - A_s}{-\omega^2}$$

Next, the TF $H_{A_s}^A$ in equation (2.5) is used to rewrite the support acceleration A_s in terms of the car acceleration A:

$$A = \frac{\frac{k}{-\omega^2} H_F^A(x)}{1 + \frac{k_0}{\omega^2} H_F^A(x_s)} \left[A_b - \frac{A}{\frac{H_F^A(x)}{H_F^A(x_s)}} \right]$$

The terms in this equation can be rearranged to combine the coefficients of A :

$$A\left[1+\frac{\frac{k}{-\omega^2}H_F^A(x)}{1+\frac{k_0}{\omega^2}H_F^A(x_s)}\frac{1}{\frac{H_F^A(x)}{H_F^A(x_s)}}\right]=A\left[1+\frac{\frac{k}{-\omega^2}H_F^A(x_s)}{1+\frac{k_0}{\omega^2}H_F^A(x_s)}\right]=A\left[\frac{1+\frac{k_0-k}{\omega^2}H_F^A(x_s)}{1+\frac{k_0}{\omega^2}H_F^A(x_s)}\right]$$
$$=\frac{\frac{k}{-\omega^2}H_F^A(x)}{1+\frac{k_0}{\omega^2}H_F^A(x_s)}A_b$$

Now the desired TF $H_{A_b}^A$ of the bogie to car body accelerations can be determined by rewriting the preceding equation in terms of the ratio A/A_b as:

$$H_{A_b}^A=\frac{A}{A_b}=\frac{\frac{k}{-\omega^2}H_F^A(x)}{1+\frac{k_0-k}{\omega^2}H_F^A(x_s)}=\frac{kH_F^A(x)}{-\omega^2+(k-k_0)H_F^A(x_s)} \tag{2.6}$$

2.3.2.3 Frequency-dependent support stiffness

As explained in the preceding section, from the measured data, one can derive an estimate for the TF $H_{A_b}^A$ as shown in Figure 2.8. One can use this TF to estimate the suspension stiffness k by rewriting equation (2.6) and solving for k:

$$k=\frac{H_{A_b}^A\left[H_F^A(x_s)k_0+\omega^2\right]}{H_{A_b}^A H_F^A(x_s)-H_F^A(x)} \tag{2.7}$$

The result is a frequency-dependent stiffness that is in terms of the TF $H_{A_b}^A$ from the measured data and the TF $H_F^A(x)$ from the finite element model. Since the analysis is in the frequency domain, damping is included by the imaginary part of the stiffness k. Basically, the damping is equal to the imaginary part of k divided by the circular frequency ω:

$$C=\frac{Im(K)}{\omega}$$

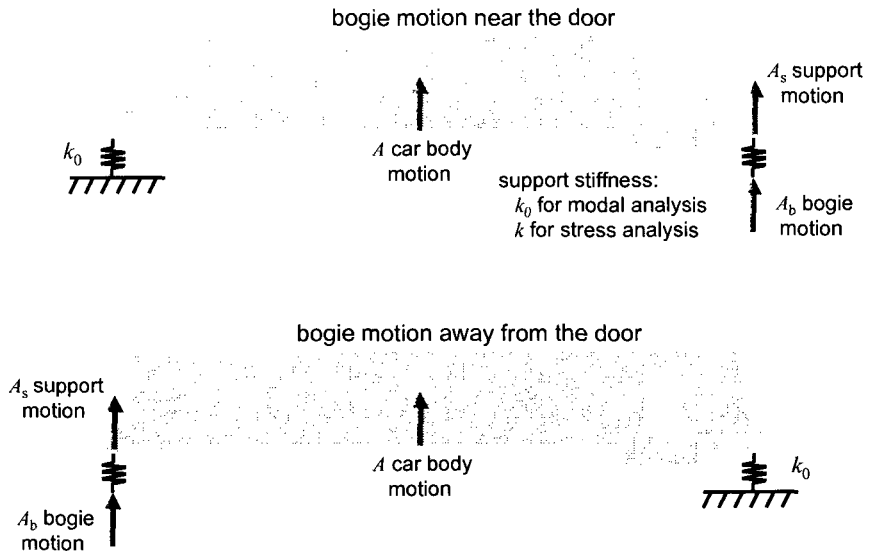

Figure 2.17: Schematic figure showing the principal vibration motion of the system for bogie motion near the door and bogie motion away from the door.

The absolute value of this stiffness is shown in Figure 2.20. In this figure, the frequency-dependent stiffness is shown when the bogie motions are at the left or right end of the car body. It can be seen that both results are similar. It is noted that the stiffness k_0 was only used in the finite element model. The above estimate for the suspension stiffness is independent of the stiffness k_0.

A simple two-parameter model for the stiffness has been determined by KRRI re-

searchers from a separate analysis of the bogie suspension, with parameters

$$k_{\text{two-parameter}} = 245.1\frac{\text{N}}{\text{mm}} + 42i\omega\frac{\text{N}-\text{s}}{\text{mm}} \tag{2.8}$$

The absolute value of this result is also shown in Figure 2.20 in red. It can be seen that the two-parameter result is significantly larger than the results obtained using the combination of car body FEM analysis and car body and bogie acceleration measurements. To further describe this difference of results, the TF for accelerations A_b and A at the bogie and car body is computed by substituting the two parameter stiffness model and the FEM model into equation (2.6). The result is shown in Figure 2.21. As expected from the preceding comments, this TF is significantly larger than the same TF obtained purely from experimental measurements shown in Figure 2.8. It is not immediately clear why there is a difference between the two results.

2.3.3 Car body stress transfer function

The TF in the preceding section is only used to find the relationships between forces and accelerations. Displacements can be obtained simply by dividing the accelerations by $-\omega^2$. The primary interest, however, is not on accelerations and displacements but on stresses.

The stress TF gives the ratio of the input, which can be a force or acceleration, and the response, which is the stress inside the car body. For linear systems, if the displacement field D at every point of the car body is known, the stresses σ_{ij} can be obtained using the

relation:

$$\sigma_{ij} = B_{ij} D$$

where B_{ij} is a matrix typically computed internally by finite element software. Therefore, if the acceleration transfer functions such as $H^A_{A_b}$ are evaluated at every point x of the car body, then dividing by $-\omega^2$, and putting the results in vector form D and multiplying by B_{ij} one can get the stresses σ_{ij}.

In practice, however, it is simpler to decouple, as much as possible, the FEM analysis of stresses and the evaluation of the TF. This is possible using the TF forms derived in the preceding section. Basically, the FEM model is used to get the stress TF from the support force F to the car body stresses σ_{ij}. Then the preceding relations are used to extend this TF to obtain the stresses in terms of unit bogie accelerations. Different stress transfer functions of interest are defined as follows:

TF	unit input	stress output	suspension
$H^\sigma_F(x)$	force at the support	car body, location x	stiffness k_0
$H^\sigma_{A_b}(x)$	acceleration at the bogie	car body, location x	stiffness k

The same derivation as the one in the preceding section 2.3.2.2 can be followed up to equation (2.6). It can be seen that the only difference is in replacing $H^A_F(x)$ by $H^\sigma_F(x)$ in the numerator of that equation. Thus, the final result for the stress transfer function for acceleration at the bogie is

$$H^\sigma_{A_b}(x) = \frac{k H^\sigma_F(x)}{-\omega^2 + (k - k_0) H^A_F(x_s)} \tag{2.9}$$

Then, using standard relations in the theory of stochastic processes (or random vibrations), one can use the above to get the auto-PSD of the stress $S_{\sigma\sigma}$ in terms of the auto-PSD of the bogie acceleration S_{bb}:

$$S_{\sigma\sigma}(f) = \left|H^{\sigma}_{A_b}(x)\right|^2 S_{\mathrm{bb}}(f) \tag{2.10}$$

Here, S_{bb} is obtained from measured data, as shown in Figure 2.5, and the stress TF is obtained using FEM analysis and equation (2.9).

Next, the results for the stress TF for the HSR-350x is illustrated. The fundamental stress TF H^{σ}_{F} from support force F to car body stress σ_{ij} is obtained by running ABAQUS repeatedly using a unit amplitude support force $F = \sin(2\pi f t)$ at a set of harmonic frequencies f ranging from 1 to 145 Hz. More densely spaced frequencies are used at frequency ranges where the auto-PSD of the car body response was large.

The stress pattern for the longitudinal stress σ_{11} at the sleeper frequency of 138 Hz is shown in Figure 2.22. This is the stress TF $H^{\sigma}_{F}(x)$ evaluated at a single frequency but for x at all locations of the car body. The results shown in the figure is a typical stress pattern at high frequencies. There are significant deformations and high stresses at the end of the car body near the vibrating bogie support. There are also high stresses at the corners of the windows and around the perimeter of the door. This is due to the expected stress concentrations occurring near openings which is analyzed in depth in chapter 4. The stress patterns at other frequencies are examined in more detail in section 2.3.4. Since the stress σ_{22} (normal stress in the vertical direction in the sides of the car body) often has the highest value, especially around the openings, for most of the studies in this chapter, the focus is on

this stress. This however is subject to change if one notices significant differences between σ_{22} and the maximum principal stress.

In Figure 2.23, the stress TF $H_F^{\sigma}(x)$ is examined at a single point and for a wide range of frequencies. As indicated in the figure, the stress σ_{22} is evaluated at the corner of the window closest to the door. The horizontal axis shows the frequencies between 1 and 145 Hz where $H_F^{\sigma}(x)$ was evaluated. The peak of the stress TF is near 25 Hz, which corresponds to the seventh mode shape shown in Figure 2.13. The other lower peaks in the stress TF correspond to other groups of modes. In section 2.3.4 the stress patterns at different frequencies and modes are examined in more detail.

To compute the stress TF $H_{A_b}^{\sigma}(x)$ for acceleration at the bogie, there is no need to re-run the FEM model in ABAQUS. Instead, it is only necessary to combine the fundamental stress TF $H_F^{\sigma}(x)$ such as that shown in Figure 2.23 with the simple analytical formula in equation (2.9). The resulting stress TF is shown in Figures 2.24 and 2.25 for the frequency-dependent and two-parameter support stiffnesses. The plot in Figure 2.25 looks similar to the fundamental stress TF in Figure 2.23 with attenuation at higher frequencies. The attenuation is due to the fact that the support damping dissipates more energy at higher frequencies. The plot in Figure 2.24 has more peaks. These peaks are located at approximately the same frequencies as the peaks of the frequency-dependent stiffness in Figure 2.20. Another major difference between the stress TFs in Figures 2.24 and 2.25 is that the result using the two-parameter stiffness is about an order of magnitude larger at frequencies below 30 Hz. This is because the two-parameter model is stiffer than the frequency-dependent model by

an order of magnitude in this low frequency range.

The auto-PSD of the stress, computed using equation (2.10), is examined next. Figures 2.26 and 2.27 are the auto-PSDs of the stress determined using the frequency-dependent and two-parameter support stiffnesses. The difference that was observed in the order of magnitude of the stress TFs is magnified in the auto-PSDs because the stress TFs are squared in equation (2.10).

2.3.4 Stress patterns

In this section the spatial patterns of stress in the car body are studied in the frequency domain. The focus is on the stress patterns resulting from harmonic forces at the supports and on the patterns associated with each mode of vibration.

2.3.4.1 Harmonic stress patterns

Figures 2.28-2.30 show the stress patterns resulting from harmonic support forces at 53, 63 and 74.5 Hz. The lower and higher frequencies are chosen because they correspond to peaks in the stress TF in Figure 2.24. The middle frequency is chosen because it is close to a natural frequency of a mode with significant local deformation. The stress patterns at all three frequencies are similar, with large stresses and deformation at the end of the car close to the harmonic force, wave deformation and associated stresses along the roof and floor and concentrated wall stresses around the edges of the windows and doors. These wall stresses increase at locations closer to the harmonic force.

Comparing the plots in Figures 2.28-2.30 with the plot in Figure 2.22 for the much higher sleeper frequency of 138 Hz, one can also see a similar pattern. The most important difference between the sleeper frequency and lower frequency results is in the number of waves that can be seen in the roof and the floor. As expected, at higher frequencies, there are nearly twice as many waves: there are about 9-10 half waves in Figure 2.22 at the sleeper frequency as compared with approximately 4-5 half waves in Figures 2.28-2.30 at frequencies between 53-74.5 Hz. (Note that only the absolute value of the displacement is plotted in these figures, so a sinusoidal displacement pattern is plotted as a series of positive half-sine waves.)

2.3.4.2 Modal stress patterns

Next, the stress patterns for modes with natural frequencies are examined. These modes are in the neighborhood of the excitations frequencies used in Figures 2.22, 2.28-2.30. The results are shown in Figures 2.31-2.34 with natural frequencies at 49, 54, 62, 73, 75, 81, 136, and 139 Hz.

It can be seen that the modes fall into two groups: local deformation (62 and 81 Hz) and global deformation (remaining modes). For the local deformation cases, there are deformation primarily in the end closest to the door at 62 Hz and there are large deformations at both ends at 81 Hz. The stress pattern for the mode at 61 Hz in Figure 2.32 (left) is found in all three harmonic stress results in Figures 2.28-2.30. This is because in the harmonic response calculations of systems with many closely spaced natural frequencies, each har-

monic load will excite a large number of modes. In this case, the harmonic loads at 53, 63, and 74.5 Hz all excited by a large number of modes around these frequencies, including the mode at 62 Hz.

From the above table and in the figures, it can be seen that most of the modes create global stress patterns with well-defined waves. This can explain the wave-like response patterns at the floor and roof for the harmonic stress patterns. There is, however, one very important stress pattern characteristic which cannot be easily explained by the modal stress patterns: The modal stress patterns have relatively smooth and low stresses around the window and door openings. This is in sharp contrast with the harmonic stress patterns which always have very localized stress concentrations around these openings, particularly at the corners. In theory, the harmonic stress patterns are a weighted combination of modal stress patterns. It is not obvious how a weighted combination of smooth modal patterns as shown in Figures 2.31-2.34 can produce the concentrated harmonic stress patterns in Figures 2.22, 2.28-2.30. This behavior is important and suggests that modes cannot be easily used to describe stress response patterns.

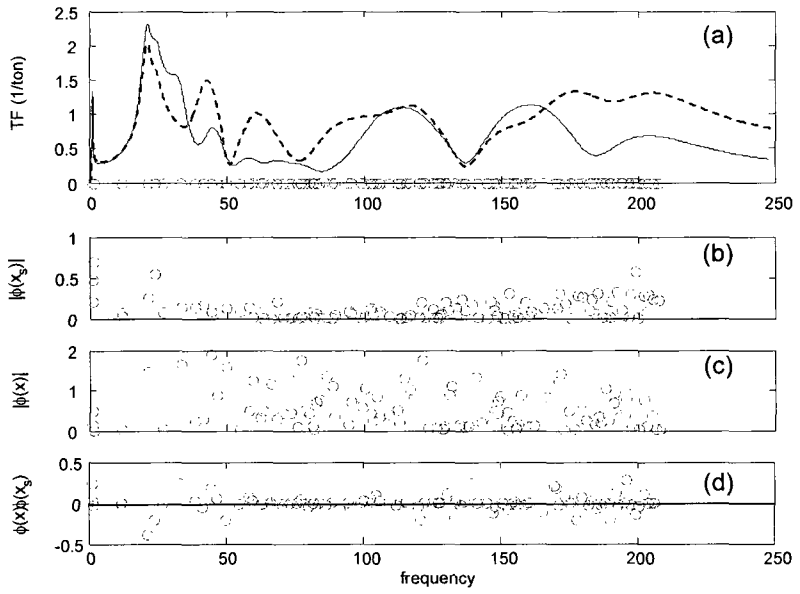

Figure 2.18: (a) Fundamental TFs for force at the support to acceleration at the car body. Force locations: (dashed) support at left end away from the door, (solid) support at right end near the door. (b) Absolute value of the mode shape at the support. (c) Absolute value of the mode shape at the car body. (d) Product of mode shapes.

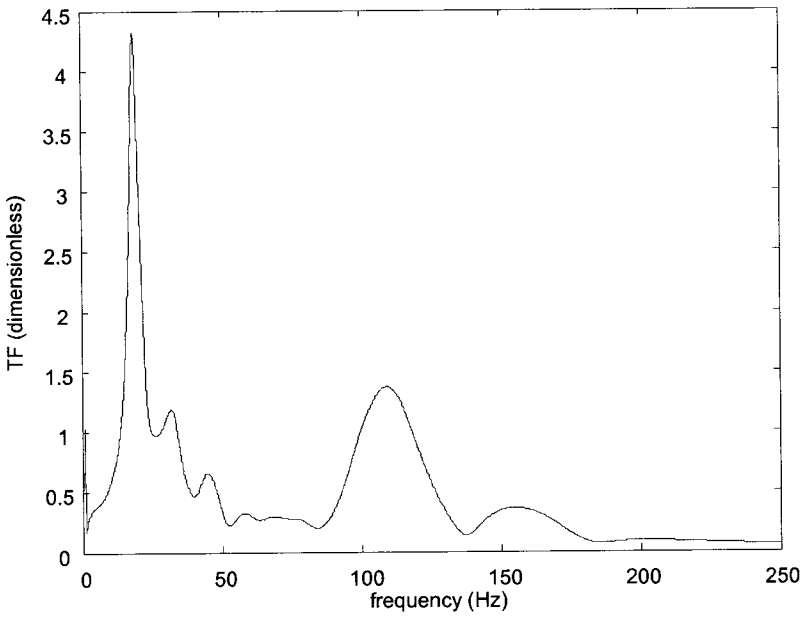

Figure 2.19: Acceleration TF from support to car body (support at right end near the door).

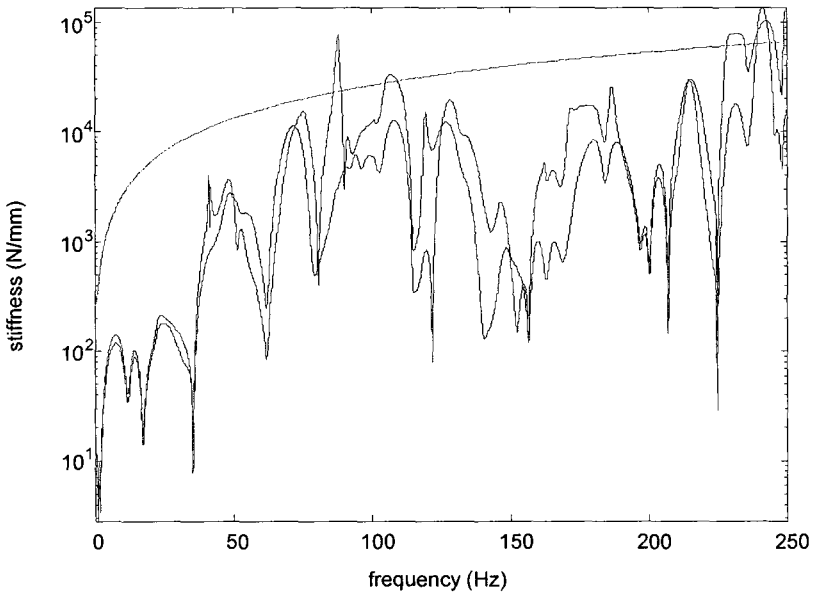

Figure 2.20: Frequency dependent stiffnesses. Model estimate from (solid) right bogie motion near the door and (dashed) left bogie motion away from the door. Simple two-parameter model (red).

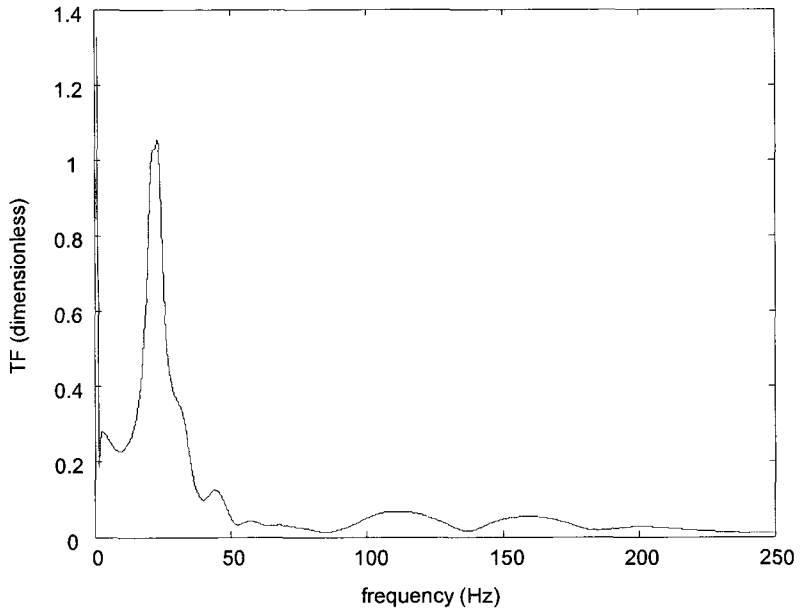

Figure 2.21: TF of bogie to car body accelerations using the two-parameter support stiffness model and the FEM model for the car body.

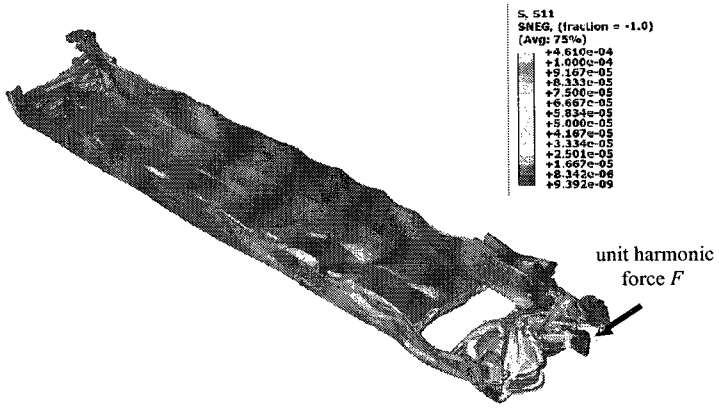

Figure 2.22: Stress pattern for the transfer function for the longitudinal stress 11 at the sleeper frequency 138 Hz.

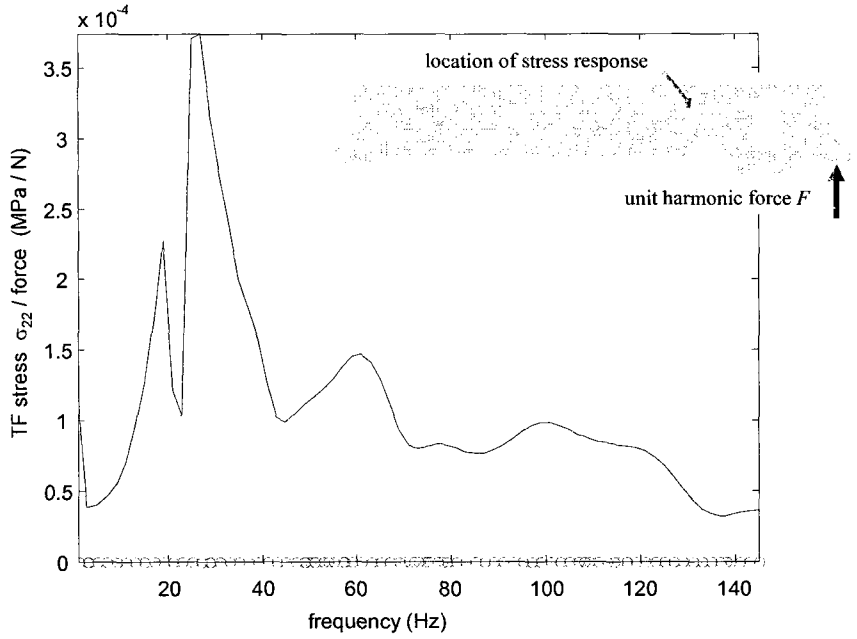

Figure 2.23: Stress transfer function for unit force at the support and stress 22 at the window corner as indicated in the diagram.

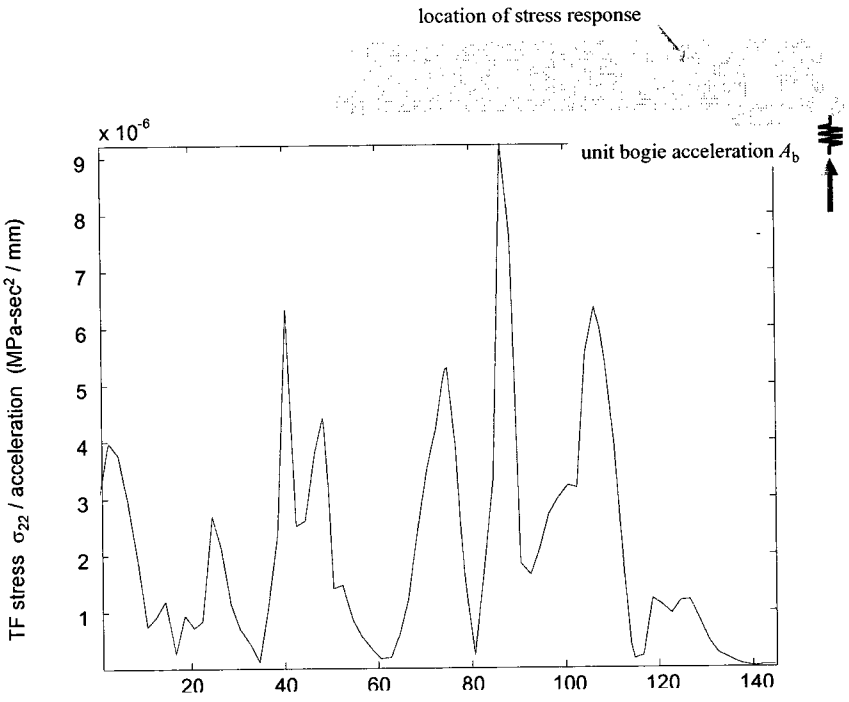

Figure 2.24: Stress transfer function for a unit acceleration at the bogie and stress at the window corner using the frequency-dependent suspension stiffness.

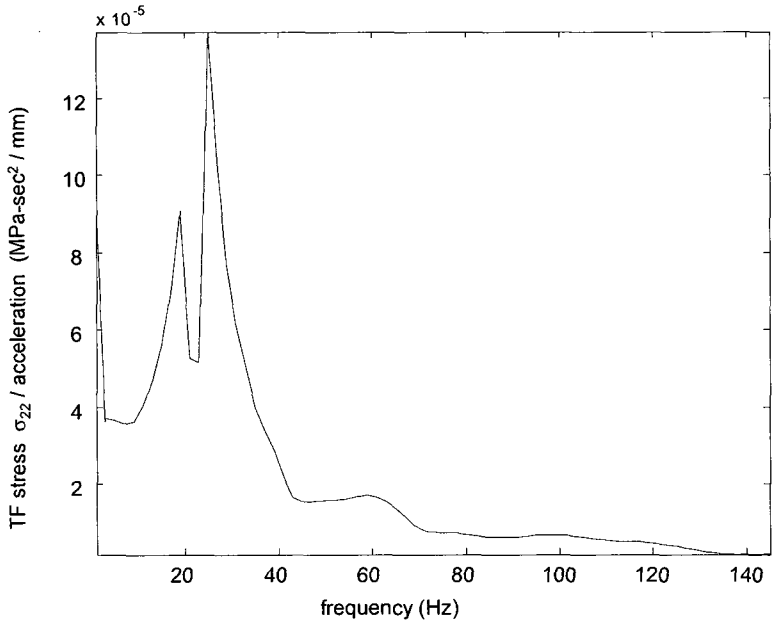

Figure 2.25: Stress transfer function for unit acceleration at the bogie and stress at the window corner using the two-parameter suspension stiffness.

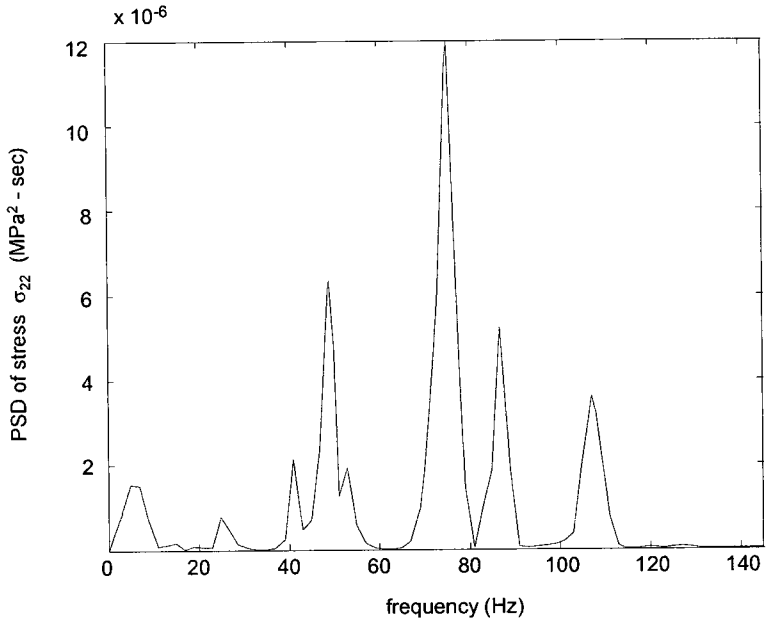

Figure 2.26: Stress PSD at the window corner using the frequency-dependent suspension stiffness.

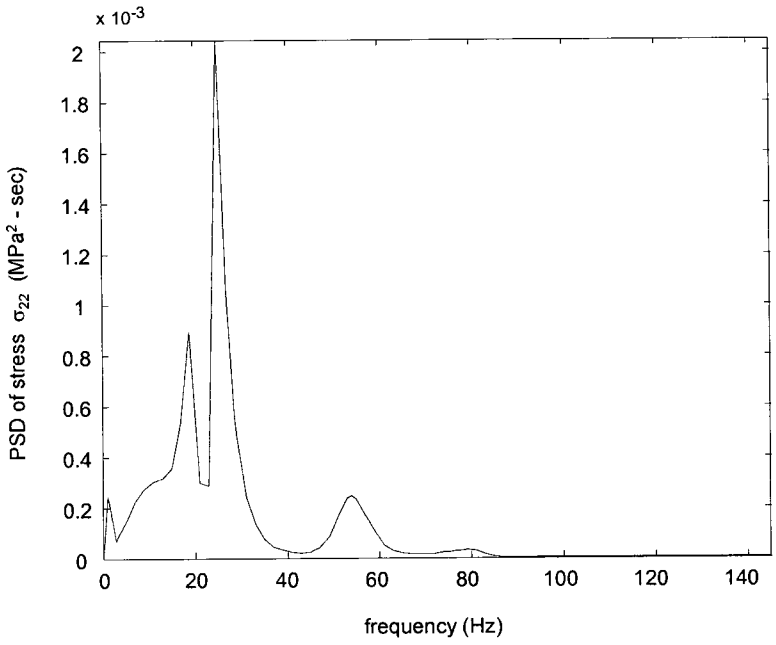

Figure 2.27: Stress PSD at the window corner using the two-parameter suspension stiffness.

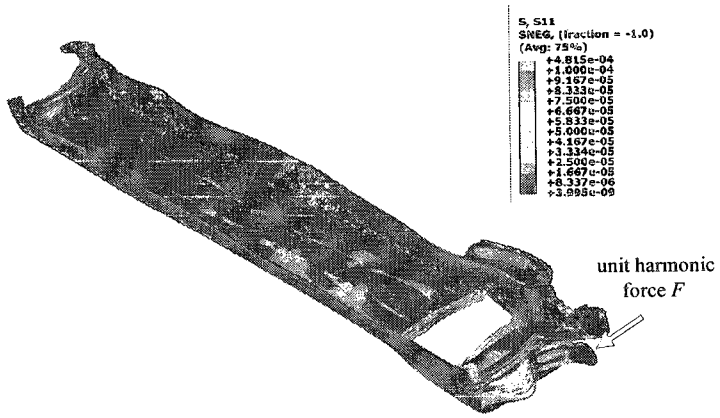

Figure 2.28: Stress pattern for a unit 53 Hz harmonic load at the bogie support.

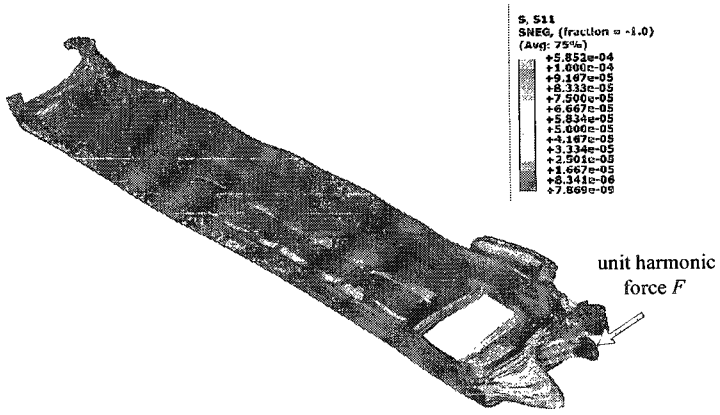

Figure 2.29: Stress pattern for a unit 63 Hz harmonic load at the bogie support.

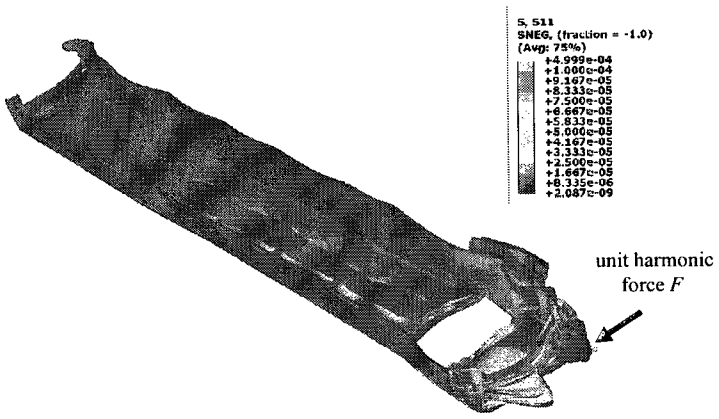

Figure 2.30: Stress pattern for a unit 74.5 Hz harmonic load at the bogie support.

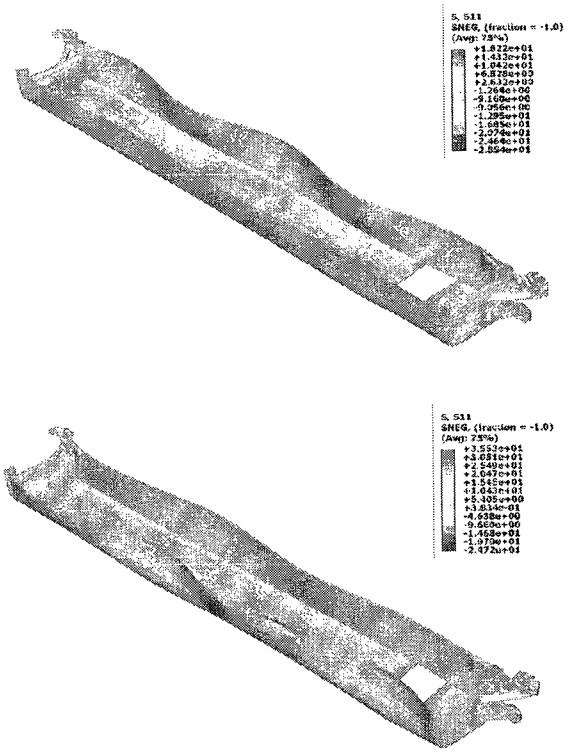

Figure 2.31: Stress patterns for the 49 and 54 Hz mode shapes.

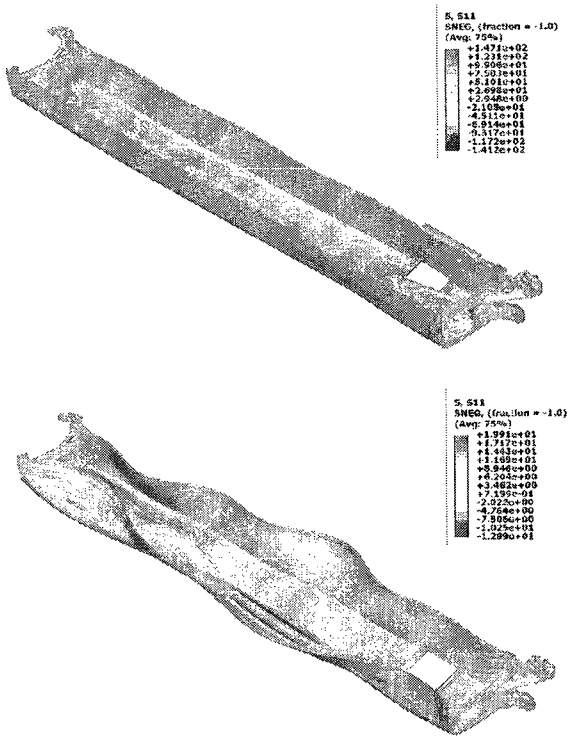

Figure 2.32: Stress patterns for the 62 and 73 Hz mode shapes.

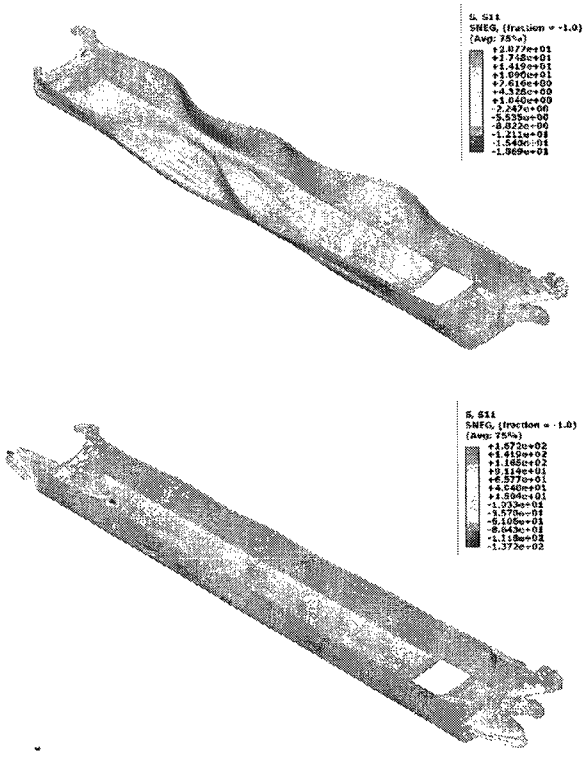

Figure 2.33: Stress patterns for the 75 and 81 Hz mode shapes.

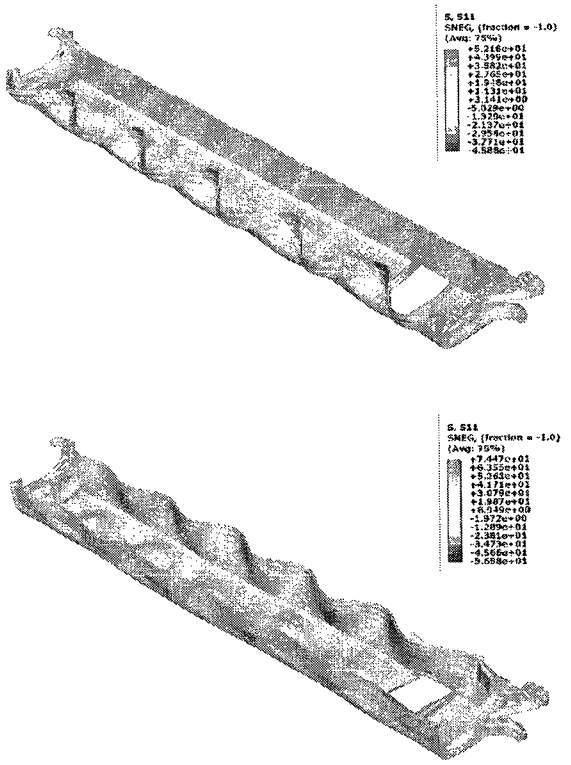

Figure 2.34: Stress patterns for the 136 and 139 Hz mode shapes.

Chapter 3

Fatigue reliability analysis of passenger cars in high speed trains

As indicated, the two goals of this study are to perform a fatigue reliability analysis of passenger car bodies and to propose fatigue test loading procedures. The characteristics of the response as studied in the previous chapter is used here to achieve these goals.

This chapter begins with a brief review of fatigue analysis. Next, the stress transfer function of the preceding chapter is used to develop a method for fatigue reliability analysis of the car body. The last part of this chapter focuses on possible test load configurations that would reproduce, as closely as possible, the types of stress patterns that are anticipated due to actual operational loads. Both static and dynamic test configurations are considered and a least-squares technique is used to determine the magnitude, direction and phase of the test loads.

3.1 Background

Structures under repeated loads below the allowable load can develop cracks. Due to cyclic loading, these cracks can continue to grow and propagate, leading to potential structural failure. Therefore structures under cyclic loads are often designed for fatigue type failure. While there are several methods for fatigue design of structures, all of them require similar information. This information include: location of fatigue failure, frequency spectrum of the load, stresses or strains due to the load in selected critical locations, and the temperature and corrosive nature of the environment. The fatigue reliability predictions are made using one of the following methodologies:

- S-N curves or stress life
- hot spot stresses
- strain life
- fracture mechanics

These methods are briefly reviewed in the following section.

3.1.1 S-N

Fatigue data is usually presented in form of S-N (Wöhler) curves. An example is shown in Figure 3.1. This plot shows the total cycles to failure N as a function of alternating stress

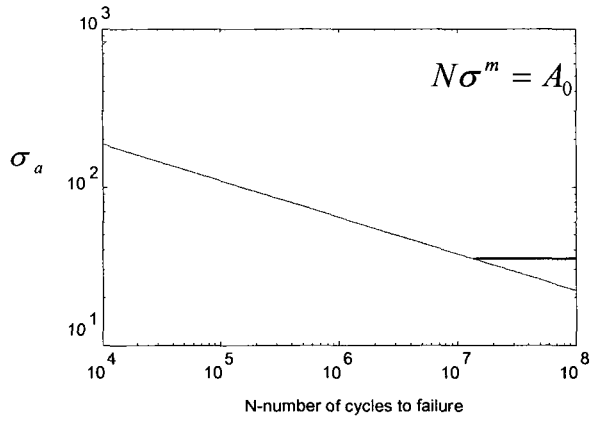

Figure 3.1: Typical shape for the S-N curve.

σ_a. Typically, the S-N curve is a linear function in log-log space, which can be expressed analytically as:

$$N\sigma^m = A_0 \tag{3.1}$$

Here m is the slope of the line in Figure 3.1 and A is a constant defining the intersection of the S-N curve at the stress axes. Allowable stresses for design are obtained by 95 percent confidence of 97.5 percent survival. There are two approaches for designing using the S-N curves: infinite life and safe life. Safe life designs are more common since it is economical

to design a structure for a finite life time rather than an infinite one.

3.1.1.1 Safe life design

In this approach the allowable stress is chosen such that failure occurs at a selected lifetime. It is noted that a safety factor must be considered for the stress, lifetime or both. The S-N curves can be used directly for loads with constant amplitudes while for varying amplitude loads cumulative failure loads such as Miner-Palmgren's law must be exploited. This method is explained in more detail in subsection 3.2.1.1.

3.1.1.2 Infinite life design

The experiments performed on loads with constant amplitude show that there exists an endurance limit below which there is no fatigue failure. This is shown as a horizontal line in the right part of Figure 3.1. The infinite life approach designs the components such that the stresses are below the endurance limit. This design approach is not appropriate for structures which are under occasional large stresses, and is usually used for the rotating components of machinery which are subjected to a large number of cycles of loads with similar magnitude.

3.1.2 Hot Spot

Hot spot stress is a type of stress concentration factor used in the design of welded structures. The hot spot stress represents a local stress increased by the geometry of the

joint. Two inputs are needed for the hot-spot stress analysis method: (1) the appropriate stress and (2) a fatigue curve for the welded construction to predict fatigue life. Hot spot stresses can be determined using measurements or by performing finite element analysis of the structure with consideration of selecting appropriate measurement locations and sufficiently fine meshes.

3.1.3 Strain-Life

This method is an appropriate approach in studying the low cycle fatigue and when the local strains are considerably higher than the yield strains. This method is commonly used in fatigue of notched components under cyclic load where the behavior of the root of the notch is considered by its strain. In this method, it is assumed that there is no crack in the component except at the highly strained region of the notch where the crack starts because of the high local strain due to the external load. The behavior of the material under high stress is evaluated by performing the experiment on a small polished unnotched specimen under constant amplitude fully reversed cycles. The material behavior is then represented in the form of a strain - life curve which accounts for both elastic and plastic strains.

The component of the local strains needs to be determined at the high strained regions and be compared to its associated value on the fatigue curve to obtain the number of cycles to failure. The strains are usually determined by measurements or finite element analysis. Since inelastic strains are needed, a nonlinear finite element analysis must be performed and the cyclic material properties must be used.

3.1.4 Fracture mechanics

This method assumes the presence of an initial flaw which propagates under cyclic loads to a size that causes failure of the component. Final fracture occurs when either the toughness of the material is exceeded or the remaining ligament yields [Anderson, 1994]. While this method is more complicated than the above approaches, it provides more information about the life of the material under discontinuity and load carrying capacity of the structure.

3.1.5 Selection of methods

The method for life prediction is usually selected based on the requirements of design codes and specifications for the particular component or structure. However, if there is no requirement, the S-N approach is the easiest method to apply and is usually considered for most preliminary designs. In the S-N method only nominal stresses are needed which are easy to find, while other techniques require information which needs more advanced analysis and increases the time and cost of the procedure.

Sometimes it is necessary to use more advanced methods to improve the accuracy of the prediction. The hot-spot stress method is useful since the high local stress due to geometry are calculated. If the rate of growth of the crack and residual stresses are important, fracture mechanics must be employed which is more complicated and expensive but provides more accurate and detailed information. For low-cycle fatigue, where the strains are large, the

strain-life is appropriate.

3.1.6 Loads and Stresses

As mentioned in section 3.1 one of the basic pieces of information needed for fatigue life prediction is the loading or stresses applied on the structure or component. In many cases the loads applied on the structure are random, and even if the cyclic loads are identical, the local stresses may vary due to changes in the details of the component. Therefore a load spectrum may be needed for such loads.

With the development of advanced testing facilities, variable amplitude loads can be applied to provide a more realistic estimate of the behavior of structures under realistic load conditions. The variable amplitude load spectra is used for a variety of different applications such as in the design of aircraft, mechanical equipment and automotive parts. The order of loads in a spectrum can also affect the fatigue life, but since many structures are subjected to random loads, the order in the sequence of loads is not important in the analysis of such loads. To specify a variable amplitude load for design, the number of cycles at each load and the magnitude of their ranges and in some cases a non-zero mean load must be specified. Therefore a cycle-counting technique must be used to determine the above information. Specifications are typically used to determine the loads, stresses or strains required for fatigue analysis, and standardized load spectra. For railroad cars, load spectra, including the number of cycles and magnitude of the loads are typically used in specifications. The Association for American Railroads (AAR) [Americal Association of

Railroads, 1986] provides a list of components that needs to be analyzed for fatigue and suggests the crack initiation locations for typical details. It also provides the load spectra for different components of several types of standard car bodies [M. L. Sharp et al., 1996, R. I. Stephens et al., 2001].

3.2 Fatigue reliability analysis of passenger car

In this section the reliability of the car body is estimated using the concept of the stress TF. In section 2.3.3, the stress transfer function was estimated using the acceleration measured on the car body and bogie and the results of finite element analyses. In this section, this stress transfer function is used to predict the fatigue stresses. The fatigue stresses in the car body are then used to assess the fatigue reliability.

3.2.1 Fatigue stress

The stress TF $H^{\sigma}_{A_b}(x)$ is used for generating stress time histories of fluctuating stress versus time. Stress time histories are important in fatigue analysis, particularly for stress evaluation algorithms such as the rainflow counting procedure that is discussed later in this section. To obtain a stress time history, one can simply take the Fourier transform of the measured bogie acceleration, A_b, multiply by the stress TF $H^{\sigma}_{A_b}(x)$ in equation (2.9) to get the Fourier transform of the stress, $\sigma(f)$, then take the inverse Fourier transform to obtain

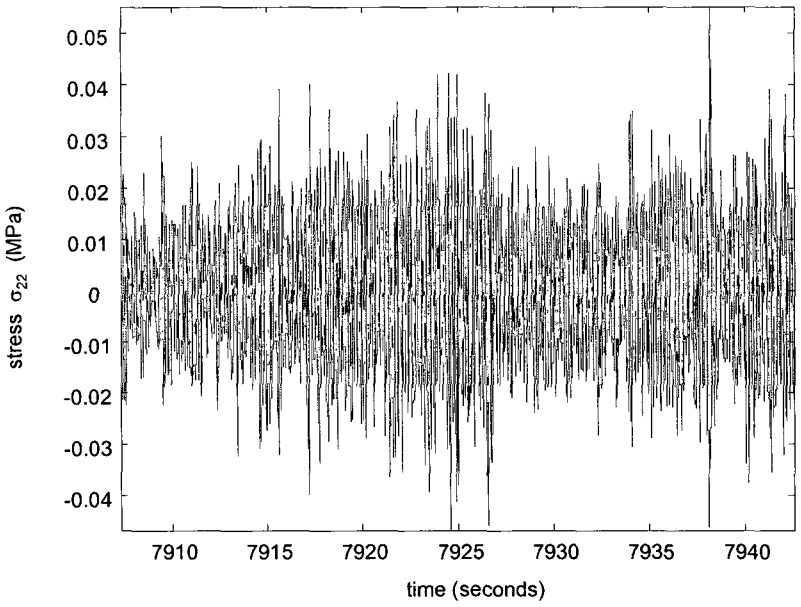

Figure 3.2: Simulated stress time history at the window corner due to recorded bogie motion.

the stress in the time domain:

$$\sigma(f) = H^{\sigma}_{A_b} A_b$$

$$\sigma(t) = \mathrm{IFFT}\left(\sigma(f)\right)$$

An illustration of the stress time history is shown in Figure 3.2. This is the stress at the corner of one of the windows resulting from bogie accelerations at both ends. The result indicates that the stress time history is very irregular and random in nature. Figure

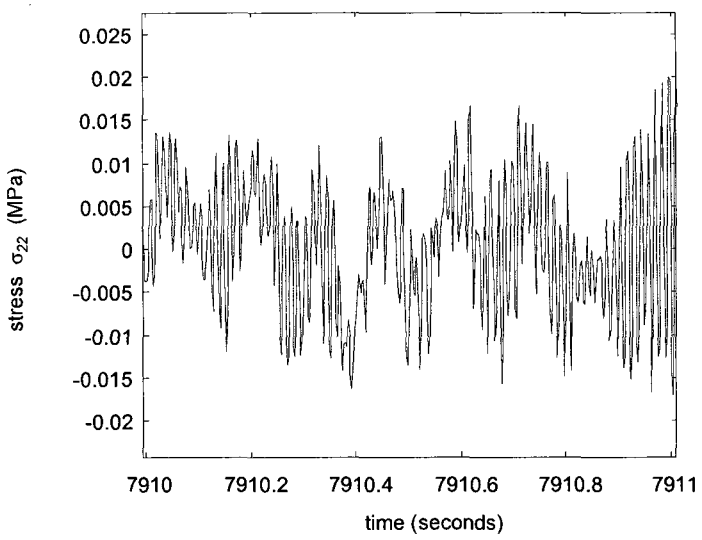

Figure 3.3: Simulated stress time history, enlarged time scale.

3.3 shows the same stress time history, magnified for a short duration in time. Here it can be seen that the stress time history has a high-frequency fluctuation of approximately 70 Hz with varying amplitude. This high frequency response is superimposed on top of a lower frequency fluctuation of approximately 7 Hz. These two predominant frequencies are in agreement with the auto-PSD in Figure 2.26: The peaks at 50 and 73 Hz in the PSD combine to produce a high-frequency fluctuation at a frequency between 50 and 73 Hz with time-varying amplitude and the relatively wide peak at 7 Hz corresponds to the low

frequency fluctuation.

Later in this section it is shown how the time history of stress at different locations of the car body can be used to perform fatigue analysis and to compute a fatigue damage index.

3.2.1.1 Fatigue stress life analysis review:

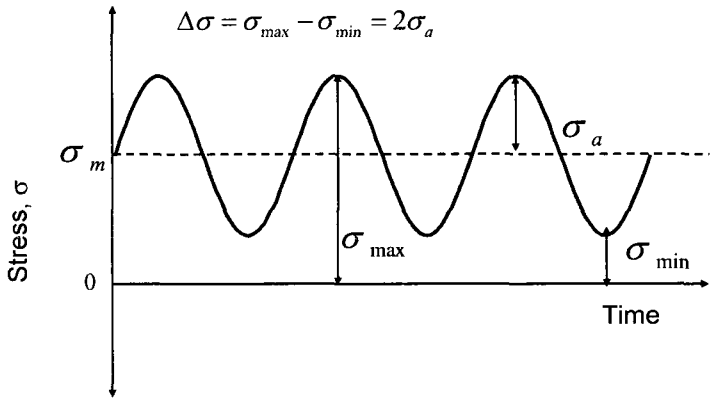

Figure 3.4: Fatigue parameter definitions.

In this section a brief review of the fatigue analysis procedure is provided. The fatigue

parameters illustrated in Figure 3.4 are:

σ_m	mean value of a stress cycle
σ_{min}	maximum value of a stress cycle
σ_{max}	minimum value of a stress cycle
$\Delta\sigma = \sigma_{max} - \sigma_{min}$	range of a stress cycle
$\sigma_a = \frac{\Delta\sigma}{2}$	amplitude of a stress cycle
$R = \frac{\sigma_{min}}{\sigma_{max}}$	ratio of maximum to minimum stresses

An example of the S-N curve showing the total cycles to failure N as a function of alternating stress σ_a is presented in Figure 3.1. The standard S-N curve is always evaluated with zero mean stress, $\sigma_m = 0$. This corresponds to the stress ratio $R = -1$. For different components of structures, however, the mean stress affects fatigue life. For instance, under cyclic loading only the tensile stresses cause the crack to propagate. Therefore, an increase in the mean stress results in shorter fatigue lifetime. To account for non-zero mean stress, a Goodman modification is used which provides a method to combine constant-amplitude S-N curves with different stress ratios. To incorporate non-zero mean stresses, a modified S-N curve formulation can be written as:

$$N\sigma^m = A_0 \left(1 - \frac{\sigma_m}{\sigma_u}\right)^m \tag{3.2}$$

where σ_u is the ultimate tensile stress at failure and N is the total number of stress cycles at failure. For the aluminum welds used in the HSR-350x, the three parameters used to define

the modified S-N curve are

$$A0 = 6.58e^{13} \ MPa$$

$$m = 4.32$$

$$\sigma_u = 247 \ MPa$$

3.2.2 Rainflow counting

When using variable amplitude loads, the number of cycles at each stress level and in some cases the mean stress level must be known for fatigue analysis methods mentioned above. Cycle counting is not obvious for loads with variable amplitudes [Tucker, 1982]. There are different types of cycle counting techniques suggested by the ASTM standard such as level-crossing counting, peak counting, simple-range counting and rainflow counting. Unfortunately, these various methods of cycle counting produce different results. Rainflow counting is shown to be accurate for most cases and is used herein [M. L. Sharp et al., 1996].

The term rainflow refers to the concept of rain falling from the time history plot when the time axis is vertically oriented so that it can be visualized as a series of pagoda roofs. A simple schematic showing such a vertically oriented time history and simulated rain is shown in Figure 3.5 and is explained as follows: The positive tips are called peaks and the negative ones are called valleys. First, the time history is rearranged such that it starts and

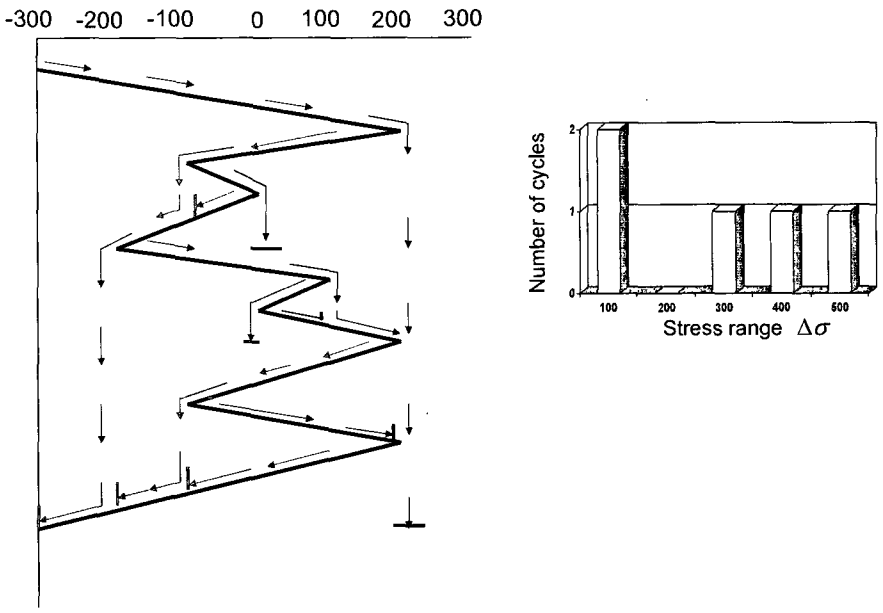

Figure 3.5: Example of rainflow counting (after M. L. Sharp et al. [1996])

ends with the highest absolute value of stress in the time history block. This rearrangement makes all half cycles of a specific stress range pair to another half cycle with that range to make a full cycle. A half cycle starts at the beginning of location of start of rainflow. The half cycle ends when one of the following occur:

- Flow reaches the end of the signal.
- Starting at a peak, flow reaches a more positive peak than it is started.
- Starting at a valley, flow reaches a more negative valley than it is started.

- It reaches to a rainflow from a roof above.

An example illustrating each of the above steps in rainflow counting is shown in the left side of Figure 3.5. The right figure is a histogram showing the number of cycles at each stress range $\Delta\sigma$ [M. L. Sharp et al., 1996].

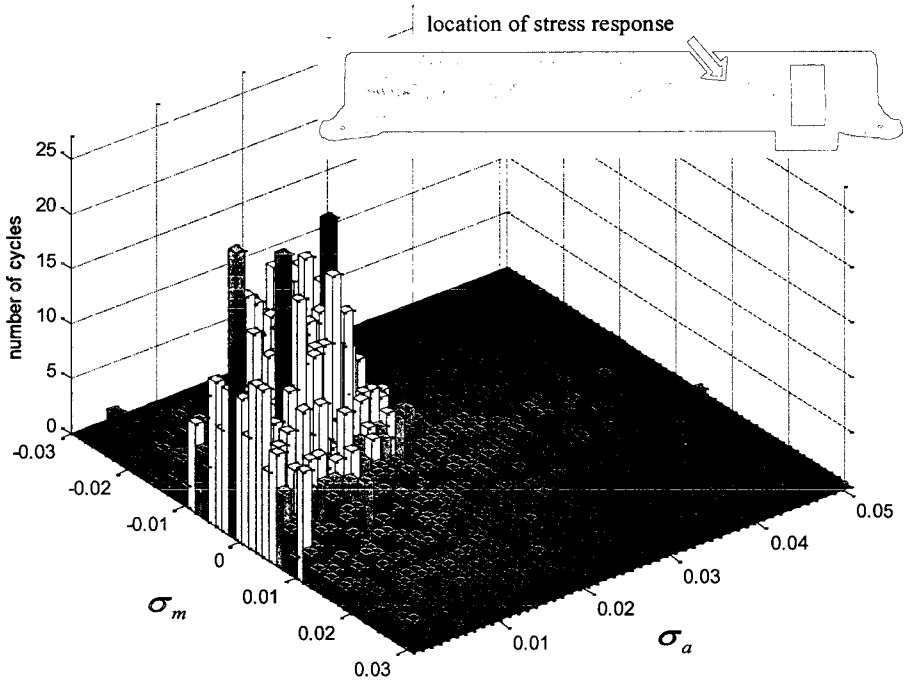

Figure 3.6: Rainflow counting matrix of stress amplitudes (MPa) and mean values for the stress (MPa) at the window corner location.

The rainflow counting algorithm was used to analyze the stress time history in Figure 3.2. There were a total of 2850 cycles. Figure 3.6 shows the rainflow counting matrix,

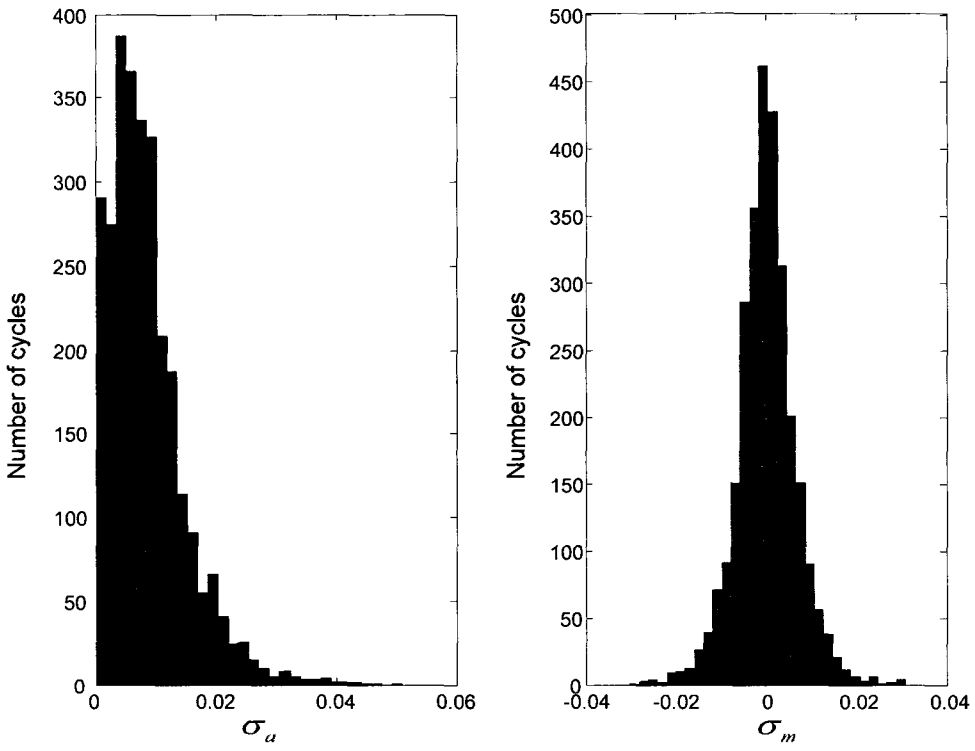

Figure 3.7: Histograms of alternating stress amplitudes (MPa) and mean values for the stress (MPa) at the window corner.

which is the joint histogram of the raw data:

$$h_{rainflow}(\sigma_a, \sigma_m) = \text{ number of cycles with stress amplitude } \sigma_a \text{ and mean stress } \sigma_m$$

This joint histogram has a standard shape showing a nearly Gaussian histogram for the mean stress σ_m at nearly zero stress amplitude, a Rayleigh histogram for the stress amplitude at nearly zero mean stress, and some 3D structure at low mean stress and stress amplitude. Figure 3.7 shows the rainflow marginal histograms of alternative and mean

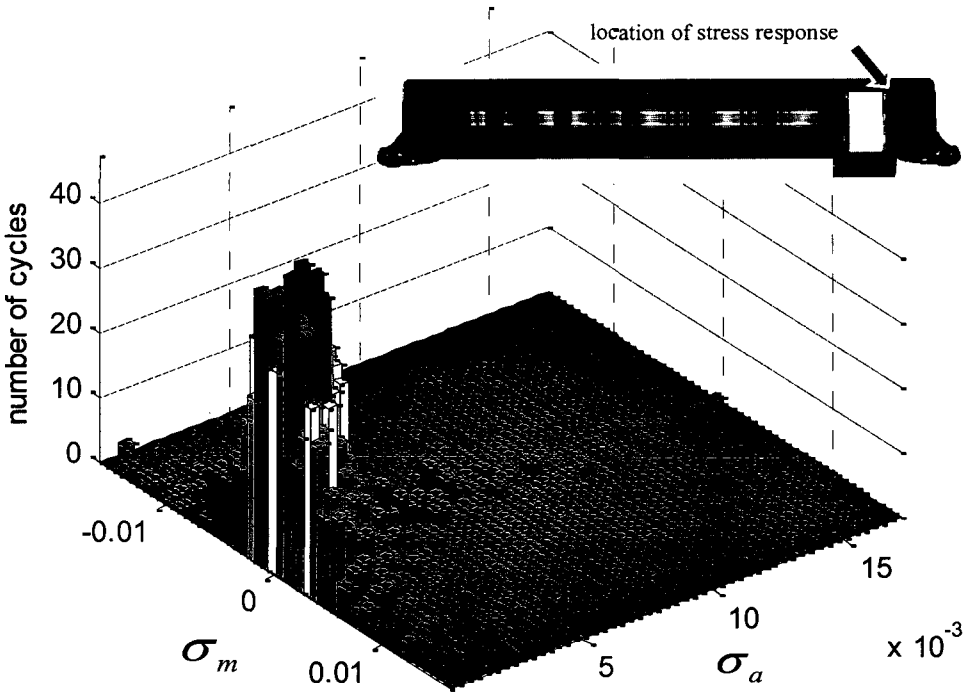

Figure 3.8: Rainflow counting matrix of stress amplitudes (MPa) and mean values for the stress (MPa) at the door corner location.

stress:

$$h_{rainflow}(\sigma_a) = \sum_{\text{all values of } \sigma_m} h_{rainflow}(\sigma_a, \sigma_m) = \text{ number of cycles with stress amplitude } \sigma_a$$

$$h_{rainflow}(\sigma_m) = \sum_{\text{all values of } \sigma_a} h_{rainflow}(\sigma_a, \sigma_m) = \text{ number of cycles with mean stress } \sigma_m$$

These histograms have the Rayleigh and Gaussian shapes, as mentioned above.

The rainflow matrix and histograms for another location at the door corner are shown in Figures 3.8 and 3.9. In this case there were 3228 cycles. The Gaussian and Rayleigh

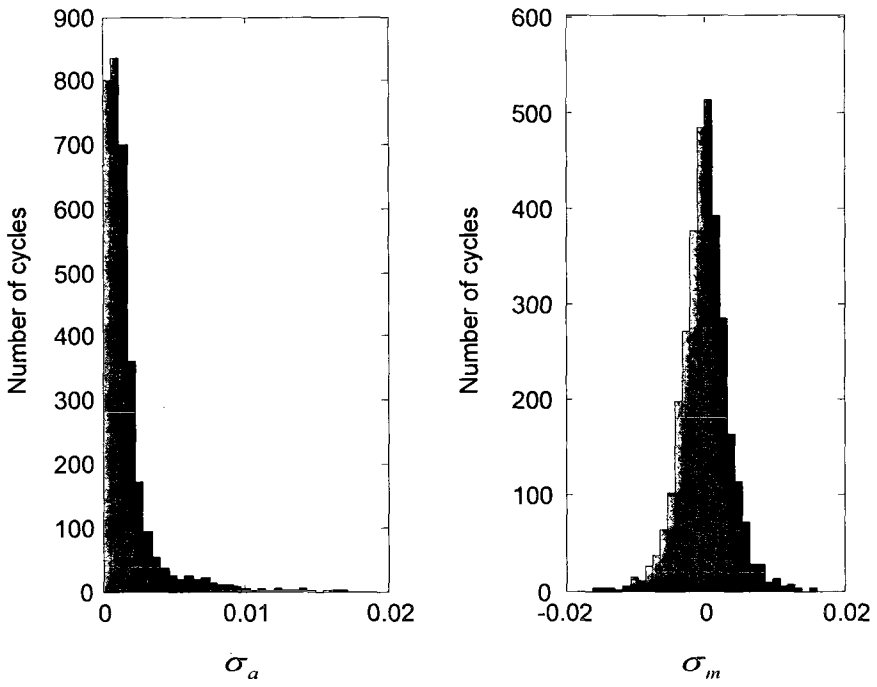

Figure 3.9: Histograms of alternating stress amplitudes (MPa) and mean values for the stress (MPa) at the door corner.

shapes in the joint histograms are even more clear than in the previous example in Figure 3.6.

3.2.3 Damage indices

When loading produces more than one stress level, damage accumulation laws must be used. The damage indicators are usually taken as zero in the initial state. They are mono-

tonically non-decreasing functions of time until failure. Their value at failure is usually one [M. L. Sharp et al., 1996]. One of the most widely used damage accumulation rules is called the Palmgren-Miner linear damage rule. This rule indicates that failure occurs when the summation of the ratio of number of cycles of load in a stress level to number of cycles to failure due to the same stress level equals to one. It is very simple, and produces generally good estimates. Here, two ways to evaluate this damage rule is presented. The first is based on a discretized form of the probability distribution of stresses, represented by histograms such as those shown in Figures 3.6-3.9. The second approach uses a continuous form of the probability distributions. Both approaches are used herein.

3.2.3.1 Discretized analysis

The damage index D in the Palmgren-Miner rule is defined as:

$$D = \sum_i \frac{n_i}{N_i} \tag{3.3}$$

with failure occurring when $D = 1$. In the above, i is index corresponding to an alternating stress range, n_i is number of cycles in the i^{th} stress range and N_i is the number of cycles to failure at the i^{th} stress range. This can be rewritten in terms of the histograms $h(\sigma_a)$ of the stress amplitudes shown in Figures 3.7 and 3.9:

$$D = \frac{t_{lifetime}}{t_{measurement}} \sum_i \frac{h(\sigma_a)^i}{N_i} \tag{3.4}$$

where $t_{lifetime}$ is the lifetime service or lifetime of the system and $t_{measurement}$ is the duration of the measurements.

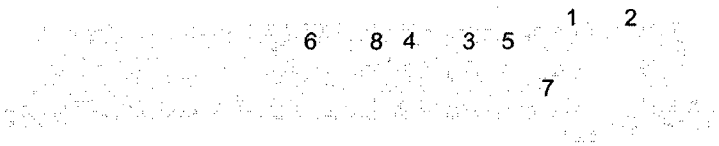

Figure 3.10: Locations of high stress responses for detailed study.

The damage index rule can be generalized to include the mean stress:

$$D = \frac{t_{\text{lifetime}}}{A_0 t_{\text{measurement}}} \sum_i \sum_j \frac{\left[\sigma_a^{(i)}\right]^m}{\left[1 - \frac{\sigma_m^{(j)}}{\sigma_u}\right]^m} h\left(\sigma_a^{(i)}, \sigma_m^{(j)}\right)$$

where j is the index corresponding to the mean stress σ_m and $h(\sigma_a, \sigma_m)$ is the joint histogram of number of stress cycles at σ_a and σ_m.

The rainflow histogram shown in Figures 3.6 and 3.8 can be used for the above histogram by the modification of adding the mean stress due to static load (gravity load for the HSR-350x car body). In the analysis we used $t_{lifetime} = 10^9$ seconds.

To illustrate this damage index, the stress time histories were computed at eight locations of the car body. These locations, indicated in Figure 3.10, are at the corners of the windows and door and correspond to the most highly stressed regions of the car body for many of the harmonic frequency loads. The stress time history in Figures 3.2 and 3.3 and the rainflow joint and marginal histograms shown in Figures 3.6 and 3.7 correspond to location 5. The rainflow histograms shown in Figures 3.8 and 3.9 correspond to location 2. The results for the damage index for all eight locations are summarized in Figure 3.11.

Figure 3.11(a) shows the damage indices considering the frequency-dependent support stiffness. The locations with the highest damage indices are at the top corners of the door. This is not surprising because the door is the largest opening in the car body and is relatively close to the support. The other two locations with the next highest damage indices are at two corners of the window closest to the door. This is also related to the proximity of these locations to the support excitation. Figure 3.11(b) shows the damage indices at the same locations, but using the simpler two-parameter support stiffness. The general trends observed in Figure 3.11(a) for the frequency-dependent stiffness can also be seen in Figure 3.11(b). There are two significant differences between the two figures. The first is that the damage indices at the windows are slightly more uniform in Figure 3.11(b). The more significant difference is that the damage indices for the two-parameter stiffness is over six orders of magnitude larger than that for the frequency dependent stiffness. This is because the differences in the relative magnitude of the stresses arising from the two types of support stiffnesses becomes magnified after the analysis using the Palmgren-Miner rule.

The analytical source of this magnification effect is the exponent of $m = 4.32$ that appears in the rule.

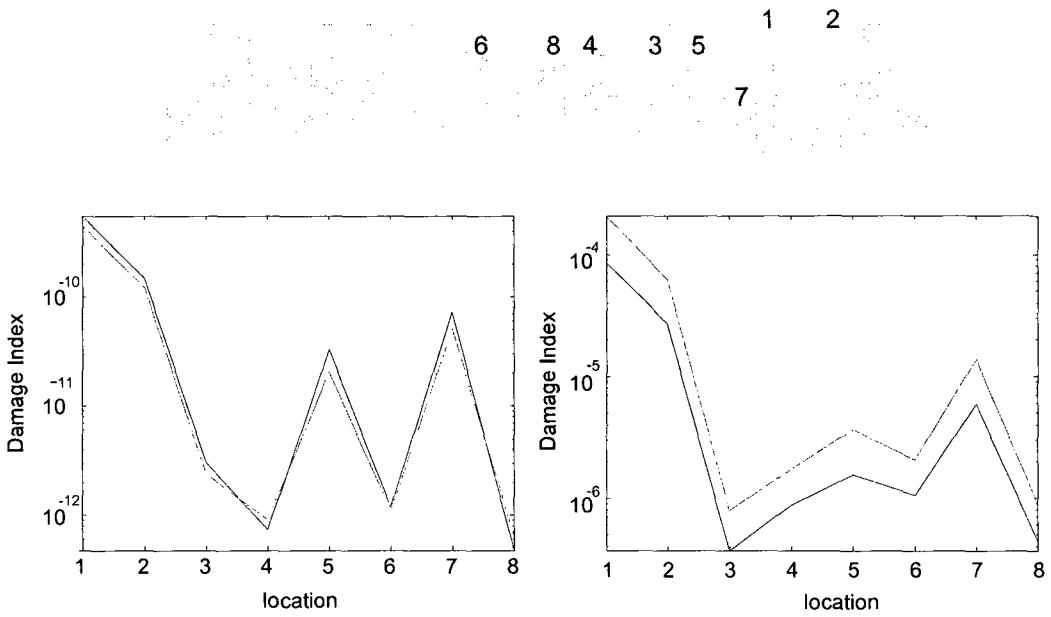

Figure 3.11: Damage index at eight locations using (a) frequency-dependent support stiffness and (b) two-parameter stiffness. Rainflow counting (dashed), simpler result using equation (17) (solid).

3.2.3.2 Continuous analysis

As stated earlier, the Palmgren-Miner rule can also be evaluated using a continuous representation of the probability distribution of stresses. This continuous analysis is briefly

reviewed herein and the results obtained using this analysis is compared with the results obtained using the discretized rainflow histograms.

There are two modeling assumptions in the continuous analysis. The first is in replacing the mean stress σ_m by constant values. For the HSR-350x, the constant value would be given by the stress due to gravity loads. This approximation is valid because the additional mean stress arising from the bogie vibrations are much smaller than the original gravity-induced mean stresses. The second modeling assumption is in replacing the marginal histogram $h_{rainflow}(\sigma_a^{(i)})$ of the stress amplitudes shown in Figures 3.7 and 3.9 by continuous probability distributions. Before continuing, some more terms are defined:

Using the theory of stochastic processes, the root mean square (RMS) of stress σ_{RMS} is evaluated by integrating the square of the stress time history:

$$\sigma_{RMS} = \left\{ \int \left[\sigma_a(t) - \sigma_m\right]^2 dt \right\}^{1/2} \tag{3.5}$$

In addition, the average zero up-crossing rate ν_0^+ can be evaluated in terms of the auto-PSD of the stress $S_{\sigma\sigma}$:

$$\nu_0^+ = \left[\frac{\int f^2 S_{\sigma\sigma}(f) df}{\int S_{\sigma\sigma}(f) df} \right]^{1/2} \tag{3.6}$$

With this estimate for the rate of zero up-crossing, the number of lifetime cycles, $n_{lifetime}$, can be evaluated in terms of the lifetime duration $t_{lifetime}$:

$$n_{lifetime} = \nu_0^+ t_{lifetime} \tag{3.7}$$

Finally, the Rayleigh distribution is typically used for the probability distribution of the

stress amplitudes. This distribution has the exponential form

$$f(\sigma_a) = \frac{\sigma_a^2}{\sigma_{\text{RMS}}^2} \exp\left(-\frac{\sigma_a^2}{2\sigma_{\text{RMS}}^2}\right) \tag{3.8}$$

It is noted that the expressions in equations (3.6), (3.7) and (3.8) for the zero up-crossing rate, lifetime number of cycles and stress probability distribution are most accurate when the stress time history is a narrow-band stochastic Gaussian process. Narrow-band stochastic processes are characterized by a time history that can be described by a sinusoidal-type oscillation with varying amplitude. The stress time history shown in Figure 3.3 has much of the character of a narrow-band stochastic process, but is slightly more complicated because of the low-frequency fluctuation. This low-frequency fluctuation, however, is relatively unimportant in fatigue analysis because the number of cycles of this fluctuation is an order of magnitude smaller than the number of cycles in the higher frequency oscillations in the stress time history. The Gaussian nature of the stress time history is evident in the histogram of stress amplitudes shown in the right of Figure 3.7.

Once the probability distribution $f(\sigma)$ of the stress amplitude is determined, then the Palmgren-Miner rule for continuous stress spectra can be evaluated [Li, 1999]. For the simpler case of zero-mean stress, this rule gives the damage index

$$D = \frac{n_{\text{lifetime}}}{A_0} \int_0^\infty \sigma^m f(\sigma) d\sigma \tag{3.9}$$

For the case where the mean stress σ_m is constant but not zero, the above equation can be modified as:

$$D = \frac{n_{\text{lifetime}}}{A_0} \int_0^\infty \frac{\sigma^m f(\sigma)}{\left(1 - \frac{\sigma_m}{\sigma_u}\right)^m} d\sigma \tag{3.10}$$

As described earlier, if the stress time history is a stationary narrow-band Gaussian process, then the results in equations (3.6), (3.7) and (3.8) can be used. When these results are substituted into equation (3.10), then the following analytical form for the damage index is obtained [Li, 1999]:

$$D = \frac{\nu_0^+ t_{\text{lifetime}}}{A_0 \left(1 - \frac{\sigma_m}{\sigma_u}\right)} \left(\sqrt{2}\sigma_{RMS}\right)^m \Gamma\left(\frac{1}{2}m + 1\right) \tag{3.11}$$

where Γ is the Gamma function. This relatively simple form for the damage index can be evaluated using only the stress time history and its auto-PSD such as shown in Figures 2.26 and 2.27.

This simpler expression for the damage index is used to evaluate the fatigue reliability at the same eight locations around the car body openings as in section 3.2.3.1. The results are plotted in Figure 3.11(a) and (b) using solid lines. The results for the frequency-dependent stiffness are nearly identical to those evaluated using the rainflow histograms. For the two-parameter stiffness, the continuous form for the damage index is lower than the corresponding damage index obtained using the rainflow histograms. The main reason is that the stress time history for the two-parameter stiffness is relatively wide band, with more widely varying frequency and amplitude. This can be seen by the wider form for the auto-PSD in Figure 2.27.

The damage indices for all three components of the stress at the eight locations of the car body as well as for the upper and lower sections of the elements are tabulated in Tables 3.1-3.4. These results are simply more detailed forms of the results summarized in Figures 3.11(a) and (b). The highest damage indices are at the two corners of the door. For the

Table 3.1: Damage index using frequency-dependent stiffness and simplified equation (3.11) for $t_{lifetime} = 10^9$.

Damage Index	Top of the element			Bottom of the element		
location	S11	S22	S12	S11	S22	S12
1	1.700E-14	3.900E-14	3.940E-13	2.851E-12	2.472E-10	6.170E-13
2	1.430E-13	1.510E-13	3.050E-13	4.298E-12	6.623E-11	5.080E-13
3	4.400E-14	1.757E-12	1.000E-14	8.000E-15	4.000E-13	1.300E-14
4	1.300E-14	2.470E-13	2.000E-15	4.000E-15	4.210E-13	3.000E-15
5	4.740E-13	1.604E-11	9.700E-14	1.650E-13	2.822E-12	1.220E-13
6	1.300E-14	5.900E-13	4.000E-15	6.000E-15	3.870E-13	6.000E-15
7	3.890E-13	3.362E-11	1.020E-13	8.900E-14	1.106E-11	8.700E-14
8	2.000E-15	5.800E-14	0.000E+00	1.000E-15	2.390E-13	1.000E-15

locations far from the bogie connection this damage index will decrease.

3.3 Loads for fatigue testing

An important goal of this research is to provide guidance for developing testing procedures for car bodies for fatigue reliability. This means that it is necessary to find ways to load the car bodies to produce the type of stress concentrations observed in the preceding sections. This analysis is useful in two ways:

Table 3.2: Damage index using frequency-dependent stiffness and rainflow counting for $t_{lifetime} = 10^9$.

Damage Index	Top of the element			Bottom of the element		
location	S11	S22	S12	S11	S22	S12
1	1.900E-14	3.400E-14	3.020E-13	2.183E-12	1.996E-10	4.680E-13
2	1.040E-13	9.400E-14	2.690E-13	3.600E-12	5.511E-11	4.480E-13
3	3.800E-14	1.431E-12	8.000E-15	7.000E-15	4.180E-13	1.200E-14
4	9.000E-15	1.740E-13	1.000E-15	2.000E-15	5.670E-13	2.000E-15
5	3.030E-13	1.018E-11	6.200E-14	1.060E-13	2.242E-12	7.700E-14
6	1.300E-14	4.960E-13	4.000E-15	6.000E-15	4.360E-13	6.000E-15
7	2.530E-13	2.369E-11	7.000E-14	5.800E-14	8.507E-12	5.700E-14
8	3.000E-15	7.600E-14	0.000E+00	1.000E-15	3.490E-13	1.000E-15

Table 3.3: Damage index using two-parameter stiffness and simplified equation (3.11) for $t_{lifetime} = 10^9$.

Damage Index	Top of the element			Bottom of the element		
location	S11	S22	S12	S11	S22	S12
1	9.738E-10	1.655E-08	4.792E-08	5.605E-07	8.587E-05	7.876E-08
2	7.441E-08	6.555E-08	1.630E-07	1.961E-06	2.704E-05	2.714E-07
3	1.447E-09	9.981E-08	7.037E-10	6.594E-10	3.695E-07	6.498E-10
4	4.447E-09	2.334E-07	1.474E-09	2.866E-09	8.681E-07	1.649E-09
5	4.152E-08	1.545E-06	6.847E-09	1.062E-08	4.358E-07	9.501E-09
6	2.955E-08	1.048E-06	5.122E-09	4.059E-09	6.154E-07	7.078E-09
7	2.944E-08	5.587E-06	1.594E-08	1.197E-08	5.893E-06	9.914E-09
8	4.600E-09	1.969E-07	8.198E-10	6.545E-10	4.348E-07	1.122E-09

Table 3.4: Damage index using two-parameter stiffness and rainflow counting for $t_{lifetime} = 10^9$.

Damage Index	Top of the element			Bottom of the element		
location	S11	S22	S12	S11	S22	S12
1	2.170E-09	3.874E-08	1.112E-07	1.329E-06	2.071E-04	1.825E-07
2	1.676E-07	1.418E-07	3.983E-07	4.607E-06	6.232E-05	6.678E-07
3	2.919E-09	2.133E-07	1.726E-09	1.456E-09	7.917E-07	1.309E-09
4	1.057E-08	5.331E-07	3.111E-09	5.774E-09	1.737E-06	3.783E-09
5	1.080E-07	3.605E-06	1.637E-08	2.388E-08	9.135E-07	2.236E-08
6	6.017E-08	2.065E-06	1.012E-08	7.761E-09	1.038E-06	1.414E-08
7	6.954E-08	1.307E-05	3.733E-08	2.771E-08	1.372E-05	2.274E-08
8	6.924E-09	2.884E-07	1.194E-09	9.810E-10	8.806E-07	1.713E-09

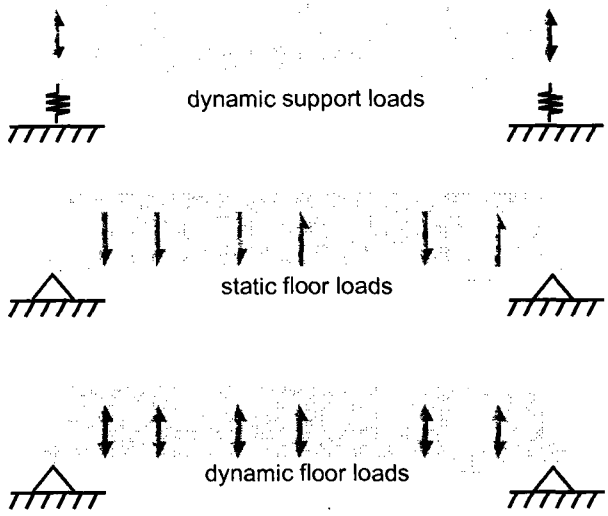

Figure 3.12: Test configurations for fatigue stresses.

1. The results can be used to develop test procedures.

2. The analysis will be useful in understanding how loads on the car body lead to stress concentrations. Such an understanding can be useful for designers so that they can develop car body designs with reduced stress concentrations.

In this section, three possible testing configurations are considered, which are shown in Figure 3.12. The first configuration, shown in the top of the figure, is the natural configuration where the car body is supported by springs at the ends and dynamic excitation loads

are applied at the support locations. This is perhaps the most obvious test configuration for satisfying (1) above. The main drawback of this configuration is that it is not very helpful in (2). It is not clear how the vibration loads at the ends leads to stress concentrations around the windows. The second configuration, shown in the middle of Figure 3.12, is to apply static loads on the floor of the car body. The idea here is to try to find static loads that will lead to the type of deformations and stress concentrations that are expected under service vibration loads. This may be the easiest test configuration for satisfying (1). Furthermore, since static loads are relatively simple to understand, the results of this analysis may be helpful in (2). There are, however, severe limitations to this approach, as shown below. The third configuration, shown in the bottom of Figure 3.12, is to apply dynamic rather than static loads on the floor of the car body. While this type of loading is more complex than the static loads, it is more realistic and is better suited for producing the stress concentrations expected under dynamic service loads.

To begin the analysis, the response pattern due to a harmonic force at one of the bogies is found. This analysis is the same as done earlier in Figures 2.22 and 2.28-2.30. Then the equivalent static or dynamic forces are determined such that they produce a similar response pattern. To find suitable forces, a least-squares fit analysis is performed. The least-square fit is performed by fitting either the displacement patterns or the stress patterns. To describe this in detail, some additional notation is introduced:

$x_d^{(j)}$ points on the car body for fitting displacements

$d_{load}^{(j)}$ displacements at $x_d^{(j)}$ due to a harmonic load at a support

$d_{test}^{(j)}$ displacements at $x_d^{(j)}$ due to the test loads

$x_\sigma^{(j)}$ points on the car body for fitting stresses

$\sigma_{load}^{(j)}$ stresses at $x_\sigma^{(j)}$ due to a harmonic load at a support

$\sigma_{test}^{(j)}$ stresses at $x_\sigma^{(j)}$ due to the test loads

$f^{(k)}$ test loads at locations k on the car body

For the displacement fitting analysis, the points $x_d^{(j)}$ are chosen at the locations where the displacements tends to be the largest for vertical support vibration loads. These points, shown in Figure 3.13, are distributed on the roof and floor of the car body. For the stress fitting analysis, the $x_\sigma^{(j)}$ are chosen at the locations of the greatest stress concentrations. These points, shown in Figure 3.14, are primarily at the corners of the windows and door with additional points along the middle of the floor-wall and wall-roof connections. This leads to test procedures which reproduces responses more accurately at these critical points.

Since the system is linear, there is a linear relation between the applied loads and the responses. Therefore, defining the vector notation

$$d_{\text{test}} = \begin{bmatrix} d_{\text{test}}^{(1)} \\ d_{\text{test}}^{(2)} \\ \vdots \end{bmatrix}, \quad \sigma_{\text{test}} = \begin{bmatrix} \sigma_{\text{test}}^{(1)} \\ \sigma_{\text{test}}^{(2)} \\ \vdots \end{bmatrix}, \quad f = \begin{bmatrix} f^{(1)} \\ f^{(2)} \\ \vdots \end{bmatrix}$$

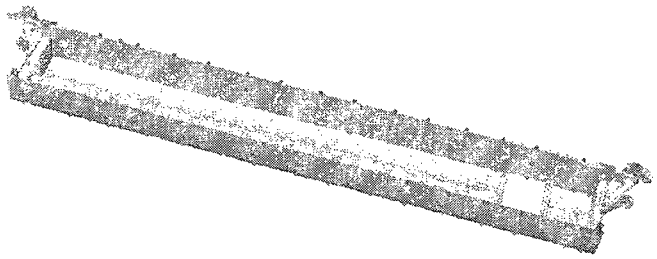

Figure 3.13: Locations for matching test displacement patterns.

with similar notation for d_{load} and σ_{load} then one can write the matrix relations

$$d_{\text{test}} = B_d f, \quad \sigma_{\text{test}} = B_\sigma f$$

In practice, the matrices B_d and B_σ can be determined by finite element analysis simply by setting the force f to be the unit vectors and solving for the displacements and stresses for each force vector. To find the static forces, a static analysis is performed, and to find harmonic forces, a harmonic analysis is performed at each frequency.

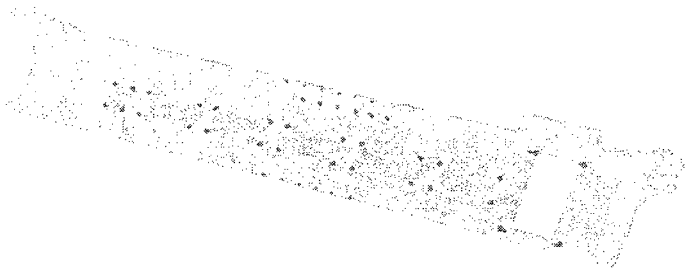

Figure 3.14: Locations for matching test stress patterns.

The fitting analysis was performed using a procedure similar to statistical regression. In the following, the details on the displacement fitting is given since the stress fitting is very similar. First, the sum of squared errors is evaluated to quantify the difference between the displacements $d_{\text{load}}^{(j)}$ due to the harmonic load at the support versus the displacements $d_{\text{test}}^{(j)}$ from the test load on the car body floor:

$$e_d = \sum_j \left[d_{\text{load}}^{(j)} - d_{\text{test}}^{(j)} \right]^2 = \text{sum of squared errors in displacement response}$$

These error quantities can be rewritten in matrix form. For the displacement case one can write

$$e_d = [d_{\text{load}} - d_{\text{test}}]^T [d_{\text{load}} - d_{\text{test}}] = [d_{\text{load}} - B_d f]^T [d_{\text{load}} - B_d f]$$

$$= d_{\text{load}}^T d_{\text{load}} - 2 d_{\text{load}}^T B_d f + f^T B_d^T B_d f$$

The goal in this fitting procedure is to find f which minimizes e_d. To find the minimum error, one can simply differentiate with respect to f and set the result to 0:

$$\frac{\partial e_d}{\partial f} = -2 d_{\text{load}}^T B_d + 2 f^T B_d^T B_d = 0$$

The solution for the test load vector f is

$$f = \left(B_d^T B_d\right)^{-1} B_d^T d_{\text{load}} \tag{3.12}$$

For fitting the stresses instead of displacements, the solution for the test load vector is

$$f = \left(B_\sigma^T B_\sigma\right)^{-1} B_\sigma^T \sigma_{\text{load}} \tag{3.13}$$

If the load vector f is constrained such that all components $f^{(k)}$ are equal to a single scalar value $f^{(0)}$, then this is the same as multiplying B_d by a unit vector

$$b_d = B_d 1 \quad \text{where 1 is a column vector of ones}$$

and it can be shown by substituting b_d for B_d in the above analysis that the solution for the scalar value $f^{(0)}$ is

$$f^{(0)} = \frac{b_d^T d_{\text{load}}}{b_d^T b_d} \tag{3.14}$$

The load vector for this constrained case is simply $f = \left[f^{(0)}\ f^{(0)}\ \cdots\right]^T$.

The above procedure is illustrated for the HSR-350x at a low and relatively high harmonic load frequencies. For the low frequency, the frequency of 2.75 Hz is chosen corresponding to the low-frequency peak of the PSD shown in Figure 2.26. The stress and displacement patterns due to this harmonic load applied to the support closest to the door are shown in Figure 3.15. The complexity of these response patterns is similar to that observed at other harmonic frequencies in section 2.3.4.

For the first test load, we try to find the uniform static loads which comes closest to matching the displacement field in Figure 3.15. To do this, the displacements $d_{\text{load}}^{(j)}$ at the locations shown in Figure 3.14 are collected and equation (3.14) is used to find the test force. The result is $f^{(0)} = -0.0132$ which is shown in Table 3.5 at all six force locations (because of the constraint). The corresponding stress and displacement fields are shown in Figure 3.16. It can be seen that the uniform load result produces stresses that are very different than the result from the harmonic load in Figure 3.15, with high stresses only in a small region near each of the six force locations. Next, a more general non-uniform set of static loads is determined to match the displacements and stresses by solving equations (3.12) and (3.13). The results for the forces are shown in Table 3.5 and the corresponding displacement and stress patterns are shown in Figures 3.17 and 3.18. Here, while there are still some localized stresses at each force location, the stress concentrations around the window can be observed. Finally, the same procedure is repeated with the same equations but using dynamic loads at 2.75 Hz frequency. The dynamic loads were very close to 0° or 180° out of phase with each other, so only $+/-$ signs are needed to describe these

Table 3.5: Test forces for matching displacements and stresses at 2.75 Hz.

Load (N) at 2.75 Hz Location	1	2	3	4	5	6
Uniform static load - displacement match	-0.0132	-0.0132	-0.0132	-0.0132	-0.0132	-0.0132
Static load - displacement match	0.0068	-0.2166	-0.1629	0.0636	0.0711	0.1204
Static load - stress match	-0.0398	-0.3606	-0.0181	-0.0386	-0.0430	0.1652
Dynamic load - displacement match	0.5994	-0.2059	-0.0211	0.0009	0.0010	0.1522
Dynamic load - stress match	1.2996	-0.2567	0.0222	-0.0158	0.0222	-0.0766

Table 3.6: Test forces for matching displacements and stresses at 74.5 Hz.

Load (N) at 74.5 Hz Location	1	2	3	4	5	6
Uniform static load - displacement match	0.0000	0.0000	0.0000	0.0000	0.0000	0.0000
Static load - displacement match	-0.0454	0.0525	-0.0032	0.0057	0.0005	-0.0107
Static load - stress match	-0.2659	0.0493	-0.0037	0.0180	-0.0073	0.0741
Dynamic load - displacement match	0.1331	0.0185	-0.0054	0.0047	-0.0032	0.0313
Dynamic load - stress match	-0.4417	0.0204	0.0120	0.0010	-0.0132	-0.0091

loads. The results are shown in Table 3.5 and Figures 3.19 and 3.20. Here, the stress concentrations around the windows and door can be seen. When comparing the responses for the five different test loads in Figures 3.16-3.20 with the harmonic load response in Figure 3.15, it can be seen that the dynamic load fitted to the stresses $\sigma_{\text{load}}^{(j)}$ gave the closest stress response pattern.

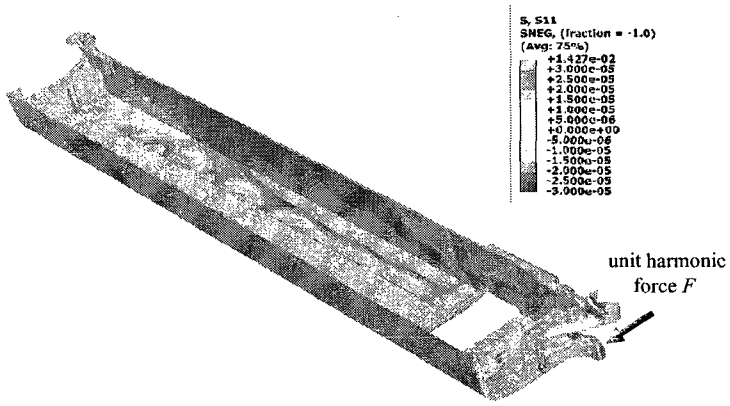

Figure 3.15: Stress pattern for a unit 2.75 Hz harmonic load at the bogie support.

This test load analysis procedure was repeated for a harmonic load at 74.5 Hz, corresponding to the relatively high-frequency peak of the PSD shown in Figure 2.26. The stress

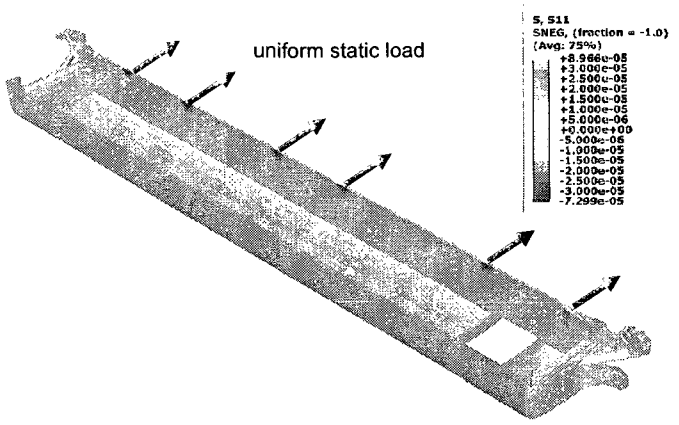

Figure 3.16: Stress pattern for a uniform static test load fitted to the 2.75 Hz displacements.

and displacement patterns due to this harmonic load applied to the support closest to the door are shown in Figure 3.21. The main differences from the low-frequency load case shown in Figure 3.15 are that there are more waves in the car body floor and roof and most of the stresses are localized around the door and windows. It is noted that the test loads evaluated here are unique because they are determined using linear regression.

The uniform static load procedure is unsatisfactory, because the load was nearly zero, as shown in Table 3.6 and indicated in the response plot in Figure 3.22. The difficulty here

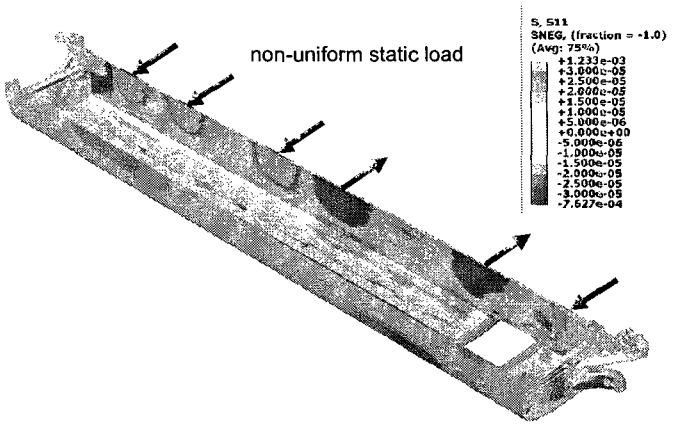

Figure 3.17: Stress pattern for a non-uniform static test load fitted to the 2.75 Hz displacements.

is that the response pattern is too complex to be approximated using a six-point static load. The more general non-uniform static loads do not produce significantly better results, as shown in Figures 3.23 and 3.24. Again, it is believed that the number of static loads – six – is too low for producing the complex response pattern at this high frequency. The results for the dynamic loads are far better, as shown in Figures 3.25 and 3.26. They produce the wave patterns in the floor and roof and the stress concentrations around the windows and door.

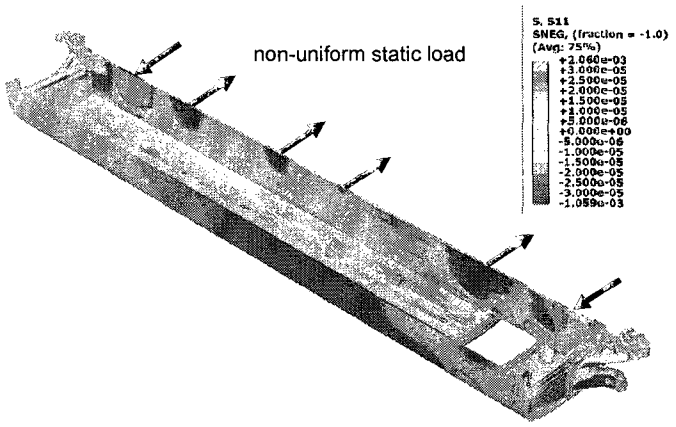

Figure 3.18: Stress pattern for a non-uniform static test load fitted to the 2.75 Hz stresses.

As for the low frequency case, the dynamic load fitted to the stresses $\sigma_{\text{load}}^{(j)}$ gave the stress response pattern closest to the original harmonic load response pattern in Figure 3.21. The results of this section are still in the preliminary stage, and there are several generalizations which can be explored.

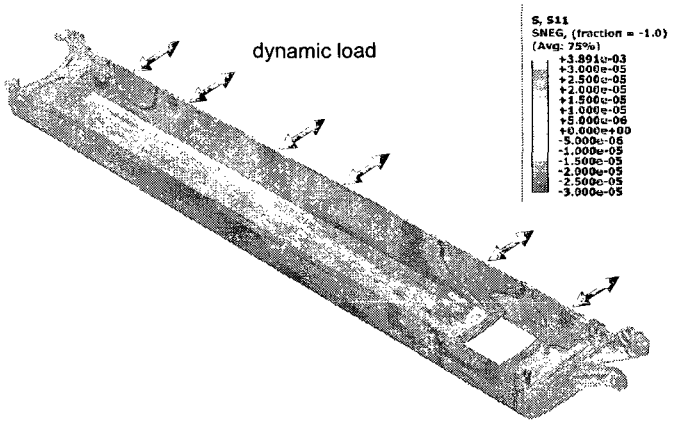

Figure 3.19: Stress pattern for a dynamic test load fitted to the 2.75 Hz displacements.

3.4 Conclusions and future study

The acceleration response measured on the car body and bogie were used to study the response characteristics of the car body. These results along with a finite element model, were then used to determine the dynamics properties of the suspension between bogie and car body and stress transfer function. The stress transfer function is used to obtain the time history of stress at different locations of the car body. The time history is then used for fatigue reliability analysis. The Palmgren-Miner rule is the cumulative damage predictor

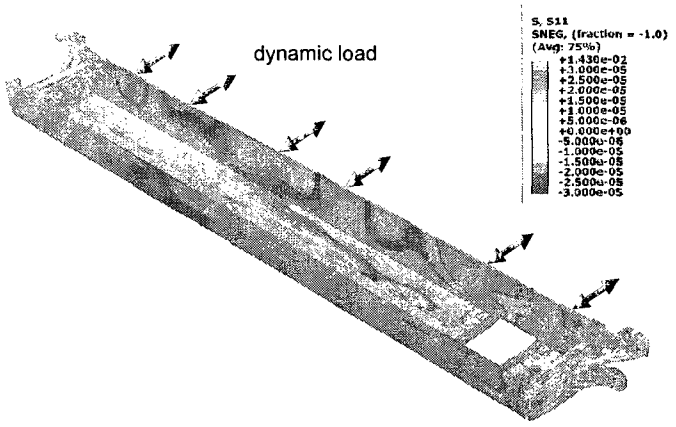

Figure 3.20: Stress pattern for a dynamic test load fitted to the 2.75 Hz stresses.

for the car body. The values for the damage index are very small even at the locations around the door and windows. One reason is that the finite element mesh is relatively coarse around the openings where the local stresses are high, so that the stress concentrations around the corners are not accurately represented. The finite element model of the car body is already complex and including fine meshes around all corners of all openings is not desirable. To overcome this problem a new numerical approach is developed in the next chapter to enhance the results of finite element analysis using coarse meshes and to more

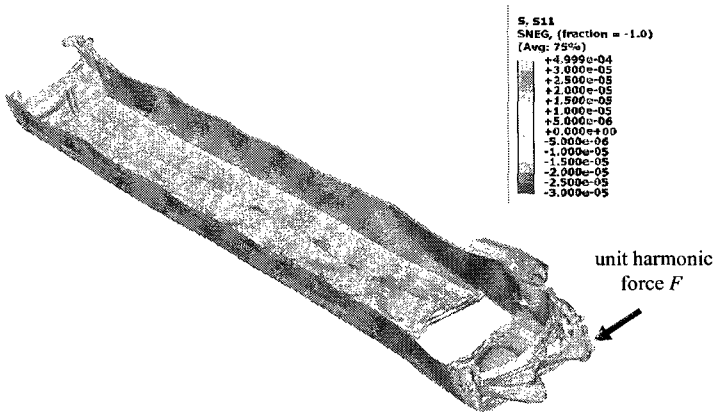

Figure 3.21: Stress pattern for a unit 74.5 Hz harmonic load at the bogie support.

accurately predict the local stresses at the corners of rectangular openings.

In the last part of this chapter, test load configurations for full-scale fatigue tests were proposed. The loads were obtained by fitting the static and dynamic displacements and stresses at various locations of the car body. The response from equivalent loads obtained by matching the dynamic stresses produce the stress patterns most similar to the harmonic response. These test load configuration results are in the preliminary stages and they can be improved in several ways. For instance the regression points for matching the dynamic

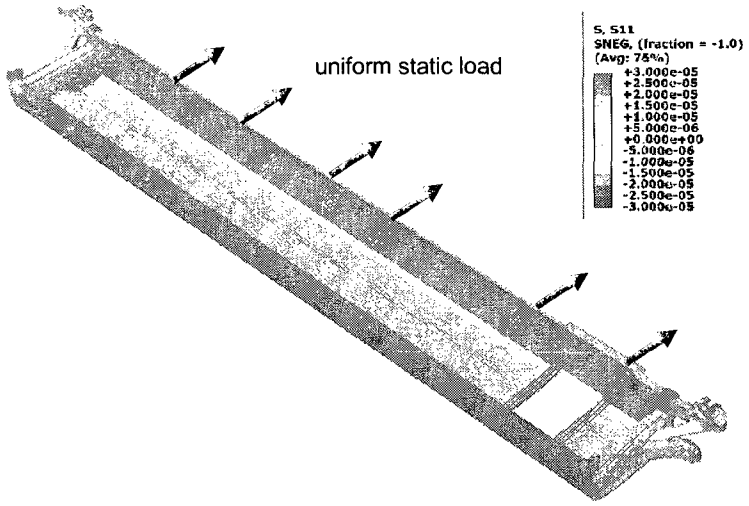

Figure 3.22: Stress pattern for a uniform static test load fitted to the 74.5 Hz displacements.

stresses can be moved to points that are closer to the regions of interest such as around the panel openings. Weighted least squares can also be used, with less weight at points away from the regions of interest such as at the ends of the car body. In addition both stresses and displacements can be fitted at the same time.

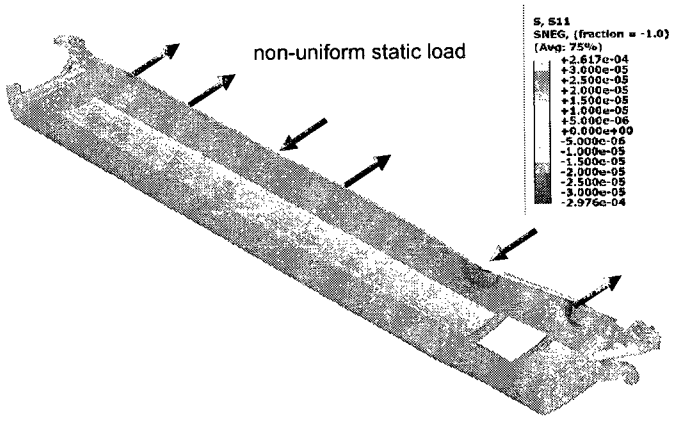

Figure 3.23: Stress pattern for a non-uniform static test load fitted to the 74.5 Hz displacements.

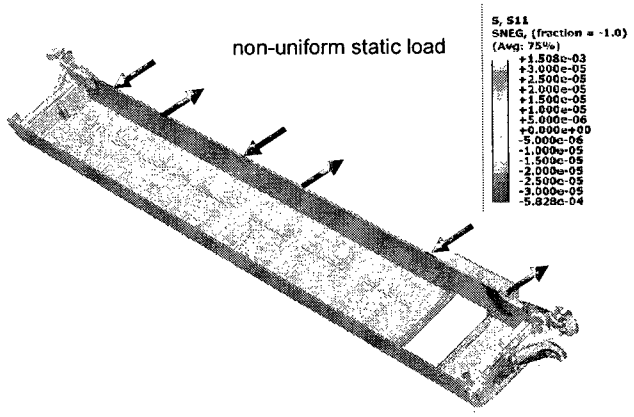

Figure 3.24: Stress pattern for a non-uniform static test load fitted to the 74.5 Hz stresses.

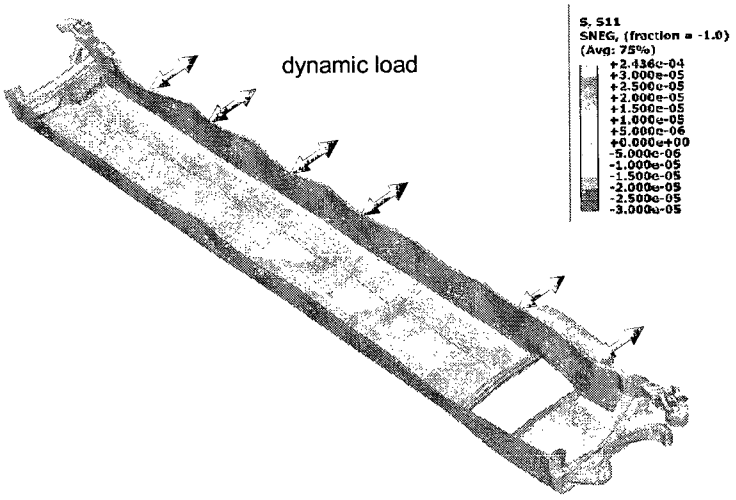

Figure 3.25: Stress pattern for a dynamic test load fitted to the 74.5 Hz displacements.

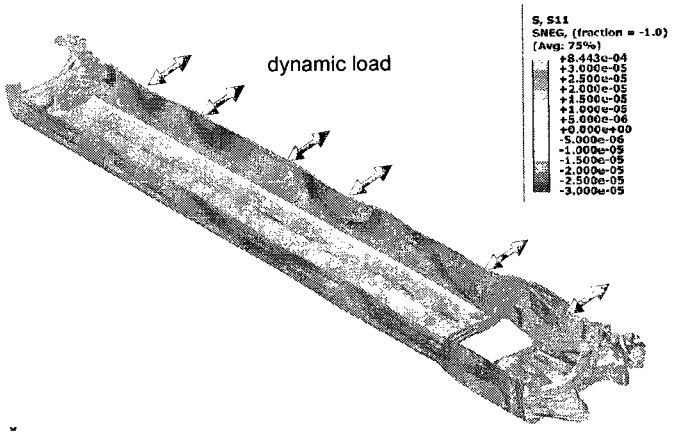

Figure 3.26: Stress pattern for a dynamic test load fitted to the 74.5 Hz stresses.

Chapter 4

Analysis of stresses in plates with rectangular openings using coarse finite element meshes

In section 3.2.3 it was found that the damage indices at the corners of windows and door were very small. It was explained that one reason for such results is that the finite element model for the train had fairly coarse meshes around these openings. In many practical problems, especially when the structures are large and complex, it is not feasible to use fine meshes around all corners of all panel openings. In such cases, the finite element analysis results will underestimate the stresses around the corners. In this chapter an analytical approach is developed that can be coupled with coarse-mesh finite element analysis to predict the stress concentrations around rectangular openings in plates.

CHAPTER 4.

4.1 Introduction

There are a variety of methods for evaluating stress concentrations in plates due to geometrical irregularities such as openings and cracks. In design it is common to use the stress concentration factor, defined as the ratio of maximum local stress to the nominal body or far-field stress. The stress concentration factor can be evaluated by using computational techniques, elasticity theory and experimental stress analysis such as photoelasticity. Peterson [1961] has provided stress concentration factors for different geometric irregularities under various types of loads. Wu and Mu [2003] developed simple methods to obtain the stress concentration factors around circular holes located in finite anisotropic plates or cylinders due to in-plane loads.

Using the edge function analysis, Hafiani and Dwyer [1999] studied the effect of the shape of the opening and the anisotropy of laminated composite plates under plane stress conditions. J. M. Henshaw et al. [1996] used finite element analysis to study the stress concentration in composite laminates with multiple openings under in-plane loads to demonstrate the increase in the stress concentration at the corners of an opening when another opening is added in its vicinity. Using integral equations Hu et al. [1993] studied the interactions between openings and cracks in different domains by breaking the problem into single hole and crack problems using the superposition principle. Chong and Pinter [1984] used finite element analysis to determine the stress concentration factor around large holes in tensile strips in terms of the size of the openings. Durelli et al. [1970] experimentally evaluated the large strains around elliptical holes and used the photoelasticity to determine

the stresses at those locations.

The method of complex variables [Muskhelishvili, 1975] provides a powerful approach to solve elasticity problems with geometric irregularities. The method uses a complex representation for the displacement field and maps the physical space of the plate with irregularity to a unit disk via a conformal transformation. The boundary conditions are then expressed in the unit disk space by a contour integral. Researchers have used this method to solve a wide variety of elasticity problems. Savin [1961] was one of the first to apply this method to the plate problem. He calculated the stress concentrations around openings of different shapes under several types of loadings at infinity.

More recent work on this problem using complex variables include papers by Ukadgaonker and Rao [2000], Xiwu et al. [1995], Wu and Cheng [1999], Chen and Hsu [1996], Bryukhanova [1967], Wang and Hasebe [2000], Tsukrov and Novak [2002] and Datsyshin and Marchenko [1985]). Ukadgaonker and Rao [2000] solved the bending problem for laminated composite plates with openings of different shapes and Xiwu et al. [1995] considered a finite laminate with elliptical hole under in-plane extensional and shear loads. Datsyshin and Marchenko [1985] solved the stress concentration around curvilinear cracks in a half-plane problem and satisfied the boundary conditions numerically using Gauss quadrature formulas. Wu and Cheng [1999] considered a circular hole in a laminated composite material under extensional loading. Chen and Hsu [1996] studied the stress concentrations around undulating cracks located at the interface of the two materials. Two sets of analytic functions are used for the two materials and the unevenness of the cracks is

modeled using perturbation. Wang and Hasebe [2000] studied bending of a plate with an inclusion and a crack. The Schwarz - Christoffel transformation is used by Tiwary et al. [2007] to generate stress functions for heterogeneities of arbitrary shapes. Ishikawa and Kohno [1993] used this transformation to determine the stresses around square openings and inclusions for plates under in-plane extension.

While the complex variable method is very powerful in solving a wide variety of elasticity problems, it is complicated and must be reformulated for each type of far-field load. The other main class of methods for evaluating stress concentration factors in plates are based on the finite element method. A special finite element is often introduced for plane stress problems. For instance, Chen [1993] developed an element with a circular hole and Piltner [1985] introduced one with circular or elliptical holes. To avoid refining the finite element mesh around the holes, these special elements are used at the hole locations while regular elements are used at other locations. The stresses in these elements are determined using a numerical implementation of the aforementioned complex variable method. The stress concentration factors for a crack (using elliptical hole) are also determined by these special finite elements. To study a composite plate under in-plane extension and shear, Nishioka and Atluri [1982] modified the complimentary energy principle and developed a special plane-stress finite element for laminated composite plates with a hole. Pan et al. [2001] developed a 3D boundary element formulation for the analysis of composite laminates with holes. They used a special Green's function which satisfies the continuity equation between the laminae and the free surface on the top and bottom faces to convert the problem to a

two-dimensional formulation to avoid desceritization in the plate thickness direction. In another study, Richards and Daniels [1986] used the conventional eight-node finite element to determine the displacements, and then utilized a complete quadratic function for redefining the displacement field for subsequent differentiation. The coefficients of the quadratic function are obtained by least squares fit of the displacements and stresses on the boundary.

Smoothing techniques have also been used in problems where strain measurements are available. Rowlands et al. [1978] and Feng and Rowlands [1991] combined smoothing with nonlinear regression to examine a plate with a hole under in-plane extension and bending. The strain measurements are obtained using photomechanical techniques. The noise presented in the measured deformation leads to erratic derivatives of displacement and therefore noisy stresses and strains. The smoothing techniques provide an approach to calculate better estimates of these derivatives.

This chapter focuses on stress concentrations around square holes in plates under different types of loads. These stresses can be determined using finite element calculations, if a sufficiently high density mesh is used in the vicinity of these corners. The goal here is to develop a method that would not require such high density meshes. This would be practical for complex structures, where a high density finite element mesh cannot be used for every rectangular opening. The key and novel aspect of this method is in extending the complex-variable method so that it can be effectively coupled with coarse finite element results to evaluate the stress concentrations around the openings. In essence, the coarse finite element results are used to provide moment and shear information at intermediate re-

gions away from the openings while the extended complex variable analytical expressions are used to obtain the stress field immediately surrounding the plate openings.

The method in Muskhelishvili [1975] and Savin [1961] is first briefly explained and used to solve for the moment distribution in a plate with a hole under bending loads. In this method the solution is represented in terms of analytic stress functions with unknown coefficients which can be determined by solving contour integral equations used for satisfying the boundary conditions. As indicated above, this purely analytical approach is complicated and has some limitations that prevent its practical use. In this chapter a numerical approach based on least squares technique is used instead of the contour integration to satisfy the boundary conditions. New expressions for moment and shear in terms of analytic functions at the hole boundary that are needed to perform this analysis are also derived. The plate bending problem for constant and linear varying moments is solved using this new method. The results are then combined with coarse-mesh finite element analysis to predict the stress concentrations as follows. First, a model for the stress distribution is fitted to the results of a coarse-mesh finite element analysis. The fitted model is then used to evaluate the stress concentration factors. To examine the performance of the proposed method a number of examples with single and adjacent, interacting holes are solved and compared with the results of more accurate finite element models or purely analytical solutions for the single hole case.

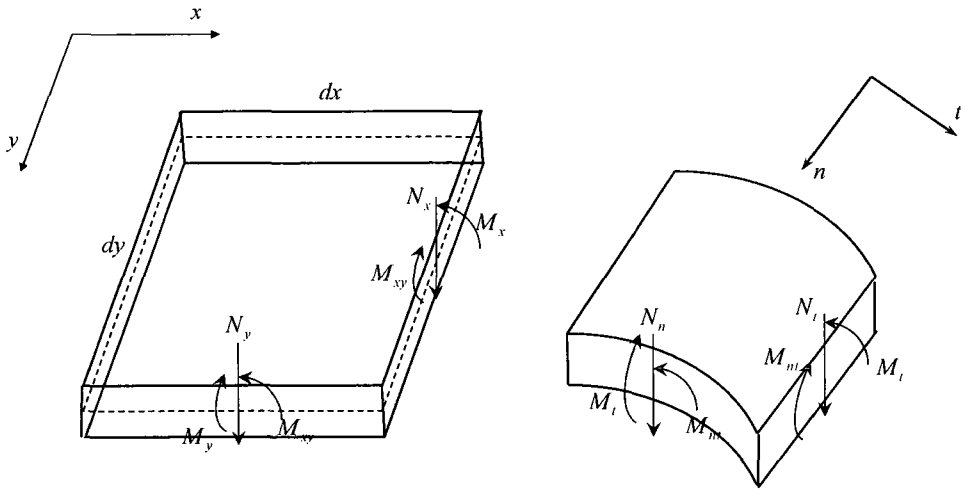

Figure 4.1: Internal forces in a plate element

4.2 Analytical results

4.2.1 Plate bending equations

Consider a plate element in the x, y plane as shown in Figure 4.1 (left). Let $w(x, y)$ be the out-of-plane deformation of the midplane in the vertical direction. In thin-plate bending theory, one can use the Kirchhoff assumption, which states:

- The deflection of the midsurface is small compared to the plate thickness. The slope

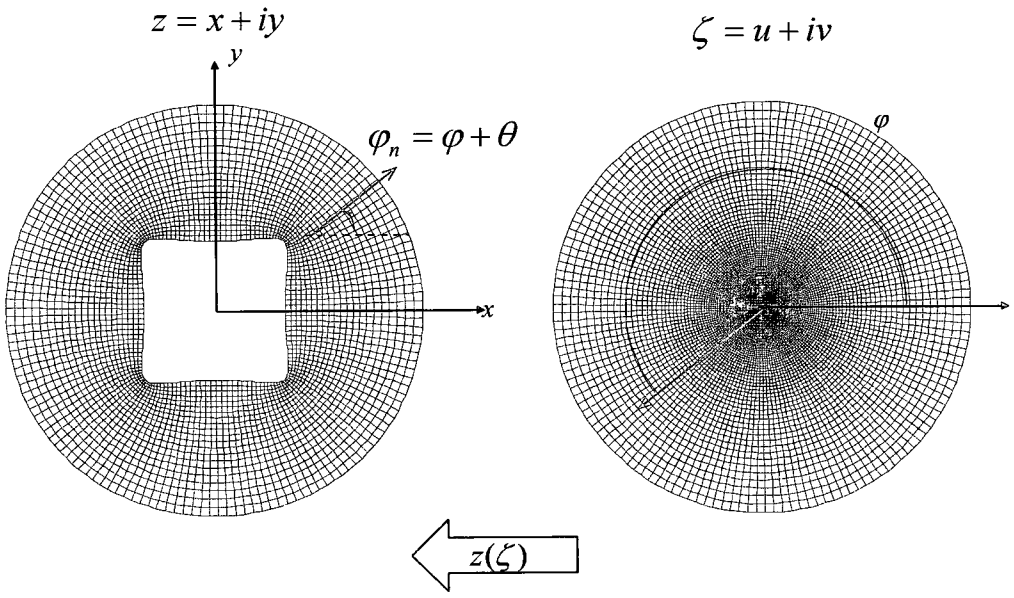

Figure 4.2: Conformal transformation to a unit circle

of the surface is much less than unity;

- The midplane of the plate is not stretched due to bending.
- Plane sections normal to the midsurface before bending remain plane and normal to the midsurface after the bending. This assumption means that the shear strains γ_{xz}, γ_{yz} and ε_z are small and can be neglected.
- The stress σ_z normal to the plane is negligible.

Using the above assumptions, the out-of-plane deformation $w(x, y)$ is independent of z and the in-plane deformations u and v and the strains can be written in terms of $w(x, y)$ as follows:

$$u(x,y) = -\tau\frac{\partial w}{\partial x}, \quad v(x,y) = -\tau\frac{\partial w}{\partial y}$$
$$\varepsilon_x = -\tau\frac{\partial^2 w}{\partial x^2} \quad \varepsilon_y = -\tau\frac{\partial^2 w}{\partial y^2}, \gamma_{xy} = -2\tau\frac{\partial^2 w}{\partial x \partial y}$$

where τ is the distance from the midplane. Using generalized Hooke's law for an isotropic material, the stresses in the plate can be obtained as follows:

$$\sigma_x = -\frac{E\tau}{(1-\nu^2)}\left(\frac{\partial^2 w}{\partial x^2} + \nu\frac{\partial^2 w}{\partial y^2}\right)$$
$$\sigma_y = -\frac{E\tau}{(1-\nu^2)}\left(\frac{\partial^2 w}{\partial y^2} + \nu\frac{\partial^2 w}{\partial x^2}\right)$$
$$\tau_{xy} = -\frac{E\tau}{(1+\nu)}\frac{\partial^2 w}{\partial x \partial y}$$

Integrating the stresses through the thickness of the plate, the resultant moments and shear forces per unit length shown in Figure 4.1 can be written as [Timoshenko and Woinowsky-

Krieger, 1959]:

$$M_x = -D\left(\frac{\partial^2 w}{\partial x^2} + \nu\frac{\partial^2 w}{\partial y^2}\right), \quad M_y = -D\left(\frac{\partial^2 w}{\partial y^2} + \nu\frac{\partial^2 w}{\partial x^2}\right), \quad M_{xy} = -D(1-\nu)\frac{\partial^2 w}{\partial x \partial y} \tag{4.1}$$

$$N_x = -D\frac{\partial \nabla^2 w}{\partial x}, \quad N_y = -D\frac{\partial \nabla^2 w}{\partial y}$$

where $D = Eh^3/12(1-\nu^2)$ is the flexural rigidity.

The bending moments and shear forces in curvilinear coordinates n and t as shown in Figure 4.1 (right) are related to the those in Cartesian coordinates through the following transformations [Savin, 1961]:

$$\begin{aligned} &M_x + M_y = M_n + M_t \\ &(M_y - M_x + 2iM_{xy})\, e^{2i\varphi_n} = M_t - M_n + 2iM_{nt}; \\ &(N_x - iN_y)\, e^{i\varphi_n} = N_n - iN_t \end{aligned} \tag{4.2}$$

where φ_n is the angle between the normal to the plane and the horizontal axis x .

The biharmonic bending equation is obtained by writing the equilibrium equations of moments and forces:

$$\begin{aligned} &\frac{\partial M_x}{\partial x} + \frac{\partial M_{xy}}{\partial y} - N_x = 0; \\ &\frac{\partial M_{xy}}{\partial x} + \frac{\partial M_y}{\partial y} - N_y = 0; \\ &\frac{\partial N_x}{\partial x} + \frac{\partial N_y}{\partial y} = 0; \end{aligned} \tag{4.3}$$

and eliminating the shear terms [Ventsel and Krauthammer, 2001]:

$$\frac{\partial^4 w}{\partial x^4} + 2\frac{\partial^4 w}{\partial x^2 \partial y^2} + \frac{\partial^4 w}{\partial y^4} = 0. \tag{4.4}$$

It is common to solve the plate bending problem by assuming a solution for w which satisfies the governing equation in coordinates x, y. One usual way is to write the solution as Fourier series expansions with unknown coefficients. The unknown coefficients are then evaluated by substituting w into the biharmonic equation. Another way to solve the plate bending problem is the method of complex variables. In this method the x, y coordinates are expressed by the complex variable $z = x + iy$. Muskhelishvili [1975] showed that the general solution to the biharmonic equation in (4.4) can be expressed as:

$$w(x, y) = Re\left(\bar{z}\phi_p(z) + \chi_p(z)\right) \tag{4.5}$$

where ϕ and χ are analytic functions, i.e. they preserve angles. The subscript p indicates that the functions are in terms of the variable z in physical space. The far-field boundary conditions are evaluated directly in physical space, but the boundary conditions at the interior of plate opening are more easily evaluated with the help of the conformal map explained in the next section.

The moments and shear forces in a plate with hole can be decomposed into two components:

$$M = M^0 + M^* \tag{4.6}$$

$$N = N^0 + N^* \tag{4.7}$$

The superscripts 0 are for the solutions for a plate without the hole and the superscripts $*$ are for the additional moments and shear forces that arise due to the existence of the hole. Hence M^0 and N^0 are the moment and shear force in an infinite unweakened plate which

can be easily evaluated using the basic bending equations (4.1). The components M^* and N^* of the moment and shear force account for the redistribution of stress associated with the existence of the hole. The conformal transformation technique explained in the next section is used to find these components. The analytic functions ϕ_p and χ_p can also be decomposed into two similar components:

$$\phi_p(z) = \phi_p^0(z) + \phi_p^*(z)$$

$$\chi_p(z) = \chi_p^0(z) + \chi_p^*(z)$$

These functions are used in finding the two components of deformation, $w^0 = Re\left(\overline{z}\phi_p^0 + \chi_p^0\right)$ which is the deformation for a plate without hole and $w^* = Re\left(\overline{z}\phi_p^* + \chi_p^*\right)$ which is the deformation component due to existence of the hole.

Experimental and numerical investigations have shown that the stresses are locally high around the hole. Therefore the moment and shear components M^* and V^* must attenuate rapidly with increasing distance from the hole. This suggests that the analytic functions ϕ^* and χ^* have the following form [Savin, 1961]:

$$f(z) = a_0 + \frac{a_1}{z} + \frac{a_2}{z^2} + \cdots$$

where a_j are constant coefficients. In the next subsection the conformal transformation properties are reviewed and the method of complex variables introduced by Muskhelishvili [1975] is briefly explained.

4.2.2 Review of analytical solution using conformal mapping

4.2.2.1 Conformal transformation definition and properties

The function $z(\zeta)$ that maps ζ in the unit disk Σ to z in physical space S is called a *conformal transformation* if it preserves angles [Ahlfors, 1979]. The Riemman mapping theorem states that any simply connected region can be mapped to a unit circle by such a conformal map. Therefore a plate with a hole can be mapped to a unit disk as shown in Figure 4.2.

The method used to transform the area of a plate with a hole to the inside of a unit circle using the function $z(\zeta)$ is explained in more detail in Savin [1961]. From the theory of functions of complex variables it is known that the inside or outside of a unit disk Σ can be transformed to the area of a plate with a polygon shape hole using the Schwarz-Christoffel integral [Savin, 1961]. For the case of a rectangular hole, the conformal transformation of the plate to the inside of a unit circle can be determined as follows [Savin, 1961]:

$$\begin{aligned} z(\zeta) = c\Big(&\tfrac{1}{\zeta} + \tfrac{a+\bar{a}}{2}\zeta + \tfrac{(a-\bar{a})^2}{24}\zeta^3 + \tfrac{(a^2-\bar{a}^2)(a-\bar{a})}{80}\zeta^5 \\ &+ \tfrac{5(a^4+\bar{a}^4)-4(a^2+\bar{a}^2)-2}{896}\zeta^7 + \tfrac{(a^5+\bar{a}^5)-5(a^3+\bar{a}^3)-2(a+\bar{a})}{2304}\zeta^9 \\ &+ \tfrac{21(a^6+\bar{a}^6)-14(a^4+\bar{a}^4)-5(a^2+\bar{a}^2)-4}{11264}\zeta^{11} + \cdots\Big) \end{aligned} \tag{4.8}$$

where $a = e^{2k\pi i}$ and $\bar{a}$ is its conjugate [Savin, 1961] and k depends on the aspect ratio of the rectangular hole.

Using the Cauchy-Riemann equations for analytic functions:

$$\frac{\partial u}{\partial x} = \frac{\partial v}{\partial y} = a, \quad \frac{\partial u}{\partial y} = -\frac{\partial v}{\partial x} = b \tag{4.9}$$

$$\frac{\partial a}{\partial x} + \frac{\partial b}{\partial y} = 0, \quad \frac{\partial a}{\partial y} - \frac{\partial b}{\partial x} = 0 \tag{4.10}$$

the Jacobian of the mapping can be represented as:

$$J = \begin{pmatrix} \frac{\partial u}{\partial x} & \frac{\partial u}{\partial y} \\ \frac{\partial v}{\partial x} & \frac{\partial v}{\partial y} \end{pmatrix} = \frac{1}{z'(\zeta)} = Ae^{-i\theta}$$

where $A^2 = a^2 + b^2$ is the ratio of the area of an infinitesimal element in the unit disk to its corresponding area in physical space and θ is the angle of rotation of the conformal transformation as shown in Figure 4.2.

4.2.2.2 Moments and shear relations using complex representation

Using the properties of analytic functions, the derivatives with respect to x and y can then be written in terms of the derivatives with respect to z:

$$\frac{\partial f(z)}{\partial x} = \frac{\partial u}{\partial x} + i\frac{\partial v}{\partial x} = f'(z)$$
$$\frac{\partial f(z)}{\partial y} = \frac{\partial u}{\partial y} + i\frac{\partial v}{\partial y} = if'(z)$$
$$\frac{\partial \overline{f(z)}}{\partial x} = \frac{\partial u}{\partial x} - i\frac{\partial v}{\partial x} = \overline{f'(z)}$$
$$\frac{\partial \overline{f(z)}}{\partial y} = \frac{\partial u}{\partial y} - i\frac{\partial v}{\partial y} = -i\overline{f'(z)}$$

Therefore the derivatives of the deformation w in (4.5) can be written as:

$$\begin{aligned}
\frac{\partial w}{\partial x} &= \frac{1}{2}\left(\phi(z) + \overline{z}\phi'(z) + z\overline{\phi'}(z) + \overline{\phi}(z) + \psi(z) + \overline{\psi}(z)\right) \\
\frac{\partial w}{\partial y} &= \frac{1}{2}\left(-i\phi(z) + i\overline{z}\phi'(z) - iz\overline{\phi'}(z) + i\overline{\phi}(z) + i\psi - i\overline{\psi}\right) \\
\frac{\partial^2 w}{\partial x^2} &= \frac{1}{2}\left(2\phi'(z) + 2\overline{\phi'}(z) + \overline{z}\phi''(z) + z\overline{\phi''}(z) + \psi'(z) + \overline{\psi'}(z)\right) \\
\frac{\partial^2 w}{\partial y^2} &= \frac{1}{2}\left(2\phi'(z) + 2\overline{\phi'}(z) - \overline{z}\phi''(z) - z\overline{\phi''}(z) - \psi'(z) - \overline{\psi'}(z)\right) \\
\frac{\partial^2 w}{\partial y \partial x} &= \frac{i}{2}\left(\overline{z}\phi''(z) - z\overline{\phi''}(z) + \psi'(z) - \overline{\psi'}(z)\right)
\end{aligned} \tag{4.11}$$

where $\psi = \partial\chi/\partial z$. The above relations are substituted into equations (4.1):

$$\begin{aligned}
M_x &= -D\left[(1+\nu)\left(\phi'(z) + \overline{\phi'}(z)\right) + \frac{1-\nu}{2}\left(\overline{z}\phi''(z) + z\overline{\phi''}(z) + \psi'(z) + \overline{\psi'}(z)\right)\right] \\
M_y &= -D\left[(1+\nu)\left(\phi'(z) + \overline{\phi'}(z)\right) - \frac{1-\nu}{2}\left(\overline{z}\phi''(z) + z\overline{\phi''}(z) + \psi'(z) + \overline{\psi'}(z)\right)\right] \\
M_{xy} &= -iD\frac{1-\nu}{2}\left[\overline{z}\phi''(z) - z\overline{\phi''}(z) + \psi'(z) - \overline{\psi'}(z)\right] \\
N_x &= -2D\left[\phi''(z) + \overline{\phi''}(z)\right] \\
N_y &= -2iD\left[\phi''(z) + \overline{\phi''}(z)\right]
\end{aligned} \tag{4.12}$$

and are rearranged to get [Savin, 1961]:

$$\begin{aligned}
M_y - M_x + 2iM_{xy} &= 2D(1-\nu)\left(\overline{z}\phi''(z) + \psi'(z)\right); \\
M_x + M_y &= -2D(1+\nu)\left(\phi'(z) + \overline{\phi'(z)}\right) \\
N_x - iN_y &= -4D\phi''(z)
\end{aligned}$$

4.2.2.3 Unweakened plate bending

As explained in section 4.2.1, the analytic functions ϕ_p and χ_p are decomposed into two components, one associated with a plate without hole (unweakened plate) and the other corresponding to the existence of the hole. Therefore the first step in solving the bending of a plate with hole is to solve the problem of the unweakened plate and find the analytic functions ϕ^0 and χ^0. This can be easily performed using the bending equations in (4.1). In the following, bending of an unweakened plate under constant moment in $M_x = M$ at far-field is reviewed and the displacements and analytic functions are determined.

Using the bending equations in (4.1) one can obtain:

$$\frac{\partial^2 w}{\partial x^2} = -\frac{M}{D(1-\nu^2)}$$
$$\frac{\partial^2 w}{\partial y^2} = \frac{\nu M}{D(1-\nu^2)}$$
$$\nabla^2_{x,y} w = -\frac{M}{D(1+\nu)}$$

The shear forces and twisting moments are zero and the deformation is:

$$w = -\frac{M(x^2 - \nu y^2)}{2D(1-\nu^2)}$$

Using the relations in (4.11) the gradient of the displacement can be written as:

$$\nabla^2 w = 4Re(\phi'^0(z)) \tag{4.13}$$

If we rewrite ϕ^0 as $\phi^0 = P + iQ$, where P and Q are real-valued functions, then since ϕ^0 is an analytic function, the following Cauchy- Riemann equation holds:

$$\phi'^0(z) = \frac{\partial P}{\partial x} + i\frac{\partial Q}{\partial x} = \frac{\partial Q}{\partial y} - i\frac{\partial P}{\partial y} \tag{4.14}$$

It follows from equations (4.13), (4.14) and (4.1) that:

$$P = -\frac{Mx}{4D(1+\nu)} + f_1(y)$$
$$Q = -\frac{My}{4D(1+\nu)} + f_2(x)$$

Since $\partial Q/\partial x = \partial P/\partial y$, the functions $f_1(y)$ and $f_2(x)$ are constants and can be set to zero. Therefore the analytic function ϕ^0 can be determined:

$$\phi^0(z) = -\frac{Mz}{4D(1+\nu)} \tag{4.15}$$

To find the analytic function χ^0, we rewrite this function as $\chi^0 = R + iS$ where R and S are real-valued functions. Since:

$$R = w - \frac{1}{2}(\overline{z}\phi^0 + z\overline{\phi^0})$$

then using the same procedure as for P and Q, we obtain:

$$S = -\frac{Mxy}{2(1-\nu)}$$
$$R = -\frac{M(x^2-y^2)}{4(1-\nu)}$$

and:

$$\chi^0(z) = -\frac{Mz^2}{4D(1-\nu)} \tag{4.16}$$

4.2.2.4 Boundary Conditions

The moments and forces in the plane normal to the hole contour must set to zero if the hole is traction free:

$$M_n = 0$$
$$\int_0^s N_n + \frac{\partial M_{nt}}{\partial s} ds = 0$$

where M_n, $M_{n,t}$ and N_n are the bending moment, twisting moment and shear force per unit length along the hole contour with outward normal n. It is noted that in the above equation $N_n + \partial M_{nt}/\partial s$ is the effective transverse force per unit length [Savin, 1961]. Let $P = \int_0^s N_n ds$ and $f_n = \int_0^s N_n + \partial M_{nt}/\partial s ds$. Then we obtain:

$$P + M_{nt} = f_n + k$$

where k is a real-valued integration constant. Bending moments and shear forces can be transformed to curvilinear coordinates:

$$M_n = M_x \cos^2(n,x) + M_y \sin^2(n,x) + 2M_{xy} \cos(n,x) \sin(n,x)$$
$$f_n + k = (M_y - M_x) \cos(n,x) \sin(n,x) + M_{xy} \left(\cos^2(n,x) - \sin^2(n,x)\right) + P$$

The above equations are rearranged in the following form:

$$M_n \cos(n,x) - (f_n + k) \sin(n,x) = M_x \cos(n,x) + (M_{xy} - P) \sin(n,x) \qquad (4.17)$$
$$M_n \sin(n,x) + (f_n + k) \cos(n,x) = M_y \sin(n,x) + (M_{xy} + P) \cos(n,x)$$

In appendix A, it is shown that the boundary condition can be written in terms of the analytic functions:

$$z\overline{\phi'} + \overline{\psi} + n\phi = 0 \tag{4.18}$$

To solve the plate bending problem for plates with a hole, a conformal transformation $z(\zeta)$ is used to establish a one-to-one mapping between the plate in physical space and the unit disk Σ with coordinate ζ shown in Figure 4.2. The boundary conditions at the hole can then be satisfied in the unit disk instead of the physical space. Using this transformation the deformation in equation (4.5) is written in terms of the variable ζ in the unit disk. Therefore the moments and shear forces are all in terms of the analytic functions $\phi(\zeta)$ and $\chi(\zeta)$, which are decomposed as:

$$\phi_p(z) = \phi(\zeta) = \phi^0(\zeta) + \phi^*(\zeta)$$

$$\chi_p(z) = \chi(\zeta) = \chi^0(\zeta) + \chi^*(\zeta)$$

In the above equations, $\phi^0(\zeta)$ and $\chi^0(\zeta)$ are analytic functions associated with the bending of the unweakened plate and can be determined by substituting $z(\zeta)$ into ϕ_p and χ_p.

Let $\sigma = e^{i\theta}$ be the value of $\zeta = \rho e^{i\theta}$ at the boundary of the unit disk and let

$$f_1^0 + if_2^0 = -\left(n\phi^0(\sigma) + \frac{z(\sigma)}{\overline{z'(\sigma)}}\overline{\phi'^0(\sigma)} + \overline{\psi^0(\sigma)}\right) \tag{4.19}$$

and $f_1^0 - if_2^0$ be its complex conjugate. Then substituting $\phi^0(\zeta), \phi^*(\zeta), \chi^0(\zeta)$ and $\chi^*(\zeta)$ into the boundary condition in (4.18) one can obtain:

$$n\phi^*(\sigma) + \overline{\psi^*(\sigma)} + \frac{z(\sigma)}{\overline{z'(\sigma)}}\overline{\phi^{*\prime}(\sigma)} = f_1^0 + if_2^0 \tag{4.20}$$

To evaluate the unknown functions $\phi_1^*(\zeta)$ and $\psi^*(\zeta)$, the functions $\phi(\zeta)$ and $\psi(\zeta)$ are first substituted into the boundary condition equations (4.20). Then both sides of the equation and its conjugate are multiplied by $d\sigma/2\pi i(\sigma-\zeta)$, and integrated along the unit circle γ as follows:

$$n\phi^*(\zeta)+\frac{1}{2\pi i}\int_\gamma \frac{z(\sigma)}{\overline{z'(\sigma)}}\overline{\phi'^*(\sigma)}\frac{d\sigma}{\sigma-\zeta}=\frac{1}{2\pi i}\int_\gamma (f_1^0+if_2^0)\frac{d\sigma}{\sigma-\zeta} \tag{4.21}$$

$$\psi^*(\zeta)+\frac{1}{2\pi i}\int_\gamma \frac{\overline{z(\sigma)}}{z'(\sigma)}\phi'^*(\sigma)\frac{d\sigma}{\sigma-\zeta}=\frac{1}{2\pi i}\int_\gamma (f_1^0-if_2^0)\frac{d\sigma}{\sigma-\zeta} \tag{4.22}$$

In the above integrals, ζ is for points inside the unit circle.

The functions $\phi^*(\zeta)$ and $\chi^*(\zeta)$ are chosen so that they vanish far from the hole. They are expressed as:

$$\phi^*(\zeta)=\sum_{j=1}^{\infty}\alpha_j\zeta^j, \quad \psi^*(\zeta)=\sum_{j=0}^{\infty}\beta_j\zeta^j \tag{4.23}$$

These functions along with ϕ^0 and ψ^0 are then substituted into the boundary conditions (4.21) and (4.22). Solving the contour integral equations, the unknown coefficients of the expansions in (4.23) are obtained and the moments and shear forces in the plate are then determined accordingly [Savin, 1961].

4.2.2.5 Example: bending of a plate with a square hole

Using equation (4.8) the conformal transformation:

$$z(\zeta)=R\left(\frac{1}{\zeta}-\frac{\zeta^3}{6}\right) \tag{4.24}$$

maps the physical space of a plate with a square hole to a unit disk [Savin, 1961]. Note however that the above conformal mapping only uses two terms of the expansion in (4.8)

resulting in a square hole with rounded corners as shown in Figure 4.2. Substituting the above transformation into the equations (4.15) and (4.16) the analytic functions associated with the unweakened plate can be determined:

$$\phi^0(\zeta) = -\frac{MR}{4D(1+\nu)}(\frac{1}{\zeta} - \frac{\zeta^3}{6}), \qquad \chi^0(\zeta) = -\frac{MR^2}{4D(1-\nu)}(\frac{1}{\zeta} - \frac{\zeta^3}{6})^2$$

The contour integral equations are then solved for satisfying the boundary conditions at the hole boundary. In this process, the unknown coefficients of the expansion in equation (4.23) are found. The analytic functions are [Savin, 1961]:

$$\phi^*(\zeta) = -\frac{MR}{2D}\left(\frac{6}{17+7\nu}\zeta + \frac{1}{6(3+\nu)}\zeta^3)\right) \tag{4.25}$$

$$\chi^*(\zeta) = \frac{MR^2}{2D}\left(\frac{1}{72(1-\nu)}\zeta^6 + \frac{1}{2(1-\nu)(3+\nu)}\zeta^4 + \frac{2(7-4\nu)}{3(1-\nu)(17+7\nu)}\zeta^2 + \frac{35+13\nu}{12(1-\nu)(3+\nu)}\ln\zeta\right) \tag{4.26}$$

Using equation (4.5) and the conformal transformation in equation (4.24), the midplane deformation can be determined:

$$w = \frac{MR^2}{2D}\left(\frac{35+13\nu}{12(1-\nu)(3+\nu)}\ln\rho - \frac{1}{2(1+\nu)}\frac{1}{\rho^2} - \frac{6}{17+7\nu}\cos(2\varphi) + \frac{2+\nu}{6(1+\nu)(3+\nu)}\rho^2\cos(4\varphi) + \frac{1}{17+7\nu}\rho^4\cos(2\varphi) - \frac{1}{72(3+\nu)}\rho^6 - \frac{1}{2(1-\nu)}\frac{\cos(2\varphi)}{\rho^2} + \frac{3(5-\nu)}{2(1-\nu)(17+7\nu)}\rho^2\cos(2\varphi) + \frac{1}{2(1-\nu)(3+\nu)}\rho^4\cos(4\varphi)\right) \tag{4.27}$$

where $\zeta = \rho e^{i\varphi}$.

It is noted that this conformal mapping technique has some practical limitations. It is fairly complicated, requiring the solution of a contour integral equation. In addition, it is

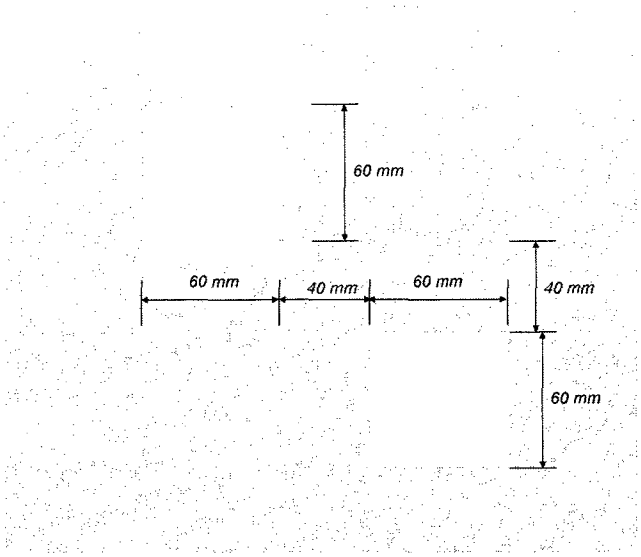

Figure 4.3: dimension and location of holes

limited to relatively simple expressions for the far-field moment. In more general configurations such as a plate with two interacting holes as shown in Figure 4.3, the conformal mapping technique becomes analytically intractable. Finally, in practice it is only necessary to examine a few critical corners, but the purely analytical approach requires an analysis of the entire near-field surrounding all openings.

4.2.3 New relations for moment and shear

The first contribution of this study is in deriving closed-form analytical relationships between the moments and shear forces in the z-plane in physical space and the analytic

functions defined inside the unit disk. The moments and shear forces in the z-plane are expressed in terms of ϕ, χ and the variable ζ inside the unit disk. These relations are needed to develop the regression formulation explained in subsection 4.3.1 which is subsequently used to couple the conformal mapping technique with finite element computations.

The analysis begins with the relation between the derivatives in physical space and the unit disk. Using the Cauchy-Riemann equations in (4.9) one can write:

$$\frac{\partial}{\partial x} = a\frac{\partial}{\partial u} - b\frac{\partial}{\partial v}, \qquad \frac{\partial}{\partial y} = b\frac{\partial}{\partial u} + a\frac{\partial}{\partial v}$$

The second derivatives can also be written as:

$$\frac{\partial^2}{\partial x^2} = \frac{\partial}{\partial x}\left(a\frac{\partial}{\partial u} - b\frac{\partial}{\partial v}\right) = a^2\frac{\partial^2}{\partial u^2} + b^2\frac{\partial^2}{\partial v^2} - 2ab\frac{\partial^2}{\partial u \partial v} + \frac{\partial a}{\partial x}\frac{\partial}{\partial u} - \frac{\partial b}{\partial x}\frac{\partial}{\partial v}$$

$$\frac{\partial^2}{\partial y^2} = \frac{\partial}{\partial y}\left(b\frac{\partial}{\partial u} + a\frac{\partial}{\partial v}\right) = b^2\frac{\partial^2}{\partial u^2} + a^2\frac{\partial^2}{\partial v^2} + 2ab\frac{\partial^2}{\partial u \partial y} + \frac{\partial b}{\partial y}\frac{\partial}{\partial u} + \frac{\partial a}{\partial y}\frac{\partial}{\partial v}$$

$$\frac{\partial^2}{\partial y \partial x} = \frac{\partial}{\partial y}\left(a\frac{\partial}{\partial u} - b\frac{\partial}{\partial v}\right) = ab\frac{\partial^2}{\partial u^2} - ab\frac{\partial^2}{\partial v^2} + (a^2 - b^2)\frac{\partial^2}{\partial u \partial v} + \frac{\partial a}{\partial y}\frac{\partial}{\partial u} - \frac{\partial b}{\partial y}\frac{\partial}{\partial v}$$

When these derivatives are substituted into the plate bending equations (4.1), the moment and shear forces in the physical space can be written in terms of the rectangular coordinates

u, v in the unit disk:

$$
\begin{aligned}
M_{xx} &= -D\left((a^2+\nu b^2)\frac{\partial^2}{\partial u^2}+(b^2+\nu a^2)\frac{\partial^2}{\partial v^2}-2ab(1-\nu)\frac{\partial^2}{\partial u\partial v}+\right.\\
&\left.\left(\frac{\partial a}{\partial x}+\nu\frac{\partial b}{\partial y}\right)\frac{\partial}{\partial u}+\left(\nu\frac{\partial a}{\partial y}-\frac{\partial b}{\partial x}\right)\frac{\partial}{\partial v}\right)w\\
M_{yy} &= -D\left((\nu a^2+b^2)\frac{\partial^2}{\partial u^2}+(\nu b^2+a^2)\frac{\partial^2}{\partial v^2}+2ab(1-\nu)\frac{\partial^2}{\partial u\partial v}+\right.\\
&\left.\left(\frac{\nu\partial a}{\partial x}+\frac{\partial b}{\partial y}\right)\frac{\partial}{\partial u}+\left(\frac{\partial a}{\partial y}-\nu\frac{\partial b}{\partial x}\right)\frac{\partial}{\partial v}\right)w\\
M_{xy} &= -D(1-\nu)\left(ab\frac{\partial^2}{\partial u^2}-ab\frac{\partial^2}{\partial v^2}+(a^2-b^2)\frac{\partial^2}{\partial u\partial v}+\frac{\partial a}{\partial y}\frac{\partial}{\partial u}-\frac{\partial b}{\partial y}\frac{\partial}{\partial v}\right)w\\
N_x &= -D\left(2\left(a\frac{\partial a}{\partial x}+b\frac{\partial b}{\partial x}\right)\nabla^2_{u,v}w+(a^2+b^2)\left(a\frac{\partial}{\partial u}-b\frac{\partial}{\partial v}\right)\nabla^2_{u,v}w\right)\\
N_y &= -D\left(2\left(a\frac{\partial a}{\partial y}+b\frac{\partial b}{\partial y}\right)\nabla^2_{u,v}w+(a^2+b^2)\left(b\frac{\partial}{\partial u}+a\frac{\partial}{\partial v}\right)\nabla^2_{u,v}w\right)
\end{aligned}
$$

Rearranging the above equations one can write:

$$
\begin{aligned}
&M_{xx}+M_{yy}=A^2\left(M_{uu}+M_{vv}\right)\\
&M_{yy}-M_{xx}+2iM_{xy}=A^2e^{-2i\theta}\left(M_{vv}-M_{uu}+2iM_{uv}\right)\\
&-2D(1-\nu)\left((-\frac{\partial w}{\partial u}+i\frac{\partial w}{\partial v})\frac{\partial Ae^{-i\theta}}{\partial x}\right)\\
&N_x-iN_y=A^3e^{-i\theta}(N_u-iN_v)-2D\left(Ae^{i\theta}\frac{\partial Ae^{-i\theta}}{\partial x}\right)\nabla^2_{u,v}w
\end{aligned}
\tag{4.28}
$$

In the above equations, it is noted that the terms $M_{uu}, M_{vv}, M_{uv}, N_u$ and N_v have the same mathematical form as moments and shear forces but do not physically represent these quantities. To get the moments and shear forces normal to the boundary one needs to transform

the above relations to curvilinear coordinates using equation (4.2):

$$
\begin{aligned}
&M_{tt} + M_{nn} = A^2 \left(M_{\varphi\varphi} + M_{\rho\rho}\right) \\
&\left(M_{tt} - M_{nn} + 2iM_{nt}\right) e^{-2i\varphi_n} = A^2 e^{-2i\theta} \left(M_{\varphi\varphi} - M_{\rho\rho} + 2iM_{\rho\varphi}\right) e^{-2i\varphi} \\
&- 2D(1-\nu) \left(e^{-i\varphi}(-\frac{\partial w}{\partial \rho} + i\frac{\partial w}{\rho \partial \varphi}) \frac{\partial A e^{-i\theta}}{\partial x} \right) \\
&\left(N_n - iN_t\right) e^{-i\varphi_n} = A^3 e^{-i\theta} (N_\rho - iN_\varphi) e^{-i\varphi} - 2D \left(A e^{i\theta} \frac{\partial A e^{-i\theta}}{\partial x} \right) \nabla^2_{\rho,\varphi} w
\end{aligned}
$$

where M_n, M_{nt} and N_n are the physical bending moment, twisting moment and shear force per unit length along the contour with the outward normal n, and M_{tt} and N_t are the bending moment and shearing force per unit length along the tangential direction. In the above equation, $\varphi_n = \theta + \varphi$ is the angle between the horizontal axis and normal to the boundary. The terms $M_{\rho\rho}, M_{\rho\varphi}, M_{\varphi\varphi}$ and N_ρ have the same mathematical form as the moments and shear forces in polar coordinates ρ, φ in the unit disk and are therefore named accordingly.

The moments and shear forces in the curvilinear coordinates in physical space can be written as:

$$
\begin{aligned}
M_{nn} &= A^2 \left(M_{\rho\rho} - D(1-\nu) Re \left(q \frac{z''(\zeta)}{z'(\zeta)} e^{i\varphi} \right) \right) \\
M_{tt} &= A^2 \left(M_{\varphi\varphi} + D(1-\nu) Re \left(q \frac{z''(\zeta)}{z'(\zeta)} e^{i\varphi} \right) \right) \\
M_{nt} &= A^2 \left(M_{\rho\rho} + D(1-\nu) Im \left(q \frac{z''(\zeta)}{z'(\zeta)} e^{i\varphi} \right) \right) \\
N_n &= A^3 \left(N_\rho + 2D \nabla^2_{\rho,\varphi} w Re \left(\frac{z''(\zeta)}{z'(\zeta)} e^{i\varphi} \right) \right)
\end{aligned}
$$

where

$$q = (-\frac{\partial w}{\partial \rho} + i\frac{\partial w}{\rho \partial \varphi})$$

The effective transverse force per unit length along the contour with normal n is:

$$V_n = N_n + \frac{\partial M_{nt}}{\partial s}$$

$$V_n = A^3 \left(N_\rho + \frac{\partial M_{\rho\varphi}}{\rho \partial \varphi} + \frac{1}{A^2}\frac{\partial A^2}{\rho \partial \varphi} M_{\rho\varphi} + 2D\nabla^2_{\rho,\varphi} w Re\left(\frac{z''(\zeta)}{z'(\zeta)} e^{i\varphi}\right) + \right.$$

$$\left. D(1-\nu) Im\left(e^{i\varphi}\frac{z''}{z'}\left(\frac{\partial q}{\rho \partial \varphi} + q(\frac{1}{A^2}\frac{\partial A^2}{\rho \partial \varphi} + \frac{i}{\rho} + ie^{i\varphi}\frac{z'''z' - z''^2}{z'z''})\right)\right)\right)$$

In the following these moments and shear forces are written in terms of the functions ϕ and χ. The derivatives of the deformation w expressed in terms of these functions, are:

$$\frac{\partial w}{\partial u} = Re\left(\overline{z'}\phi + \phi'\overline{z} + \chi'\right)$$

$$\frac{\partial w}{\partial v} = Re\left(-i\overline{z'}\phi + i\phi'\overline{z} + i\chi'\right)$$

$$\frac{\partial^2 w}{\partial u^2} = Re\left(\overline{z''}\phi + 2\overline{z'}\phi' + \overline{z}\phi'' + \chi''\right)$$

$$\frac{\partial^2 w}{\partial u \partial v} = Re\left(-i\overline{z''}\phi + i\overline{z}\phi'' + i\chi''\right)$$

$$\frac{\partial^2 w}{\partial v^2} = Re\left(-\overline{z''}\phi + 2\overline{z'}\phi' - \overline{z}\phi'' - \chi''\right)$$

$$\frac{\partial w}{\partial \rho} = c\frac{\partial w}{\partial u} + s\frac{\partial w}{\partial v} = Re(e^{i\varphi}(\phi'\overline{z} + z'\overline{\phi} + \chi'))$$

$$\frac{\partial w}{\rho\partial \varphi} = -s\frac{\partial w}{\partial u} + c\frac{\partial w}{\partial v} = -Im(e^{i\varphi}(\phi'\overline{z} + z'\overline{\phi} + \chi'))$$

$$\frac{\partial^2 w}{\partial \rho^2} = Re(e^{2i\varphi}(\phi''\overline{z} + z''\overline{\phi} + \chi'') + (\phi'\overline{z'} + z'\overline{\phi'}))$$

$$\frac{\partial^2 w}{\rho\partial\varphi\partial\rho} = Re(\frac{ie^{i\varphi}}{\rho}(\phi'\overline{z} + z'\overline{\phi} + \chi') + ie^{2i\varphi}(\phi''\overline{z} + z''\overline{\phi} + \chi'') - i(\phi'\overline{z'} + z'\overline{\phi'}))$$

$$\frac{\partial^2 w}{\rho^2\partial\varphi^2} = -Im(\frac{ie^{i\varphi}}{\rho}(\phi'\overline{z} + z'\overline{\phi} + \chi') + ie^{2i\varphi}(\phi''\overline{z} + z''\overline{\phi} + \chi'') - i(\phi'\overline{z'} + z'\overline{\phi'}))$$

$$q = -e^{i\varphi}(\phi'\overline{z} + z'\overline{\phi} + \chi')$$

$$\frac{\partial q}{\rho\partial\varphi} = -ie^{2i\varphi}(\phi''\overline{z} + z''\overline{\phi} + \chi'') + i(\phi'\overline{z'} + z'\overline{\phi'}) - \frac{ie^{i\varphi}}{\rho}(\phi'\overline{z} + z'\overline{\phi} + \chi')$$

The moments and the shear forces are then written as:

$$M_{nn} = A^2\left(M_{\rho\rho} - D(1-\nu)Re\left(-e^{i\varphi}(\phi'\overline{z} + z'\overline{\phi} + \chi')\frac{z''}{z'}e^{i\varphi}\right)\right) \tag{4.29}$$

$$M_{tt} = A^2\left(M_{\varphi\varphi} + D(1-\nu)Re\left(-e^{i\varphi}(\phi'\overline{z} + z'\overline{\phi} + \chi')\frac{z''}{z'}e^{i\varphi}\right)\right) \tag{4.30}$$

$$M_{nt} = A^2\left(M_{\rho\varphi} + D(1-\nu)Im\left(-e^{i\varphi}(\phi'\overline{z} + z'\overline{\phi} + \chi')\frac{z''}{z'}e^{i\varphi}\right)\right) \tag{4.31}$$

$$N_n = A^3\left(N_\rho + 8DRe\left(\overline{z'}\phi'\right)Re\left(\frac{z''}{z'}e^{i\varphi}\right)\right) \tag{4.32}$$

$$V_n = A^3\left(N_\rho + \frac{\partial M_{\rho\varphi}}{\rho\partial\varphi} + \frac{1}{A^2}\frac{\partial A^2}{\rho\partial\varphi}M_{\rho\varphi} + 8DRe\left(\overline{z'}\phi'\right)Re\left(\frac{z''}{z'}e^{i\varphi}\right) + \right. \tag{4.33}$$

$$D(1-\nu)Im\left(e^{i\varphi}\frac{z''}{z'}\left(-ie^{2i\varphi}(\phi''\overline{z} + z''\overline{\phi} + \chi'') + i(\phi'\overline{z'} + z'\overline{\phi'}) - \frac{ie^{i\varphi}}{\rho}(\phi'\overline{z} + z'\overline{\phi} + \chi')\right.\right.$$

$$\left.\left.\left.-e^{i\varphi}(\phi'\overline{z} + z'\overline{\phi} + \chi')(\frac{1}{A^2}\frac{\partial A^2}{\rho\partial\varphi} + \frac{i}{\rho} + ie^{i\varphi}\frac{z'''z' - z''^2}{z'z''})\right)\right)\right)$$

In the above equations the terms $M_{\rho\rho}$, $M_{\rho\phi}$, $M_{\phi\phi}$ and N_ρ can also be written in terms of the

functions ϕ and χ:

$$M_{\rho\rho} = -D\left(\frac{\partial^2}{\partial\rho^2} + \frac{\nu}{\rho}\frac{\partial}{\partial\rho} + \frac{\nu}{\rho^2}\frac{\partial^2}{\partial\varphi^2}\right) w = -D\,Re\left(e^{2i\varphi}(\phi''\overline{z} + z''\overline{\phi} + \chi'')(1-\nu)\right.$$

$$\left.+(\phi'\overline{z'} + z'\overline{\phi'})(1+\nu)\right) \tag{4.34}$$

$$M_{\rho\varphi} = \frac{-D\,(1-\nu)}{\rho}\left(\frac{\partial^2}{\partial\rho\partial\varphi} - \frac{\partial}{\rho\partial\varphi}\right) w = D(1-\nu)Im\left(e^{2i\varphi}(\phi''\overline{z} + z''\overline{\phi} + \chi'')\right) \tag{4.35}$$

$$M_{\varphi\varphi} = -D\left(\nu\frac{\partial^2}{\partial\rho^2} + \frac{1}{\rho}\frac{\partial}{\partial\rho} + \frac{1}{\rho^2}\frac{\partial^2}{\partial\varphi^2}\right) w = -D\,Re\left(-e^{2i\varphi}(\phi''\overline{z} + z''\overline{\phi} + \chi'')(1-\nu)\right.$$

$$\left.+(\phi'\overline{z'} + z'\overline{\phi'})(1+\nu)\right) \tag{4.36}$$

$$N_\rho = -D\frac{\partial}{\partial\rho}\nabla^2 w = -4DRe\left(e^{i\varphi}(\phi''\overline{z'} + \overline{\phi'}z'')\right) \tag{4.37}$$

Previous studies of the conformal mapping techniques for plate problems did not consider the derivation of these equations because they are not needed in evaluating the contour integrals associated with the boundary conditions. In the following, an alternate approach to solving the boundary value problem is formulated in terms of the new analytical results derived in this section.

4.3 Numerical Method

In this section a numerical approach is developed for satisfying the boundary conditions without contour integration. Specifically, the form and coefficients of the analytic functions ϕ^* and ψ^* in equation 4.23 are determined by regression using the results of the previous section. The form of the analytic functions ϕ^0 and χ^0 for an unweakened plate provides guidelines on the form of the expansions for ϕ^* and χ^*. This means the covariate matrices

of the regression analysis for ϕ^* and χ^* should include functions that are compatible with the form of ϕ^0 and χ^0. In other words, using those covariates, one must be able to cancel the moments and shear forces of the unweakened plate at the near-field due to the functions ϕ^0 and χ^0. To choose these covariate matrices properly we need to investigate the form of equation (4.5) for w. A close look at this equation reveals that the power of χ in z should be one plus the power of ϕ in z. On the other hand, one notices that the conformal transformations for rectangular and square holes in equation (4.8) consists of odd powers of ζ. These facts imply that if ϕ can be written in terms of odd powers of ζ then χ can only include the even powers and vice versa. To clarify this even further let us consider the case of a plate under constant moment at far-field. The analytic functions ϕ^0 and χ^0 for this case have the following form:

$$\phi^0(\zeta) = \sum_{j=1}^{n} \frac{c_j}{\zeta^{2j-1}} + \sum_{j=1}^{m} b_j^0 \zeta^{2j-1} \tag{4.38}$$

$$\chi^0(\zeta) = \sum_{k=1}^{n'} \frac{c_k'}{\zeta^{2k}} + \sum_{k=1}^{m'} b_k'^0 \zeta^{2k} \tag{4.39}$$

where for the square hole example we have $n = 1$, $m = 2$, $n' = 1$ and $m' = 3$. The following expansions are then chosen for analytic functions ϕ^* and χ^*:

$$\phi^* = \sum_{j=1}^{m} b_j \zeta^{2j-1} \tag{4.40}$$

$$\chi^* = b_0' \ln \zeta + \sum_{k=1}^{m'} b_k' \zeta^{2k} \tag{4.41}$$

These equations are compatible with the analytic functions ϕ^0 and χ^0 since they can cancel the moments and shear forces of the unweakened plate at the near-field.

4.3.1 Imposing boundary conditions via linear regression

To formulate the linear regression problem, analytic functions can be written in the following matrix form:

$$\phi(\zeta) = \phi^0 + U_1 b$$
$$\chi(\zeta) = \chi^0 + U_2 b \tag{4.42}$$

where b is a vector of unknown coefficients and U_1 and U_2 are the covariate matrices corresponding to ϕ^* and χ^*. For the square hole example, the analytical solution for b_j can be expressed as the following vector:

$$b = \frac{MR}{2D}\left[\begin{array}{cccccc} \frac{6}{17+7\nu} & \frac{1}{6(3+\nu)} & R\frac{35+13\nu}{12(1-\nu)(3+\nu)} & R\frac{2(7-4\nu)}{3(1-\nu)(17+7\nu)} & R\frac{1}{2(1-\nu)(3+\nu)} & R\frac{1}{72(1-\nu)} \end{array}\right]^T$$

where

$$U_1 = \left[\begin{array}{cccccc} \zeta^1 & \zeta^3 & 0 & 0 & 0 & 0 \end{array}\right], \qquad U_2 = \left[\begin{array}{cccccc} 0 & 0 & \ln\zeta & \zeta^2 & \zeta^4 & \zeta^6 \end{array}\right]$$

are the covariate matrices. The above results for b are valid only for a plate with a square hole under constant far-field moment M [Savin, 1961]. They were obtained through a contour integration approach. Below it is shown how these coefficients can be obtained without contour integration for more general hole geometries and loads through the use of the analytical results in section 4.2.3. The appropriate covariates as explained in section 4.3 are placed in U_1 and U_2 matrices corresponding to ϕ^* and χ^* respectively. These matrices are arranged inserting submatrices of zeros such that only a single vector of unknown coefficients is needed for representing ϕ^* and χ^*. For the case of constant moments at far-field

these matrices can be written as:

$$U_1 = \begin{bmatrix} \zeta_1^1 & \zeta_1^3 & \cdots & \zeta_1^{2m-1} & 0 & \cdots & 0 \\ \vdots & \vdots & \vdots & \vdots & \vdots & & \vdots \\ \zeta_n^1 & \zeta_n^3 & \cdots & \zeta_1^{2m-1} & 0 & \cdots & 0 \end{bmatrix}, \qquad U_2 = \begin{bmatrix} 0 & \cdots & 0 & \ln\zeta_1 & \zeta_1^2 & \cdots & \zeta_1^{2m'} \\ \vdots & \vdots & \vdots & \vdots & \vdots & & \vdots \\ 0 & \cdots & 0 & \ln\zeta_n & \zeta_n^2 & \cdots & \zeta_n^{2m'} \end{bmatrix}$$

The rows of the above matrices are the covariates evaluated at n different locations at the boundary. The moments and shear forces at the boundary of the hole where $\rho = 1$ are evaluated in the direction normal to the boundary using equations (4.29) and (4.33). They are then set to zero to determine the unknown coefficients of the analytic functions. One can arrange the equations for the bending moment and shear forces normal to the boundary as follows:

$$M_{nn} = M_{nn}^0 + M_n^* = M_{nn}^0 + U_{M_{nn}} b$$

$$V_{nn} = V_{nn}^0 + V_n^* = V_n^0 + U_{V_n} b$$

where M_{nn}^0 and V_n^0 are the moment and shear components associated with the unweakened plate and can be evaluated by substituting the analytic functions ϕ^0 and χ^0 in equations (4.29) and (4.33). In the above equations, $U_{M_{nn}}$ and U_{V_n} are matrices of covariates corresponding to the bending moment and shear forces normal to the boundary due to the existence of the hole. The matrices of moment covariates are constructed by arranging the different derivatives of components of U_1 and U_2 according to equations (4.29) and (4.33). Then the following least-squares problem is solved to determine the unknown vector b so

that the moments and shear forces normal to the boundary will vanish.

$$\min_b (M_{nn}^0 + U_{M_{nn}} b)^T (M_{nn}^0 + U_{M_{nn}} b) + (V_n^0 + U_{V_n} b)^T (V_n^0 + U_{V_n} b)$$

This can be rewritten as:

$$\min_b (U_n b + F^0)^T (U_n b + F^0) \tag{4.43}$$

where:

$$U_n = \begin{bmatrix} U_{M_{nn}} \\ U_{V_n} \end{bmatrix} \qquad F^0 = \begin{bmatrix} M_{nn}^0 \\ V_n^0 \end{bmatrix}$$

The unknown coefficients b are readily determined by the standard regression equation:

$$b = (U_n^T U_n)^{-1} U_n^T F^0$$

4.3.1.1 Numerical results and discussion

As mentioned in section 4.2.2.3, the first step in formulating the linear regression problem is to find the analytic functions ϕ^0 and χ^0 associated with the unweakened infinite plate under the specified load. Using the basic plate bending equations in (4.1) the analytic functions, displacement field, and the moments and shear forces distributions can be determined. A set of results for the constant and linearly varying moment loads is summarized in Table 4.1. Using the results in this table and substituting the conformal transformation in equation (4.24) into the functions ϕ^0 and χ^0, the powers of ζ in ϕ^0 and χ^0 are evaluated. Consequently the regression covariates are chosen to be compatible with the analytic

Table 4.1: The distribution of moment and shear forces, and the deformation and analytic functions for a plate without hole under different types of moments at far-field

M_x	M_y	M_{xy}	N_x	N_y	w	ϕ_p	χ_p
m	0	0	0	0	$-\frac{m}{2D(1-\nu^2)}\left(x^2-\nu y^2\right)$	$-\frac{mz}{4D(1+\nu)}$	$\frac{mz^2}{4D(1-\nu)}$
0	m	0	0	0	$-\frac{m}{2D(1-\nu^2)}\left(x^2-\nu y^2\right)$	$-\frac{mz}{4D(1+\nu)}$	$\frac{mz^2}{4D(1-\nu)}$
mx	0	$-\frac{\nu my}{1+\nu}$	$\frac{m}{1+\nu}$	0	$-\frac{m}{2D(1-\nu^2)}\left(\frac{x^3}{3}-\nu xy^2\right)$	$-\frac{mz^2}{8D(1+\nu)}$	$-\frac{m(1+3\nu)z^3}{24D(1-\nu^2)}$
0	mx	$\frac{my}{1+\nu}$	$\frac{m}{1+\nu}$	0	$-\frac{m}{2D(1-\nu^2)}\left(xy^2-\nu\frac{x^3}{3}\right)$	$-\frac{mz^2}{8D(1+\nu)}$	$\frac{m(3+\nu)z^3}{24D(1-\nu^2)}$
my	0	$\frac{mx}{1+\nu}$	0	$\frac{m}{1+\nu}$	$-\frac{m}{2D(1-\nu^2)}\left(yx^2-\nu\frac{y^3}{3}\right)$	$\frac{imz^2}{8D(1+\nu)}$	$\frac{im(3+\nu)z^3}{24D(1-\nu^2)}$
0	my	$-\frac{\nu mx}{1+\nu}$	0	$\frac{m}{1+\nu}$	$-\frac{m}{2D(1-\nu^2)}\left(\frac{y^3}{3}-\nu x^2y\right)$	$\frac{imz^2}{8D(1+\nu)}$	$-\frac{im(1+3\nu)z^3}{24D(1-\nu^2)}$

functions ϕ^0 and χ^0 corresponding to the unweakened plate. For constant moment at infinity, six unknown coefficients are used to determine the analytic functions ϕ^* and χ^*. For the case of linearly varying moment at far-field, the powers of z in ϕ^0 and χ^0 is two and three. Substituting the conformal transformation for a square hole in (4.24), ϕ^0 consists of even powers of ζ to the maximum of six and the terms in χ^0 have odd powers of ζ to ζ^9. Therefore the following covariates are used in the case of linear far-field moments:

$$U_1 = \begin{bmatrix} \zeta^2 & \zeta^4 & \zeta^4 & 0 & 0 & 0 & 0 & 0 & 0 \end{bmatrix}, \quad U_2 = \begin{bmatrix} 0 & 0 & 0 & \ln\zeta & \zeta & \zeta^3 & \zeta^5 & \zeta^7 & \zeta^9 \end{bmatrix}$$

A total of nine unknowns appear in vector b in equation (4.42).

Finally, the linear regression formulation is used to obtain the unknown coefficients b by enforcing the boundary conditions. The coefficients of the analytic functions for the case of constant moment $M_x = 1$ is determined using the linear regression formulations

and the procedure explained in section 4.3.1. The results for $D = 1$, $R = 35$ and $\nu = 0.3$ are shown in first column of Table 4.2. The coefficients obtained here are equal to the exact analytical coefficients in equation (4.25) up to sixteen significant digits. In the more general case of non-constant moments, it is cumbersome to obtain the exact analytical results using contour integration, and this analysis was not carried out herein. Instead, the proposed semi-analytical approach was verified by examining the magnitudes of the stresses in the boundary of the hole. For the case of a constant unit far-field moment $M_x = 1$, the ratio of maximum absolute value of the normal stress at the boundary to the normal stress due to far-field moment at the boundary is $1.5987e^{-14}$. This proves the accuracy of the analysis. The results for several other cases of far-field moments are summarized in Table 4.1. The unknown coefficients are evaluated using the linear regression formulation. In order to quantify the accuracy of regression analysis the ratio of the maximum normal and shear stresses to the maximum value of normal stresses due to far-field moment at the boundary is evaluated. These ratios are shown in the last two rows of Table 4.2. It can be seen that these ratios are in the order of computational round-off errors, which indicates that the proposed semi-analytical method provides the same numerical results as those obtained through contour integration.

4.3.2 Enhancing coarse finite element results

In this section it is shown how the semi-analytical method in subsection 4.3.1 can be coupled with coarse-mesh finite element analysis to estimate the stress concentrations

Table 4.2: Coefficients of the analytic functions and ratio of maximum normal stress σ_n and maximum shear stress τ to maximum value of normal stress due to far-field moment σ_{nf} at the boundary of the hole.

moments	$M_x = 1$	$M_y = 1$	$M_x = x$	$M_x = y$	$M_y = x$	$M_y = y$
b_1	-5.4974	5.4974	-107.0804	-78.5256	$78.5256i$	$107.0804i$
b_2	-0.8838	-0.8838	8.3285	8.3285	$8.3285i$	$8.3285i$
b_3	859.5328	859.5328	3.2719	-3.2719	$3.2719i$	$-3.2719i$
b_4	177.1379	-177.1379	0	0	0	0
b_5	132.5758	132.5758	23359.3952	13151.0619	$13151.0619i$	$23359.3952i$
b_6	12.1528	-12.1528	3202.9935	1488.7153	$-1488.7153i$	$-3202.9935i$
b_7	–	–	2021.1429	1170.4485	$1170.4485i$	$2021.1429i$
b_8	–	–	0	0	0	0
b_9	–	–	-17.2684	29.9924	$29.9924i$	$-17.2684i$
σ_n/σ_{nf}	$1.5987e^{-14}$	$1.5654e^{-014}$	$4.4823e^{-013}$	$1.9943e^{-013}$	$1.7129e^{-12}$	$1.3867e^{-13}$
τ/σ_{nf}	$2.2725e^{-14}$	$4.6455e^{-014}$	$9.1417e^{-013}$	$2.5624e^{-013}$	$2.3750e^{-012}$	$3.6947e^{-013}$

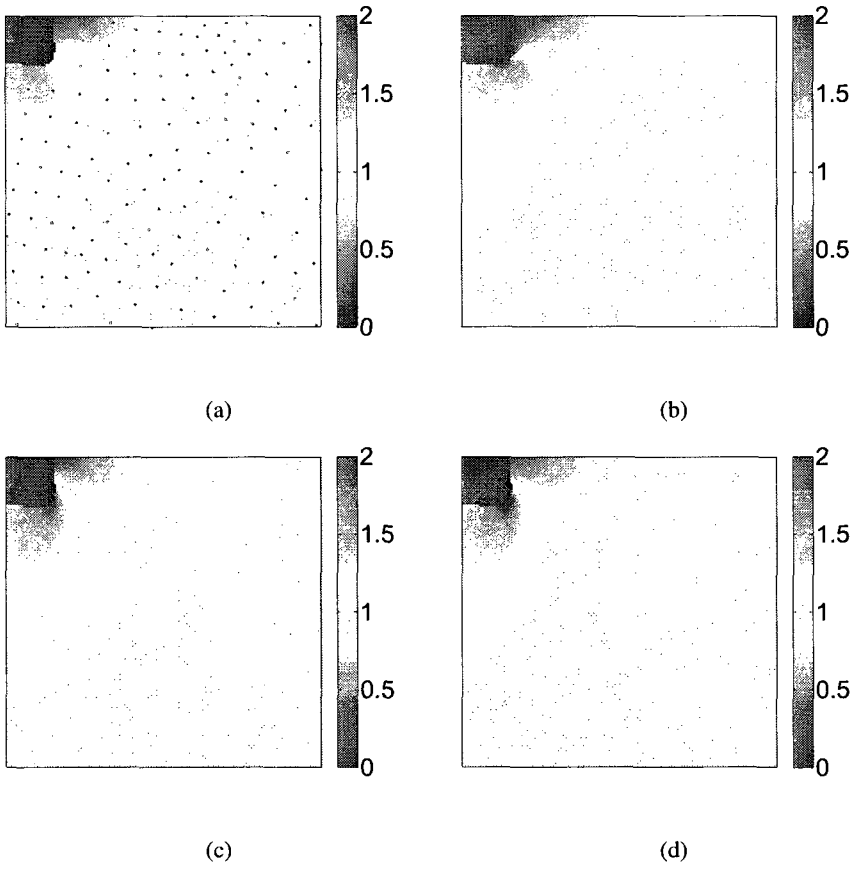

Figure 4.4: Distribution of moments around a corner for $M_x = 1$ at infinity, (a) : finite element results with coarse mesh, (b) : finite element results with fine mesh, (c) : exact analytical solution [Savin, 1961] and (d) : result using linear regression

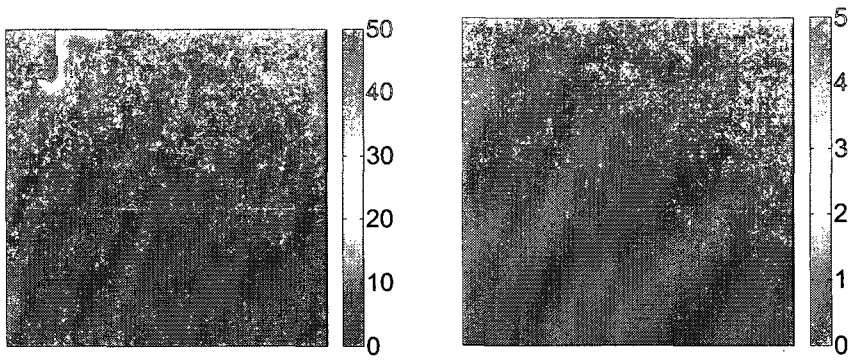

(a) (b)

Figure 4.5: Percent error of distribution of moments around a corner for $M_x = 1$ at infinity, (a) : coarse-mesh finite element result, (b) : result using linear regression

around rectangular holes. The basic idea is to use the finite element results to find the distributions of stresses in the far field where the coarse mesh can provide results with good accuracy. For thin plates the relationship between stress and moment is given by:

$$\sigma = M\frac{12\tau}{h^3}$$

where h is the plate thickness. Once these far-field moments are determined, the moment distribution around the holes can be computed using the results in Table 4.1 in the following manner. The distribution of moments can be written as:

$$M_{FEM} = U_m M_\infty$$

where M_{FEM} is the vector of moments evaluated at points (x_k, y_k) for $k = 1, 2, \cdots, n$ using a coarse-mesh finite element analysis. The matrix U_m is the matrix of covariates

evaluated at (x_k, y_k) and M_∞ is the vector of unknown coefficients for the far-field moment. The points (x_k, y_k) are chosen at points in the vicinity of, but not too close to the boundary because of the errors in the coarse-mesh finite element analysis. The coefficient vector M_∞ is evaluated by the following procedure. The first step is to determine the matrix of covariates U_m. The columns of this matrix are associated with various far-field moments shown in Table (4.2) at points (x_k, y_k). The components of this matrix are decomposed into near-field and far-field. The far-field component of U_m is evaluated at points (x_k, y_k) by substituting the functions ϕ^0 and χ^0 from Table 4.2 into the analytical relations in (4.29) - (4.31) for constant or linear moments. The near-field component can also be evaluated by applying the same procedure to ϕ^* and χ^*. However, since the finite element analysis with coarse mesh does not provide an accurate near-field moment distribution, using the analytical relations in (4.29)-(4.31) for the near-field components results in inaccurate estimates for unknown far-field moments. In order to overcome this problem, the near-field components of covariates in U_m are evaluated using the results of finite element analysis with coarse mesh as follows. Six separate finite element analyses are performed for the constant and linearly varying far-field moments shown in Table 4.1. The distribution of moments evaluated at (x_k, y_k) from each finite element analysis is the near-field component associated with the corresponding column of covariate matrix U_m. The covariate matrix is then obtained by adding these moments to the far-field components and the coefficient vector M_∞ is determined by the standard regression formulation as:

$$M_\infty = (U_m^T U_m)^{-1} U_m^T M_{FEM}$$

4.3.2.1 Numerical examples

In the following, the accuracy of the proposed semi-analytical approach is examined through a series of examples. The first example is a plate with a square hole under constant moment $M_x = 1$ at the far-field. Figure 4.4 shows the moment distribution around one corner of the square hole. The distribution of moments using coarse and fine-mesh finite element, and exact analytical solution are presented and compared with the proposed approach. The regression points are also shown in the figure as red dots on the coarse finite element results. As expected, the results from the model with the coarse mesh do not come close to representing the stress concentrations around the hole. This can also be observed in Figure 4.5 which compares the error of coarse-mesh finite element results with the predicted results using the new semi-analytical approach. The predicted moment distribution by the proposed approach, however, is very close to the exact results of the fine-mesh finite element analyses.

For the second example, the moment per unit length is:

$$M_x = 1 + 0.2y$$

As in Figure 4.4, the moments determined by the proposed approach are compared with exact and two different finite element analyses in Figure 4.6. The far-field moments are subtracted from the moment distribution so that variations in the near-field moments can be seen more clearly. As for the constant moment case, the moments determined from the proposed method are close to the exact and fine-mesh finite element results.

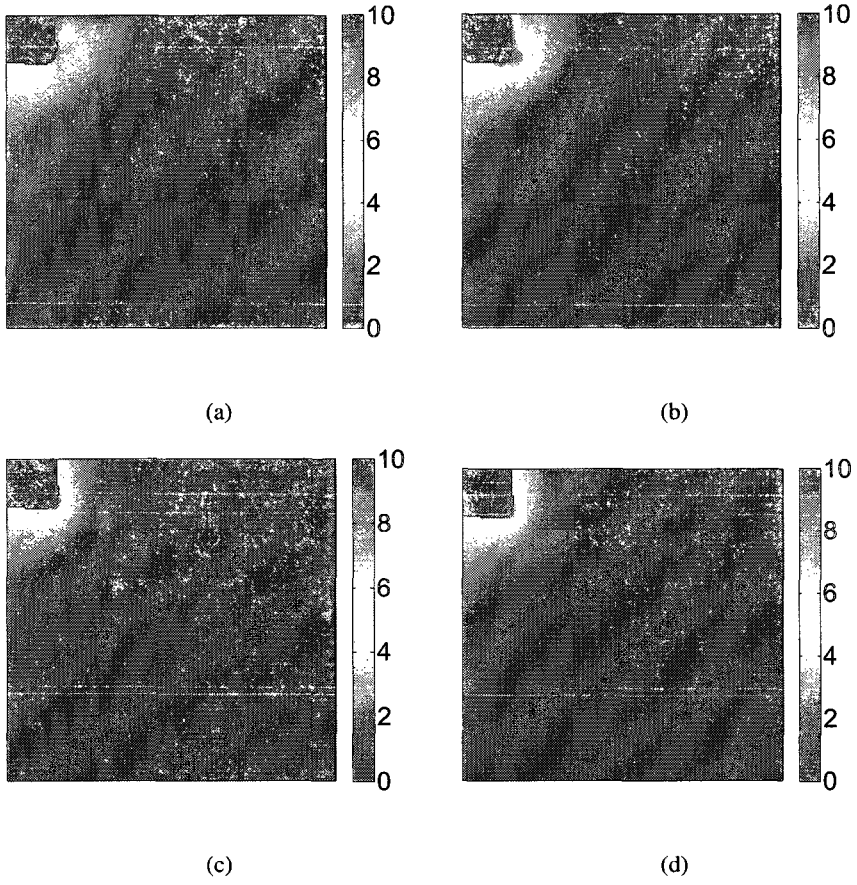

Figure 4.6: Distribution of near-field moments around a corner for $M_x = 1 + 0.2y$ at infinity, (a) : finite element results with coarse mesh, (b) : finite element results with fine mesh, (c) : exact analytical solution and (d) : result using linear regression

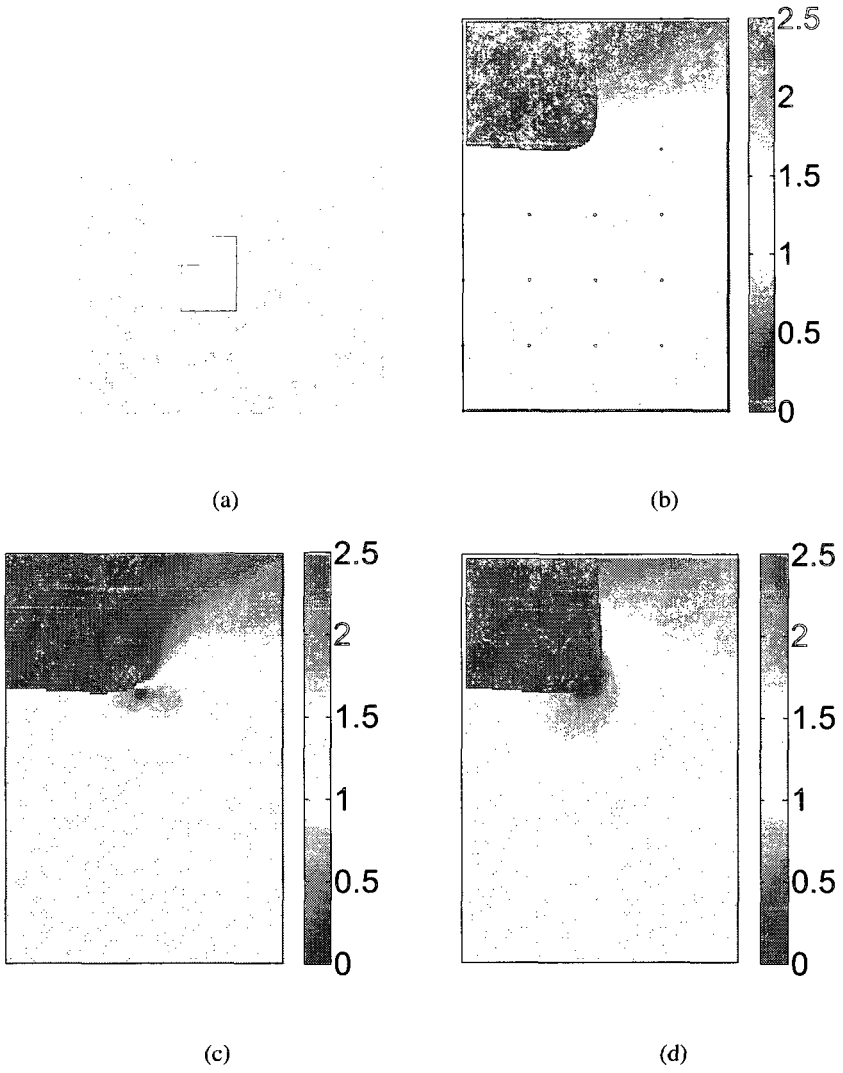

Figure 4.7: Distribution of moments around a corner for $M_x = 1$ at infinity, (a) : The corner that is being analyzed, (b) : finite element results with coarse mesh, (c) : finite element results with fine mesh, and (d) : result using linear regression

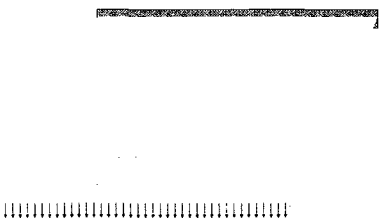

Figure 4.8: Loading and boundary conditions

A third more complex example is examined to test the versatility of the proposed analytical method. A plate with two diagonally staggered holes is considered as shown in Figure 4.3. The moment distributions for the proposed method and the fine- and coarse-mesh finite element analyses are compared in the region shown in Figure 4.7. The distribution of moments is more complicated due to the interactions between the two holes. As before the coarse-mesh finite element model results miss the stress concentrations. While the moments evaluated using the proposed numerical approach have a spatial pattern that is somewhat different than the fine-mesh finite element results, the magnitudes of the moments are very similar.

In the final pair of examples a cantilever plate with two holes is examined. The plate is analyzed under two different types of loads shown in Figures 4.8 and 4.10. The moment comparison in Figures 4.9 and 4.11 show that the proposed semi-analytical approach is accurate in predicting the magnitude of moments, but it is not accurate in reproducing the spatial patterns found by the fine-mesh finite element results. One reason is that the semi-

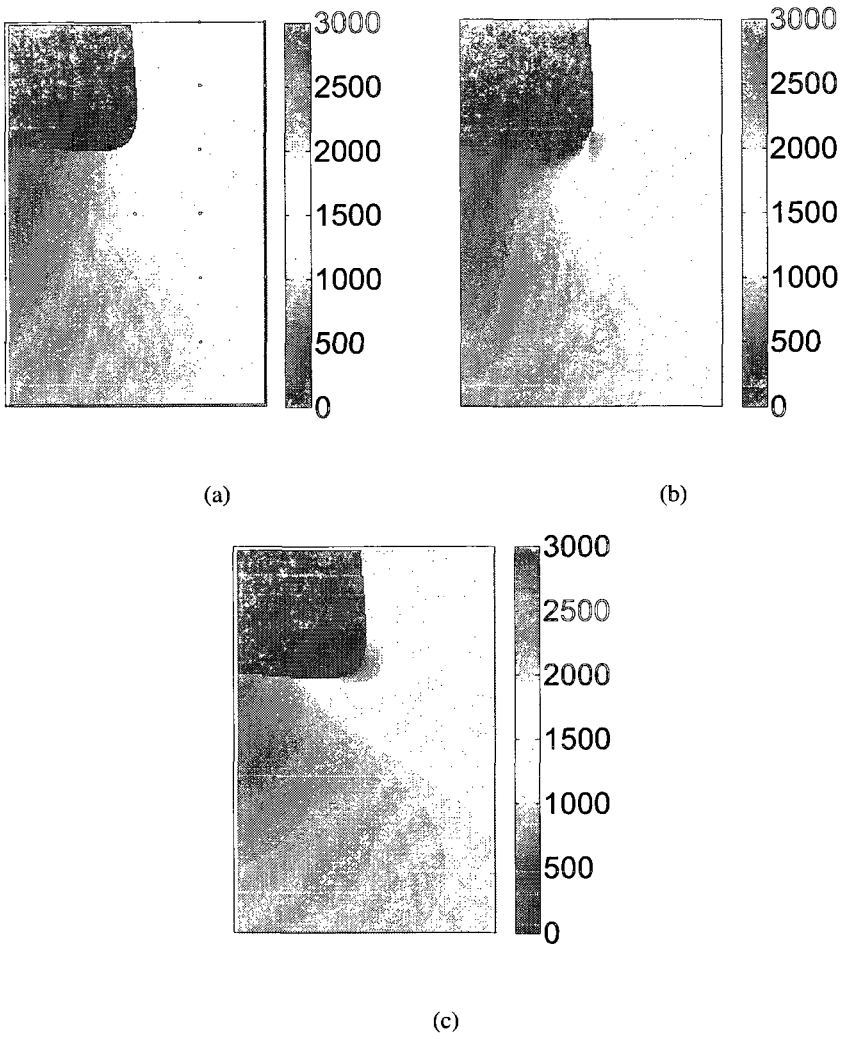

Figure 4.9: Distribution of moments around a corner for loading shown in Figure 4.8, (a) : finite element analysis results with coarse mesh, (b) : finite element analysis results with fine mesh and (c) : result using linear regression

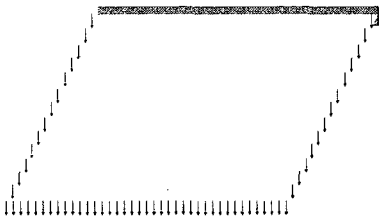

Figure 4.10: Loading and boundary conditions

analytical formulation can model only constant and linearly varying far-field moments.

4.4 Conclusion

A semi-analytical method is developed to enhance the results of coarse-mesh finite element analysis around rectangular holes. The method of complex variables [Muskhelishvili, 1975] is used to evaluate the distribution of moments for a plate with square hole. Unlike previous studies, in the proposed method a numerical approach based on least-squares technique is used instead of contour integration for satisfying the boundary condition at the interior of opening. The proposed method is used to solve bending of a plate with hole under constant and linear far-field moments. The results are then used to enhance the results from a coarse-mesh finite element analysis to determine the stress concentrations around the openings. The proposed approach is very useful for complex and large finite element models where using fine meshes around each opening is not feasible.

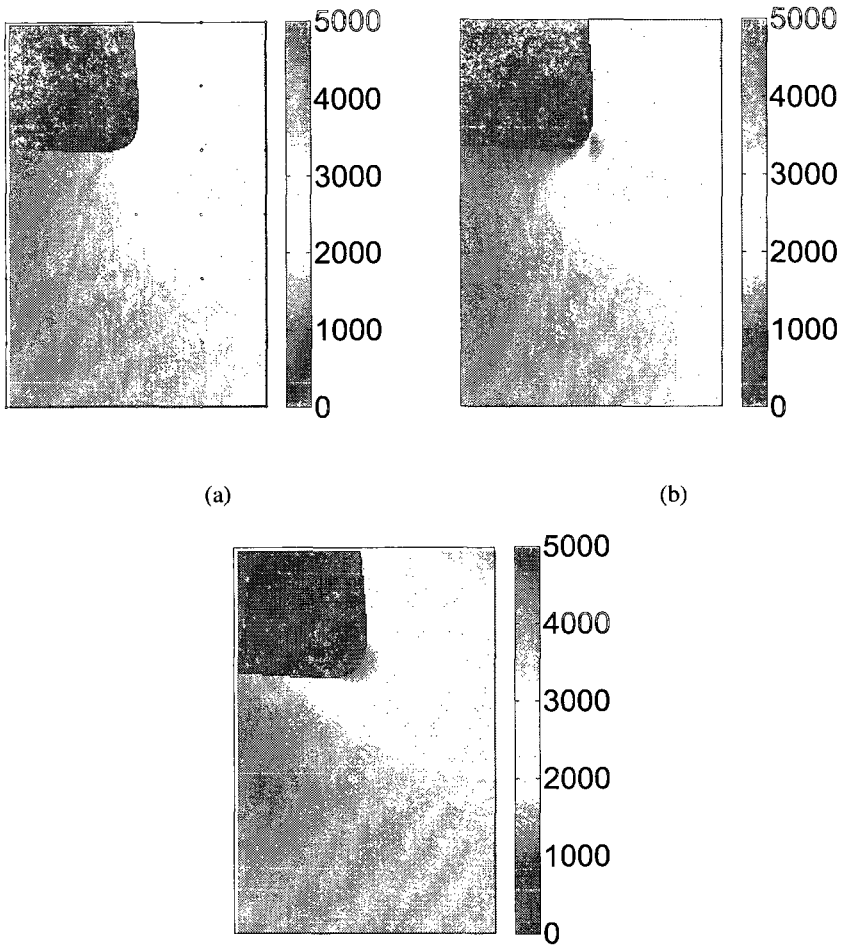

Figure 4.11: Distribution of moments around a corner for loading shown in Figure 4.10, (a) : finite element analysis results with coarse mesh, (b) : finite element analysis results with fine mesh and (c) : result using linear regression

CHAPTER 4.

A series of example studies were used to assess the accuracy of the proposed approach. It was found that the magnitude of the stress concentrations can be determined, but the spatial stress distributions are less accurately reproduced. This is due to the fact that only linearly varying moments at the far-field were considered. Future studies will include more general variations of the far-field moments to make the proposed method more versatile. They will also include the investigations on how the interaction with the adjacent holes will affect the quality of results.

Chapter 5

Vibration of cylindrical shells-review and minor extensions

In the next generations of high-speed trains, the passenger cars are designed as essentially shell-like structures to provide more strength and stiffness. The vibration behavior of these structures are somewhat similar to the vibrations of cylindrical shells. The stress distribution in the car body and a cylindrical shell in Figures 5.1 and 5.2 illustrates this resemblance.

The similarity between the mode shapes of these two structures, vibrating in low and higher frequency, motivates the vibration study of cylindrical shells. The goal of this study is to understand the behavior of the shell vibrations in relation to the shell properties using basic principles of mechanics.

In this chapter the free vibrations of cylinders is studied. The mechanics of compos-

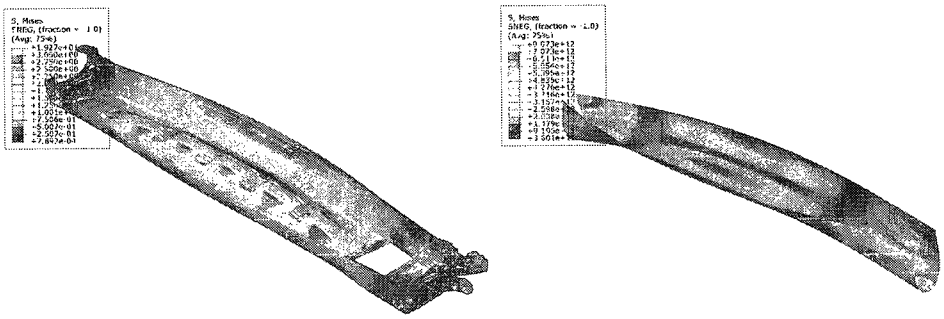

Figure 5.1: Distribution of stresses in car body and cylindrical shell for low frequency modes

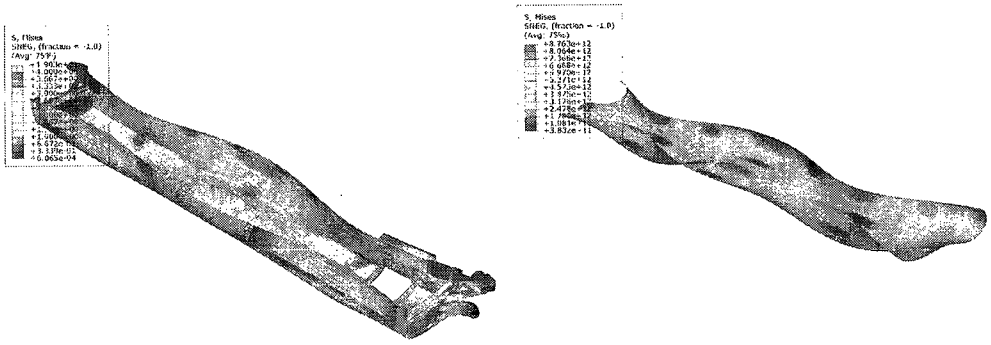

Figure 5.2: Distribution of stresses in car body and cylindrical shell for high frequency modes

ite laminates and the vibrations of cylindrical shells are briefly reviewed. The numerical method for solving the exact equations for the natural frequencies and mode shapes is also reviewed and compared with the energy approach for solving the free vibration problem. The approximate energy method is extended to solve for the natural frequencies and mode shapes using the Flügge instead of the Love-Timoshenko shell theory [Sharma and Darvizeh, 1987]. In deriving the Flügge shell equations there is no approximation other than Kirchhoff hypothesis which results in more accurate equilibrium equations. In Chapter 6, perturbation is used to find approximate analytical expressions for the dispersion relation and to develop a simple approach to solve for the natural frequencies and mode shapes of cylinders.

5.1 Literature review of vibrations of composite cylinders

Composite materials are widely used in engineering applications because of their favorable properties such as high strength or stiffness to weight ratio. Cylindrical shells are also used in many vehicle structures and aircraft components. Therefore there is a considerable interest in studying the behavior of composite cylinders.

A comprehensive review on different theories of shell vibration is summarized in the classical treatise by Leissa [1973]. The theories are based on Kirchhof assumptions which states that normals to the undeformed midsurface remain straight and normal to the de-

formed midsurface. Different assumptions in the strain-displacement equations result in different shell theories such as the Flügge, Love-Timoshenko, Sanders, and Donnell-Mushtari theories. Each of these theories lead to their own set of equations of motion. A comprehensive study of other strain-displacement relationships can be found in Leissa [1973]. There are also several methods to solve these equations. Herein, the focus is on semi-analytical methods such as Fourier series and energy approaches such as the Rayleigh-Ritz technique to find the natural frequencies and mode shapes of composite cylinders. A review of numerical methods such as finite element and finite difference is not included herein.

The vibration characteristics of cylinders was studied for limited types of boundary conditions such as simply supported ends [Leissa, 1973]. The frequencies and mode shapes were evaluated using a Fourier series expansion in both longitudinal and circumferential directions. Forsberg [1964, 1969] solved the Flügge shell equation for several kinds of boundary conditions for isotropic cylindrical shells. An eighth-order algebraic equation is solved iteratively to determine the natural frequencies.

A brief review of different methods used in literature to obtain the solutions for the natural frequencies and mode shapes of cylindrical shells is summarized in Table 5.1. Dong [1968] used Fourier series expansions of the shell displacement field using the Donnell-Mushtari shell equations. C. W. Bert et al. [1969] solved the equilibrium equations to find the natural frequencies of symmetrical and unsymmetrical laminates. Shao and Ma [2007] used the Fourier series expansions for the axial displacements. Sharma and Johns [1971]

Table 5.1: Summary of different studies performed on vibrations of cylinders, (SS: simply supported, CL: clamped, F: free)

reference	shell theory	material	boundary conditions
Dong [1968]	Donnell-Mushtari	orthotropic	SS-SS
C. W. Bert et al. [1969]	Love-Timoshenko	anisotropic	SS-SS
Shao and Ma [2007]	Love-Timoshenko	orthotropic	CL-CL, CL-SS, CL-F,SS-SS
Sharma and Johns [1971]	Flügge	isotropic	CL-F, CL-SS, CL-CL
Sharma and Darvizeh [1987]	Love-Timoshenko	orthotropic	CL-F, CL-SS, CL-CL
Sharma [1974]	Love- Timoshenko	composite laminates	CL-F
Lam and Loy [1995]	Love-Timoshenko	orthotropic	CL-CL, CL-SS, CL-F
Ip et al. [1968]	Love-Timoshenko	orthotropic	F-F
Forsberg [1964]	Flügge	isotropic	variety of boundary conditions

and Sharma and Darvizeh [1987] used the Rayleigh-Ritz energy approach for isotropic and anisotropic material under several boundary conditions. Lam and Loy [1995] assumed that the longitudinal component of the mode shapes is a beam mode. Using the Ritz method on the Lagrangian function associated with the energy method, they obtained a sixth-order equation for determining the natural frequencies. Ip et al. [1968] used experiments as well as the Rayleigh-Ritz energy method by utilizing the characteristic beam functions in axial direction to study the vibration characteristics of cylinders. In Sharma [1974] the functions in longitudinal directions are assumed to be the combination of the beam mode shapes for clamped-free and clamped-pin beams which leads to sextic and cubic equations respectively. Simplifications are introduced to the problem by assuming zero hoop and shear strains in both strain and kinetic energy expressions, leading to quadratic and linear equations. This gives good results for long shells. The linear expression for the frequency parameter is improved in Sharma [1977] by assuming zero shear and hoop strains only in kinetic energy.

The focus of this chapter is to examine the free vibration of free-free composite cylindrical shells. In section 5.2, the mechanics of composite laminates and in section 5.3, the vibration theory of cylindrical shells are briefly reviewed. It is shown how the equations of equilibrium and the boundary conditions are obtained using Hamilton's variational principle and how the solution to the equilibrium equations are determined using a numerical iterative approach. These results are presented primarily as background information for chapter 6.

Next, in section 5.3.2 the approximate solution for the vibration of cylinders using the energy method is reviewed and the frequency and mode shapes are obtained for Flügge shell theory. The solution to the Flügge shell equations for orthotropic cylinders with free-free boundary conditions is not found in the literature, hence this minor extension to existing theories and methods appears to be a new contribution.

5.2 Review of the mechanics of fiber-reinforced composites

The car body shell is essentially a curved orthotropic shell. Here, we generalize the material to include laminated composites.

Each layer in a fiber-reinforced composite consists of long and continuous fibers embedded in a matrix material. This type of the composite material, when properly designed, can be efficient in terms of stiffness and strength. The fibers can be parallel to each other (unidirectional), can be perpendicular to each other (cross-ply or woven fabric), or can be oriented along different directions (multidirectional). Laminated composites are composed of different layers, called ply or lamina, which are bonded together. A lamina or ply is a plane layer of a unidirectional fiber or woven fabric in a matrix. Let the first principal axis of a lamina x_1 be in the fiber's direction. The second direction x_2 is in the plane and the third one x_3 is normal to the plane of the lamina [Daniel and Ishai, 1994].

5.2.1 Lamina mechanical properties

In the case of anisotropic materials there is no plane of symmetry, the state of stress and strain at any point can be expressed by second-order tensors of stress and strain. The relationship between the stress and strain tensors σ_{ij} and ϵ_{kl} can be written as:

$$\sigma_{ij} = C_{ijkl}\epsilon_{kl} \tag{5.1}$$

where C is a fourth-order tensor of stiffness. Noting that the stress and strain tensors are symmetric, the stress-strain relationship can be reduced and rearranged as follows:

$$\begin{pmatrix} \sigma_1 \\ \sigma_2 \\ \sigma_3 \\ \tau_{23} \\ \tau_{13} \\ \tau_{12} \end{pmatrix} = \begin{pmatrix} C_{11} & C_{12} & C_{13} & C_{14} & C_{15} & C_{16} \\ C_{21} & C_{22} & C_{23} & C_{24} & C_{25} & C_{26} \\ C_{31} & C_{32} & C_{33} & C_{34} & C_{35} & C_{36} \\ C_{41} & C_{42} & C_{43} & C_{44} & C_{45} & C_{46} \\ C_{51} & C_{52} & C_{53} & C_{54} & C_{55} & C_{56} \\ C_{61} & C_{62} & C_{63} & C_{64} & C_{65} & C_{66} \end{pmatrix} \begin{pmatrix} \epsilon_1 \\ \epsilon_2 \\ \epsilon_3 \\ \gamma_{23} \\ \gamma_{13} \\ \gamma_{12} \end{pmatrix} \tag{5.2}$$

Here C_{ij} are the components of the stiffness matrix $[C]$ in the x_1, x_2 and x_3 coordinate system. This equation also can be written in terms of compliance matrix $S = [C]^{-1}$

$$\{\epsilon\} = [S]\{\sigma\} \tag{5.3}$$

where $\{\epsilon\}$ and $\{\sigma\}$ are the strain and stress vectors. Using path independency of strain energy, it can be shown that the stiffness and compliance matrices are also symmetric. Therefore the stiffness matrix, in general, has only 21 independent components.

For orthotropic materials there are three perpendicular planes of symmetry, usually chosen such that they are perpendicular to the symmetry planes. For such materials, normal stresses do not produce shear stresses. Therefore, it can be concluded that $S_{14} = S_{15} = S_{16} = S_{24} = S_{25} = S_{26} = S_{34} = S_{35} = S_{36} = 0$. Another argument can be used for applying the shear stress to show that $S_{45} = S_{46} = S_{56} = 0$. Hence the stiffness matrix can be expressed in the following form:

$$\begin{pmatrix} C_{11} & C_{12} & C_{13} & 0 & 0 & 0 \\ C_{12} & C_{22} & C_{23} & 0 & 0 & 0 \\ C_{13} & C_{23} & C_{33} & 0 & 0 & 0 \\ 0 & 0 & 0 & C_{44} & 0 & 0 \\ 0 & 0 & 0 & 0 & C_{55} & 0 \\ 0 & 0 & 0 & 0 & 0 & C_{66} \end{pmatrix} \tag{5.4}$$

5.2.1.1 Thin lamina

For thin unidirectional lamina, if the forces are applied in the plane of lamina, the plane stress approximation can be used as follows:

$$\sigma_3 = \tau_{13} = \tau_{23} = 0 \tag{5.5}$$

Therefore the stress-strain relationship is:

$$\begin{pmatrix} \sigma_1 \\ \sigma_2 \\ \tau_{12} \end{pmatrix} = \begin{pmatrix} Q_{11} & Q_{12} & Q_{16} \\ Q_{12} & Q_{22} & Q_{26} \\ Q_{16} & Q_{26} & Q_{66} \end{pmatrix} \begin{pmatrix} \epsilon_1 \\ \epsilon_2 \\ \gamma_{12} \end{pmatrix} \tag{5.6}$$

where

$$\begin{pmatrix} Q_{11} & Q_{12} & Q_{16} \\ Q_{12} & Q_{22} & Q_{26} \\ Q_{16} & Q_{26} & Q_{66} \end{pmatrix} = \begin{pmatrix} S_{11} & S_{12} & S_{16} \\ S_{12} & S_{22} & S_{26} \\ S_{16} & S_{26} & S_{66} \end{pmatrix}^{-1} \tag{5.7}$$

In the above $[Q]$ and $[S]$ are the stiffness and compliance matrices for the plane stress condition. The components of the stiffness matrix can be determined using Hooke's law and considering the plane stress approximations as follows:

$$Q_{11} = \frac{E_1}{1 - \nu_{12}\nu_{21}}$$

$$Q_{22} = \frac{E_2}{1 - \nu_{12}\nu_{21}}$$

$$Q_{12} = \frac{\nu_{21}E_1}{1 - \nu_{12}\nu_{21}} = \frac{\nu_{12}E_2}{1 - \nu_{12}\nu_{21}}$$

$$Q_{66} = G_{12}$$

where E_1 and E_2 are the elastic moduli, in which subscripts 1 and 2 correspond to directions parallel and perpendicular to the fiber and ν_{12} and ν_{21} are the Poisson ratios.

5.2.2 Mechanical properties of laminated composites

In this section, the stiffness matrix for a laminated composite is reviewed. The analysis is based on laminated plate theory under small deformations. It is assumed that:

- The strains vary linearly across the thickness of the laminate

- The shear deformations are negligible and can be disregarded
- The out-of-plane normal stress σ_z and the shear stresses τ_{xz} and τ_{yz} are negligible comparing to the in-plane shear stresses

It is concluded from the above approximations that the plane-stress assumptions can be used to determine the stiffness of the laminated composites [Kollar and Springer, 2003]. Since we are interested in symmetric laminates, the reference plane is the midplane. The strain in the midplane can be written in terms of the in-plane displacement components as follows:

$$\epsilon_x = \frac{\partial u}{\partial x} \quad \epsilon_y = \frac{\partial v}{\partial x} \quad \epsilon_{xy} = \frac{\partial u}{\partial y} + \frac{\partial v}{\partial x} \tag{5.8}$$

and the strains at a general point are:

$$\begin{pmatrix} e_x \\ e_y \\ \gamma_{xy} \end{pmatrix} = \begin{pmatrix} \epsilon_x \\ \epsilon_y \\ \epsilon_{xy} \end{pmatrix} + z \begin{pmatrix} \kappa_x \\ \kappa_y \\ \kappa_{xy} \end{pmatrix} \tag{5.9}$$

where z is the distance from the reference plane and:

$$\kappa_x = -\frac{\partial^2 w}{\partial x^2} \quad \kappa_y = -\frac{\partial^2 w}{\partial y^2} \quad \kappa_{xy} = -\frac{2\partial^2 w}{\partial x \partial y} \tag{5.10}$$

are the curvatures of the midplane. In order to evaluate the in-plane forces shown in Figure 5.3 the stresses first need to be evaluated and integrated along the thickness of laminate:

$$\begin{aligned} N_x &= \int_{-h_b}^{h_t} \sigma_x dz \qquad N_y = \int_{-h_b}^{h_t} \sigma_y dz \qquad N_{xy} = \int_{-h_b}^{h_t} \tau_{xy} dz \\ M_x &= \int_{-h_b}^{h_t} z\sigma_x dz \qquad M_y = \int_{-h_b}^{h_t} z\sigma_y dz \qquad M_{xy} = \int_{-h_b}^{h_t} z\tau_{xy} dz \end{aligned} \tag{5.11}$$

where N and M are the in-plane forces and moments per unit length, and h_t and h_b are the distances to the top and bottom of the laminate from the midplane. In order to calculate the internal in-plane forces, for each lamina the stresses in the principal directions must be transformed to the x, y, z coordinates. Therefore for each lamina one can write:

$$\begin{pmatrix} \sigma_x \\ \sigma_y \\ \tau_{xy} \end{pmatrix} = \begin{pmatrix} \overline{Q}_{11} & \overline{Q}_{12} & \overline{Q}_{16} \\ \overline{Q}_{12} & \overline{Q}_{22} & \overline{Q}_{26} \\ \overline{Q}_{16} & \overline{Q}_{26} & \overline{Q}_{66} \end{pmatrix} \begin{pmatrix} e_x \\ e_y \\ \gamma_{xy} \end{pmatrix} \tag{5.12}$$

where

$$[\overline{Q}] = \begin{pmatrix} \overline{Q}_{11} & \overline{Q}_{12} & \overline{Q}_{16} \\ \overline{Q}_{12} & \overline{Q}_{22} & \overline{Q}_{26} \\ \overline{Q}_{16} & \overline{Q}_{26} & \overline{Q}_{66} \end{pmatrix} = \begin{pmatrix} c^2 & s^2 & 2cs \\ s^2 & c^2 & -2cs \\ -cs & cs & c^2 - s^2 \end{pmatrix} [Q] \begin{pmatrix} c^2 & s^2 & cs \\ s^2 & c^2 & -cs \\ -2cs & 2cs & c^2 - s^2 \end{pmatrix}^{-1} \tag{5.13}$$

In the above equation $c = \cos\theta$ and $s = \sin\theta$, where θ is the angle between the first axis of the laminate, x, and the first principal axis of the lamina. Noting that the matrix $[\overline{Q}]$ does not vary across each ply, the integrals in equation (5.11) can be written as summations. The in-plane forces and moments can be related to the strains and curvatures of the midplane as

follows:

$$\begin{pmatrix} N_x \\ N_y \\ N_{xy} \\ M_x \\ M_y \\ M_{xy} \end{pmatrix} = \begin{pmatrix} A_{11} & A_{12} & A_{16} & B_{11} & B_{12} & B_{16} \\ A_{12} & A_{22} & A_{26} & B_{12} & B_{22} & B_{26} \\ A_{16} & A_{26} & A_{66} & B_{16} & B_{26} & B_{66} \\ B_{11} & B_{12} & B_{16} & D_{11} & D_{12} & D_{16} \\ B_{12} & B_{22} & B_{26} & D_{12} & D_{22} & D_{26} \\ B_{16} & B_{26} & B_{66} & D_{16} & D_{26} & D_{66} \end{pmatrix} \begin{pmatrix} \epsilon_x \\ \epsilon_y \\ \gamma_{xy} \\ \kappa_x \\ \kappa_y \\ \kappa_{xy} \end{pmatrix}$$

where:

$$\begin{aligned} A_{ij} &= \sum_{k=1}^{K} (\overline{Q}_{ij})_k (z_k - z_{k-1}) \\ B_{ij} &= \frac{1}{2} \sum_{k=1}^{K} (\overline{Q}_{ij})_k (z_k^2 - z_{k-1}^2) \\ D_{ij} &= \frac{1}{3} \sum_{k=1}^{K} (\overline{Q}_{ij})_k (z_k^3 - z_{k-1}^3) \end{aligned} \tag{5.14}$$

Here K is the total number of plies and z_k and z_{k-1} are the distances from the reference plane to the top and bottom surfaces of the k^{th} ply. The matrices A, B and D are the stiffness matrices of the laminate.

5.3 Vibration of thin cylindrical shells

In this section, the vibration of cylindrical shells is briefly reviewed. Let u, v and w be the axial, circumferential and radial displacements and r, θ and x be the corresponding axes in cylindrical coordinates. Let z be the distance from the reference plane. It is assumed

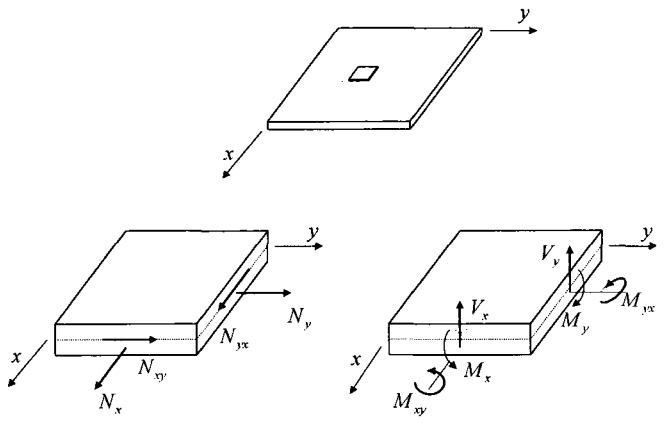

Figure 5.3: Internal forces in a plate

that:

- The thickness of the shell is small compared to the radius.
- The displacements are small such that second-order terms can be neglected. This assumption results in linear differential equations.
- The transverse normal stress is negligible comparing to the other normal stresses.
- Normals to the middle surface remain normal and straight after deformation (Kirch-

hoff's Hypothesis) which results in:

$$\gamma_{zx} = \gamma_{z\theta} = \epsilon_z = 0$$

The strains and curvatures of the midplane of a cylinder are related to its displacements using the following equations [Leissa, 1973]:

$$\epsilon_x = \frac{\partial u}{\partial x}$$

$$\epsilon_\theta = \frac{1}{R}\frac{\partial v}{\partial \theta} + \frac{w}{R}$$

$$\epsilon_{x\theta} = \frac{\partial v}{\partial x} + \frac{1}{R}\frac{\partial u}{\partial \theta} \tag{5.15}$$

$$\kappa_x = -\frac{\partial^2 w}{\partial^2 x} \tag{5.16}$$

$$\kappa_\theta = \frac{1}{R^2}\left(\frac{\partial v}{\partial \theta} - \frac{\partial^2 w}{\partial \theta^2}\right)$$

$$\tau = \frac{2}{R}\left(\frac{\partial v}{\partial x} - \frac{\partial^2 w}{\partial \theta \partial x}\right)$$

These strain-displacement relationships can be simplified using physically motivated assumptions. In Flügge shell theory no other simplifications are assumed and the total strains are obtained as [Leissa, 1973]:

$$e_x = (\epsilon_x + z\kappa_x)$$

$$e_\theta = \frac{1}{1+\frac{z}{R}}(\epsilon_\theta + z\kappa_\theta)$$

$$\gamma_{x\theta} = \frac{1}{1+\frac{z}{R}}\left(\epsilon_{x\theta} + z\left(1+\frac{z}{2R}\right)\tau\right)$$

For instance, in Love-Timoshenko shell theory it is assumed that z/R is negligible compared to unity, leading to the following strain-displacement relationships:

$$e_x = \epsilon_x + z\kappa_x$$

$$e_\theta = \epsilon_\theta + z\kappa_\theta$$

$$\gamma_{x\theta} = \epsilon_{x\theta} + z\tau$$

A comprehensive study of other strain-displacement relationships can be found in Leissa [1973].

5.3.1 Equations of motion and boundary conditions: a variational formulation

In this section, Hamilton's variational formulation is used to find the equations of motion and boundary conditions for a cylindrical shell. The analysis begins with Hamilton's Principle [Soedel, 2004]

$$\delta \int_{t_1}^{t_2} (T - U)\, dt = 0 \tag{5.17}$$

where T is the kinetic energy:

$$T = \frac{1}{2} \int_v \rho \left(\dot{u}^2 + \dot{v}^2 + \dot{w}^2\right) R d\theta dx dz$$

and U is the elastic strain energy:

$$U = \frac{1}{2}\int_v \begin{bmatrix} e_x \\ e_y \\ \gamma_{xy} \end{bmatrix}^T \begin{bmatrix} \overline{Q}_{11} & \overline{Q}_{12} & \overline{Q}_{16} \\ \overline{Q}_{12} & \overline{Q}_{22} & \overline{Q}_{26} \\ \overline{Q}_{16} & \overline{Q}_{26} & \overline{Q}_{66} \end{bmatrix} \begin{bmatrix} e_x \\ e_y \\ \gamma_{xy} \end{bmatrix} Rd\theta dx dz$$

For convenience, the formulations are written for a cylinder with unit radius. The results can easily be converted to the general case by scaling the wave number and stiffness matrix. Using the Love-Timoshenko shell theory assumptions, the total strains are:

$$e_x = u_x - zw_{xx}$$

$$e_\theta = v_\theta + w + z\left(v_\theta - w_{\theta\theta}\right)$$

$$\gamma_{x\theta} = u_\theta + v_x + 2z\left(v_x - w_{x\theta}\right)$$

In these expressions the indices of u, v and w indicate partial derivatives. The potential energy can be written as:

$$U = \frac{1}{2}\int_v \left(\overline{Q}_{11}(u_x - zw_{xx})^2 + 2\left(u_x - zw_{xx}\right)\overline{Q}_{12}\left[v_\theta + w + z\left(v_\theta - w_{\theta\theta}\right)\right] + \right.$$

$$2\left(u_x - zw_{xx}\right)\overline{Q}_{16}\left[v_x + u_\theta + 2z\left(v_x - w_{x\theta}\right)\right] + \overline{Q}_{22}\left[v_\theta + w + z\left(v_\theta - w_{\theta\theta}\right)\right]^2 +$$

$$2\left[v_\theta + w + z\left(v_\theta - w_{\theta\theta}\right)\right]\overline{Q}_{26}\left[v_x + u_\theta + 2z\left(v_x - w_{,x\theta}\right)\right] +$$

$$\left.\overline{Q}_{66}\left[v_x + u_\theta + 2z\left(v_x - w_{x\theta}\right)\right]^2\right) dV$$

Here we assume that the laminates are symmetric so that $B = 0$ in equation (5.14) . Taking the variational operator inside the integral, substituting $\overline{Q_{ij}}$ from equation (5.13) and performing the integration in the thickness direction, the variation of the potential and kinetic

energies can be written as:

$$\delta U = \int_v (A_{11} u_x \delta u_x + D_{11} w_{xx} \delta w_{xx} + A_{12} \left(u_x \delta \left(v_\theta + w\right) + \left(v_\theta + w\right) \delta u_x\right)$$

$$- D_{12} \left(w_{xx} \delta \left(v_\theta - w_{\theta\theta}\right) + \left(v_\theta - w_{\theta\theta}\right) \delta w_{xx}\right) + A_{16} \left(u_x \delta \left(v_x + u_\theta\right) + \left(v_x + u_\theta\right) \delta u_x\right)$$

$$- 2D_{16} \left(w_{xx} \delta \left(v_x - w_{x\theta}\right) + \left(v_x - w_{x\theta}\right) \delta w_{xx}\right) + A_{22} \left(v_\theta + w\right) \delta \left(v_\theta + w\right)$$

$$+ D_{22} \left(v_\theta - w_{\theta\theta}\right) \delta \left(v_\theta - w_{\theta\theta}\right) + A_{26} \left(\left(v_\theta + w\right) \delta \left(v_x + u_\theta\right) + \left(v_x + u_\theta\right) \delta \left(v_\theta + w\right)\right)$$

$$+ 2D_{26} \left(\left(v_\theta - w_{\theta\theta}\right) \delta \left(v_x - w_{x\theta}\right) + \left(v_x - w_{x\theta}\right) \delta \left(v_\theta - w_{\theta\theta}\right)\right) + A_{66} \left(v_x + u_\theta\right) \delta \left(v_x + u_\theta\right)$$

$$+ 4D_{66} \left(v_x - w_{x\theta}\right) \delta \left(v_x - w_{x\theta}\right)) dV$$

$$\delta T = \int_v \rho \left(\dot{u} \delta \dot{u} + \dot{v} \delta \dot{v} + \dot{w} \delta \dot{w}\right) R d\theta dx dz$$

Finally, after integrating by parts equation (5.17) becomes:

$$
\begin{aligned}
&\int_{\theta} \left(A_{11}u_x + A_{12}\left(v_\theta + w\right) + A_{16}\left(v_x + u_\theta\right)\right)\delta u d\theta + \\
&\int_{\theta} \left(\begin{array}{c} A_{16}u_x + A_{66}\left(v_x + u_\theta\right) - 2D_{16}w_{xx} + 4D_{66}\left(v_x - w_{x\theta}\right) \\ +A_{26}\left(v_\theta + w\right) + 2D_{26}\left(v_\theta - w_{\theta\theta}\right) \end{array} \right)\delta v + \\
&\int_{\theta} \left(\begin{array}{c} -D_{11}w_{xxx} + \left(D_{12} + 4D_{66}\right)\left(v_{x\theta} - w_{x\theta\theta}\right) + 2D_{16}\left(v_{xx} - 2w_{xx\theta}\right) \\ +2D_{26}\left(v_{\theta\theta} - w_{\theta\theta\theta}\right) \end{array} \right)\delta w + \\
&\int_{\theta} \left(D_{11}w_{xx} - D_{12}\left(v_\theta - w_{\theta\theta}\right) - 2D_{16}\left(v_x - w_{x\theta}\right)\right)\delta w_x + \\
&\int_{V} - \left(\begin{array}{c} A_{11}u_{xx} + A_{12}\left(v_{x\theta} + w_x\right) + A_{16}\left(v_{xx} + 2u_{x\theta}\right) + A_{26}\left(v_{\theta\theta} + w_\theta\right) \\ +A_{66}\left(v_{x\theta} + u_{\theta\theta}\right) - \rho_T \ddot{u} \end{array} \right)\delta u dV + \\
&\int_{V} - \left(\begin{array}{c} A_{12}u_{x\theta} - D_{12}w_{xx\theta} + A_{22}\left(v_{\theta\theta} + w_\theta\right) + D_{22}\left(v_{\theta\theta} - w_{\theta\theta\theta}\right) \\ +A_{66}\left(v_{xx} + u_{x\theta}\right) + 4D_{66}\left(v_{xx} - w_{xx\theta}\right) + A_{16}u_{xx} - 2D_{16}w_{xxx} \\ +A_{26}\left(2v_{\theta x} + w_x + u_{\theta\theta}\right) + 4D_{26}\left(v_{x\theta} - w_{x\theta\theta}\right) - \rho_T \ddot{v} \end{array} \right)\delta v dV + \\
&\int_{V} - \left(\begin{array}{c} -D_{11}w_{xxxx} - A_{12}u_x + D_{12}\left(v_{xx\theta} - 2w_{xx\theta\theta}\right) - A_{22}\left(v_\theta + w\right) \\ +D_{22}\left(v_{\theta\theta\theta} - w_{\theta\theta\theta\theta}\right) + 2D_{16}\left(v_{xxx} - 2w_{xxx\theta}\right) - A_{26}\left(v_x + u_\theta\right) \\ +4D_{26}\left(v_{x\theta\theta} - w_{x\theta\theta\theta}\right) + 4D_{66}\left(v_{xx\theta} - w_{xx\theta\theta}\right) - \rho_T \ddot{w} \end{array} \right)\delta w dV = 0
\end{aligned}
$$

Since the variational displacements $\delta u, \delta v$ and δw are arbitrary this equation can only be satisfied when the integrands inside the double and single integrals vanish. This results in three equilibrium equations and four equations for the boundary conditions. The final

equilibrium equations are:

$$A_{11}u_{xx} + 2A_{16}u_{x\theta} + A_{66}u_{\theta\theta} + A_{16}v_{xx} + A_{26}v_{\theta\theta} + (A_{12} + A_{66})\,v_{x\theta} + A_{12}w_x$$

$$+ A_{26}w_\theta - \rho_T\ddot{u} = 0$$

$$A_{16}u_{xx} + (A_{12} + A_{66})\,u_{x\theta} + A_{26}u_{\theta\theta} + (A_{66} + 4D_{66})\,v_{xx} + 2\,(A_{26} + 2D_{26})\,v_{x\theta}$$

$$+ (A_{22} + D_{22})\,v_{\theta\theta} + A_{26}w_x + A_{22}w_\theta - D_{22}w_{\theta\theta\theta} - (4D_{66} + D_{12})\,w_{xx\theta}$$

$$- 2D_{16}w_{xxx} - 4D_{26}w_{x\theta\theta} - \rho_T\ddot{v} = 0$$

$$A_{12}u_x + A_{26}u_\theta + A_{26}v_x + A_{22}v_\theta - (D_{12} + 4D_{66})\,v_{xx\theta} - D_{22}v_{\theta\theta\theta}$$

$$- 2D_{16}v_{xxx} - 4D_{26}v_{x\theta\theta} + A_{22}w + 2\,(D_{12} + 2D_{16} + 2D_{66})\,w_{xx\theta\theta} + D_{22}w_{\theta\theta\theta\theta}$$

$$+ 4D_{26}w_{x\theta\theta\theta} + D_{11}w_{xxxx} + \rho_T\ddot{w} = 0$$

which can be written in an operator form as:

$$\begin{pmatrix} L_{11} & L_{12} & L_{13} \\ L_{12} & L_{22} & L_{23} \\ L_{13} & L_{23} & L_{33} \end{pmatrix} \begin{pmatrix} u \\ v \\ w \end{pmatrix} = \begin{pmatrix} 0 \\ 0 \\ 0 \end{pmatrix} \tag{5.18}$$

where:

$$
\begin{aligned}
L_{11} &= A_{11}\frac{\partial^2}{\partial x^2} + 2A_{16}\frac{\partial^2}{\partial x \partial \theta} + A_{66}\frac{\partial^2}{\partial \theta^2} - \rho_T \frac{\partial^2}{\partial t^2} \\
L_{12} &= L_{21} = A_{16}\frac{\partial^2}{\partial x^2} + (A_{12} + A_{66})\frac{\partial^2}{\partial x \partial \theta} + A_{26}\frac{\partial^2}{\partial \theta^2} \\
L_{13} &= L_{31} = A_{12}\frac{\partial}{\partial x} + A_{26}\frac{\partial}{\partial \theta} \\
L_{22} &= (A_{66} + 4D_{66})\frac{\partial^2}{\partial x^2} + 2(A_{26} + 2D_{26})\frac{\partial^2}{\partial x \partial \theta} + (A_{22} + D_{22})\frac{\partial^2}{\partial \theta^2} - \rho_T \frac{\partial^2}{\partial t^2} \\
L_{23} &= L_{32} = A_{26}\frac{\partial}{\partial x} + A_{22}\frac{\partial}{\partial \theta} - D_{22}\frac{\partial^3}{\partial \theta^3} - (D_{12} + 4D_{66})\frac{\partial^3}{\partial x^2 \partial \theta} \\
&\quad -2D_{16}\frac{\partial^3}{\partial x^3} - 4D_{26}\frac{\partial^3}{\partial x \partial \theta^2} \\
L_{33} &= A_{22} + 2(D_{12} + 2D_{16} + 2D_{66})\frac{\partial^4}{\partial x^2 \partial \theta^2} + D_{22}\frac{\partial^4}{\partial \theta^4} \\
&\quad +4D_{26}\frac{\partial^4}{\partial x \partial \theta^3} + D_{11}\frac{\partial^4}{\partial x^4} + \rho_T \frac{\partial^2}{\partial t^2}
\end{aligned}
$$

The boundary conditions are:

$$
\begin{aligned}
&\delta u = 0, \quad A_{11}u_x + A_{12}(v_\theta + w) + A_{16}(v_x + u_\theta) = 0 \\
&\delta v = 0, \quad A_{16}u_x + A_{66}(v_x + u_\theta) - 2D_{16}w_{xx} + 4D_{66}(v_x - w_{x\theta}) + A_{26}(v_\theta + w) \\
&+ 2D_{26}(v_\theta - w_{\theta\theta}) = 0 \\
&\delta w = 0, \quad -D_{11}w_{xxx} + (D_{12} + 4D_{66})(v_{x\theta} - w_{x\theta\theta}) + 2D_{16}(v_{xx} - 2w_{xx\theta}) \\
&+ 2D_{26}(v_{\theta\theta} - w_{\theta\theta\theta}) = 0 \\
&\delta w_x = 0, \quad D_{11}w_{xx} - D_{12}(v_\theta - w_{\theta\theta}) - 2D_{16}(v_x - w_{x\theta}) = 0
\end{aligned}
\tag{5.19}
$$

5.3.1.1 Exact numerical solution

In this section the solution for the mode shapes and natural frequencies of a free-free cylinder is obtained using an iterative numerical approach. First the solutions to the mode shapes are expressed as a Fourier series in circumferential direction and an exponential series in the longitudinal direction:

$$u = \sum_j C_j \alpha_j e^{\lambda_j x} e^{in\theta}, \quad v = \sum_j C_j \beta_j e^{\lambda_j x} e^{in\theta}, \quad w = \sum_j C_j e^{\lambda_j x} e^{in\theta} \tag{5.20}$$

Substituting the above solutions, the equilibrium equations in (5.18) can be written in matrix form.

$$\begin{bmatrix} E_{11} & E_{12} & E_{13} \\ E_{12} & E_{22} & E_{23} \\ E_{12} & E_{23} & E_{33} \end{bmatrix} \begin{bmatrix} \alpha \\ \beta \\ 1 \end{bmatrix} e^{\lambda x} e^{in\theta} = 0 \tag{5.21}$$

where:

$$\begin{aligned}
E_{11} &= A_{11}\lambda^2 + 2in\lambda A_{16} - n^2 A_{66} + \eta \\
E_{12} &= A_{16}\lambda^2 + in\lambda\left(A_{12} + A_{66}\right) - n^2 A_{26} \\
E_{13} &= A_{12}\lambda + inA_{26} \\
E_{22} &= \left(A_{66} + 4D_{66}\right)\lambda^2 + 2in\lambda\left(A_{26} + 2D_{26}\right) - n^2\left(A_{22} + D_{22}\right) + \eta \\
E_{23} &= \lambda A_{26} + inA_{22} - in\lambda^2\left(D_{12} + 4D_{66}\right) - 2\lambda^3 D_{16} + 4n^2\lambda D_{26} + in^3 D_{22} \\
E_{33} &= A_{22} - 2n^2\lambda^2\left(D_{12} + 2D_{16} + 2D_{66}\right) + n^4 D_{22} - 4in^3\lambda D_{26} + \lambda^4 D_{11} - \eta
\end{aligned} \tag{5.22}$$

in which $\eta = \rho_T \omega^2$, and $\rho_T = \int \rho dz$.

The eighth-order characteristic equation giving the so-called dispersion relationship between the frequency parameter η and wavenumber λ is given by $|E| = 0$. For each η, the characteristic equation yields eight values of λ. Furthermore for each λ, the corresponding amplitudes of the displacements, α and β can be determined from equation (5.21). To obtain the natural frequencies and mode shapes, the boundary conditions must be satisfied. For a free-free cylinder the boundary conditions are:

$$N_x = \sum_j \left(A_{11}\lambda_j\alpha_j + A_{12}\left(in\beta_j + 1\right) + A_{16}\left(\lambda_j\beta_j + in\alpha_j\right)\right) C_j e^{\pm\frac{\lambda_j L}{2}} = 0 \tag{5.23}$$

$$M_x = \sum_j \left(D_{11}^2\lambda_j^2 - nD_{12}\left(i\beta_j + n\right) - 2\lambda_j D_{16}\left(\beta_j - in\right)\right) C_j e^{\pm\frac{\lambda_j L}{2}} = 0 \tag{5.24}$$

$$N_{x\theta} - M_{x\theta}/R = \sum_j \left(A_{16}\lambda_j\alpha_j + A_{66}\left(\lambda_j\beta_j + in\alpha_j\right) - 2D_{16}\lambda_j^2 + \right.$$

$$\left. 4\lambda_j D_{66}\left(\beta_j - in\right) + A_{26}\left(in\beta_j + 1\right) + 2nD_{26}\left(i\beta_j + n\right)\right) C_j e^{\pm\frac{\lambda_j L}{2}} = 0 \tag{5.25}$$

$$Q = \sum_j \left(-D_{11}\lambda_j^3 + n\lambda_j\left(D_{12} + 4D_{66}\right)\left(i\beta_j + n\right) + 2\lambda_j^2 D_{16}\left(\beta_j - 2in\right) + \right.$$

$$\left. 2n^2 D_{26}\left(-\beta_j + in\right)\right) C_j e^{\pm\frac{\lambda_j L}{2}} = 0 \tag{5.26}$$

An iterative approach is used to find the natural frequencies and mode shapes of cylinders. For each value of η the corresponding λ_j, α_j and β_j are evaluated using the dispersion relation in (5.21). The obtained values are then substituted into the boundary conditions in (6.5)-(6.8), and rearranged to the following matrix form:

$$NC = 0 \tag{5.27}$$

where C is the vector of unknown coefficients C_j for $j = 1, 2, \cdots 8$. In order to have nontrivial solutions we must have $|N| = 0$. Solving this equation numerically the natural

Table 5.2: Properties of the isotropic copper pipe

Length	.2133 (m)
Thickness	.75774 (mm)
Radius	10.8 (mm)
E (Elastic modulus)	129.35 GPa
ν (Poisson ratio)	0.34
ρ (Density)	8970(Kg/m^3)

frequencies of the cylinder is determined. The coefficients C_j can then be evaluated from the equation (5.27). The obtained values for λ_j, α_j, β_j and C_j is substituted into equation (5.20) to obtain the mode shapes.

5.3.1.2 Numerical results

As an example, the natural frequencies and mode shapes of a copper cylinder are evaluated. The properties of the copper pipe are shown in Table 5.2. The natural frequencies of the copper pipe using the solution of equations (5.21)-(6.8) and finite element analysis are compared in Table 5.3. Figures 5.4 and 5.5 compare the solutions for the mode shapes associated with circumferential wave number $n = 1$. In the finite element model using ABAQUS general shell element $S4$ is used where Sanders-Koiter shell theory is utilized in element formulations [Abaqus documentation, 2007]. The model consists of 161 and 80 shell elements in longitudinal and circumferential directions. Figures 5.6 - 5.8 show the

Table 5.3: Natural frequencies of copper pipe using numerical method for solving equilibrium and boundary conditions, compared with finite element analysis

n	f(Hz)	f(Hz) (ABAQUS)	% error
1	2097	2103	0.2
1	5206	5219	0.2
2	3200	3178	0.6
2	3208	3186	0.7
2	3331	3310	0.6
2	3836	3820	0.4
2	4963	4960	0.0
2	6676	6688	0.2
2	8809	8837	0.3
3	9041	8973	0.7
3	9050	8981	0.8

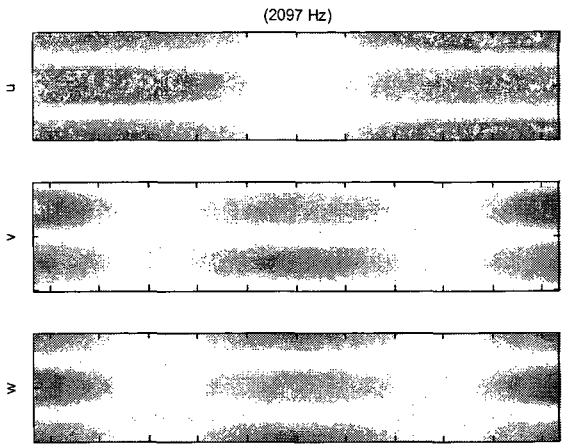

Figure 5.4: Mode shape associated with $n = 1$ using exact numerical solution

mode shapes associated with circumferential wave number $n = 2$ using equations (5.21)-(6.8) and Figures 5.9 - 5.11 show the corresponding mode shapes calculated by finite element analysis. Figures 5.12 and 5.13 compare the mode shape results for circumferential wave number $n = 3$. It can be seen that the natural frequencies and the mode shapes obtained from equations (5.21)-(6.8) are in close agreement with the finite element results.

As another example, we consider the more general case of an orthotropic cylinder with properties shown in Table 5.4. The natural frequencies of the cylinder obtained using equations (5.21) - (6.8) and finite element analysis are compared in Table 5.5. The mode shapes for circumferential wave number $n = 1$ are presented in Figures 5.14, 5.15 and 5.16, 5.17 and those for $n = 2$ are shown in Figures 5.18- 5.23. As in the isotropic example, the results obtained from equations (5.21)-(6.8) are in close agreement with the finite element

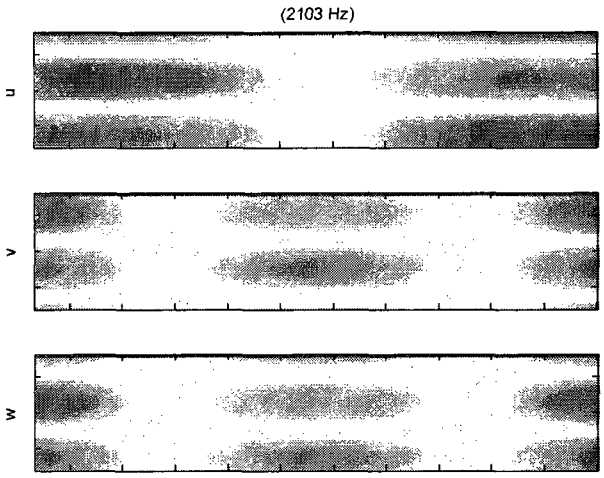

Figure 5.5: Mode shape associated with $n = 1$ using finite element analysis (ABAQUS)

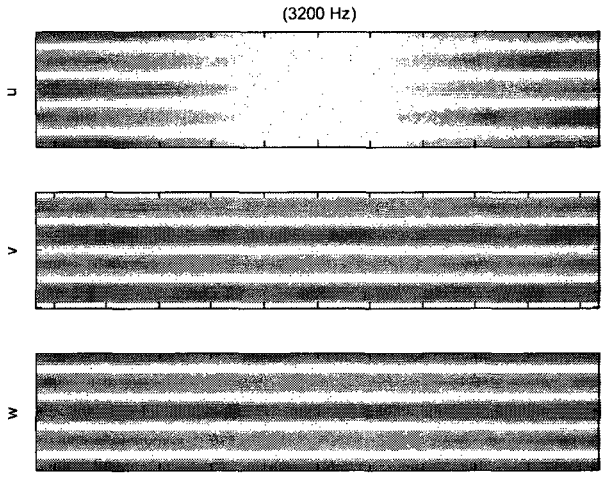

Figure 5.6: Mode shape associated with $n = 2$ using exact numerical solution

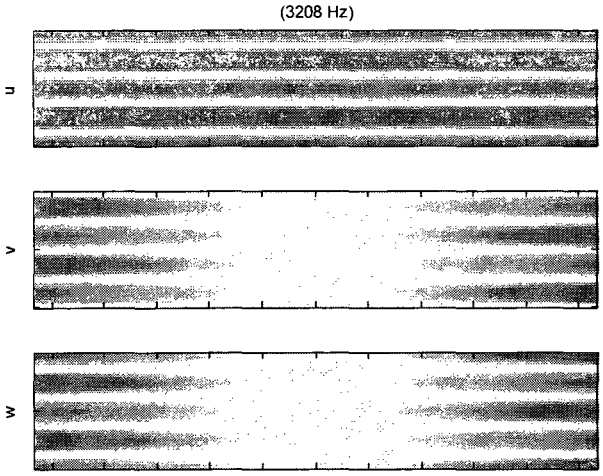

Figure 5.7: Mode shape associated with $n = 2$ using exact numerical solution

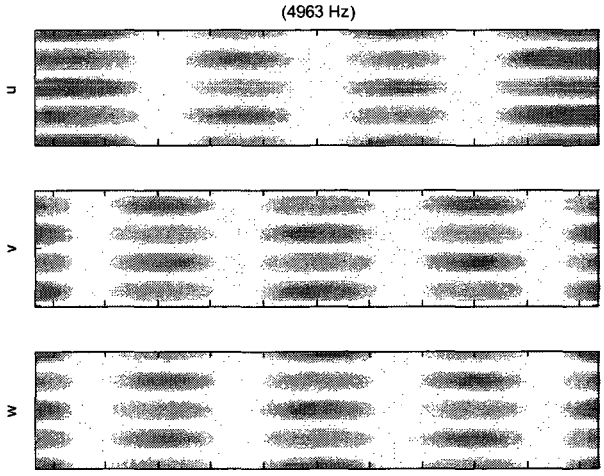

Figure 5.8: Mode shape associated with $n = 2$ using exact numerical solution

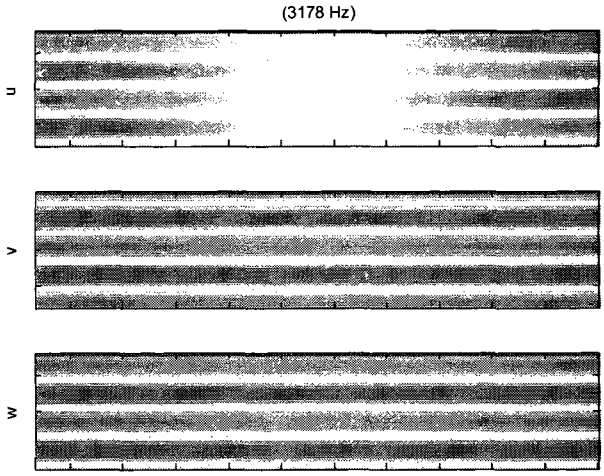

Figure 5.9: Mode shape associated with $n = 2$ using finite element analysis (ABAQUS)

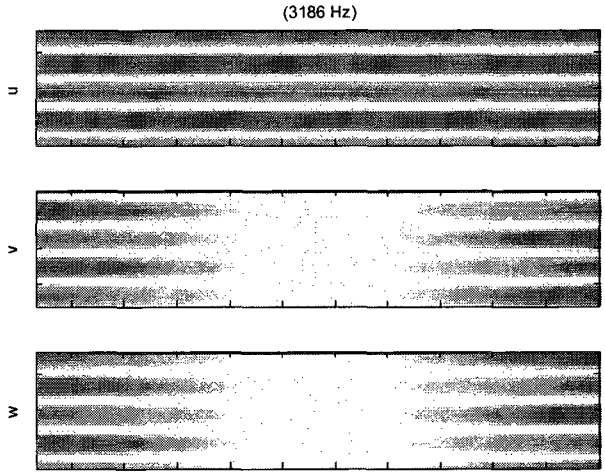

Figure 5.10: Mode shape associated with $n = 2$ using finite element analysis (ABAQUS)

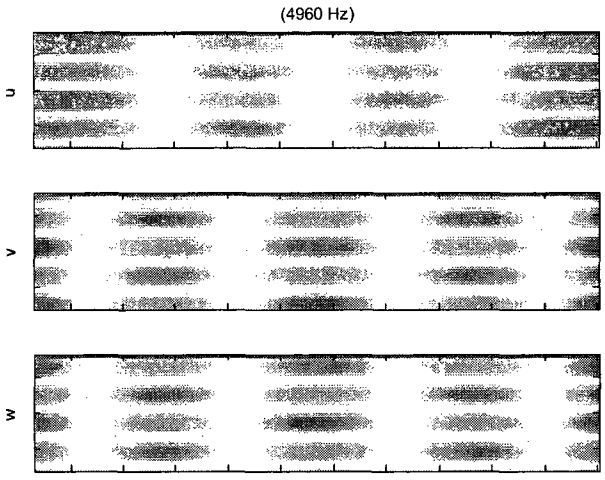

Figure 5.11: Mode shape associated with $n = 2$ using finite element analysis (ABAQUS)

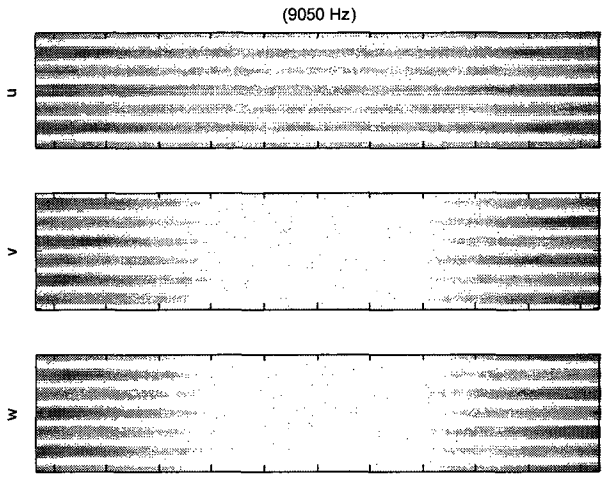

Figure 5.12: Mode shape associated with $n = 3$ using exact numerical solution

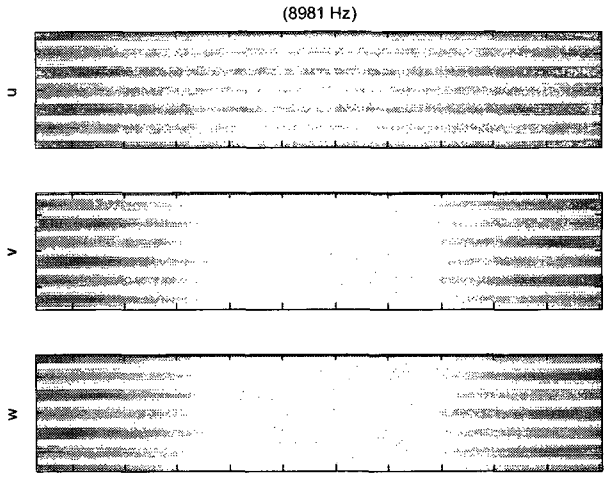

Figure 5.13: Mode shape associated with $n = 3$ using finite element analysis (ABAQUS)

Table 5.4: Properties of the orthotropic cylinder

Length	$7.5\ in$
Thickness	$0.0169\ in$
Radius	$0.3642\ in$
Lay up	[90 0 90 90 0 90]
$E11$	$4.3e^7\ Psi$
$E22$	$8.2e^5\ Psi$
$G12$	$7.0e^5\ Psi$
$NU12$	0.25
ρ (Density)	$1.50104e^{-4}\ (slug/in^3)$

Table 5.5: Natural frequencies of orthotropic cylinder using numerical method for solving equilibrium and boundary conditions, compared with finite element analysis

n	f(Hz)	f(Hz) (ABAQUS)	% error
1	3985	3987	0.0
1	7652	7657	0.0
1	11333	11342	0.0
2	7280	7138	2.0
2	7431	7289	1.9
2	8104	7976	1.6
2	10984	10904	0.7
3	20599	19734	4.3

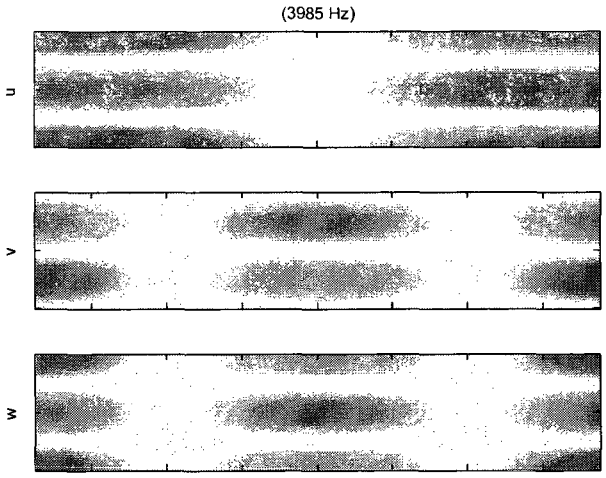

Figure 5.14: Mode shape associated with $n = 1$ using exact numerical solution for orthotropic cylinder

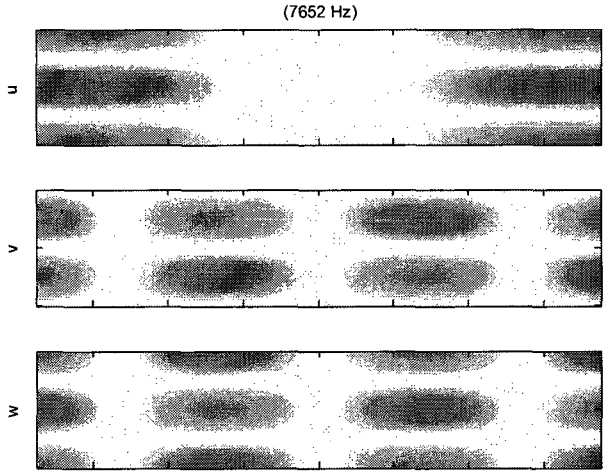

Figure 5.15: Mode shape associated with $n = 1$ using exact numerical solution for orthotropic cylinder

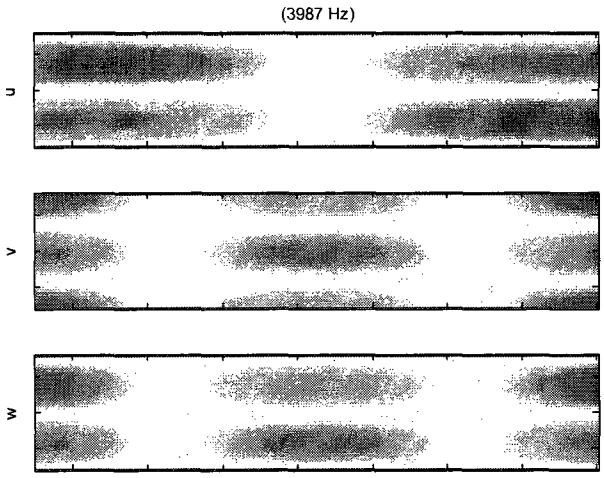

Figure 5.16: Mode shape associated with $n = 1$ using finite element analysis (ABAQUS) for orthotropic cylinder

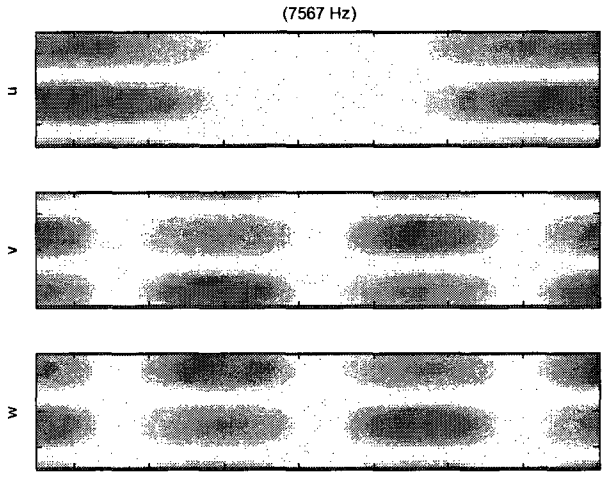

Figure 5.17: Mode shape associated with $n = 1$ using finite element analysis (ABAQUS) for orthotropic cylinder

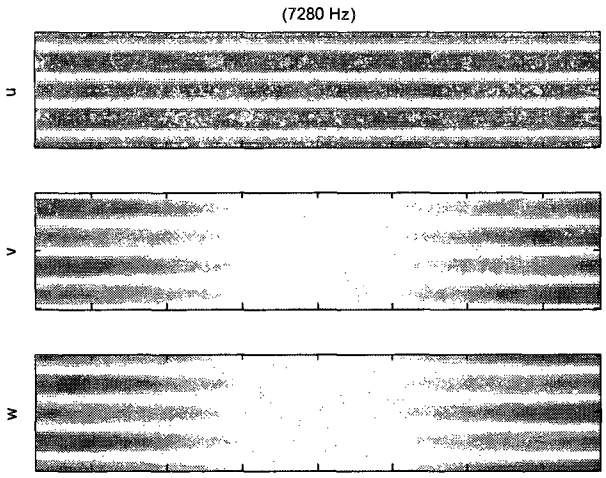

Figure 5.18: Mode shape associated with $n = 2$ using exact numerical solution for orthotropic cylinder

analysis results.

5.3.2 Approximate solution using Rayleigh-Ritz technique

It is noted that the only approximations in equations (5.21)-(6.8) are the approximations in the strain-displacement relations of the shell theory. The only problem in the numerical approach based on these equations is that numerically finding some of the solutions, η, is difficult. Hence approximate methods are often used for finding the natural frequencies and mode shapes of cylinders. One method is to use the Fourier series expansions for the

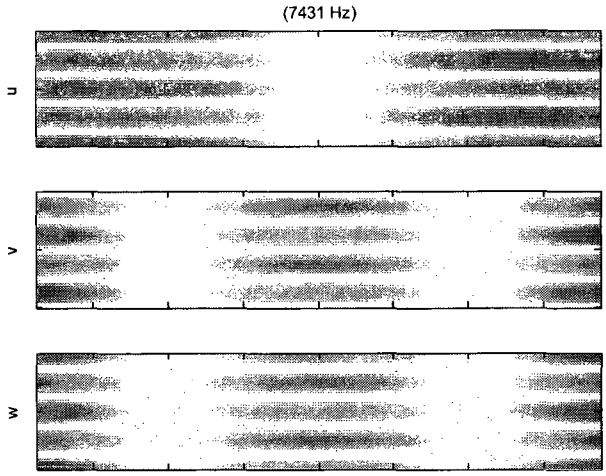

Figure 5.19: Mode shape associated with $n = 2$ using exact numerical solution for orthotropic cylinder

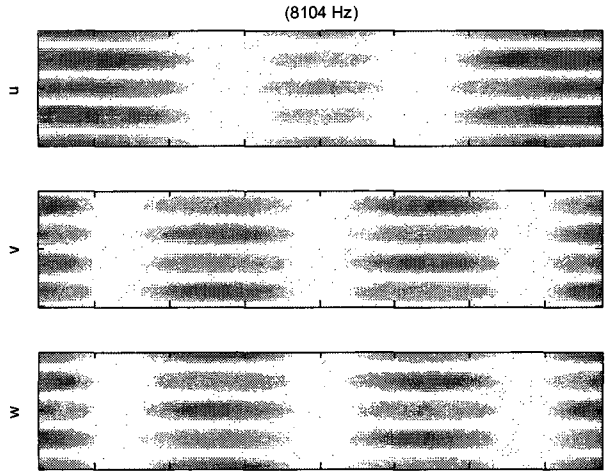

Figure 5.20: Mode shape associated with $n = 2$ using exact numerical solution for orthotropic cylinder

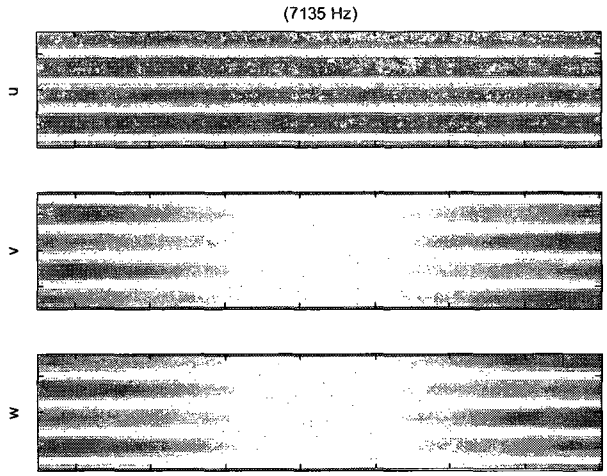

Figure 5.21: Mode shape associated with $n = 2$ using finite element analysis (ABAQUS) for orthotropic cylinder

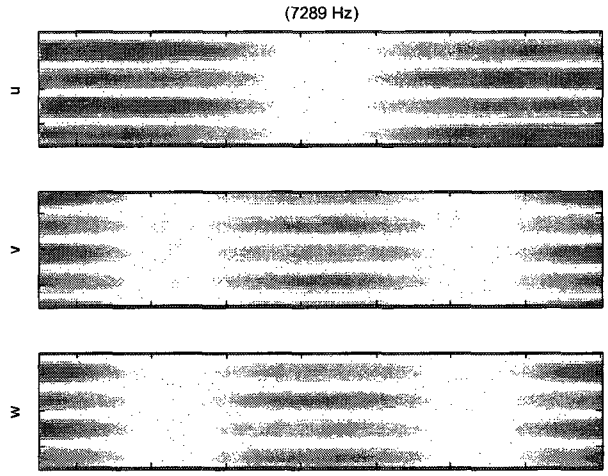

Figure 5.22: Mode shape associated with $n = 2$ using finite element analysis (ABAQUS) for orthotropic cylinder

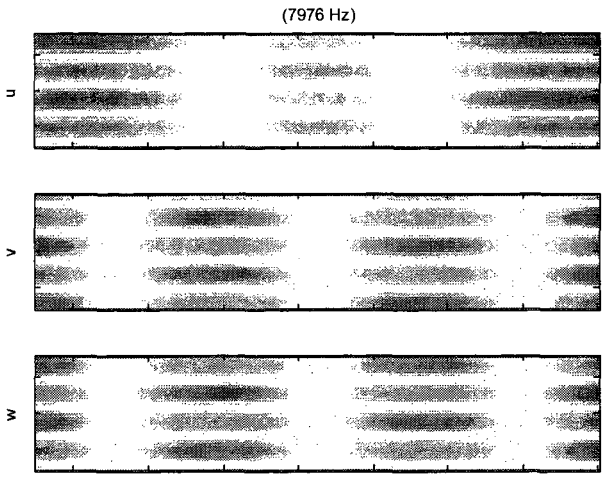

Figure 5.23: Mode shape associated with $n = 2$ using finite element analysis (ABAQUS) for orthotropic cylinder

longitudinal dependence of mode shapes. Here the approximation arises from the truncation of this series. It is noted that no truncation is performed in the numerical method explained in section 5.3.1.1 and the solutions obtained from the dispersion relation and boundary conditions equations in (5.21)-(6.8) are exact and the only approximation is due to the root finding procedure in numerically determining η. The most commonly used approximate technique to compute the natural frequencies and mode shapes of the cylinder is the Rayleigh-Ritz technique. In the simplest form of this approach, one writes the modal displacements as the product of two appropriately defined functions, one in the axial coordinate and the other in the circumferential coordinate. These functions are chosen such that they satisfy the boundary conditions. The case of simply supported cylinders is the

most straight forward because trigonometric functions can be used in both directions. If we denote m and n as the wave numbers in the axial and circumferential directions, then we have:

$$\begin{aligned} u_{mn} &= A_{mn} \cos \frac{m\pi x}{L} \cos n\theta e^{i\omega_{mn}t} \\ v_{mn} &= B_{mn} \sin \frac{m\pi x}{L} \sin n\theta e^{i\omega_{mn}t} \\ w_{mn} &= C_{mn} \cos \frac{m\pi x}{L} \cos n\theta e^{i\omega_{mn}t} \end{aligned} \tag{5.28}$$

where u_{mn}, v_{mn}, and u_{mn} are the modal displacements in axial, circumferential and radial directions. The coefficients A_{mn}, B_{mn} and C_{mn} are the amplitudes of the modal displacements in each direction. For each pair of wave numbers, m and n, the amplitudes A_{mn}, B_{mn} and C_{mn} as well as the natural frequencies ω_{mn} must be evaluated. As noted in section 5.1, Sharma and Darvizeh [1987], Sharma and Johns [1971] have shown how this can be done using the Rayleigh-Ritz technique.

For the free-free cylinder, a slightly more complicated function is needed for the longitudinal component. The typical procedure is to use a two-term truncated series expansion for this longitudinal function. The form for this function is obtained using beam-like modes. This results in solutions with surprisingly good accuracy particularly for longer shells. Furthermore if the shell is very long ($L/mR > 8$) then classical beam theory may be used for finding the $n = 1$ mode shapes of the cylinder. In the next section we review the derivations of mode shapes for a free-free Euler-Bernoulli beam. These mode shapes are then used in the Rayleigh-Ritz method as explained above.

5.3.2.1 Mode shapes of a free-free Euler-Bernoulli beam

The equation of motion for an Euler-Bernoulli beam with mass per unit length m and constant flexural rigidity EI can be written as:

$$EI\frac{\partial^4 w}{\partial x^4} + m\frac{\partial^2 w}{\partial t^2} = 0$$

If the beam is free at both ends the boundary conditions can be expressed as:

$$M = EI\frac{\partial^2 w}{\partial x^2} = 0, \quad V = -EI\frac{\partial^3 w}{\partial x^3} = 0$$

at $x = 0, L$, where M and V are the bending moment and vertical shear force. The j^{th} mode shape can be written as:

$$\phi_j = \sum_k C_{kj} e^{\lambda_{kj} x}$$

Therefore, the dispersion relationship between the frequency and wavenumber is:

$$\lambda^4 - \frac{m\omega_j^2}{EI} = 0 \tag{5.29}$$

If $s_j = \sqrt[4]{m\omega_j^2/EI}$, then the solutions to the above equation are $\pm s_j$ and $\pm i s_j$, and one can write:

$$\phi_j = C_1 \sin s_j x + C_2 \cos s_j x + C_3 \sinh s_j x + C_4 \cosh s_j x \tag{5.30}$$

Let $\lambda_j = s_j L$, then substituting the above equation into the boundary conditions one can write:

$$\begin{bmatrix} 0 & -1 & 0 & 1 \\ -1 & 0 & 1 & 0 \\ -\sin\lambda_j & -\cos\lambda_j & \sinh\lambda_j & \cosh\lambda_j \\ -\cos\lambda_j & +\sin\lambda_j & \cosh\lambda_j & \sinh\lambda_j \end{bmatrix} \begin{bmatrix} C_1 \\ C_2 \\ C_3 \\ C_4 \end{bmatrix} e^{\lambda x} = 0 \tag{5.31}$$

Table 5.6: Frequency number $\lambda_j = L\sqrt[4]{m\omega_j^2/EI}$ for free-free beam for the first 5 modes

j	λ_j
1	4.73004074
2	7.85320462
3	10.9956078
4	14.1371655
5	17.2787597

In order to have non-trivial solutions for the above equations the determinant of the matrix must be zero which results in the following equation:

$$\cos\lambda_j \cosh\lambda_j = 1$$

Solving the above equation numerically, the wavenumbers λ_j are evaluated. The first five wavenumbers are shown in Table 5.6. Once the wave numbers are obtained the unknown coefficients C_j for mode shapes are determined using equation (5.31). Finally, the j^{th} natural frequency is $\omega_j = \sqrt{\lambda_j EI/mL}$ and the j^{th} mode shape $\phi_j(x)$ is obtained from equation (5.30):

$$\phi_j = \cos\frac{\lambda_j x}{L} + \cosh\frac{\lambda_j x}{L} - \frac{\cosh\lambda_j - \cos\lambda_j}{\sinh\lambda_j - \sin\lambda_j}\left(\sinh\frac{\lambda_j x}{L} + \sin\frac{\lambda_j x}{L}\right) \tag{5.32}$$

5.3.2.2 Frequencies and mode shapes of a free-free composite cylinder

As explained in section 5.3.2 in the approximate method one must assume the mode shapes. It has been shown that the beam mode shapes can be used instead of the trigonometric terms in equation (5.28) for the dependence in the longitudinal axis. The solution to the equations of motion can be written as [Sharma and Darvizeh, 1987, Blevins, 1979]:

$$\begin{aligned} u_{mn} &= A_{mn}\phi'_m(x)\cos n\theta e^{i\omega_{mn}t} \\ v_{mn} &= B_{mn}\phi_m(x)\sin n\theta e^{i\omega_{mn}t} \\ w_{mn} &= C_{mn}\phi_m(x)\cos n\theta e^{i\omega_{mn}t} \end{aligned} \tag{5.33}$$

where ϕ_m is m^{th} beam mode shape given in the equation (5.32) and, as before, ω_{mn} is the natural frequency associated with the longitudinal wavenumber m and circumferential wavenumber n. The first step of the Rayleigh-Ritz technique is to calculate the kinetic and potential energy. The unknown coefficients A_{mn}, B_{mn} and C_{mn} are then obtained by minimizing the total energy. Substituting equation (5.33) into the strain relations yields:

$$e_x = (\frac{\lambda_m}{L})\left(A_{mn} - (\frac{\lambda_m}{L})zC_{mn}\right)\phi''_m(x)\cos n\theta e^{i\omega t}$$

$$e_\theta = \frac{1}{1+\frac{z}{R}}\left(\frac{nB_{mn}}{R} + \frac{C_{mn}}{R} + \frac{nzB_{mn}}{R^2} + \frac{n^2zC_{mn}}{R^2}\right)\phi_m(x)\cos n\theta e^{i\omega t}$$

$$\gamma_{x\theta} = \frac{1}{1+\frac{z}{R}}\left((\frac{\lambda_m}{L})B_{mn} - \frac{nA_{mn}}{R} + (\frac{2z}{R}+\frac{z^2}{R^2})(\frac{\lambda_m}{L})(B_{mn}+nC_{mn})\right)\phi'_m(x)\sin n\theta e^{i\omega t}$$

The potential energy of the laminated composite cylinder is:

$$U = \int\int\int \overline{Q}_{11}e_x^2 + \overline{Q}_{22}e_\theta^2 + \overline{Q}_{66}\gamma_{x\theta}^2 + 2\left(\overline{Q}_{12}e_xe_\theta + \overline{Q}_{16}e_x\gamma_{x\theta} + \overline{Q}_{26}e_\theta\gamma_{x\theta}\right)R(1+\frac{z}{R})d\theta dxdz$$

and the kinetic energy is:

$$T = \frac{1}{2}\int\int\int \rho\left(\dot{u}^2 + \dot{v}^2 + \dot{w}^2\right) R(1 + \frac{z}{R})d\theta dx dz$$

The set of equations in (5.33) are now substituted in the expression for total energy:

$$\Pi = U + T$$

and the total energy is minimized by taking the derivatives with respect to the unknown coefficients:

$$\frac{\partial \Pi}{\partial A_{mn}} = 0, \quad \frac{\partial \Pi}{\partial B_{mn}} = 0, \quad \frac{\partial \Pi}{\partial C_{mn}} = 0$$

This leads to a homogeneous system of linear equations in the unknown coefficients:

$$\begin{pmatrix} a_{11} - \alpha_2\Omega^2 & a_{12} & a_{13} \\ a_{12} & a_{22} - \Omega^2 & a_{23} \\ a_{13} & a_{23} & a_{33} - \Omega^2 \end{pmatrix} \begin{pmatrix} A_{mn} \\ B_{mn} \\ C_{mn} \end{pmatrix} = 0 \tag{5.34}$$

where

$$\Omega^2 = \omega^2 \rho_t R^2$$

and:

$$a_{11} = (\frac{\lambda_m}{L})^2 \left(A_{11}R^2 + B_{11}R\right) + n^2\alpha^2 \left(A_{66} - \frac{B_{66}}{R} + \frac{D_{66}}{R^2}\right)$$

$$a_{12} = n(\frac{\lambda_m}{L}) \left((A_{12}R + B_{12})\alpha 1 - (A_{66}R + B_{66})\alpha 2\right)$$

$$a_{13} = n(\frac{\lambda_m}{L}) \left(-(\frac{\lambda_m}{L})^2(B_{11}R^2 + D_{11}R) - n^2(2B_{66}R - \frac{D_{66}}{R})\alpha 2 + (n^2B_{12} + A_{12}R)\alpha 1\right)$$

$$a_{22} = n^2A_{22} + \frac{n^2}{R}B_{22} + (\frac{\lambda_m}{L})^2 \left(A_{66}R^2 + 3B_{66}R + 3D_{66}\right)\alpha 2$$

$$a_{23} = nA_{22} + \frac{n^3}{R}B_{22} + (\frac{\lambda_m}{L})^2 n \left((2B_{66}R + 3D_{66})\alpha 2 - (B_{12}R + D_{12})\alpha 1\right)$$

$$a_{33} = (\frac{\lambda_m}{L})^4 D_{11}R^2 + A_{22} + \frac{(2n^2-1)B_{22}}{R} + \frac{(1-n^2)^2 D_{22}}{R^2}$$

$$+ (\frac{\lambda_m}{L})^2 \left(4nD_{66}\alpha_2 - (B_{12}R + n^2D_{12})2\alpha_1\right)$$

$$\alpha_1 = \frac{1}{L}\int \phi''\phi dx, \qquad \alpha_2 = \frac{1}{L}\int (\phi')^2 dx$$

To have a nontrivial solution for the above equation the determinant of the 3×3 matrix in equation (5.34) must be zero. This yields a cubic equation in Ω^2. Only the positive roots are retained. Therefore, associated with each pair of wave numbers m and n, three natural frequencies and three sets of mode shapes can be determined. These three modes generally correspond to motions which are predominantly radial, circumferential and axial.

5.3.2.3 Numerical result

Here the two examples in section 5.3.1.1 are considered. For the isotropic example, the natural frequencies obtained using the Rayleigh-Ritz method are compared with the finite element results in Table 5.7. The mode shapes for the first modes associated with circumferential wavenumbers $n = 1, 2$ and 3 are also shown in Figures 5.24 - 5.28. The

Table 5.7: Natural frequencies of copper pipe using the the approximate energy method

n	m	f (Hz) (energy)	f (Hz) (ABAQUS)	% error
1	1	2171	2103	3.2
1	2	5416	5218	3.8
2	0	3164	3178	0.4
2	0	3177	3186	0.3
2	1	3308	3310	0.0
2	2	3833	3820	0.3
2	3	5009	4960	1.0
3	0	8966	8981	0.2

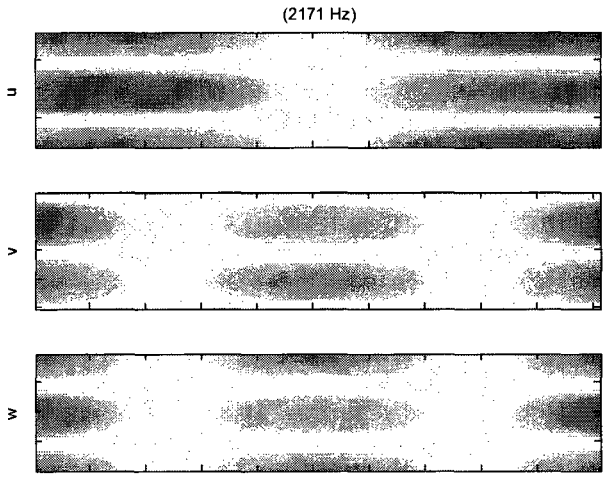

Figure 5.24: Mode shape associated with $n = 1$ using Rayleigh-Ritz method

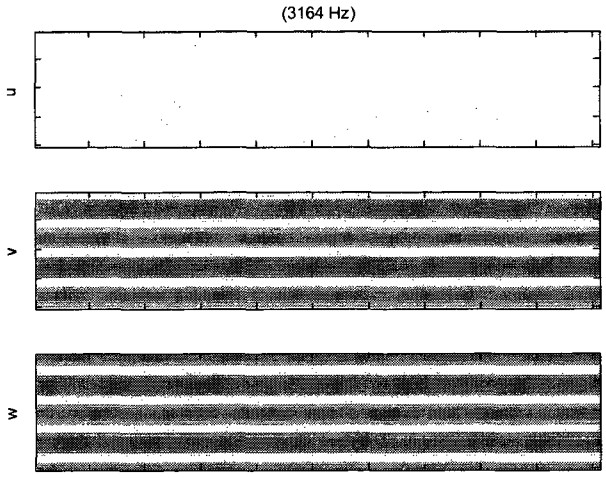

Figure 5.25: Mode shape associated with $n = 2$ using Rayleigh-Ritz method

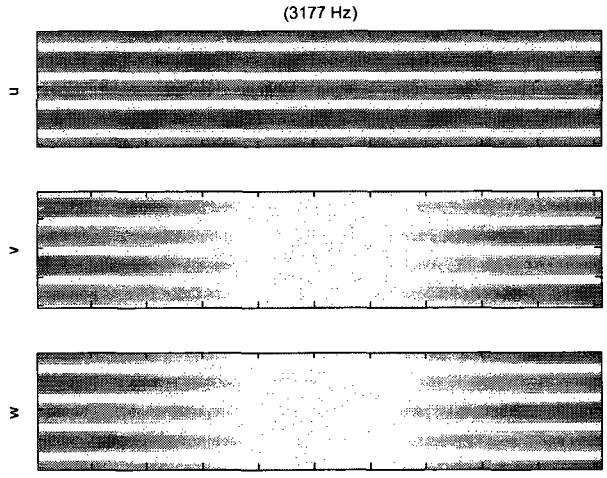

Figure 5.26: Mode shape associated with $n = 2$ using Rayleigh-Ritz method

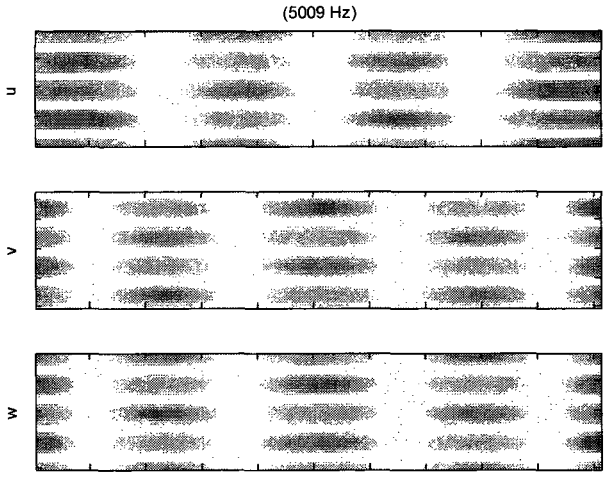

Figure 5.27: Mode shape associated with $n = 2$ using Rayleigh-Ritz method

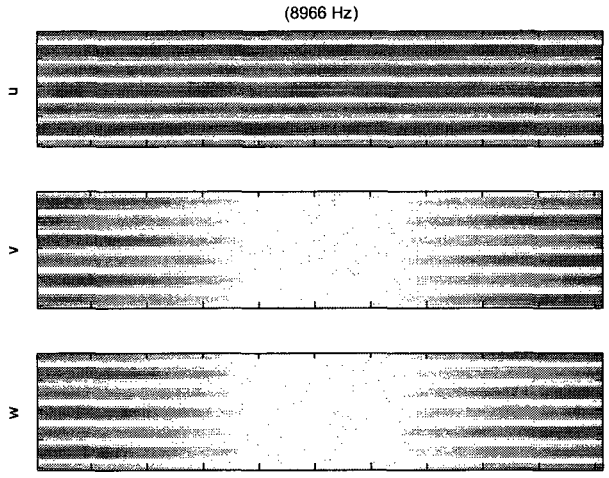

Figure 5.28: Mode shape associated with $n = 3$ using Rayleigh-Ritz method

Table 5.8: Natural frequencies of thin, balanced and symmetric laminate with properties shown in Table 5.4

n	m	f (Hz) (energy)	f (Hz) (ABAQUS)	% error
1	1	4129	3987	3.6
1	2	8459	7657	10.5
1	3	12442	11342	9.7
2	0	7284	7135	2.1
2	0	7281	7138	2
2	1	7436	7289	2
2	2	8183	7976	2.6
2	3	9603	9257	3.7
2	4	11409	10904	4.6
2	5	13382	12748	5.0
3	0	20603	19734	4.4

Rayleigh-Ritz method was also used to analysis the orthotropic cylinder example and the results for the natural frequencies and mode shapes are shown in Table 5.8 and Figures 5.29 - 5.33.

Tables 5.7 and 5.8 show that the natural frequencies obtained by the Rayleigh-Ritz method are accurate. However, a comparison of mode shapes in Figures 5.24 - 5.30 with the corresponding mode shapes in Figures 5.4 - 5.23 obtained by equations (5.21) -(6.8)

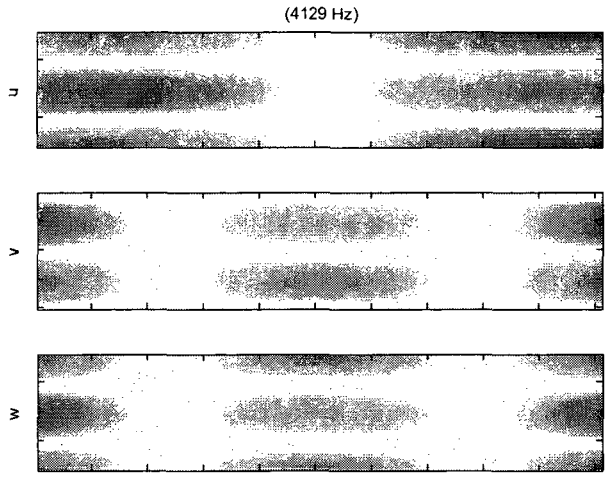

Figure 5.29: Mode shape associated with $n = 1$ using Rayleigh-Ritz method for orthotropic cylinder

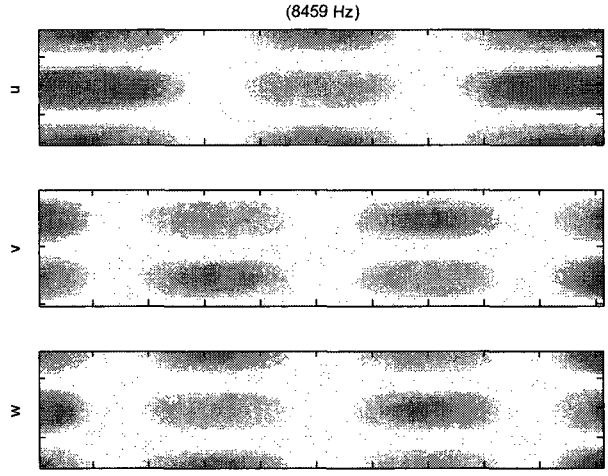

Figure 5.30: Mode shape associated with $n = 1$ using Rayleigh-Ritz method for orthotropic cylinder

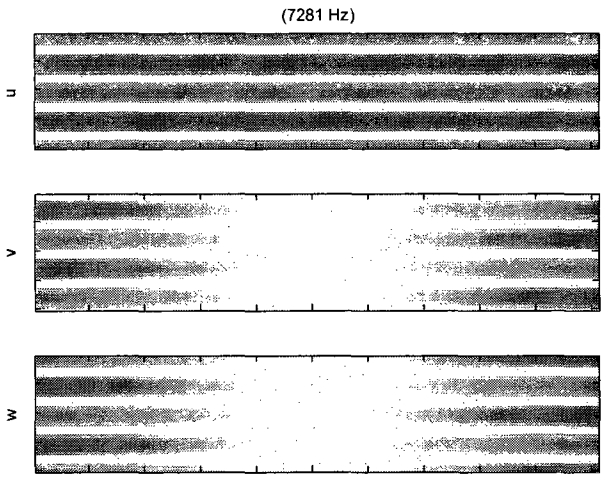

Figure 5.31: Mode shape associated with $n = 2$ using Rayleigh-Ritz method for orthotropic cylinder

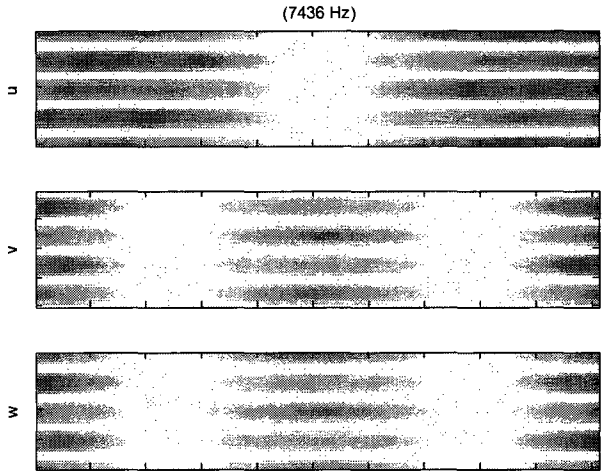

Figure 5.32: Mode shape associated with $n = 2$ using Rayleigh-Ritz method for orthotropic cylinder

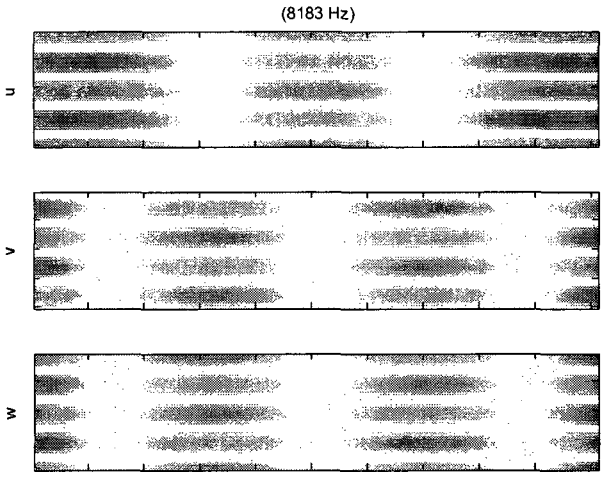

Figure 5.33: Mode shape associated with $n = 2$ using Rayleigh-Ritz method for orthotropic cylinder

and finite element analysis reveals some inaccuracy of the Rayleigh-Ritz procedure, particularly near the boundaries. This is clearly seen by comparing Figure 5.25 with Figures 5.6 and 5.9 for the first mode associated with the circumferential wavenumber $n = 2$ of the isotropic cylinder. The basic reason for this discrepancy is that the beam modes used in the longitudinal components of the mode shapes do not precisely satisfy the three dimensional boundary conditions. This leads to nonzero stresses at the edges of the cylinder.

A more closer look at the stress distribution of the mode shapes at the free ends reveals very rapid variation of the stresses and strains in longitudinal direction as shown in Figures 5.34 and 5.35 for the first mode shape associated with the circumferential wavenumber $n = 2$ of the isotropic cylinder. This is denoted as the edge effect. The beam mode shapes

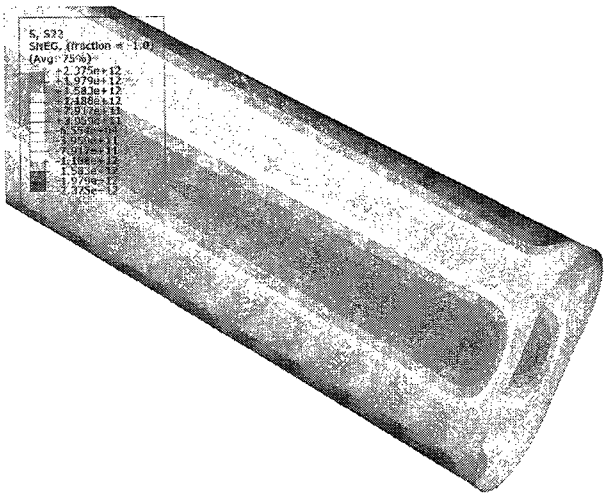

Figure 5.34: Stresses at the edge of cylinder for the first mode shape

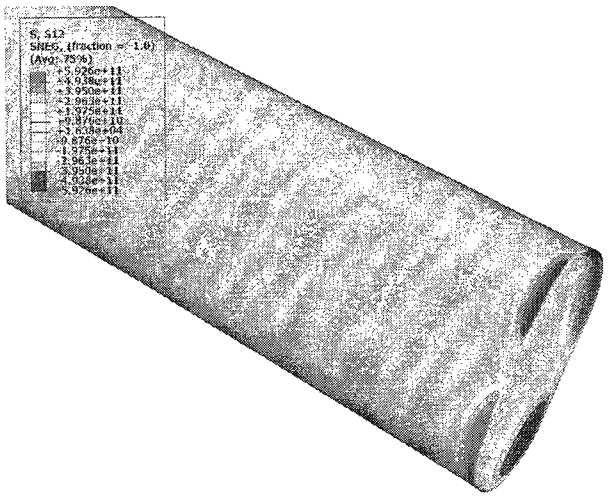

Figure 5.35: Stresses at the edge of cylinder for the first mode shape

used in the Rayleigh-Ritz method do not include this effect. The edge effect is difficult to analyze, because even if Fourier series expansions are used to approximate the mode shapes in the longitudinal direction, a large number of terms is needed to model the displacement variation near the edge.

Chapter 6

Perturbation analysis of the modal properties of composite cylinders

In chapter 5, the mode shapes and natural frequencies of composite cylinders were obtained either by combining the dispersion relation with the equations for the boundary condition or by a Rayleigh-Ritz technique. In both approaches, numerical analysis was used to obtain the modal properties. While such numerical procedures are generally useful, they do not provide a deep understanding of the vibration behavior of cylindrical shells. In this chapter, perturbation analysis is used to derive analytical results that describe the free vibration of cylinders. These results are in terms of relatively simple closed-form mathematical expressions that provide insight in cylinder vibration behavior. It is shown that these expressions are also useful for system identification, where free-vibration measurements are used to determine the elastic properties of the cylinder.

CHAPTER 6.

In cylindrical shells, the equations of motion and boundary conditions are complex even for the isotropic case and become considerably more complicated when considering composite laminate material properties. The essence of the perturbation analysis as developed herein is to focus on the dominant characteristics of the vibration problem and to eliminate all terms that are of secondary importance in the derivations of the modal properties.

In this chapter the focus is on cylindrical shells with either isotropic or orthotropic material properties. Some results are also derived for the more general case of symmetric, balanced composite laminates. The perturbation analysis begins by reducing the intractable eighth-order characteristic equation for the dispersion relation into decoupled bi-quadratic forms. These bi-quadratic forms lead to relatively simple closed-form analytical expressions for the wavelength as a function of natural frequency and the cylinder material properties. Perturbation is used to derived simplified results for the internal forces and moments. These results are used in the boundary conditions to arrive at the final analytical expressions for the natural frequencies and mode shapes.

Closed form results for the dispersion and modal properties have been previously derived for canonical structures such as beams, plates and isotropic, simply supported cylinders. The results in this chapter for orthotropic free-free cylinders are new. The chapter concludes with some remarks on how the results can be used for system identification and on extensions to more general composite materials.

6.1 Framework of the perturbation analysis

Before beginning the perturbation analysis of the cylinder vibration problem, it is necessary to define some additional notation and to very briefly outline the perturbation process. The essence of this process is to express the analytics in a manner such that small terms can be separated from the relatively large terms. This implies that every term should be non-dimensional, so that small would always mean small in comparison with unity.

In perturbation theory, it is convenient to use the big O and small o (Landau) notation. If ϵ is small compared with unity then we use the notation $O(\epsilon)$ for terms that are of the same order of magnitude as ϵ and $o(\epsilon)$ for terms that are at least an order of magnitude smaller than ϵ. For instance, we have:

$$\frac{1}{1+\epsilon} = 1 - \epsilon + \epsilon^2 - \epsilon^3 + \cdots = 1 - \epsilon + o(\epsilon) = 1 + O(\epsilon) \tag{6.1}$$

$$\sqrt{1+\epsilon} = 1 + \frac{\epsilon}{2} + o(\epsilon) = 1 + O(\epsilon) \tag{6.2}$$

In perturbation theory terminology, the zeroth-order expressions are those which involve only the largest terms, typically of order 1, or $O(1)$. The first-order expressions typically involve terms of order $O(\epsilon)$, the second-order expressions involve terms of order $O(\epsilon^2)$ and so on. Hence, the first- and second-order approximations to $1/(1+\epsilon)$ are $1+\epsilon$ and $1+\epsilon-\epsilon^2$.

For the cylinder problem, we begin with the following non-dimensional parameters:

$$\widetilde{h} = \frac{h}{R}$$
$$\widetilde{x} = \frac{x}{R}$$
$$\widetilde{A}_{ij} = \frac{A_{ij}}{A_{22}}$$
$$\widetilde{D}_{ij} = \frac{D_{ij}}{A_{22}R^2}$$
$$\widetilde{N} = \frac{N}{A_{22}}$$
$$\widetilde{M} = \frac{M}{A_{22}R}$$
$$\widetilde{\eta} = \frac{\eta}{A_{22}R^2}$$
$$\widetilde{\lambda} = \lambda R$$
$$\widetilde{L} = \frac{L}{R}$$

To gain some insight into these newly defined parameters, we consider the isotropic case. We have:

$$\widetilde{A}_{11} = 1, \quad \widetilde{A}_{12} = \nu, \quad \widetilde{A}_{66} = \frac{1-\nu}{2}, \quad \widetilde{A}_{16} = \widetilde{A}_{26} = 0$$
$$\widetilde{D}_{11} = \frac{h^2}{12R^2}, \quad \widetilde{D}_{12} = \nu\frac{h^2}{12R^2}, \quad \widetilde{D}_{66} = \frac{1-\nu}{2}\frac{h^2}{12R^2}, \quad \widetilde{D}_{16} = \widetilde{D}_{26} = 0$$

Herein we examine thin shells where $h \ll R$, so that $\widetilde{D}_{ij}$ are all small. Our perturbation parameter is $\epsilon = \sqrt{h/R}$ so that $\widetilde{D}_{ij} = O(\epsilon^4)$. As a numerical example, we have, for the

copper and orthotropic examples, the following forms for the matrices $\widetilde{A}$ and $\widetilde{D}$:

$$\widetilde{A}_{copper} = \begin{bmatrix} 1 & 0.340 & 0 \\ 0.340 & 1 & 0 \\ 0 & 0 & 0.330 \end{bmatrix}$$

$$\widetilde{D}_{copper} = \begin{bmatrix} 0.413 & 0.140 & 0 \\ 0.140 & 0.413 & 0 \\ 0 & 0 & 0.136 \end{bmatrix} 10^{-3}$$

$$\widetilde{A}_{orthotropic} = \begin{bmatrix} 8.260 & 1.667 & 0 \\ 1.667 & 1 & 0 \\ 0 & 0 & 1.808 \end{bmatrix}$$

$$\widetilde{D}_{orthotropic} = \begin{bmatrix} 1.409 & 0.333 & 0 \\ 0.333 & 0.196 & 0 \\ 0 & 0 & 0.358 \end{bmatrix} 10^{-3}$$

For notational simplicity, we drop the tilde notation in the remainder of this chapter.

Next we restate the equilibrium equations and boundary conditions using the above non-dimensional form for the parameters. The equations of equilibrium in (5.21) can be expressed as:

$$\begin{bmatrix} E_{11} & E_{12} & E_{13} \\ E_{12} & E_{22} & E_{23} \\ E_{12} & E_{23} & E_{33} \end{bmatrix} \begin{bmatrix} \alpha \\ \beta \\ 1 \end{bmatrix} = 0$$

where

$$
\begin{aligned}
E_{11} &= A_{11}\lambda^2 + 2in\lambda A_{16} - n^2 A_{66} + \eta \\
E_{12} &= A_{16}\lambda^2 + in\lambda\left(A_{12} + A_{66}\right) - n^2 A_{26} \\
E_{13} &= A_{12}\lambda + inA_{26} \\
E_{22} &= \left(A_{66} + 4D_{66}\right)\lambda^2 + 2in\lambda\left(A_{26} + 2D_{26}\right) - n^2\left(1 + D_{22}\right) + \eta \\
E_{23} &= \lambda A_{26} + in - in\lambda^2\left(D_{12} + 4D_{66}\right) - 2\lambda^3 D_{16} + 4n^2\lambda D_{26} + in^3 D_{22} \\
E_{33} &= 1 - 2n^2\lambda^2\left(D_{12} + 2D_{16} + 2D_{66}\right) + n^4 D_{22} - 4in^3\lambda D_{26} + \lambda^4 D_{11} - \eta
\end{aligned}
\tag{6.3}
$$

This is a generalized eigenvector problem that yields displacement components α and β and longitudinal wave number λ for each frequency parameter η.

To find the dispersion relation between λ_j and η_j the determinant of the matrix E is set to zero, leading to an eighth-order equation in λ. For a symmetric and balanced laminate where $B = 0$ and $A_{16} = A_{26} = 0$, this equation is:

$$
\begin{aligned}
&A_{11}\left(-4D_{16}^2 + D_{11}d_6\right)\lambda^8 + 4iA_{11}\left(-D_{16}d_5 + nD_{11}D_{26}\right)\lambda^7 + \\
&\left(A_{11}m_1 + D_{11}\left(d_8^2 + d_6d_7\right) - 4d_7D_{16}^2\right)\lambda^6 + \\
&4i\left(D_{16}\left(A_{11}d_4 - A_{12}d_8 - d_5d_7\right) + nD_{26}A_{11}m_5 + nD_{11}D_{26}d_7\right)\lambda^5 + \\
&\left(-A_{12}\left(A_{12}d_6 - 2d_5d_8\right) - d_3d_8^2 + A_{11}m_2 + d_7m_1\right)\lambda^4 + \\
&4i\left(D_{16}d_4d_7 + nD_{26}\left(A_{12}\left(-A_{12} + 2nd_8\right) + A_{11}m_3 + d_7m_5 - n^2d_8^2\right)\right)\lambda^3 + \\
&\left(A_{11}m_4 - A_{12}\left(A_{12}d_2 + 2d_4d_8\right) + d_1d_8^2 + d_7m_2\right)\lambda^2 + 4inD_{26}d_7m_3\lambda + d_7m_4
\end{aligned}
$$

where

$$d_1 = 1 + D_{22}n^4 - \eta$$

$$d_2 = -\left(1 + D_{22}\right)n^2 + \eta$$

$$d_3 = 2n^2\left(D_{12} + 2D_{66} + 2D_{16}\right)$$

$$d_4 = n\left(n^2 D_{22} + 1\right)$$

$$d_5 = n\left(4D_{66} + D_{12}\right)$$

$$d_6 = A_{66} + 4D_{66}$$

$$d_7 = \eta - n^2 A_{66}$$

$$d_8 = \left(A_{12} + A_{66}\right)n$$

$$d_9 = 2n\left(A_{26} + 2D_{26}\right)$$

$$d_{10} = A_{26} + 4n^2 D_{26}$$

and

$$m_1 = d_5^2 - d_3 d_6 + 16n^2 D_{16} D_{26} + D_{11} d_2$$

$$m_2 = -d_2 d_3 + d_1 d_6 - 2d_4 d_5$$

$$m_3 = d_1 - 2n d_4 - n^2 d_2$$

$$m_4 = d_4^2 + d_1 d_2$$

$$m_5 = -d_3 + 2n d_5 - n^2 d_6$$

We recall from chapter 5, equation (5.20), that the general form for the mode shape is:

$$u = \sum_j C_j \alpha_j e^{\lambda_j x} e^{in\theta}, \quad v = \sum_j C_j \beta_j e^{\lambda_j x} e^{in\theta}, \quad w = \sum_j C_j e^{\lambda_j x} e^{in\theta} \tag{6.4}$$

To solve for the coefficients C_j, the boundary conditions must be satisfied. These boundary conditions are:

$$N_x = \sum_j \left(A_{11}\lambda_j\alpha_j + A_{12}\left(in\beta_j + 1\right) + A_{16}\left(\lambda_j\beta_j + in\alpha_j\right)\right) C_j e^{\pm\frac{\lambda_j L}{2}} = 0 \tag{6.5}$$

$$M_x = \sum_j \left(D_{11}^2\lambda_j^2 - nD_{12}\left(i\beta_j + n\right) - 2\lambda_j D_{16}\left(\beta_j - in\right)\right) C_j e^{\pm\frac{\lambda_j L}{2}} = 0 \tag{6.6}$$

$$N_{x\theta} - M_{x\theta}/R = \sum_j \left(A_{16}\lambda_j\alpha_j + A_{66}\left(\lambda_j\beta_j + in\alpha_j\right) - 2D_{16}\lambda_j^2 + \right.$$

$$\left. 4\lambda_j D_{66}\left(\beta_j - in\right) + A_{26}\left(in\beta_j + 1\right) + 2nD_{26}\left(i\beta_j + n\right)\right) C_j e^{\pm\frac{\lambda_j L}{2}} = 0 \tag{6.7}$$

$$Q = \sum_j \left(-D_{11}\lambda_j^3 + n\lambda_j\left(D_{12} + 4D_{66}\right)\left(i\beta_j + n\right) + 2\lambda_j^2 D_{16}\left(\beta_j - 2in\right) + \right.$$

$$\left. 2n^2 D_{26}\left(-\beta_j + in\right)\right) C_j e^{\pm\frac{\lambda_j L}{2}} = 0 \tag{6.8}$$

in which $\eta = \rho_T\omega^2/A_{22}R^2$, and $\rho_T = \int \rho dz$.

6.2 Dispersion

The perturbation analysis begins with the dispersion relation, the relation between the frequency parameter η and the longitudinal wavenumber parameter λ. We begin by examining numerical results for the dispersion relation using equations (6.3) before preceding to the analytical derivations. For the isotropic copper pipe example used in the previous

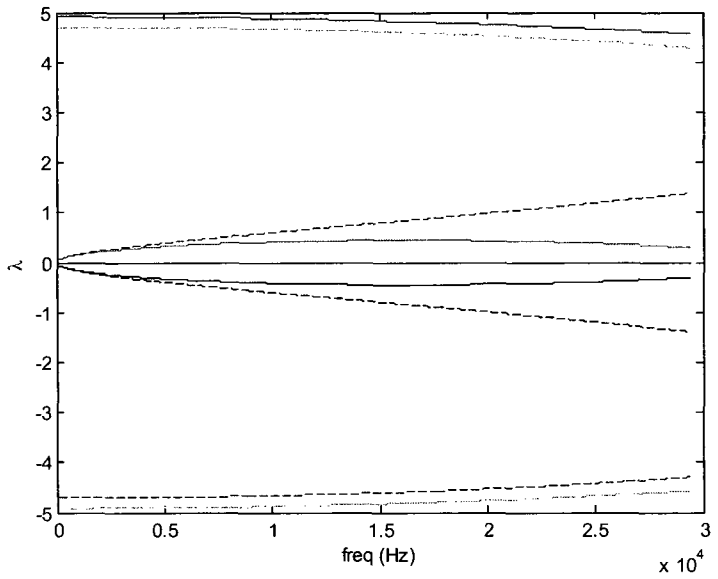

Figure 6.1: Exact λ_j versus frequency for circumferential mode $n = 1$, solid line: real part, dotted line: imaginary part

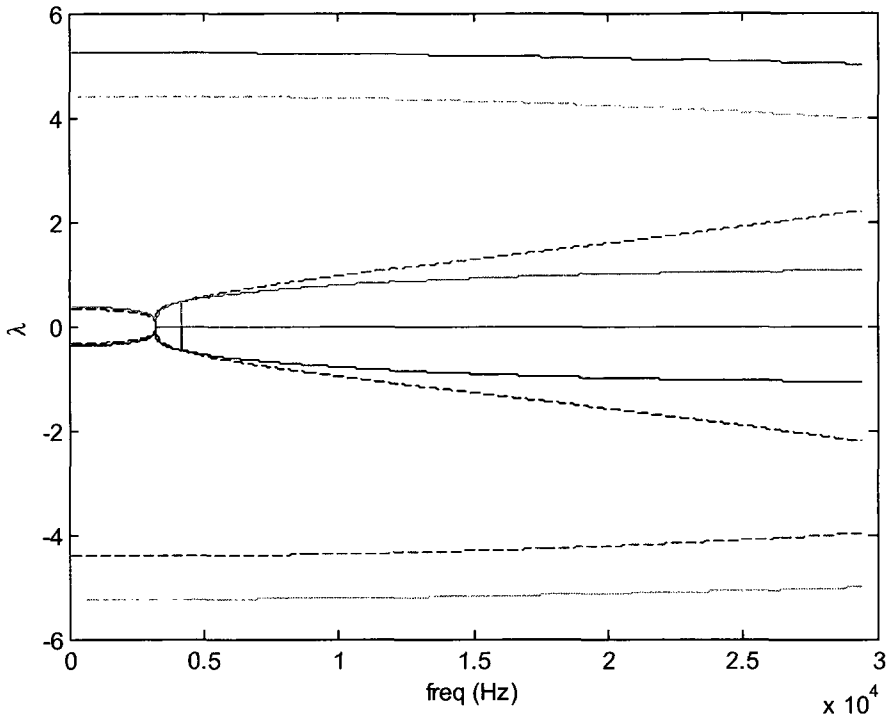

Figure 6.2: Exact λ_j versus frequency for circumferential mode $n = 2$, solid line: real part, dotted line: imaginary part

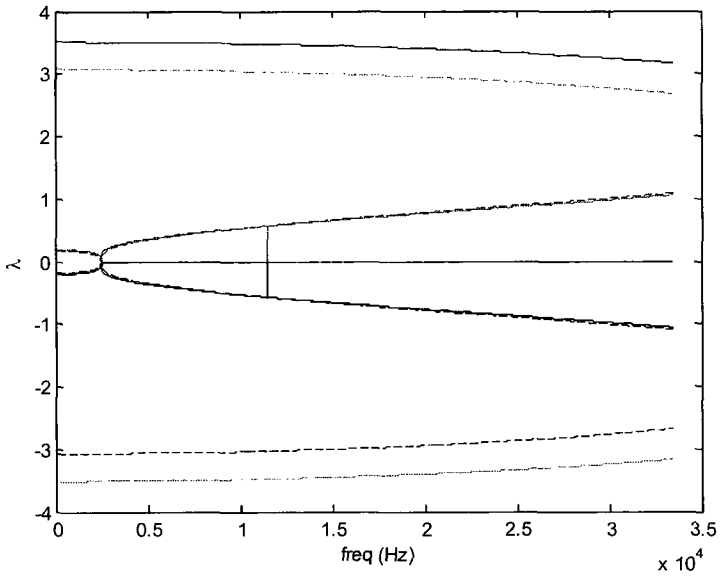

Figure 6.3: Exact λ_j versus frequency for circumferential mode $n = 2$, for orthotropic laminate, solid line: real part, dotted line: imaginary part

chapter, the dispersion relation is plotted in Figures 6.1 and 6.2 for circumferential wave numbers $n = 1, 2$. Figure 6.3 shows the exact dispersion for $n = 2$ for the orthotropic example. The solid lines in these figures show the real part and the dotted lines show the imaginary part of λ_j. It can be seen that the wavenumbers λ_j are in conjugate pairs and positive-negative pairs.

6.2.1 Perturbation analysis of the dispersion relation

There are two groups of λ_j: the first group which we denote as λ_{sj} are relatively small and correspond to relatively slowly varying displacements with respect to the longitudinal coordinate x. The second group, λ_{Lj}, are large and correspond to steep exponential variations in x. These two groups of λ_j can be seen in Figures 6.1 - 6.3.

For orthotropic laminates, we have $D_{16} = D_{26} = 0$ so that the coefficients of the characteristic equation are real. This immediately implies that the roots λ_j are in complex conjugate pairs. Furthermore, the odd powers of λ vanish for these laminates. Hence, if λ is a solution of the characteristic equation, then $-\lambda$ is also a solution. In summary, for each group of λ_j, there are four solutions of the form $\lambda_j = \pm\lambda_R \pm \lambda_I i$.

In this subsection, perturbation analysis is used to obtain explicit closed-form analytical expressions for the dispersion relation for both groups of λ_j. It can be seen in Figures 6.1 - 6.3 that the dispersion relations for the smaller λ_j begin at a point (η, λ) with $\lambda = 0$. This corresponds to the lowest natural frequency of an infinite cylinder vibrating with mode shapes that are constant with respect to the longitudinal coordinate, x. We begin

the perturbation analysis by obtaining analytical expressions for η at this critical natural frequency.

6.2.1.1 Case I: $\lambda = 0$

In this case the equilibrium equations in (5.21) reduce to:

$$\begin{bmatrix} \eta - n^2 A_{66} & 0 & 0 \\ 0 & -n^2 (D_{22} + 1) + \eta & in (1 + n^2 D_{22}) \\ 0 & in (1 + n^2 D_{22}) & 1 + n^4 D_{22} - \eta \end{bmatrix} \begin{bmatrix} \alpha \\ \beta \\ 1 \end{bmatrix} = 0$$

As described above, the solution to these equations correspond to the first set of mode shapes of an infinite cylinder. The modes associated with $\eta = n^2 A_{66}$ are shear modes with mode shapes given by in-plane shear motion: $u = \cos n\theta, v = 0, w = 0$. These modes have high natural with frequencies $\eta = O(1)$ and are not of interest herein. The remaining modes, with $\alpha = 0$, are determined by:

$$\begin{bmatrix} -n^2 (D_{22} + 1) + \eta & in (1 + n^2 D_{22}) \\ in (1 + n^2 D_{22}) & 1 + n^4 D_{22} - \eta \end{bmatrix} \begin{bmatrix} \beta \\ 1 \end{bmatrix} = 0$$

The dispersion relation obtained by setting the determinant of the above matrix to zero is:

$$-\eta^2 + \left(n^2 + 1\right) \left(1 + n^2 D_{22}\right) \eta - n^2 D_{22} \left(n^2 - 1\right)^2 = 0$$

The solution to this quadratic is:

$$\eta = \frac{\left(n^2 + 1\right) \left(1 + n^2 D_{22}\right) \pm \sqrt{\left(n^2 + 1\right)^2 \left(1 + n^2 D_{22}\right)^2 - 4n^2 D_{22} \left(n^2 - 1\right)^2}}{2}$$

$$\approx \frac{\left(n^2 + 1\right)}{2} \left[n^2 D_{22} + 1 - \sqrt{1 + \left(-4n^2 \left(\frac{n^2 - 1}{n^2 + 1} \right)^2 + 2n^2 \right) D_{22}} \right]$$

where we are only interested in the low frequency mode. We recall from equations (5.14) that the D components of the stiffness matrix are of order $O(\epsilon^4)$ and therefore are small compared to the A matrix components which are of order one. Hence, the radical in the above can be approximated by the first two terms in the Taylor series expansion, as noted in equation (6.2), resulting in the following first-order approximation for η, which we donate as η_0:

$$\eta_0 = \frac{n^2 \left(n^2-1\right)^2 D_{22}}{\left(n^2+1\right)} \tag{6.9}$$

which is of order $O(\epsilon^4)$. The corresponding first- and zeroth-order approximations for the coefficient β in (6.4) is:

$$\beta = -\frac{1+n^4 D_{22}-\eta_0}{in\left(1+n^2 D_{22}\right)} = i\frac{\left(\left(n^2+1\right)+n^2 D_{22}\left(3n^2-1\right)\right)}{n\left(n^2+1\right)\left(1+n^2 D_{22}\right)}$$

$$\beta \approx \frac{i}{n} + 2inD_{22}\frac{n^2-1}{n^2+1} \quad \text{first-order} \tag{6.10}$$

$$\beta \approx \frac{i}{n} \quad \text{zeroth-order} \tag{6.11}$$

The zeroth-order result for β is well known and is often used to develop approximate shell theories [Sharma and Johns, 1971]. The first order result is new.

6.2.1.2 Case II: $\lambda = \lambda_s$

In this section we consider the smaller group of four λ_j. In perturbation analysis it is useful to use mathematical assumptions for some of the parameters in the beginning of the analysis so that the derivations can proceed. These assumptions are then verified at the end of the derivations. Due to the nonlinear relationships in many of the intermediate expres-

sions, there are some iterations needed as different assumptions are examined. Herein, only the final iteration is presented. In the present case, we assume based partly on the analysis of the preceding subsection, that $\eta = O(\epsilon^4)$, $\alpha = O(\epsilon)$, $\beta = i/n + O(\epsilon^4)$ and $\lambda = O(\epsilon)$. The first equilibrium equation given in the first row of equation (5.21) can be written in terms of α, β and λ:

$$\left(A_{11}\lambda^2 - n^2 A_{66} + \eta\right)\alpha + in\lambda\left(A_{12} + A_{66}\right)\beta + A_{12}\lambda = 0$$

which simplifies to:

$$\left(A_{11}\lambda^2 - n^2 A_{66}\right)\alpha - \lambda A_{66} = 0$$

after disregarding $o(\epsilon^4)$ terms. The results for α are:

$$\alpha = \frac{\lambda A_{66}}{A_{11}\lambda^2 - n^2 A_{66}} \quad \text{first-order} \tag{6.12}$$

$$\alpha = -\frac{\lambda}{n^2} \quad \text{zeroth-order} \tag{6.13}$$

In the next step we focus on finding the dispersion relation for small λ. Here we are interested in frequencies of order D, or $O(\epsilon^4)$. We retain terms up to order $O(\epsilon^5)$ in the characteristic equation to obtain a linear relation for η:

$$a_{12}\lambda^4 - 4in^3\left(n^2 - 1\right)^2 D_{26}\lambda + n^2\left(\eta_0 - \eta\right)\left(n^2 + 1\right) = 0$$

where

$$a_{12} = A_{11} - A_{12}^2$$

with solution

$$\eta = \eta_0 + \frac{a_{12}\lambda^4}{n^2\left(n^2 + 1\right)} \quad \text{zeroth-order} \tag{6.14}$$

for orthotropic materials. The zeroth-order results include terms of order $O(\epsilon^4)$ and it is easily inverted, yielding the approximate solution for λ in terms of η:

$$\lambda \approx \pm n\sqrt{\frac{1}{a_{12}}\left(\eta-\eta_0\right)\left(n^2+1\right)},\ \pm in\sqrt{\frac{1}{a_{12}}\left(\eta-\eta_0\right)\left(n^2+1\right)} \tag{6.15}$$

This simple dispersion relation for small λ indicates that there are two pure imaginary and pure real solutions for λ, all of the same absolute magnitude, and all of order ϵ. We examine higher order results for λ in the next subsection.

It is necessary to include terms of order $O(\epsilon^6)$ to obtain more accurate approximations for the dispersion relation for orthotropic and more general symmetric and balanced laminates.

6.2.1.2.1 MORE ACCURATE DISPERSION RELATION FOR SMALL λ

In this subsection we obtain the first-order approximation for the frequency parameter η. We retain terms up to $O(\epsilon^6)$ in the characteristic equation:

$$\begin{aligned} &A_{66}a_{12}\lambda^4+\left(\left(a_{12}\left(n^2+1\right)+A_{66}-2n^2A_{12}A_{66}\right)\eta+\left(2n^4D_{22}A_{12}A_{66}\left(n^2-1\right)\right.\right.\\ &\left.\left.-A_{66}\left(4n^6D_{16}+2n^4D_{12}\left(n^2-1\right)+4n^2D_{66}\left(n^2-1\right)^2\right)-\eta_0a_{12}\left(n^2+1\right)\right)\right)\lambda^2\\ &+\left(-4in^3D_{26}A_{66}\left(n^2-1\right)^2\right)\lambda+n^2\left(\eta_0-\eta\right)\left(n^2+1\right)A_{66}=0 \end{aligned}$$

After some straightforward but somewhat tedious algebraic and perturbation analysis, the final first-order results for η is obtained for case of orthotropic materials:

$$\eta = -\frac{\left(\begin{array}{c} \lambda^4 A_{66} a_{12} - \lambda^2 \left(\begin{array}{c} 2n^2 A_{66} \left(n^2 D_{12} \left(n^2 - 1 \right) + 2 D_{66} \left(n^2 - 1 \right)^2 \right) \\ + \eta_0 a_{12} \left(n^2 + 1 \right) - 2n^4 D_{22} A_{12} A_{66} \left(n^2 - 1 \right) \end{array} \right) \\ + n^2 \eta_0 A_{66} \left(n^2 + 1 \right) \end{array} \right)}{\left(A_{66} + a_{12} \left(n^2 + 1 \right) - 2n^2 A_{12} A_{66} \right) \lambda^2 - n^2 A_{66} \left(n^2 + 1 \right)} \tag{6.16}$$

To invert this relation to derive the corresponding solution for λ in terms of η, we use the following simple perturbation result. For a quadratic equation of the form $ax^2 + bx - c = 0$ where $b << \sqrt{4ac}$, the first-order expressions for the solutions are:

$$x = \frac{-b \pm \sqrt{b^2 + 4ac}}{2a} = \frac{1}{2a} \left[-b \pm \sqrt{4ac} \sqrt{\frac{b^2}{4ac} + 1} \right] \approx \frac{1}{2a} \left[-b \pm \sqrt{4ac} \left(\frac{b^2}{8ac} + 1 \right) \right]$$
$$\approx \frac{-b \pm \sqrt{4ac}}{2a}$$

Applying this to equation (6.16) we obtain:

$$\lambda^2 = \frac{-\left(\eta - \eta_0 \right) \left(n^2 + 1 \right)}{2A_{66}} \pm n \sqrt{\frac{\left(n^2 + 1 \right) \left(\eta_0 - \eta \right)}{a_{12}}} - \frac{\left(\eta \left(1 - 2n^2 A_{12} \right) - 2n^4 \left(n^2 - 1 \right) \left(D_{12} - D_{22} A_{12} \right) - 4n^2 D_{66} \left(n^2 - 1 \right)^2 \right)}{2a_{12}}$$

This concludes the analysis of the dispersion relation for small λ.

6.2.1.3 Case III: Large λ, $\eta \approx 0$

To derive the perturbation results for large λ, we begin with the assumptions $\eta = O(\epsilon)$, $\lambda = O(\epsilon^{-1})$, $\alpha = O(\epsilon)$ and $\beta = O(\epsilon^2)$ to obtain the following approximation for the

equilibrium equations:

$$\begin{bmatrix} A_{11}\lambda^2 & in\lambda\left(A_{12}+A_{66}\right) & A_{12}\lambda \\ in\lambda\left(A_{12}+A_{66}\right) & A_{66}\lambda^2 & in \\ A_{12}\lambda & in & 1+\lambda^4 D_{11} \end{bmatrix} \begin{bmatrix} \alpha \\ \beta \\ 1 \end{bmatrix} = 0$$

Dividing the first row and column by λ, the matrix relation becomes:

$$\begin{bmatrix} A_{11} & in\left(A_{12}+A_{66}\right) & A_{12} \\ in\left(A_{12}+A_{66}\right) & A_{66}\lambda^2 & in \\ A_{12} & in & 1+\lambda^4 D_{11} \end{bmatrix} \begin{bmatrix} \lambda\alpha \\ \beta \\ 1 \end{bmatrix} = 0$$

Taking the determinant of the matrix and setting it to zero yields the characteristic equation:

$$\lambda^6 + n^2\frac{\left(A_{12}+A_{66}\right)^2}{A_{11}A_{66}}\lambda^4 + \lambda_a^4\lambda^2 + n^2\frac{\left(a_{12}+A_{66}^2\right)}{A_{11}A_{66}D_{11}} = 0$$

where:

$$\lambda_a = \sqrt[4]{\frac{a_{12}}{D_{11}A_{11}}}$$

It can be seen that there are only even powers of λ all with real coefficients so that the solutions for λ are in conjugate pairs and in positive-negative pairs.

For $n = 0$ the characteristic equation reduces to:

$$\lambda_0^4 + \lambda_a^4 = 0$$

where the solutions for λ are denoted by λ_0. The expression for λ_0 in terms of λ_a is $\lambda_0^4 = -\lambda_a^4$ which can be rewritten as $\lambda_0^2 = \pm i\lambda_a^2$ or:

$$\lambda_0 = \pm\frac{1 \pm i}{\sqrt{2}}\lambda_a$$

It can be seen that λ_0 corresponds to the characteristic equation where $n = 0$, which are the axisymmetric modes. The matrix equation becomes:

$$\begin{bmatrix} A_{11} & 0 & A_{12} \\ 0 & A_{66}\lambda^2 & 0 \\ A_{12} & 0 & \frac{A_{12}^2}{A_{11}} \end{bmatrix} \begin{bmatrix} \lambda_0\alpha_0 \\ \beta_0 \\ 1 \end{bmatrix} = 0$$

where we multiply α_0 by λ_0. The solutions are $\alpha_0 = 0$ and $\beta_0 = \infty$ which corresponds to pure torsional motion or $\alpha_0 = -A_{12}/\left(\lambda_0 A_{11}\right)$ and $\beta_0 = 0$ which corresponds to combined radial and longitudinal motions.

To obtain the first-order expression for α, β and λ, we start from the zeroth-order results $\lambda \approx \frac{1+i}{\sqrt{2}}\lambda_a$ which is associated with $\lambda_0^2 \approx i\lambda_a^2$. To find the perturbation q from the zeroth-order solution, we use the following expansions:

$$\lambda^2 = \lambda_0^2\left(1 - iq\right), \quad \lambda^4 = \lambda_0^4\left(1 - 2iq\right), \quad \lambda^6 = \lambda_0^6\left(1 - 3iq\right)$$

The characteristic equation can be rewritten in terms of q:

$$\lambda_0^6\left(1 - 3iq\right) + n^2\frac{\left(A_{12} + A_{66}\right)^2}{A_{11}A_{66}}\lambda_0^4\left(1 - 2iq\right) - \lambda_0^6\left(1 - iq\right) + n^2\frac{\left(a_{12} + A_{66}^2\right)}{A_{11}A_{66}D_{11}} = 0$$

Since this is linear in q, the solution for this perturbation parameter is readily found:

$$\begin{aligned} q &= -i\frac{n^2\left(-a_{12}\left(A_{12} + A_{66}\right)^2 + A_{11}a_{12} + A_{11}A_{66}^2\right)}{2\lambda_0^4\left(A_{11}^2A_{66}D_{11}\lambda_0^2 + n^2\left(A_{12} + A_{66}\right)^2A_{11}D_{11}\right)} \\ &= \frac{n^2\left(\left(A_{12}^2 - A_{11}\right)\left(A_{12} + A_{66}\right)^2 - A_{11}\left(A_{12}^2 - A_{11}\right) + A_{11}A_{66}^2\right)}{2\left(A_{11} - A_{12}^2\right)\left(iA_{11}A_{66}\sqrt{\frac{A_{11} - A_{12}^2}{D_{11}A_{11}}} + n^2\left(A_{12} + A_{66}\right)^2\right)} \end{aligned}$$

We have to get the right sign for the radical. In the above, we use $Im(\lambda_0^2) > 0$, so that $q > 0$. If we use $Im(\lambda_0^2 < 0)$, then we need a negative sign so that $-q < 0$. The final

results for λ are

$$Im(\lambda_0^2 > 0) : \lambda = \pm\lambda_0 (1 - iq/2) \approx \pm (Re(\lambda_0)) (1 + i) e^{-iq/2} = \pm\lambda_a e^{i\pi/4 - iq/2}$$

and

$$Im(\lambda_0^2) < 0 : \lambda = \pm\lambda_0 (1 + iq/2) \approx \pm (Re(\lambda_0)) (1 - i) e^{iq/2} = \pm\lambda_a e^{-i\pi/4 + iq/2}$$

We continue the analysis by determining the corresponding first-order expressions for α and β. First we express

$$\alpha = \alpha_0 + \frac{\delta_a}{\lambda} = \frac{(\delta_\alpha - A_{12}/A_{11})}{\lambda}$$

and substitute into the characteristic matrix equation. Retaining only the dominant terms, we obtain:

$$\begin{bmatrix} A_{11} & in(A_{12} + A_{66}) & A_{12} \\ in(A_{12} + A_{66}) & A_{66}\lambda_0^2 & in \\ A_{12} & in & \frac{A_{12}^2}{A_{11}} - 2iq\lambda_0^4 D_{11} \end{bmatrix} \begin{bmatrix} \delta_\alpha - A_{12}/A_{11} \\ \beta \\ 1 \end{bmatrix} = 0$$

or

$$\begin{bmatrix} \delta_\alpha A_{11} + in\beta(A_{12} + A_{66}) \\ in(-A_{12}^2 + A_{11} - A_{12}A_{66}) + \beta\lambda_0^2 A_{11}A_{66} \\ \delta_\alpha A_{12} - 2iq\lambda_0^4 D_{11} + in\beta \end{bmatrix} = 0$$

In the above it is assumed that $\beta = O(\epsilon^2)$ and the q term is not needed in the middle element of the matrix. Solving for β and δ_a (corresponding to $Im(\lambda_0^2) > 0$) yields:

$$\beta = -\frac{in(-A_{12}^2 + A_{11} - A_{12}A_{66})}{\lambda_0^2 A_{11}A_{66}} = -\frac{n(-A_{12}^2 + A_{11} - A_{12}A_{66})}{\lambda_a^2 A_{11}A_{66}} = -\beta_a$$

$$\beta_a = \frac{n(-A_{12}^2 + A_{11} - A_{66}A_{12})}{A_{11}^2 A_{66}\lambda_a^2}$$

and:

$$\delta_\alpha = -\frac{in\beta\,(A_{12}+A_{66})}{A_{11}} = \frac{in\beta_a\,(A_{12}+A_{66})}{A_{11}}$$

It is noted that λ, δ_a, β and α are in conjugate pairs and when λ changes sign, α also changes sign but δ_a and β do not change sign.

6.3 Boundary conditions

While the equilibrium equations are used to obtain the functional form of the dispersion relation, the boundary conditions are needed along with the dispersion relation to obtain the actual natural frequencies and mode shapes. As in the preceding section, the terms in the boundary conditions are examined separately for small and large λ. Due to the complexity of the analytical forms of the modal properties, the focus on the remainder of this chapter is on orthotropic materials where the roots λ are in complex conjugate pairs and positive-negative pairs. It is noted that for the more general case of symmetric, balanced laminates, the roots λ do not follow these simple interrelationships.

6.3.1 Case I : small λ

6.3.1.1 Zeroth-order results

We begin with the zeroth-order results for λ from equation (6.15): $\lambda_j = \pm\lambda_S$ and $\pm i\lambda_S$ and from symmetry arguments we have, for the four corresponding coefficients $C_j =$

$c/2, c/2, 1/2, 1/2$ in equation (6.4). The corresponding solution for η is:

$$\eta = \eta_0 + \frac{a_{12}\lambda^4}{n^2\left(n^2+1\right)}$$

After a series of substitution and perturbation analysis steps, we obtain, for the symmetric modes:

$$N_x = \frac{\lambda^2 A_{11}A_{66}}{A_{11}\lambda^2 - A_{66}n^2}\left(c\cosh\lambda x - \cos\lambda x\right) \approx \frac{-\lambda^2 A_{11}}{n^2}\left(c\cosh\lambda x - \cos\lambda x\right)$$

$$M_x = \lambda^2 D_{11}\left(c\cosh\lambda x - \cos\lambda x\right) - nD_{12}\left(n - \frac{1}{n}\right)\left(c\cosh\lambda x + \cos\lambda x\right)$$

$$N_{x\theta} - M_{x\theta}/R = \frac{iA_{66}A_{11}\lambda^3}{n}\left(\frac{c\sinh\lambda x}{A_{11}\lambda^2 - n^2A_{66}} + \frac{\sin\lambda x}{-A_{11}\lambda^2 - n^2A_{66}}\right) -$$

$$4i\lambda D_{66}\left(n - \frac{1}{n}\right)\left(c\sinh\lambda x - \sin\lambda x\right)$$

$$Q = -\lambda^3 D_{11}\left(c\sinh\lambda x + \sin\lambda x\right) + n\lambda\left(D_{12} + 4D_{66}\right)\left(n - \frac{1}{n}\right)\left(c\sinh\lambda x - \sin\lambda x\right)$$

If we use the zeroth-order approximation of $c\cosh\lambda x - \cos\lambda x = 0$ to satisfy the first boundary condition and if we also assume that λ satisfies the equation $c\sinh\lambda x + \sin\lambda x = 0$ the above can be rewritten as:

$$N_x = 0$$

$$M_x = -nD_{12}\left(n - \frac{1}{n}\right)\left(c\cosh\lambda x + \cos\lambda x\right)$$

$$N_{x\theta} - M_{x\theta}/R = \frac{iA_{66}A_{11}\lambda^3}{n}\left(\frac{c\sinh\lambda x}{A_{11}\lambda^2 - n^2A_{66}} + \frac{\sin\lambda x}{-A_{11}\lambda^2 - n^2A_{66}}\right)$$

$$- 4i\lambda D_{66}\left(n - \frac{1}{n}\right)\left(c\sinh\lambda x - \sin\lambda x\right)$$

$$Q = n\lambda\left(D_{12} + 4D_{66}\right)\left(n - \frac{1}{n}\right)\left(c\sinh\lambda x - \sin\lambda x\right)$$

Similarly, for anti-symmetric modes one can write:

$$N_x = \frac{\lambda^2 A_{11} A_{66}}{A_{11}\lambda^2 - A_{66} n^2} \left(c \sinh \lambda x - \sin \lambda x\right) \approx \frac{-\lambda^2 A_{11}}{n^2} \left(c \sinh \lambda x - \sin \lambda x\right)$$

$$M_x = \lambda^2 D_{11} \left(c \sinh \lambda x - \sin \lambda x\right) - n D_{12} \left(n - \frac{1}{n}\right) \left(c \sinh \lambda x + \sin \lambda x\right)$$

$$N_{x\theta} - M_{x\theta}/R = \frac{i A_{66} A_{11} \lambda^3}{n} \left(\frac{c \cosh \lambda x}{A_{11}\lambda^2 - n^2 A_{66}} + \frac{-\cos \lambda x}{-A_{11}\lambda^2 - n^2 A_{66}}\right)$$

$$- 4 i \lambda D_{66} \left(n - \frac{1}{n}\right) \left(c \cosh \lambda x + \cos \lambda x\right)$$

$$Q = -\lambda^3 D_{11} \left(c \cosh \lambda x - \cos \lambda x\right) + n\lambda \left(D_{12} + 4 D_{66}\right) \left(n - \frac{1}{n}\right) \left(c \cosh \lambda x + \cos \lambda x\right)$$

Next we perturb the above results to obtain first-order results.

6.3.1.2 First-order results

Here we consider the case where the absolute value of the real and imaginary solutions for λ are not equal, so that we have $\lambda_j = \pm\lambda_1, \pm i\lambda_2$. First, we consider the symmetric boundary conditions and use $\pm\lambda_1$ for the real roots and $\pm i\lambda_2$ for the imaginary roots with

corresponding coefficients $C = c/2$ and $1/2$ to get:

$$N_x = A_{11}A_{66}\left(c\frac{\lambda_1^2\cosh\lambda_1 x}{A_{11}\lambda_1^2 - A_{66}n^2} - \frac{\lambda_2^2\cos\lambda_2 x}{-A_{11}\lambda_2^2 - A_{66}n^2}\right)$$

$$M_x = D_{11}\left(\lambda_1^2 c_1\cosh\lambda_1 x - \lambda_2^2\cos\lambda_2 x\right) - nD_{12}\left(n - \frac{1}{n}\right)\left(c_1\cosh\lambda_1 x + \cos\lambda_2 x\right)$$

$$N_{x\theta} - M_{x\theta}/R = \frac{iA_{11}A_{66}}{n}\left(c\frac{\lambda_1^3\sinh\lambda_1 x}{A_{11}\lambda_1^2 - A_{66}n^2} + \frac{\lambda_2^3\sin\lambda_2 x}{-A_{11}\lambda_2^2 - A_{66}n^2}\right)$$

$$- 4iD_{66}\left(n - \frac{1}{n}\right)\left(c_1\lambda_1\sinh\lambda_1 x - \lambda_2\sin\lambda_2 x\right)$$

$$Q = -D_{11}\left(c\lambda_1^3\sinh\lambda_1 x + \lambda_2^3\sin\lambda_2 x\right) + n\left(D_{12} + 4D_{66}\right)\left(n - \frac{1}{n}\right)$$

$$\left(c_1\lambda_1\sinh\lambda_1 x - \lambda_2\sin\lambda_2 x\right)$$

It is noted that in the above equation, the first-order approximation for α is used. The equation for the first row can be rewritten as:

$$\begin{bmatrix} \frac{\lambda_1^2\cosh(\lambda_1 x)}{A_{11}\lambda_1^2 - A_{66}n^2} & -\frac{\lambda_2^2\cos(\lambda_2 x)}{-A_{11}\lambda_2^2 - A_{66}n^2} \\ \frac{\lambda_1^3\sinh(\lambda_1 x)}{A_{11}\lambda_1^2 - A_{66}n^2} & \frac{\lambda_2^3\sin(\lambda_2 x)}{-A_{11}\lambda_2^2 - A_{66}n^2} \end{bmatrix} \begin{bmatrix} c \\ 1 \end{bmatrix} = 0 \tag{6.17}$$

The determinant of the matrix is:

$$\lambda_2\sin x\lambda_2\cosh x\lambda_1 + \lambda_1\cos x\lambda_2\sinh x\lambda_1 = 0$$

To solve this it is necessary to determine the size of the smaller real λ_1 given the larger imaginary $i\lambda_2$ and find η in this process. We begin with $\lambda = i\lambda_2$ and obtain:

$$\eta = \frac{\left(\begin{array}{c} \lambda_2^4 A_{66}a_{12} + \lambda_2^2\left(\begin{array}{c} 2n^2A_{66}\left(n^2D_{12}\left(n^2-1\right) + 2D_{66}\left(n^2-1\right)^2\right) \\ +\eta_0 a_{12}\left(n^2+1\right) - 2n^4D_{22}A_{12}A_{66}\left(n^2-1\right) \end{array}\right) \\ +n^2\eta_0 A_{66}\left(n^2+1\right) \end{array}\right)}{\left(A_{66} + a_{12}\left(n^2+1\right) - 2n^2A_{12}A_{66}\right)\lambda_2^2 + n^2A_{66}\left(n^2+1\right)} \tag{6.18}$$

Then we invert this to get λ_1^2:

$$\lambda_1^2 = \frac{-(\eta-\eta_0)(n^2+1)}{2A_{66}} \pm n\sqrt{\frac{(n^2+1)(\eta_0-\eta)}{a_{12}} - \frac{\left(\eta(1-2n^2A_{12}) - 2n^4(n^2-1)(D_{12}-D_{22}A_{12}) - 4n^2D_{66}(n^2-1)^2\right)}{2a_{12}}} \tag{6.19}$$

The boundary conditions then become:

$$N_x = 0$$

$$M_x = D_{11}\left(\lambda_1^2 c_1 \cosh\lambda_1 x - \lambda_2^2 \cos\lambda_2 x\right) - nD_{12}\left(n-\frac{1}{n}\right)(c_1\cosh\lambda_1 x + \cos\lambda_2 x)$$

$$N_{x\theta} - M_{x\theta}/R = -4iD_{66}\left(n-\frac{1}{n}\right)(c_1\lambda_1\sinh\lambda_1 x - \lambda_2\sin\lambda_2 x)$$

$$Q = -D_{11}\left(c\lambda_1^3\sinh\lambda_1 x + \lambda_2^3\sin\lambda_2 x\right) + n(D_{12}+4D_{66})\left(n-\frac{1}{n}\right)$$

$$(c_1\lambda_1\sinh\lambda_1 x - \lambda_2\sin\lambda_2 x)$$

The higher powers of λ in the second and fourth boundary conditions can be disregarded for small λ:

$$N_x = 0$$

$$M_x = -nD_{12}\left(n-\frac{1}{n}\right)(c_1\cosh\lambda_1 x + \cos\lambda_2 x)$$

$$N_{x\theta} - M_{x\theta}/R = -4iD_{66}\left(n-\frac{1}{n}\right)(c_1\lambda_1\sinh\lambda_1 x - \lambda_2\sin\lambda_2 x)$$

$$Q = n(D_{12}+4D_{66})\left(n-\frac{1}{n}\right)(c_1\lambda_1\sinh\lambda_1 x - \lambda_2\sin\lambda_2 x)$$

6.3.2 Case II $\lambda = \lambda_L$

Next we examine the boundary conditions for large λ_L:

$$N_x = \sum \left(A_{11}\alpha\lambda + A_{12}\left(in\beta + 1\right) + A_{16}\left(\lambda\beta + in\alpha\right)\right) Ce^{\lambda x}$$

$$M_x = \sum \left(D_{11}\lambda^2\right) Ce^{\lambda x}$$

$$N_{x\theta} - M_{x\theta}/R = \sum \left(A_{16}\alpha\lambda + A_{66}\left(\lambda\beta + in\alpha\right) - 2D_{16}\lambda^2 + A_{26}\left(in\beta + 1\right)\right) Ce^{\lambda x}$$

$$Q = \sum \left(-D_{11}\lambda^3 + 2\lambda^2\left(\beta - 2in\right)D_{16}\right) Ce^{\lambda x}$$

At the left boundary the large λ_j with negative real part are important for the edge effect. We recall the following large λ results from section 6.2.1.3:

$$\lambda_0 = \frac{-1+i}{\sqrt{2}}\lambda_a, \quad \lambda_0^2 = -i\lambda_a^2, \quad \lambda_0^3 = \frac{1+i}{\sqrt{2}}\lambda_a^3, \quad \lambda_a = \sqrt[4]{\frac{A_{11} - A_{12}^2}{A_{11}D_{11}}}$$

$$\beta_a = \frac{n\left(-A_{12}^2 + A_{11} - A_{66}A_{12}\right)}{A_{11}^2 A_{66}\lambda_a^2}, \quad \beta = \beta_a$$

$$\alpha = \alpha_0 + \frac{\delta_a}{\lambda} = \frac{\delta_\alpha - A_{12}/A_{11}}{\lambda}, \quad \delta_\alpha = -\frac{in\beta\left(A_{12} + A_{66}\right)}{A_{11}} = -\frac{in\beta_a\left(A_{12} + A_{66}\right)}{A_{11}}$$

The expression for α in terms of β_a becomes

$$\alpha = -\frac{\left(A_{12} + A_{66}\right)ni\beta_a + A_{12}}{\lambda A_{11}}$$

Note that the coefficients of the terms with complex conjugate λ_j are in complex conjugate pairs. We need to take the sum of two terms with negative real part with coefficients $c_0 \exp\left(\pm i\phi\right)$. The displacements associated with the large λ_j at the left boundary can be

written as:

$$w = 2c_0 \exp(-\frac{\lambda_a x}{\sqrt{2}}) \cos(\frac{\lambda_a x}{\sqrt{2}} + \phi)$$

$$v = 2c_0\beta_a \exp(-\frac{\lambda_a x}{\sqrt{2}}) \cos(\frac{\lambda_a x}{\sqrt{2}} + \phi)$$

$$u = \frac{\sqrt{2}}{\lambda_a} c_0 \frac{((A_{12} + A_{66})\, ni\beta_a + A_{12})}{A_{11}} \exp(-\frac{\lambda_a x}{\sqrt{2}}) \left(\cos(\frac{\lambda_a x}{\sqrt{2}} + \phi) - \sin(\frac{\lambda_a x}{\sqrt{2}} + \phi)\right)$$

The derivatives of the displacements in the boundary conditions are:

$$w_x = -\sqrt{2}\lambda_a c_0 \exp(-\frac{\lambda_a x}{\sqrt{2}}) \left(\cos(\frac{\lambda_a x}{\sqrt{2}} + \phi) + \sin(\frac{\lambda_a x}{\sqrt{2}} + \phi)\right)$$

$$w_{xx} = 2\lambda_a^2 c_0 \exp(-\frac{\lambda_a x}{\sqrt{2}}) \sin(\frac{\lambda_a x}{\sqrt{2}} + \phi)$$

$$w_{xxx} = \sqrt{2}\lambda_a^3 c_0 \exp(-\frac{\lambda_a x}{\sqrt{2}}) \left(\cos(\frac{\lambda_a x}{\sqrt{2}} + \phi) - \sin(\frac{\lambda_a x}{\sqrt{2}} + \phi)\right)$$

$$v_x = -\sqrt{2}\lambda_a \beta_a c_0 \exp(-\frac{\lambda_a x}{\sqrt{2}}) \left(\cos(\frac{\lambda_a x}{\sqrt{2}} + \phi) + \sin(\frac{\lambda_a x}{\sqrt{2}} + \phi)\right)$$

$$u_x = -2c_0 \frac{((A_{12} + A_{66})\, ni\beta_a + A_{12})}{A_{11}} \cos(\frac{\lambda_a x}{\sqrt{2}} + \phi) \exp(-\frac{\lambda_a x}{\sqrt{2}})$$

Finally the boundary conditions can be written as:

$$N_x = A_{11}u_x + A_{12}\,(v_\theta + w) = -2inc_0\beta_a A_{66} \exp(-\frac{\lambda_a x}{\sqrt{2}}) \cos(\frac{\lambda_a x}{\sqrt{2}} + \phi)$$

$$M_x = D_{11}w_{xx} = 2\lambda_a^2 D_{11} c_0 \exp(-\frac{\lambda_a x}{\sqrt{2}}) \sin(\frac{\lambda_a x}{\sqrt{2}} + \phi)$$

$$N_{x\theta} - M_{x\theta}/R = A_{66}\,(v_x + u_\theta) = -\frac{A_{66}\sqrt{2}c_0}{A_{11}\lambda_a} \exp(-\frac{\lambda_a x}{\sqrt{2}})$$

$$\left(\left(\lambda_a^2\beta_a A_{11} + n^2\left(\left(A_{12} + A_{66}\right)\beta_a - inA_{12}\right)\right) \cos(\frac{\lambda_a x}{\sqrt{2}} + \phi)\right.$$

$$\left. + \left(\lambda_a^2\beta_a A_{11} - n^2\left(\left(A_{12} + A_{66}\right)\beta_a + inA_{12}\right)\right) \sin(\frac{\lambda_a x}{\sqrt{2}} + \phi)\right)$$

$$Q = -D_{11}w_{xxx} = -c_0\sqrt{2}D_{11}\lambda_a^3 \exp(-\frac{\lambda_a x}{\sqrt{2}}) \left(\cos(\frac{\lambda_a x}{\sqrt{2}} + \phi) - \sin(\frac{\lambda_a x}{\sqrt{2}} + \phi)\right)$$

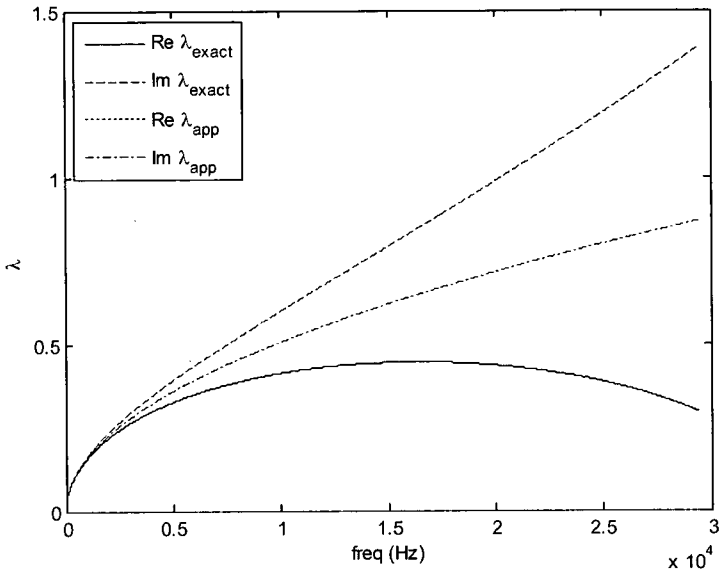

Figure 6.4: Comparison of exact dispersion relation with the zeroth-order approximation, for circumferential mode $n = 1$

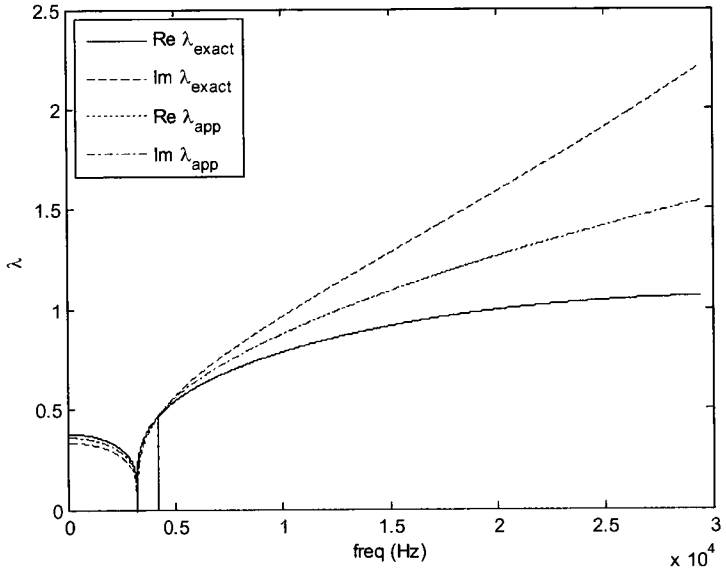

Figure 6.5: Comparison of exact dispersion relation with the zeroth-order approximation, for circumferential mode $n = 2$

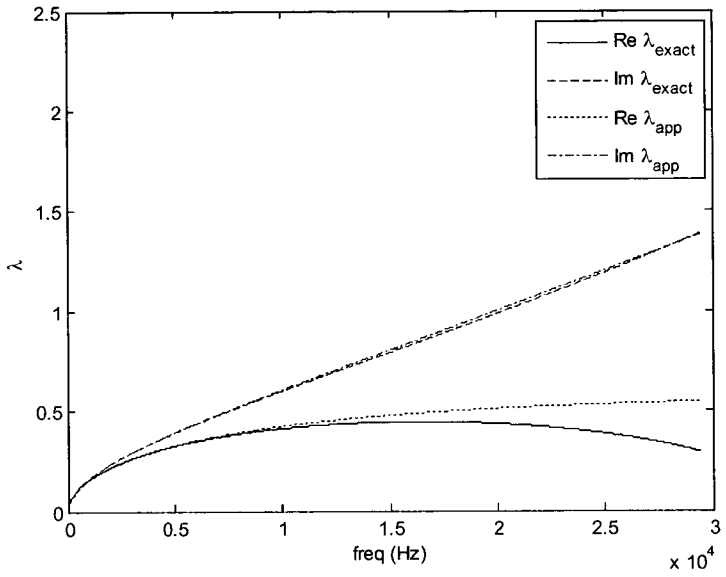

Figure 6.6: Comparison of exact dispersion relation with the first-order approximation, for circumferential mode $n = 1$

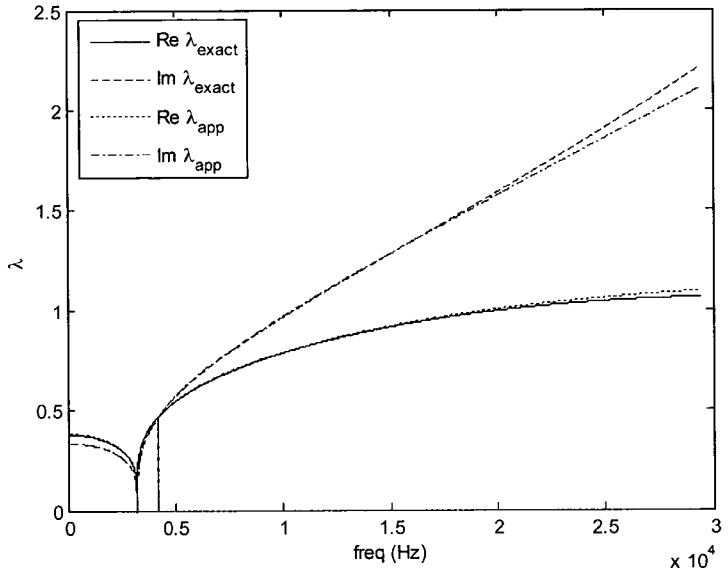

Figure 6.7: Comparison of exact dispersion relation with the first-order approximation, for circumferential mode $n = 2$

6.3.3 Combining the boundary conditions

Here we identify and combine the dominant contributions of the eight terms – four for small λ and four for large λ – that are summed for each boundary condition. Parametric studies indicate that the second and fourth boundary conditions are satisfied by the large λ components. The large λ contributions are:

$$M_x = 2c_0 D_{11} \lambda_a^2 \sin\phi = -b_1 \tag{6.20}$$

$$Q = -\sqrt{2} c_0 D_{11} \lambda_a^3 (\cos\phi + \sin\phi) = -b_2$$

which must be equal and opposite to the small λ ($\lambda = \pm\lambda_1$ and $\lambda = \pm i\lambda_2$) contributions to the boundary conditions:

$$b_1 = -nD_{12}(-1/n + n)(c_1 \cosh(\lambda_{s_1} x) + \cos(\lambda_{s_2} x))$$

$$b_2 = n(D_{12} + 4D_{66})(-1/n + n)(c_1 \lambda_{s_1} \sinh(\lambda_{s_1} x) - \lambda_{s_2} \sin(\lambda_{s_2} x))$$

By enforcing these two boundary conditions, we can solve for c_0 and ϕ:

$$\frac{b_2}{b_1} = -\frac{\lambda_a}{\sqrt{2}}(\cot\phi - 1) \quad \text{or} \quad \cot\phi = 1 - \frac{\sqrt{2} b_2}{\lambda_a b_1}$$

$$c_0 = \frac{-b_1}{2D_{11}\lambda_a^2 \sin\phi}$$

Given these results for the coefficient c and the angle ϕ, the mode shapes can be obtained. This completes the perturbation analysis of the modal properties of the vibrating, free-free orthotropic cylinder.

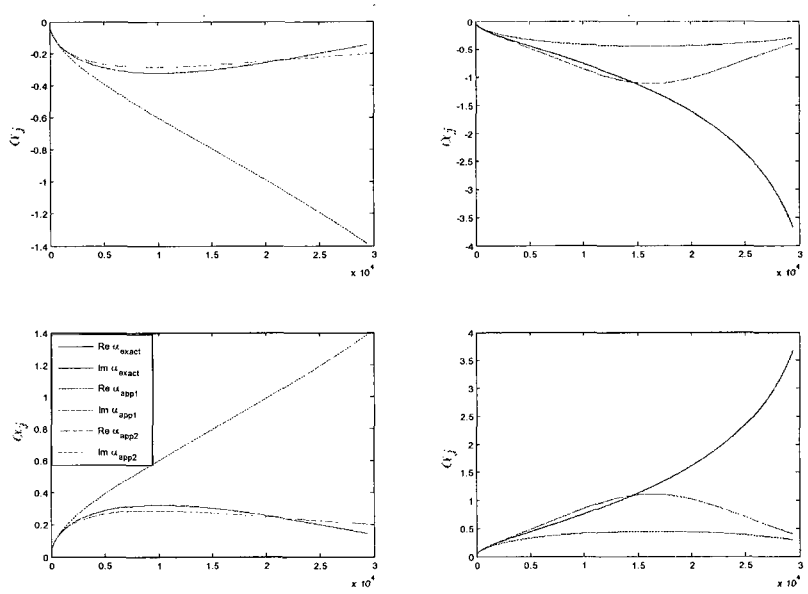

Figure 6.8: Comparison of exact, zeroth- and first-order approximation of α, for circumferential mode $n = 1$

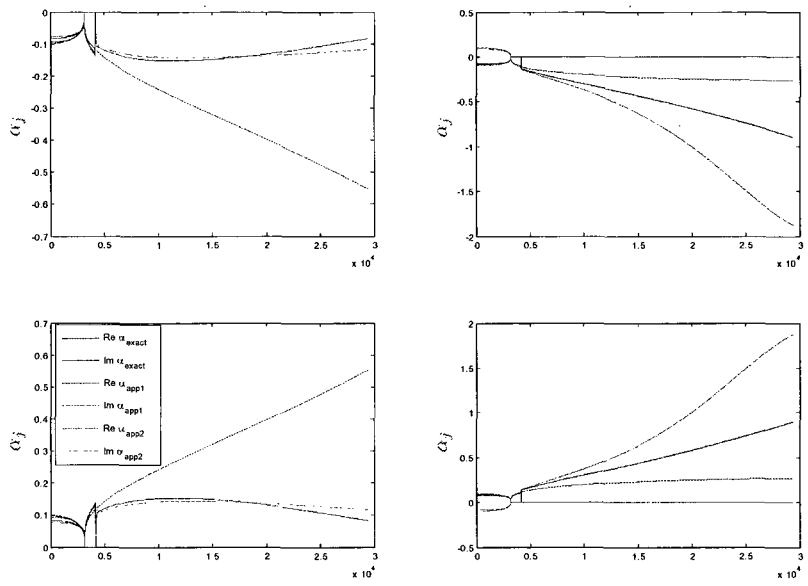

Figure 6.9: Comparison of exact, zeroth- and first-order approximation of α, for circumferential mode $n = 2$

6.4 Results and discussion

As a numerical example the isotropic copper pipe in the previous chapter is considered. The approach introduced in the previous sections is used to find the dispersion relation and to determine the natural frequencies and mode shapes of the cylinder. Figures 6.4 and 6.5 show the comparison between the exact and the zeroth-order approximation of the dispersion relation. In Figures 6.6 and 6.7 the first-order approximation of the dispersion relation is compared to the exact dispersion relation. As it can be seen, the first-order approximation for the dispersion relation is very accurate for the frequencies lower than 15000 (Hz). It is noted that there is no D term in the zeroth-order approximation except for the D_{22} term in η_0.

The exact, zeroth- and first-order approximations for α are shown and compared in Figures 6.8 and 6.9. The zeroth- and first-order approximations for α are determined by equations (6.13) and (6.12). It can be seen that the zeroth-order approximation is not accurate while the first-order approximation for α improves for low to medium frequencies.

The wave numbers and natural frequencies are also determined using the first-order approximation of the dispersion relation in equation (6.16). The wave numbers are compared with the exact λ_j obtained by solving the eighth-order characteristic equation (6.3). Figures 6.10 and 6.11 show the comparison between the exact wave numbers and natural frequencies and those obtained by first-order approximation of the dispersion relation. The wave numbers shown in these figures are the absolute value of the imaginary wave number

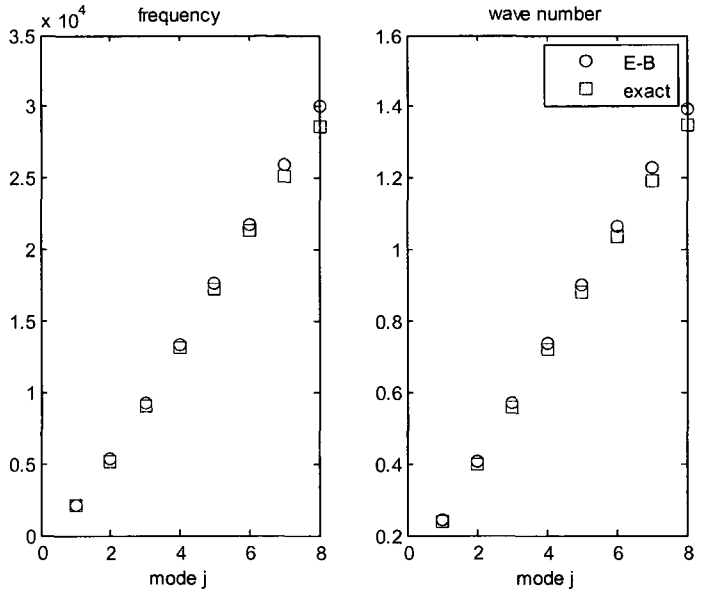

Figure 6.10: Comparison of exact and approximate natural frequencies and wave numbers using the first-order approximation, for circumferential mode $n = 1$

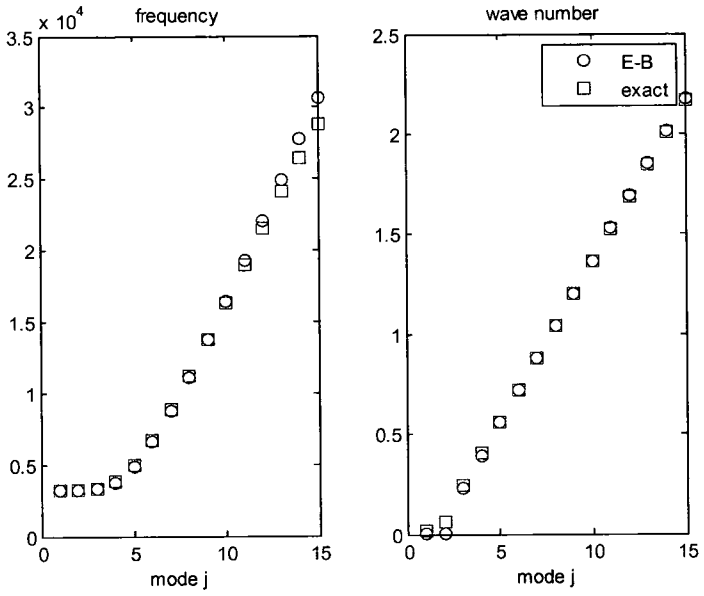

Figure 6.11: Comparison of exact and approximate natural frequencies and wave numbers using the first-order approximation, for circumferential mode $n = 2$

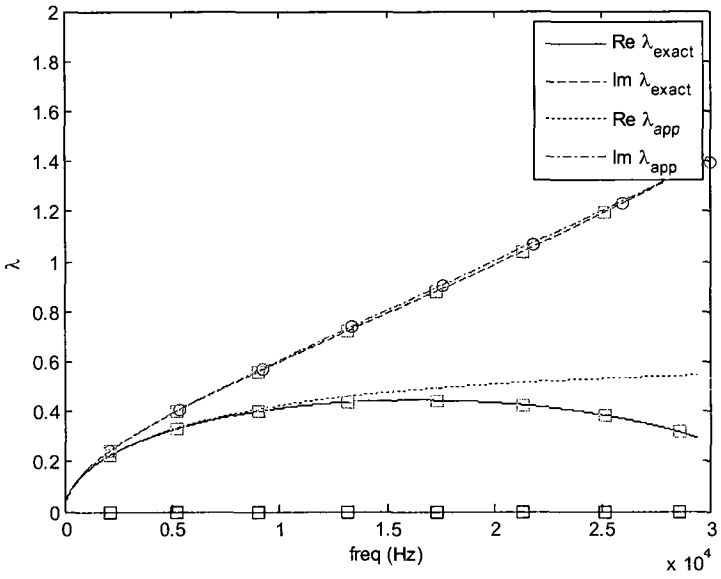

Figure 6.12: Comparison of exact and approximate natural frequencies and wave numbers using the first-order approximation for the dispersion equation, for circumferential mode $n = 1$

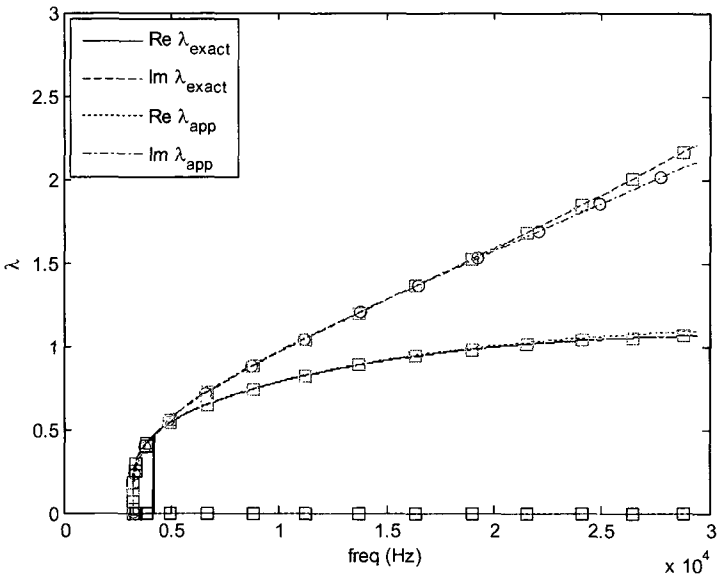

Figure 6.13: Comparison of exact and approximate natural frequencies and wave numbers using the first-order approximation for the dispersion equation, for circumferential mode $n = 2$

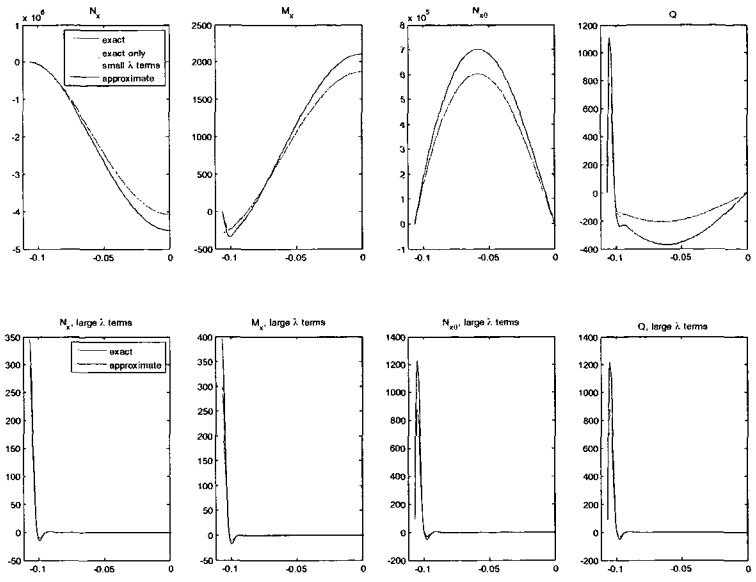

Figure 6.14: Internal forces and moments comparison, for circumferential mode $n = 1$, first mode shape

$\lambda = i\lambda_2$.

The exact wave numbers and natural frequencies are also compared with the first-order approximation in Figures 6.12 and 6.13. The circles indicate the locations of the natural frequencies on the dispersion curve using the first-order approximation of the dispersion relation and the squares show the corresponding exact value. In these figures both real and imaginary wave numbers $\lambda = \lambda_1$ and $\lambda = i\lambda_2$ are shown. It is noted that the real roots are determined using equations (6.18) and (6.19) as explained in the previous section. The natural frequency is also approximated using the eigenvalue problem in equation (6.17).

To consider the edge effect at the free ends of the cylinder, the results of the analysis

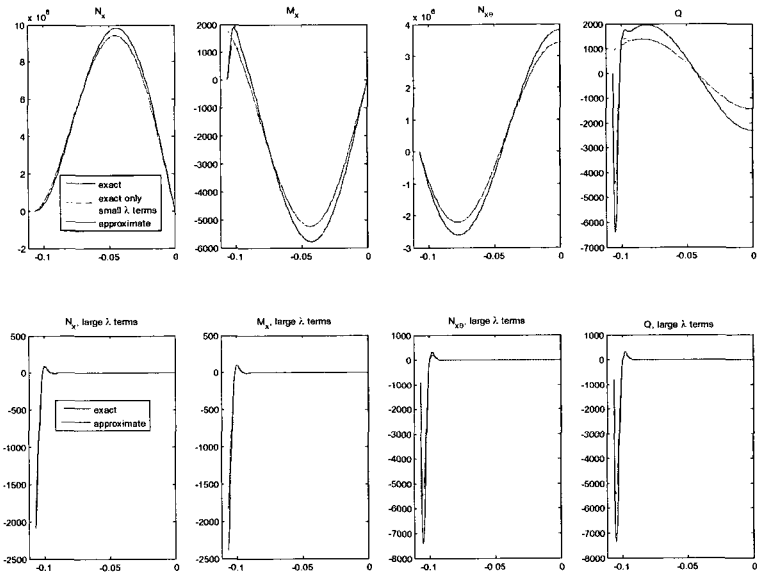

Figure 6.15: Internal forces and moments comparison, for circumferential mode $n = 1$, second mode shape

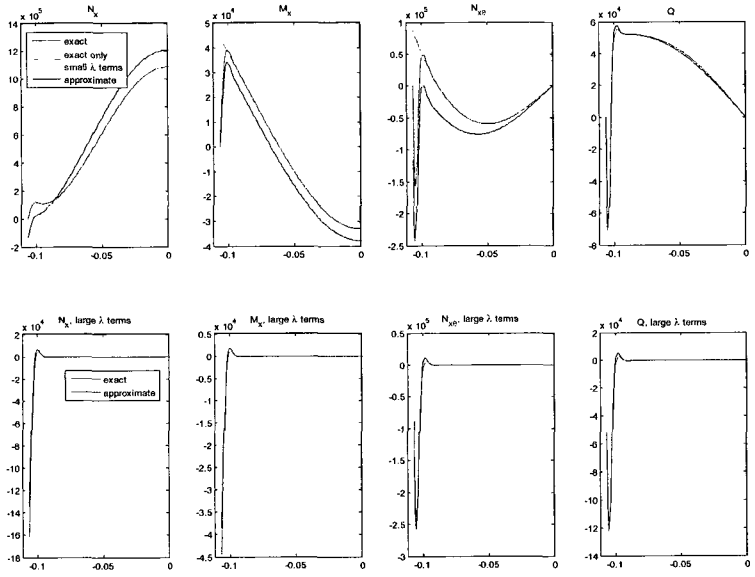

Figure 6.16: Internal forces and moments comparison, for circumferential mode $n = 2$, first mode shape

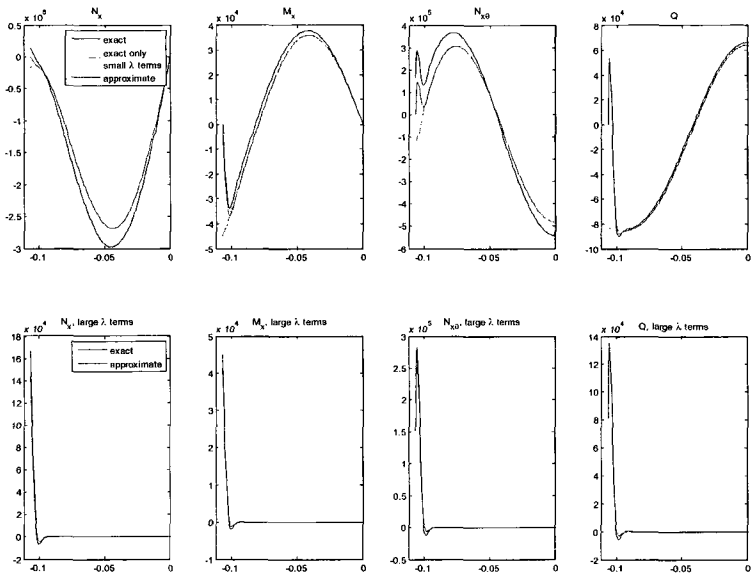

Figure 6.17: Internal forces and moments comparison, for circumferential mode $n = 1$, second mode shape

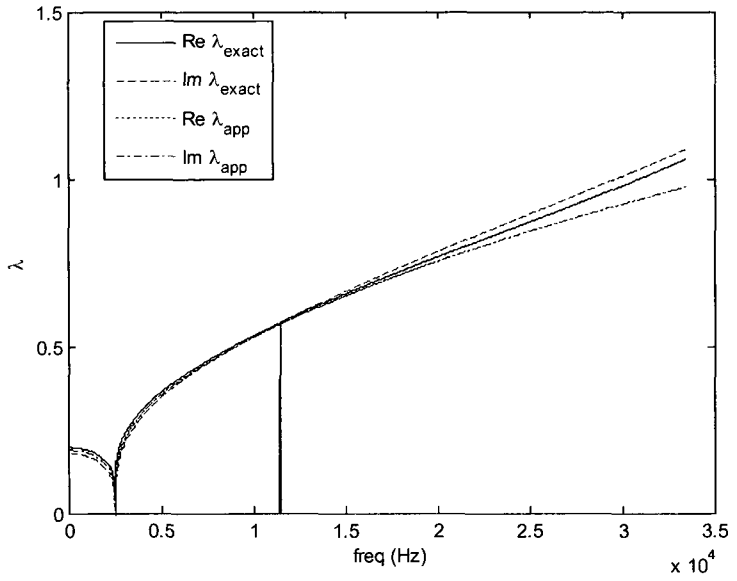

Figure 6.18: Comparison of exact dispersion relation for orthotropic laminate with the zeroth-order approximation for the dispersion relation, for circumferential mode $n = 2$

of the boundary conditions in section 6.3.3 are examined in detail. The internal forces and moments (per unit circumferential length) are plotted in Figures 6.14 - 6.17 for circumferential wave numbers $n = 1, 2$ for the first two modes. The left half of the cylinder is shown in these figures. The first row of plots shows the comparison between the exact and approximate internal forces and the second row shows the contribution of the large λ components to the internal forces which is significant only at the edges as expected. It can be seen that at the boundaries the conditions $M_x = 0$ and $Q = 0$ are satisfied. This is because these two boundary conditions are the ones used for finding the coefficients c_0 and ϕ in equation (6.20). The other two boundary conditions are approximately satisfied.

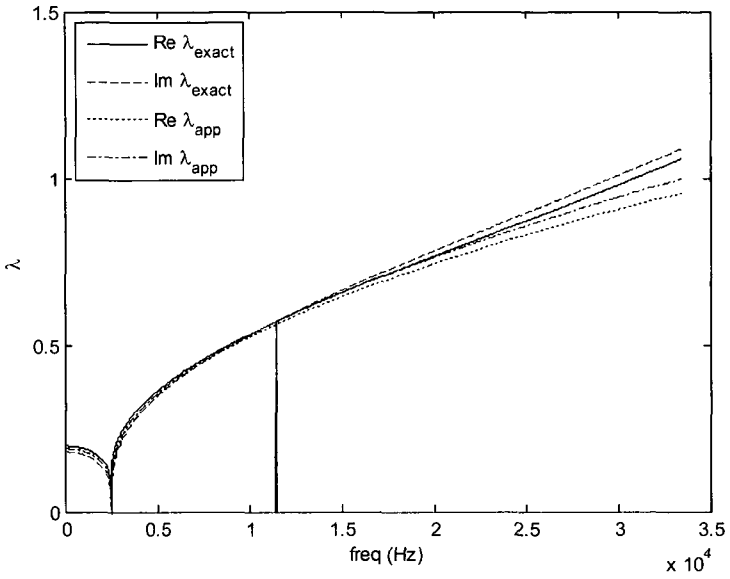

Figure 6.19: Comparison of exact dispersion relation for orthotropic laminate with the first-order approximation for the dispersion relation, for circumferential mode $n = 2$

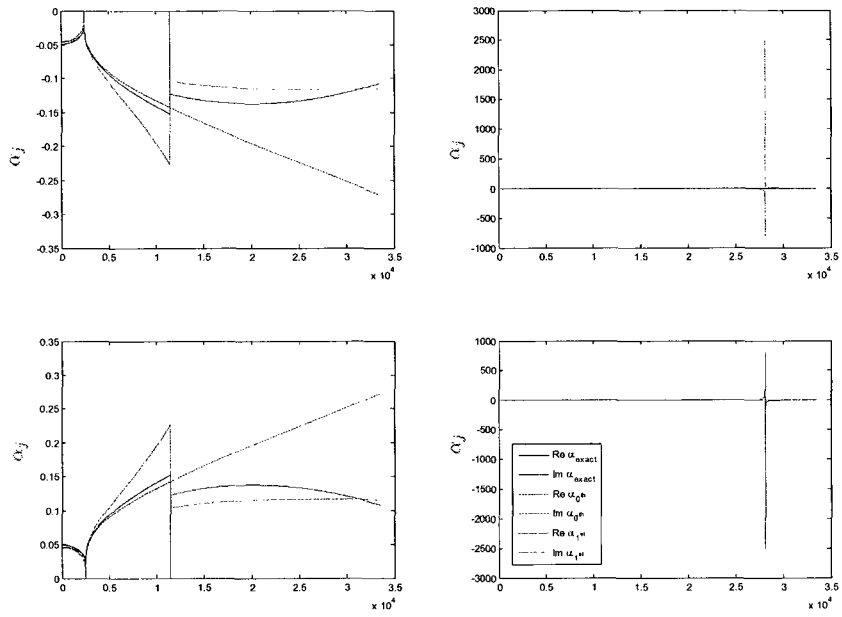

Figure 6.20: Comparison of exact, zeroth- and first-order approximations of α for orthotropic laminate, for circumferential mode $n = 2$

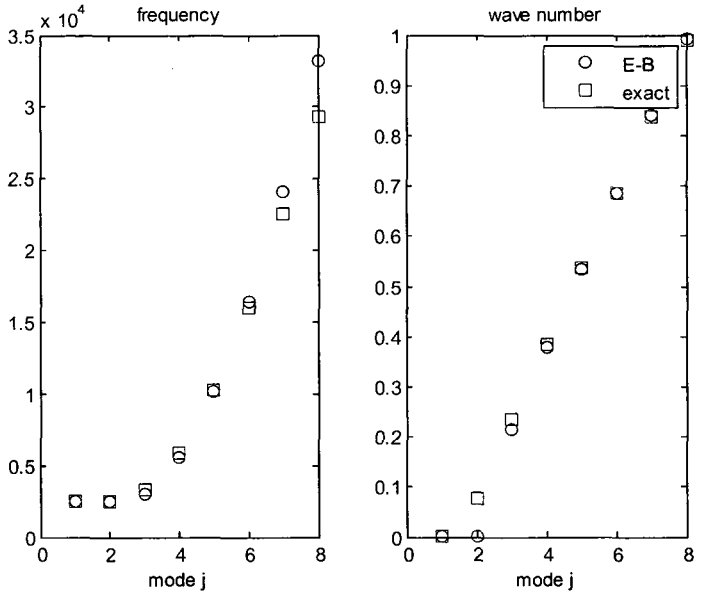

Figure 6.21: Comparison of exact and approximate natural frequencies and wave numbers for orthotropic laminate using the first-order approximation, for circumferential mode $n = 2$

For our second example, the orthotropic cylinder is considered. The results for circumferential wave number $n = 2$ are presented here. Figures 6.18 and 6.19 show the approximate dispersion relation using zeroth- and first-order approximations. It can be observed that first-order approximation is very accurate. The exact coefficient α is compared with its zeroth- and first-order approximation in Figure 6.20.

The comparison of exact and first-order approximations of natural frequencies and imaginary wave numbers are shown in Figures 6.21. In Figure 6.22, both real and imaginary wave numbers associated with the natural frequencies are shown on the dispersion

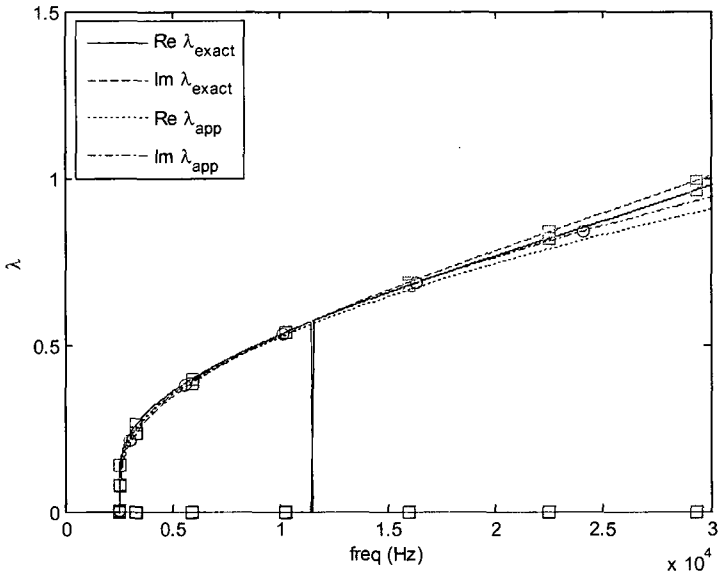

Figure 6.22: Comparison of exact and approximate natural frequencies and wave numbers for orthotropic laminate using the first-order approximation for the dispersion relation, for circumferential mode $n = 2$

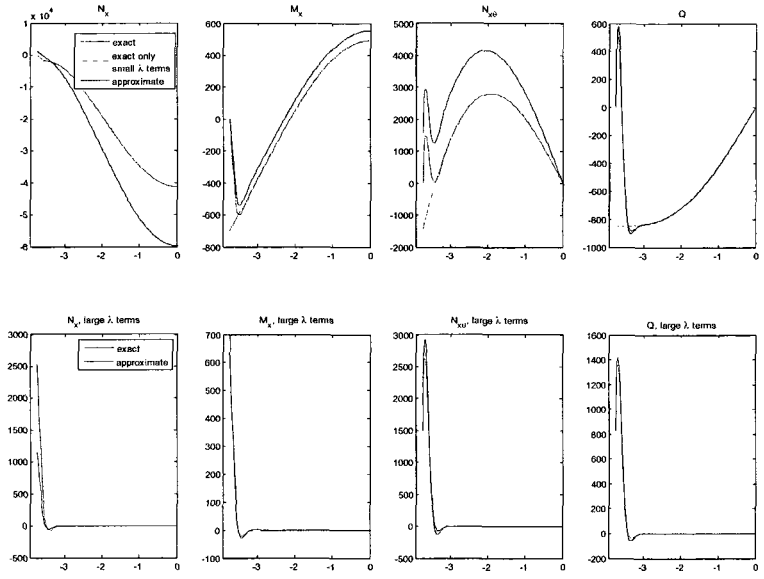

Figure 6.23: Internal forces and moments comparison for orthotropic laminate, for circumferential mode $n = 2$

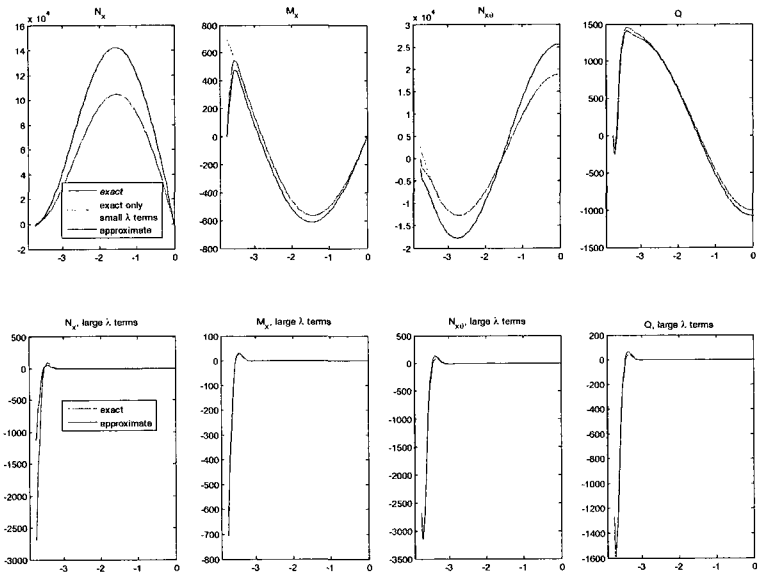

Figure 6.24: Internal forces and moments comparison for orthotropic laminate, for circumferential mode $n = 2$

curves. The squares are the exact values while the circles are the first-order approximation results. It can be seen that the wave number approximations are relatively accurate while the accuracy of the natural frequencies is good only for low to mid frequencies. The internal forces for the left half of the cylinder is shown in Figures 6.23 and 6.24 for the first two modes.

6.4.1 Application to system identification

The perturbation results in sections 6.2.1.1 - section 6.2.1.3 provides simplified dispersion relations and expressions for modal properties which can be used for system identification. If the natural frequencies of a cylinder is known from experiments, then by using the dispersion relations for the first circumferential wave number one can determine several of the material properties. For instance, the density of the natural frequencies with respect to frequency (also known as the modal density) increases in the vicinity of the point η_0. This can be seen in Figures 6.13 and 6.22. Using this property one can determine the location of η_0 and therefore evaluate D_{22} using equation (6.9). Subsequently, the zeroth-order approximation of η can be used to find a_{12}. After finding these parameters one can use the first-order dispersion relation, which contains more parameters, to evaluate the relationship between these unknowns. It is noted that the system identification application of this study is still in its preliminary stages and can progress substantially further as explained in section 7.2.

Chapter 7

Concluding remarks

In this thesis we develop new methods in solid mechanics that can be used for studying the vibration behavior of passenger car bodies in high-speed trains. Some of these methods are fundamental in nature and can be applied to other structural systems. Three related topics were examined. First, the propagation of vibration energy from the wheels of the high-speed train to the car body is investigated. Using a finite element model of the car and response data under test runs, fatigue reliability of the aluminum car body is examined. In addition, fatigue test procedures with static and dynamic loads are proposed. In the next part of the thesis, highly localized stresses near the openings are examined. A semi-analytical approach based on a method of complex variables is developed to enhance the results of coarse-mesh finite element models to predict the stress concentrations around openings. In the last part of the thesis, the vibrations of cylindrical shells are examined. This study is motivated by the fact that advanced car body designs for high-speed rail tend

to have tubular frames with orthotropic shell properties. Perturbation analysis is used to find relatively simple closed-form analytical expressions for the dispersion relation and the modal properties of the vibrating cylinders. It is shown how these relations can be used for system identification purposes. A more extended summary of this thesis is given in the following section.

7.1 Summary of results

The dynamic behavior of the passenger car in HSR-350X is studied using a combination of analytical, computational and experimental techniques. The relationships between the characteristics of the excitation and response as measured during test runs of the train under operating conditions are examined using random vibration techniques. The frequency dependent properties for the suspension between the car body and bogie are evaluated using these results and the results of a finite element analysis of the car body. This properties of the suspension are then used to obtain the power spectral density of stress due to bogie motion. These properties are also used to compute the stress transfer function at locations of the car body where the stresses are high. The stress time history due to the motion at the bogies is used to assess the fatigue reliability of the passenger cars using deterministic rainflow counting procedures as well as using stochastic techniques.

The stress patterns in the car body are examined in detail using finite element analysis. Localized stress concentrations are noted around the corners of the door and windows of the

passenger car body. Fatigue testing procedures are then proposed to reproduce, as closely as possible, these observed stress patterns. The loads for fatigue testing are determined by fitting the static and dynamic stresses and displacements to the aforementioned stress patterns.

In assessing the reliability of the car body it was found that the predicted damage due to fatigue is very small even around the door and window openings. One reason is that the mesh of the finite-element model is not fine enough to capture the stress concentration around the corners of openings. To address this limitation, a semi-analytical method is developed that can enhance the results of coarse-mesh finite element analysis to better predict the stress concentrations around rectangular openings. This method is based on a complex variable technique, but differs from previous approaches in that the boundary conditions are satisfied using regression instead of complicated contour integrals. This new semi-analytical method is used to evaluate stress concentrations around openings due to constant and linearly varying far-field moments. While the stress distributions evaluated using the proposed numerical approach have a spatial pattern that is somewhat different than fine-mesh finite element results, the magnitudes of the stresses are very similar.

The global characteristics of car body vibrations are examined by studying the vibrations of orthotropic and other types of cylindrical shells. Numerical methods for solving the exact equations for the natural frequencies and mode shapes are reviewed and compared with the results of the Rayleigh-Ritz approach. The Rayleigh-Ritz approach is extended using Flügge shell theory. It is shown that, while in many cases the energy method provides

good estimates of natural frequencies, it does not result in accurate mode shapes because the mode functions assumed for the longitudinally varying components do not satisfy the three dimensional boundary conditions and do not account for edge effects.

In the last part of this thesis, perturbation analysis is used to derive analytical expressions that describe the free vibration of cylinders. These results are in terms of relatively simple closed-form mathematical expressions that provide insight into the cylinder vibration behavior. It is shown that these expressions are also useful for system identification, where free-vibration measurements are used to determine the elastic properties of the cylinder.

7.2 Future research

The high-speed train HSR-350x is now in commercial passenger operation and KRRI will soon be testing the next generation HEMU-400x with operating speed of 370 km/h. The proposed test procedures for fatigue assessment will be used in testing the new generation train. These test procedures are in the preliminary stages of development and need to be improved. For instance more points for fitting the displacements and stresses can be used in the least-squares analysis. The locations of the regression points can also be moved to the places with high stress. Alternatively, weighted least-squares analysis can be used to put more emphasis on the locations of high stress. Although only concentrated loads were considered in this study, it is planned to use distributed loads which may result in more

accuracy in matching actual loads.

In studying the highly localized stresses around corners, it was found that the spatial stress patterns estimated by the proposed approach are not completely similar to the stress patterns obtained by fine-mesh finite element analysis. It is believed that this is the result of considering only linear and constant far-field moments. We thus intend to include nonlinear variations of the far-field moments in our future studies. One other possible extension is to use the results obtained in this study in micro-mechanics problems since many micro-mechanical theories are based on models of inclusions in infinite domains. The proposed method can also be used for evaluating stress concentrations for more complex geometries. The conformal transformations can be determined numerically for holes and inclusions of a wide variety of shapes.

The perturbation analysis provides zeroth- and first-order approximations of the dispersion relation which relates wave numbers to the natural frequencies. These approximations can be used for the identification of cylinder material properties provided that experimental measurements from free vibration of the cylinder are available. For example, the perturbation analysis shows the frequency associated with the high modal density region (the region that pertains to very small longitudinal wave numbers) in the dispersion plots is related to only one of the material properties. Therefore if one can identify this frequency from experimental measurements the corresponding material property can be found accordingly. On the other hand the zeroth order approximation of the dispersion curve includes only one extra material property in addition to the one that is already identified. This material

property can be identified by matching this dispersion curve with the one obtained from experimental measurements. Once these parameters are found, one can use the higher order dispersion relations, which contain more parameters, to find the relationships between these parameters. It is noted that in the analysis developed in chapter 6 was generally restricted to orthotropic material properties. The analysis can be extended to the more general case of symmetric, balanced laminated cylinders.

Appendix A

Boundary conditions at the hole

In this appendix it is shown how the boundary conditions in equation (4.17) for a traction free hole can be rewritten in terms of the analytic functions $\phi(z)$ and $\psi(z)$. Then it is shown how these boundary conditions can be transformed into a much simpler form.

Let $s = \sin\theta$ and $c = \cos\theta$. Then equation (4.17) can be rewritten as:

$$-ks = M_x c + (M_{xy} - P)s \tag{A.1}$$

$$kc = M_y s + (M_{xy} + P)c$$

At the boundary, which corresponds to the unit circle, we have:

$$z = c + is$$

$$\overline{z} = \frac{1}{z} = c - is$$

$$\frac{dz}{d\theta} = -s + ic$$

In addition one can show:

$$2Re\int(f'dz) = \int\left(-(f'+\overline{f'})s + (f'-\overline{f'})ic\right)d\theta = (f+\overline{f}) \tag{A.2}$$

$$2Im\int(f'dz) = \int\left((f'-\overline{f'})is + (f'+\overline{f'})c\right)d\theta = -i(f-\overline{f}) \tag{A.3}$$

Therefore:

$$P = \int_0^s N_n ds = \int_0^s (N_x c + N_y s)d\theta = -2D\int_0^s \left((\phi''-\overline{\phi''})is + (\phi''+\overline{\phi''})c\right)d\theta$$

$$P = 2iD\left(\phi'-\overline{\phi'}\right)$$

Substituting the above integral into equations (A.1), the expressions for the boundary conditions in terms of the analytic functions ϕ and ψ become:

$$-D\left[(1+\nu)\left(\phi'+\overline{\phi'}\right)c + \frac{1-\nu}{2}\left((\overline{z}\phi''+z\overline{\phi''})c + (\overline{z}\phi''-z\overline{\phi''})is\right) + \right.$$
$$\left.\frac{1-\nu}{2}\left((\psi'+\overline{\psi'})c + (\psi'-\overline{\psi'})is\right) + 2i\left(\phi'-\overline{\phi'}\right)s\right] = -ks$$

$$-D\left[(1+\nu)\left(\phi'+\overline{\phi'}\right)s - \frac{1-\nu}{2}\left((\overline{z}\phi''+z\overline{\phi''})s - (\overline{z}\phi''-z\overline{\phi''})ic\right) - \right.$$
$$\left.\frac{1-\nu}{2}\left((\psi'+\overline{\psi'})s - (\psi'-\overline{\psi'})ic\right) - 2i\left(\phi'-\overline{\phi'}\right)c\right] = kc \tag{A.4}$$

These boundary conditions can be transformed into a simpler form using some integral relations. Using the relation in (A.3) one can write:

$$2Im\int(\overline{z}\phi')'dz = -i\left(\overline{z}\phi'-z\overline{\phi'}\right)$$
$$= \int\left[(\overline{z}\phi''-z\overline{\phi''})is + (\overline{z}\phi''+z\overline{\phi''})c\right]d\theta - \int\left[(\frac{\phi'}{z^2}-\frac{\overline{\phi'}}{\overline{z}^2})is + (\frac{\phi'}{z^2}+\frac{\overline{\phi'}}{\overline{z}^2})c\right]d\theta$$

The argument of the second integral in the above equation can be simplified as:

$$(\frac{\phi'}{z^2}-\frac{\overline{\phi'}}{\overline{z}^2})is + (\frac{\phi'}{z^2}+\frac{\overline{\phi'}}{\overline{z}^2})c = \frac{\phi'}{z}+\frac{\overline{\phi'}}{\overline{z}} = (\phi'+\overline{\phi'})c + (\phi'-\overline{\phi'})is$$

Therefore:

$$\int i(\overline{z}\phi'' - z\overline{\phi''})s + (\overline{z}\phi'' + z\overline{\phi''})cd\theta = \int (\phi' + \overline{\phi'})c - i(\phi' - \overline{\phi'})sd\theta - i\left(\overline{z}\phi' - z\overline{\phi'}\right)$$

The same argument can be used to show:

$$\int (\overline{z}\phi'' + z\overline{\phi''})s - i(\overline{z}\phi'' - z\overline{\phi''})cd\theta = -\int (\phi' + \overline{\phi'})s + i(\phi' - \overline{\phi'})cd\theta - \left(\overline{z}\phi' + z\overline{\phi'}\right)$$

Integrating the equations (A.4) for the boundary conditions and using the above formula one can write:

$$i\frac{1-\nu}{2}\left(\overline{z}\phi' - z\overline{\phi'} + \psi - \overline{\psi}\right) + i\frac{3+\nu}{2}\left(\phi - \overline{\phi}\right) = -\frac{1}{D}\int ksd\theta$$
$$-\frac{1-\nu}{2}\left(\overline{z}\phi' + z\overline{\phi'} + \psi + \overline{\psi}\right) + \frac{3+\nu}{2}\left(\phi + \overline{\phi}\right) = \frac{1}{D}\int kcd\theta$$

The above equations can be rewritten as:

$$z\overline{\phi'} + \overline{\psi} + n\phi = kz + k'$$

where $n = -(3+\nu)/(1-\nu)$ and k' is a complex constant of integration. It can be shown that for the case of a plate with a hole, the constants k and k' can be set to zero [Savin, 1961].

Bibliography

Abaqus documentation. *Abaqus version 6.7, ABAQUS Inc.*, 2007.

L.V. Ahlfors. *Complex analysis: An introduction to the theory of analytic functions of one complex variable.* third edition, 1979.

Americal Association of Railroads. *Specification for design, fabrication and construction of freight cars, M-100*, January 1986. Standard, Manual for standard and recommended practices, Section C, Part II.

T. L. Anderson. *Fracture mechanics.* Taylor and francis group, third edition, 1994.

R.D. Blevins. *Formulas for natural frequency and mode shape.* Robert E Krieger Co., 1979.

E. N. Bryukhanova. Thermal stress in a circular cylinder with regularly arranged circular cavities. *Internation Journal of applied mechanics*, 5(4):380–384, 1967.

C. W. Bert, J. L. Baker, and D. M. Egle. Free vibrations of multilayer cylindrical shells. *Journal of composite materials*, 3:480–499, 1969.

BIBLIOGRAPHY

C. Chen and J. Hsu. The stress intensity factors of slightly undulating interface cracks of bimaterials. *International journal of fracture*, 80:277–293, 1996.

H. C. Chen. Special finite element including stress concentration effects of a hole. *Journal of finite element analysis and design*, 13:249–258, 1993.

K. P. Chong and W. J. Pinter. Stress concentrations of tensile strips with large holes. *Journal of computers and structures*, 19(4):583–589, 1984.

R. W. Clough and J. Penzien. *Dynamics of structures*. McGraw Hill Inc, second edition, 1993.

I. M. Daniel and O. Ishai. *Engineering mechanics of composite materials*. Oxford University Press, 1994.

A. P. Datsyshin and G. P. Marchenko. Interaction of curvllinear cracks with the boundary of an elastic half-plane. *Journal of material science*, 20(5):466–473, 1985.

D.J. Thompson and C.J. Jones. A review of the modeling of wheelrail noise generation. *Journal of sound and vibration*, 231(3):519–536, 1999.

S. B. Dong. Free vibrations of laminated orthotropic cylindrical shells. *Journal of acousitical society of America*, 44(6):1628–1635, 1968.

A. J. Durelli, V. J. Parks, and V. J. Lopardo. Stresses and finite strains around an elliptic hole in finite plates subjected to uniform load. *International journal of nonlinear mechanics*, 5:397–411, 1970.

BIBLIOGRAPHY

J. Farm. Interior structure-borne sound caused by the sleeper passing frequency. *Journal of sound and vibration*, 231(3):831–837, 2000.

Z. Feng and R. E. Rowlands. Smoothing finite element and experimental hybrid technique for stress analyzing composites. *Journal of computers and structures*, 39(6):631–639, 1991.

K. Forsberg. Influence of boundary conditions on the modal characteristics of thin cylindrical shells. *Journal of AIAA*, 2(12):2150–2157, 1964.

K. Forsberg. Axisymmetric and beam-type vibrations of thin cylindrical shells. *Journal of AIAA*, 7(2):221–227, 1969.

H. Hafiani and J. F. Dwyer. Edge function analysis of anisotropic materials with holes and cracks. *Journal of computers and structures*, 72:779–791, 1999.

K. X. Hu, A. Chandra, and Y. Huang. Multiple void-crack interaction. *International journal of solids and structures*, 30(11):1473–1489, 1993.

T. Igusa. Development of design recommendations for light car bodies with high structural reliability. Technical report, KRRI Research Reports, 2008.

I.L. Ver, C.S. Ventres, and M.M. Myles. Wheelrail noise- partiii: Impact noise generation by wheel and rail discontinuities. *Journal of sound and vibration*, 46(3):395–417, 1976.

K. H. Ip, W. K. Chan, P. C. Tse, and T. C. Lai. Free vibrations of laminated orthotropic cylindrical shells. *Journal of acousitical society of America*, 44(6):1628–1635, 1968.

BIBLIOGRAPHY

H. Ishikawa and Y. Kohno. Analysis of stress singularities at the corner point of square hole and rigid square inclusion in elastic plates by conformal mapping. *International journal of engineering science*, 31(8):1197–1213, 1993.

J. M. Henshaw, J. R. Sorem Jr, and E. H. Glaessgen. Finite element analysis of ply-by-ply and equivalent stress concentrations in composite plates with multiple holes under tensile and shear loading. *Journal of composite structures*, 36:45–58, 1996.

J. S. Kim. Fatigue assessment of tilting bogie frame for korean tilting train: analysis and static test. *Journal of engineering failure analysis*, 13:1326–1337, 2006.

L. P. Kollar and G. S. Springer. *Mechanics of composite structures*. Cambridge University Press, 2003.

K. Y. Lam and C. T. Loy. Influence of boundary conditions and fibre orientation on the natural frequencies of thin orthotropic laminated cylindrical shells. *Journal of composite structures*, 31:21–30, 1995.

A.W. Leissa. *Vibration of shells*. NASA SP 288, 1973.

R. S. Li. A methodology for fatigue prediction of electronic components under random vibration load. *Journal of electronic packaging*, 123(4):394–400, 1999.

M. Heckl, G. Hauck, and R. Wettschureck. Structure-borne and sound vibration from rail traffic. *Journal of sound and vibration*, 193(1):175–184, 1996.

BIBLIOGRAPHY

M. L. Sharp, G. E. Nordmark, and C. C. Menzemer. *Fatigue design of aluminum components and structures*. McGraw-Hill, 1996.

N. I. Muskhelishvili. *Some basic problems of the mathematical theory of elasticity*. Noordhoff International Publishing, forth edition, 1975.

D. E. Newland. *An introduction to random vibrations, spectral and wavelet analysis*. Longman, third edition, 1995.

T. Nishioka and S. N. Atluri. Stress analysis of holes in angle-ply laminated: An efficient assumed stress special-hole-element approach and a simple estimation method. *Journal of computers and structures*, 15(2):135–147, 1982.

E. Pan, B. Yang, G. Cai, and F. G. Yuan. Stress analyses around holes in composite laminates using boundary element method. *Journal of engineering analysis with boundary elements*, 25:31–40, 2001.

C. S. Park. PhD thesis, Department of Mechanical Engineering, Yonesei University, 2004.

R. E. Peterson. *Peterson's stress Concentration factors*. John Wiley and Sons Inc., 1961.

R. Piltner. Special finite elements with holes and internal cracks. *International journal for numerical methods in engineering*, 21:1471–1485, 1985.

R. I. Stephens, A. Fatemi, R. R. Stephens, and H. O. Fuchs. *Metal fatigue in engineering*. John Wiley and Sons Inc., second edition, 2001.

BIBLIOGRAPHY

T. H. Richards and M. J. Daniels. Enhancing finite element boundary stress predictions for plane and axisymmetric situations. *Journal of strain analysis*, 21(1):33–44, 1986.

R. E. Rowlands, K. D. Winters, and J. A. Jensen. Full-field numerical differentiation. *Journal of strain analysis*, 13(3):177–183, 1978.

S. I. Seo, C. S. Park, K. H. Kim, B. C. Shin, and O. K. Min. Fatigue strength evaluation of the aluminum carbody of urban transit unit by large scale dynamic load test. *JSME international journal series A*, 48(1):27–34, 2005.

G. N. Savin. *Stress concentration around holes.* International series of monographs in aeronautics and astronautics. Pergamon Press, 1961.

Z. S. Shao and G. W. Ma. Free vibration analysis of laminated cylindrical shells by using fourier series expansion method. *Journal of thermoplastic composite materials*, 20:551–573, 2007.

C. B. Sharma. Calculation of natural frequencies of fixed-free circular cylindrical shells. *Journal of Sound and Vibration*, 35(1):55–76, 1974.

C. B. Sharma. Simple linear formulas for critical frequencies for cantilever circular cylindrical shells. *Journal of Sound and Vibration*, 55(3):467–471, 1977.

C. B. Sharma and M. Darvizeh. Free vibration of specially orthotropic, multilayered, thin cylindrical shells with various end conditions. *Composite Structures*, 7:123–138, 1987.

BIBLIOGRAPHY

C. B. Sharma and D. J. Johns. Vibration characteristics of a clamped-free and clamped-ring-stiffened circular cylindrical shell. *Journal of Sound and Vibration*, 14(4):459–474, 1971.

W. Soedel. *Vibrations of shells and plates*. Marcel Dekker Inc, 2004.

S. Timoshenko and S. Woinowsky-Krieger. *Theory of plates and shells*. McGraw Hill, second edition, 1959.

A. Tiwary, C. Hu, and S. Ghosh. Numerical conformal mapping method based voronoi cell finite element model for analyzing microstructures with irregular heterogeneities. *Journal of finite elements in analysis and design*, 43:504–520, 2007.

I. Tsukrov and J. Novak. Effective elastic properties of solids with defects of irregular shapes. *International journal of solids and structures*, 39:1539–1555, 2002.

L. E. Tucker. Cumulative damage analysis, sea paper 820686. Warrendale, PA, 1982. Society of automotive engineers.

T.X. Wu and D.J. Thompson. Theoretical investigation of wheelrail nonlinear interaction due to roughness excitation. Technical Report 852, Institute of sound and vibration research dynamic group, university of Shouthampton, 2000.

T.X. Wu and D.J. Thompson. A hybrid model for wheeltrack dynamic interaction and noise generation due to wheel flats. Technical Report 859, Institute of sound and vibration research dynamic group, university of Shouthampton, 2001.

BIBLIOGRAPHY

T.X. Wu and D.J. Thompson. On the parametric excitation of the wheeltrack system. Technical Report 908, Institute of sound and vibration research dynamic group, university of Shouthampton, 2003.

V.G. Ukadgaonker and D. K. N. Rao. A general solution for moments around holes in symmetric laminates. *Journal of composite structures*, 49:41–54, 2000.

E. Ventsel and T. Krauthammer. *Thin plates and shells, theory, analysis and applications.* Marcel, Dekker, Inc., 2001.

X. F. Wang and N. Hasebe. Bending of a thin plate containing a rigid inclusion and a crack. *Engineering analysis with boundary elements*, 24:145–153, 2000.

H. C. Wu and B. Mu. On stress concentrations for isotropicorthotropic plates and cylinders with a circular hole. *Journal of composites PartB: Engineering*, 34:127–134, 2003.

X. J. Wu and S. M. Cheng. A higher order theory for plane stress conditions of laminates consisting of isotropic layers. *Journal of applied mechanics*, 66:95–100, 1999.

X. Xiwu, S. Liangxin, and F. Xuqi. Stress concentration of finite composite laminates with elliptical hole. *Journal of computers and structures*, 57(1):29–34, 1995.

Y. G. Kim, S. Choi, S. W. Kim, Y. M. Kim, and T. W. Park. An experimental study on the ride comfort of the korean high-speed train. *Experimental techniques*, 33(6):30–37, 2008.

Vita

Argahvan Louhghalam was born on August19, 1978 in Tehran, Iran. After getting her high-school diploma in Tehran, she attended Iran University of Science and Technology (IUST) and received her bachelor of science in Civil Engineering in 2000. She then entered the graduate program at University of Tehran where she received her master of science in Earthquake Engineering in 2002. After graduation she worked in MAPNA Co. for two years. She then joined the Department of Civil Engineering at the Johns Hopkins University in September 2004. At Hopkins she worked under the supervision of Dr. Sanjay Arwade and received her second master of science in 2007. She has been working under supervision of Dr. Takeru Igusa since October 2007 and she is currently a candidate for PhD degree in Structural Engineering.